Measurement and Calculation of Frictional Loss in Large Two-Stroke Engines

Vølund, Anders

Publication date:
2003

Document Version
Publisher's PDF, also known as Version of record

Anders Vølund

Measurement and Calculation of Frictional Loss in Large Two-Stroke Engines

A dissertation submitted for the degree of Doctor of Philosophy

MEK-02.26.A

Department of Mechanical Engineering

Technical University of Denmark

Measurement and Calculation of Frictional Loss in Large Two-Stroke Engines
A dissertation submitted for the degree of Doctor of Philosophy

January 23, 2003

Technical University of Denmark

by Anders Vølund

MEK-02.26.A

ISBN 87-90130-36-7

Press: DTU-Tryk, 2003

Abstract

The total frictional loss in a large two-stroke marine diesel engine is rather well determined. However, the contribution (size and distribution) from the different machine elements are not well known. The aim of this study is to establish methods to measure and calculate friction in the piston assembly and guide shoe system for a large two-stroke marine diesel engine. These components are, according to Abanteriba [1995], the two major contributors to the total friction in a two-stroke marine diesel engine. The piston pack represents approximately 60% of the total mechanical loss at full load and the guide shoe system 23%. The rest of the mechanical loss is situated in the piston rod 2%, piston skirt 3% and main bearings and connecting rod bearing 12%. The mentioned values are theoretically determined by Abanteriba [1995]. Information about the friction distribution can be used in future design of these machine elements. Theoretical models for determination of frictional losses for both aforementioned bearing types are presented. Experiments revealing the size and distribution frictional loss are carried out. The results of the friction measurements are used for verification of theoretical models. This requires additional information such as oil film thickness, pressure and temperature. These parameters are measured and compared with simulations. Studies concerning reduction of the overall frictional loss for both bearings are carried out.

Note: Since the measurements are conducted on a T50MX engine (the research engine located at MAN B&W Diesel A/S's facility) data for the given engine will be used in this paper. Drawings of the most important components are presented in Appendix A.1.

Abstrakt (Dansk)

Det totale friktionstab i en stor totakts skibsdieselmotor er relativt veldefineret.
Imidlertid er størrelse og fordeling af friktionstab fra de enkelte maskinelementer ikke umiddelbart kendte. Målet med dette studie er at generere metoder til at måle og beregne friktion i stempelringsmekanismen og guideskolejet i en stor totakts skibsdieselmotor.
Disse to komponenter er ifølge Abanteriba [1995] de to største individuelle bidragsydere til det totale mekaniske tab. Stempelringspakken står for ca. 60% af det samlede mekaniske tab ved fuldlast og guideskolejet for ca 23%.
Resten af friktionstabene fordeler sig med 2% i stempelstangspakdåsen, 3% i stempelskørtet og hovedlejer og plejlstangslejer står for tilsammen 12%. De førnævnte værdier er teoretisk bestemt ved fuldlast af Abanteriba [1995] .
Information vedrørende fordelingen af friktionstab kan benyttes i fremtidige design af disse maskin elementer. En teoretisk model til bestemmelse af friktionstabene for hvert leje er presenteret. Yderligere er der foretaget en eksperimentiel bestemmelse af friktionstabene.
Måleresultaterne er benyttet til verifikation af de teoretiske modeller. For at gøre dette er information om for eksempel oliefilm tykkelse, tryk og temperatur nødvendige. De nødvendige parametre er målt og sammenlignet med beregnede størrelser. Endeligt er der foretaget et studie vedrørende sænkning af friktionstabet på begge lejer.
Note: Da målingerne blev udført på MAN B&W Diesel A/S's testmotor er alle data, der er benyttet, relateret til netop denne motor. Tegninger af de vigtigste komponenter er presenteret i Appendix A.1.

Contents

Nomenclature

A	Constant of integration	[]
A_C	Contact area of asperities	$[m^2]$
B	Constant of integration	[]
$B_{i,j}$	Damping coefficient of oil *	$[Nms, Ns/m]$
B_{oil}	Damping stiffness of oil	$[Ns/m]$
$B_{rot,oil}$	Rotational damping stiffness of oil	$[Ns]$
C	Total clearance in bearing	$[m]$
C_r	Location of height of arc	$[-]$
D_{piston}	Bore of engine	$[m]$
D_{shoe}	Half the Distance from one guide shoe bearing surface to the other	[m]
F_{asp}	Load carried by asperities	$[N]$
$F_{fric,asp}$	Friction generated by asperities	$[N]$
$F_{fric,oil}$	Friction generated by oil film	$[N]$
$F_{fric,reac}$	Friction reaction force	$[N]$
F_{fric}	Total friction in bearing	$[N]$
F_{oil}	Load carrying capacity of oil film	$[N]$
$F_{press,i}$	Load acting from pressure in direction i	$[N]$

F_{reac} Reaction force ..... $[N]$

H_T Dimensionless average oil film thickness ..... $[-]$

H_m Dimensionless nominal oil film thickness ..... $[-]$

$K_{i,j}$ Stiffness coefficient of oil * ..... $[N/m, N]$

K_{oil} Stiffness of oil ..... $[N/m]$

$K_{rot,oil}$ Rotational stiffness of oil ..... $[N]$

L Length of connecting rod ..... $[m]$

L_{plane} Length of guide plane ..... $[m]$

L_{shoe} Length of guide shoe ..... $[m]$

MEP Middle induced Pressure ..... $[Pa]$

M_{ext} Moment externally applied ..... $[Nm]$

M_{fric} Moment generated by shearing ..... $[Nm]$

M_{oil} Moment generated by oil film ..... $[Nm]$

N_{groove} Number of oil grooves on bearing surface ..... $[-]$

POS Vertical position of center of gravity of guide shoe ..... $[m]$

P_{lost} Lost power ..... $[hp]$

R_a Arithmetic average of surface roughness ..... $[m]$

S Stroke of engine ..... $[m]$

TT Temperature of oil ..... $[K]$

W_C Load carried by asperities ..... $[N/m]$

W_{ring} Width of piston ring ..... $[m]$

W_{shoe} Width of guide shoe ..... $[m]$

α	Coefficient of friction	[]
α_{oil}	Viscosity temperature coefficient	$[1/K]$
β	Radius of curvature at the peak of the asperity	$[m]$
δ_i	Local roughness amplitude	$[m]$
η	Dynamic viscosity	$[Pas]$
η_s	Asperity density	$[-]$
γ_i	Orientation of surface roughness at surface i	$[-]$
$\overline{T}$	Load carrying capacity *	$[N, Nm]$
$\overline{\dot{v}}$	Speed *	$[m/s, rad/s]$
$\overline{h_T}$	Average oil film thickness	$[m]$
$\overline{p}$	Average pressure in oil film	$[Pa]$
$\overline{v}$	Position *	$[m, rad]$
ϕ_s	Shear flow factor	$[-]$
ϕ_x	Pressure flow factor direction x	$[-]$
ϕ_z	Pressure flow factor direction z	$[-]$
ϕ_{fp}	Mean pressure flow factor	$[-]$
ϕ_{fs}	Shear stress flow factor	$[-]$
ϕ_f	Shear stress flow factor	$[-]$
ρ	Density of oil	$[kg/m^3]$
σ	Standard deviation of the combined surface roughness	$[m]$
σ_i	Standard deviation of surface roughness at surface i	$[m]$
τ	Shearing of oil film	$[Pa]$

τ_0 Shear strength of surface film ..... $[Pa]$

φ Attitude angle ..... $[-]$

f_i^j Constant ..... $[-]$

h Oil film thickness ..... $[m]$

h_0 Oil film thickness ..... $[m]$

h_T Local oil film thickness ..... $[m]$

h_∞ Oil film thickness left on liner ..... $[m]$

h_{in} Oil film thickness at inlet ..... $[m]$

h_{min} Minimum oil film thickness ..... $[m]$

h_{out} Oil film thickness at outlet ..... $[m]$

m Viscosity temperature coefficient ..... $[-]$

p Pressure in oil film ..... $[Pa]$

$p_{comb,max}$ Maximum combustion pressure ..... $[Pa]$

$p_{combustion}$ Pressure in combustion chamber ..... $[Pa]$

p_{down} Pressure below piston ring ..... $[Pa]$

$p_{interringi-j}$ Pressure between ring i and j ..... $[Pa]$

p_{max} Maximum pressure in bearing ..... $[Pa]$

p_{min} Minimum pressure ..... $[Pa]$

p_{pre} Pre-tension load from tension of ring ..... $[Pa]$

$p_{scavenging}$ Pressure in scavenging ports ..... $[Pa]$

p_{up} Pressure above piston ring ..... $[Pa]$

q_{cav} Flow into the cavitated region ..... $[m^2/s]$

r_p	Radius of curvature	$[m]$
t	Time	[s]
$t_{runintime}$	Time needed for running in	[s]
u	Sliding speed in x-direction	$[m/s]$
v	Sliding speed in z-direction	$[m/s]$
w	Squeeze term	$[m/s]$
*	Unit depends on problem	

Chapter 1

Introduction

Two-stroke marine diesel engines are typically installed in large ships. These can for instance be crude carriers, tankers or container ships. The demand for transportation over sea is increasing and therefore also the demand for new engines. These two stroke engines are ranging in power from 2000 to over 100000 horse power rated output.

1.1 Typical Engines for Large Ships

Generally speaking there are 3 propulsion systems for large ships. These are listed below.

- Steam Turbines
- Four-stroke Engines
- Two-stroke Engines

Steam turbines are not used very much anymore for large ships since they are quite fuel inefficient. Furthermore, they require a reduction gear with a gear ratio of approximately 40 or more in order to maximize propeller performance. Four-stroke engines are comparable to two stroke engines in fuel consumption but their main disadvantage is the speed. Since they usually run at higher revolutions a reduction gear is needed. This is due to the fact that the speed of the propeller has to stay as low as possible in order to maximize propeller efficiency. Two stroke engines which fires at every cycle can operate with a smaller fuel consumption than four stroke engines. Furthermore no reduction gear is required in order get the right angular velocity of the shaft. One disadvantage is their relatively larger physical dimensions.

1.2 Historical Review

Since the first B&W engine was installed in 1912 in 'Selandia' the engine has undertaken a huge development. The major advances have been achieved in the increased thermal efficiency

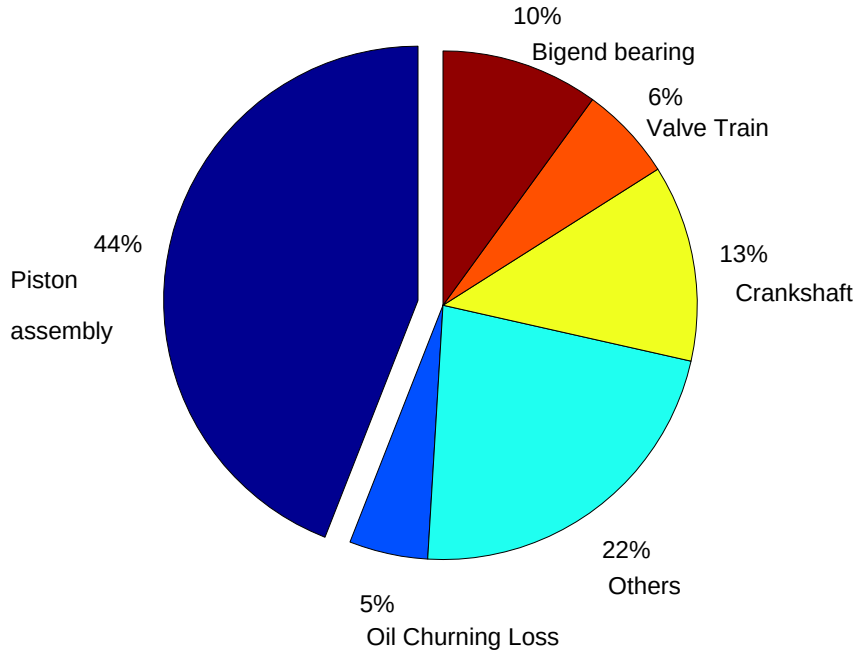

Figure 1.1: The distribution of frictional losses in four stroke engines

in order to reduce the size and increase the power and reliability. However, the layout has not changed much. One of the major advances in thermal efficiency has been the introduction of the turbocharger. Running an engine without turbocharger required large engines to produce the required amount of propulsion energy. Furthermore, the fuel consumption of the larger engines was a significant running cost. This, however, was not a very central aspect prior to the energy crisis in the early seventies. Once the turbocharger was implemented in the 1950's the relative size was significantly reduced. It was the energy crisis in 1970's which really put focus on fuel consumption. Until then steam turbines were used on many ships (mostly tankers) for propulsion system, but that dramatically changed since the two-stroke engine was approximately twice as fuel efficient as the steam turbine. Ever since the energy crisis fuel consumption has been a very important and competitive parameter. Therefore a lot of effort has been put into improving the thermal efficiency. The thermal efficiency is now approaching the optimal value. Going through the engine for power losses - the mechanical loss is relevant. This has been done for instance by Priest et al. [1998] and Ruddy and Hildyard [1993] who revealed that approximately $5-7\%$ of the total generated power is lost to mechanical friction. Examining the distribution and size of the friction loss can supply the manufacturer with a tool for minimizing the total mechanical loss. See figure 1.1 for distribution according to Ruddy and Hildyard [1993].

1.3 Presentation of a Typical Two-stroke Engine

A side view of a typical two-stroke marine diesel engine is presented in figure 1.2.

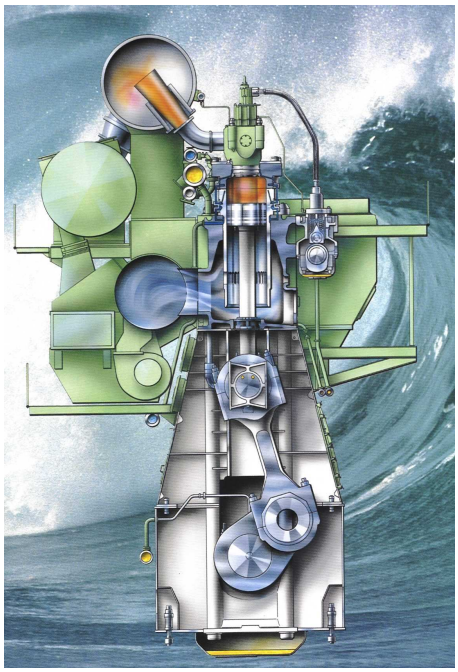

Figure 1.2: Cross section view of a large two stroke engine

The two major contributors to the mechanical frictional loss are the guide shoe bearing and the piston ring pack.
The guide shoe is seen in figure 1.3. The function of the guide shoe is to counteract the horizontal force generated by the connecting rod mechanism.
The piston pack and liner is seen in figure 1.4. The function of the piston is to transport the cylinder pressure on to the piston rod. The function of the piston rings is to maintain a pressure difference over the piston such that the resultant force on the piston is as large as possible. At present there are four piston rings installed. The function of the piston skirt is to counteract side forces arising from a misalignment or from external inputs. These inputs could for instance be generated from a rolling motion of the ship or simply by vibration of the entire engine.
The distribution of the mechanical losses has been examined for small two-stroke engines and for four-stroke engines. A comparison study regarding the total mechanical loss for a large two-stroke and a four-stroke marine engine has been carried out by Abanteriba [1995].
This revealed that the total amount of lost power for the two components mentioned above was up to $\approx$ 80% of the total mechanical loss, which is approximately 5% of the total generated power. The same is seen in figure 1.1 for a typical four stroke engine. Note that the 44% lost in the piston assembly may be correlated to the losses in the guide bearing and

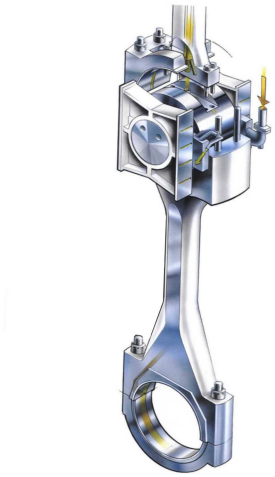

Figure 1.3: Guide shoe arrangement

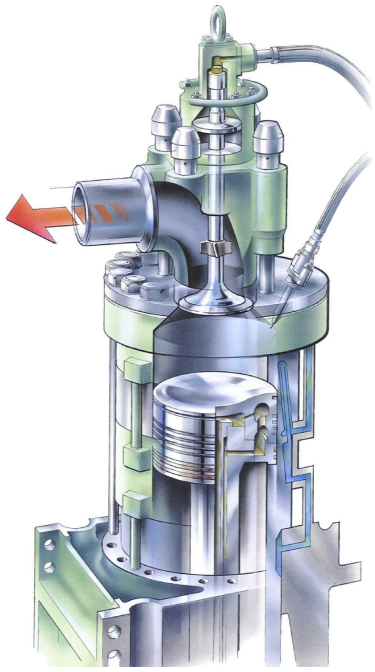

Figure 1.4: Piston assembly arrangement

piston rings for a two stroke engines. Note that the sources of friction are different between the two representations. Abanteriba [1995] does not include the 'Valve train', 'Oil churning loss' and 'Others' as the presentation shown in figure 1.1 shown by Ruddy et al. [1981].

1.4 Characterization of Friction and Lubrication

Two surfaces having a relative motion generates heat by friction. The nature of friction is determined by for instance the load, the material of the surfaces, the appearance (The surface finish) and the fluid (air, water, oil etc.) trapped between the two surfaces.
The traditional understanding of friction is related to a coefficient of friction ($\mu = \frac{F_{friction}}{F_{normalload}}$), as introduced by Amonton and Coulomb. The basic models have been extended over the years but generally speaking the coefficient of friction depends on the surface topography, the material, the relative motion and the load.
Friction can be either constructive or destructive. Bearing friction is often destructive since heat is generated and power is lost.
There are ways of controlling the coefficient of friction. Lubricating the surfaces with a fluid is a way of reducing the coefficient of friction by several orders of magnitude. The nature of the lubrication regimes can be characterized by the fluid film parameter given in equation 1.1.

$$\lambda = \frac{h_{min}}{\sqrt{\sigma_i^2 + \sigma_j^2}} \tag{1.1}$$

Where

- σ_i is the root mean square of the surface roughness at surface i.
- h_{min} is the minimum film thickness.

The value of λ determines the lubrication regime. The different regimes are listed in the next three sections indicating the value of λ as well.

Fluid Film Lubrication ($2 < \lambda < 100$)

An ideal situation is obtained if the solid surfaces operate such that the two surfaces are fully separated. This is called fluid film lubrication and it is a condition which is to prefer in most bearings. The bearings listed below usually operate under these circumstances.

- Journal bearings
- Thrust bearings
- Slider bearings

Within this lubrication regime the nature of lubrication can be divided into different categories regarding the relative load.

- Hydrodynamic Lubrication (HL)($5 < \lambda < 100$)
- Elasto Hydrodynamic Lubrication (EHL)($2 < \lambda < 100$)
  - Hard EHL($2 < \lambda < 5$)
  - Soft EHL($5 < \lambda < 100$)

If the relative load is small - Hydrodynamic Lubrication is present. If the load increases such that the surfaces of the bearing deforms, the lubrication condition is elasto-hydrodynamic. There are two modes of EHL, soft and hard EHL. Viscosity-pressure effects are not important in soft EHL. If the load is very high as for instance in rolling element bearings ($p_{max} > 0.7$ GPa) hard EHL is present and the viscosity may change several orders of magnitude.

Partial Lubrication ($1 < \lambda < 3$)

Sometimes it cannot be ensured that the two surfaces do not touch each other. If the degree of interaction is small Partial (or Mixed) Lubrication is present. In Partial Lubrication the surface roughness of the surfaces compared to the minimum film thickness are of the same order of magnitude. This means that the two surfaces occasionally touch each other due to the surface roughness. Since the surface roughness parameter σ_i is a statistical value some asperities will be larger than this value and therefore asperity interaction may occur. In this context some wear will be present and therefore the component must eventually be exchanged. However, the most important load absorber is still the lubricant trapped between the bearing surfaces. Partial lubrication can for instance be seen in :

- Piston rings
- Cam system

When this takes place both HL and EHL can be present in the regions where asperity interaction is not present.

Boundary Lubrication ($\lambda < 1$)

If the λ is less than one boundary lubrication is present. It is no longer the lubricant that carries the most of the load but the asperities. This configuration is subjected to significant wear and therefore the component must be exchanged after some time. Boundary lubrication can for instance be seen in :

- Piston rings (Depending on the actual operating condition)

- Rubbing sleeve bearings
- Break pads

1.5 Comments on Guide Shoe Friction

The function of the guide shoe is to counteract the horizontal force generated by the connecting rod mechanism. The bearing design reveals that this is designed to be a fluid film bearing, which means that the parts are always fully separated by oil. The guide shoe consists of two bearing pads. The guide shoe system for a two-stroke engine was investigated theoretically by Abanteriba [1995] by the use of infinitely wide bearing theory with finite width correction factors. The system was assumed to be viewed as a rectangular thrust bearing with parallel surfaces. This information is also available in the common literature on lubrication, see for instance Hamrock [1994], where general theory for thrust bearings is presented. In the same context a tapered bearing is examined but not the correlation between the two. A similar approach was presented by Rodkiewicz and C. [1974] for a thermal active bearing and by Rohde and Kong [1975] for a regular slider bearing. Including the inclination of the guide shoe and examining the characteristics concerning structural elasticity will be examined in the dissertation. Furthermore, a practical approach is addressed such that the friction and other relevant parameters are measured in order to discuss the correlation of the models to be applied to the problem. No prior work has been done in the experimental part of this problem.

1.5.1 The Contribution From This Thesis

The aim of this work is to analyze and measure guide shoe friction. An examination of the correlation between measurement and experiment of the guide shoe system is performed. Furthermore, characteristic parameters that control friction are identified along with suggestions on how to lower the frictional loss.

1.6 Comments on Piston Ring Friction

Since there are more than one friction mechanism for the piston ring lubrication of this will be further investigated. Piston rings are subjected to a varying load and speed which often reveals that all three lubrication regimes (mentioned above) are present. Fluid film lubrication is present in the mid part of the stroke and partial lubrication is present at the ends of the stroke. Depending on the surface topography and the appearance of the surface of the components boundary lubrication might be present at the end of the strokes.
A lot of research in piston ring lubrication is taking place, but most of this research is directed on automotive engines. 2D Hydrodynamic models are widely used for instance by

Sherrington et al. [1995a], Sherrington et al. [1995b] and Yang and Keith [1996a], Yang and Keith [1996b] and Liu et al. [1998]. These models take into account that the roundness of the ring and the liner might not be the same and furthermore the influence of the ring gab. The aforementioned approaches assume that hydrodynamic lubrication is present. However, experiments have shown that mixed lubrication is present. Patir and Cheng [1978] and Patir and Cheng [1979] developed a flow model for rough surfaces. Ruddy et al. [1981] applied this model on an oil control ring. Later Nakai et al. [1996], Ping and Susumu [1993] and Priest et al. [2000] applied this on a loaded piston ring for a four stoke engine. Priest et al. [2000] has also examined different cavitation models to be applied to the problem.
However, a few studies have been conducted on two-stroke marine diesel engines. Saburi et al. [1995] calculated piston ring oil film thickness using purely hydrodynamic lubrication theory. Furthermore, wave cut was implemented in this model. However, a simple model of the piston ring was used as well as a no wear profile of the liner was used.
In the present analysis a numerical simulation will be conducted on a two-stroke marine diesel engine (Saburi et al. [1995]) but including a cavitation model (Priest et al. [2000]) and an asperity model (Greenwood and Tripp [1971]) and the surface roughness model (Patir and Cheng [1978]). The analysis will be conducted as a 2D analysis because of the appearance of the system as done by Sherrington et al. [1991]. Furthermore, the effect from the rings passing the scavenging ports will be included.
As an input for the model knowledge about the pressure drop over the rings must be known. Ting and Mayer [1974a], Ting and Mayer [1974b] has established a simple model for predicting pressure drop in the piston ring package. This model is used but with some modifications. The profile of the ring, thermal expansion of components and ring lift has been implemented in the flow model.
Measurements have shown that the frictional loss is typically in the range from 1% to 3% of the generated power. Since there is an experimental part of this project a literature study was conducted in order to see which relevant approaches have already been used. The instantaneous friction method has been tested by Mehmet and Patterson [1984], Mehmet and Patterson [1983] and Ping and Susumu [1993] with diverging conclusions. Another method 'The floating liner' method is widely used for smaller engines in order to evaluate frictional loss. For instance Halsband [1995], Wakuri et al. [1995] and Furuhama and Takiguchi [1979] have been using that method and research is ongoing in that field. The approach given by the latter will be used in the experimental part of the thesis.

1.6.1 The Contribution From This Thesis

The aim of this thesis is to analyze piston ring friction for a two stroke marine diesel engine. Parameters traditionally used in the automotive research area are included. Furthermore, it is the goal to measure friction in the piston ring pack by an approach used on automotive engines. Lastly the correlation between theory and experiment will be examined and the cha-

racteristic parameters that control friction are identified along with suggestions for lowering the frictional loss.

1.7 General info - Engine Presentation

The work presented in this thesis originates in one particular engine design. The chosen engine is as mentioned in the abstract the research engine located at the research facility which is located at the headquarter of MAN B&W Diesel A/S (MBD) two stroke division. Therefore all dimensions and properties related to the specific models used in this thesis match the components mounted inside the research engine.

Engine presentation

The engine - 4T50MX is a four cylinder two stroke engine with a bore (D_{piston}) of 500 mm. Its nominal performance is 9076 hp which is generated at a speed (n_{rev}) of 123 rpm. It has a stroke (S) of 2200 mm which is transmitted to the crank shaft via a 2885 mm long connecting rod. This engine is a bit untypical since this engine is designed to meet the future demands of engines required for the marine propulsion market. This means that the engine is designed to operate at a larger maximum pressure $p_{comb,max}$ and mean induced pressure MEP than any of the engines currently seen in the engine programme offered by MAN B&W Diesel A/S. However, it is the authors opinion that it is close enough to present and future engine designs to enable a comparison between measured and calculated frictional properties. It can thus be used to calibrate / examine the calculations carried out.

Chapter 2

Guide Shoe Presentation

The guide shoe system is mounted in a two-stroke marine diesel engine. The guide shoe is mounted on the cross head pin. The cross head transfers forces in the piston rod to the connecting rod. See figure 1.3 for assembled view and figure 2.1 for a view of the guide shoe only.

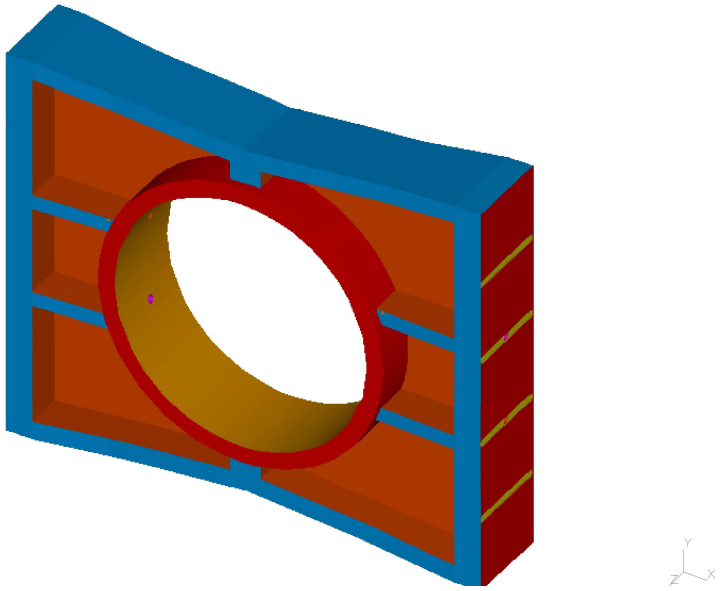

Figure 2.1: Guide Shoe

The horizontal forces generated by the connecting rod are absorbed in the guide shoe bearing. Since there are two guide shoes each consisting of two bearing surfaces the load will be distributed. The normal load depends on the engine load. As all ready mentioned the guide shoe consists of two planar bearing surfaces with four oil grooves distributed on each surface. The two central grooves are connected to the external lubrication system. The guide shoe is sliding on a guide plane. This is a long flat plane which is supported by the rest of the structure called the frame box. The design of the sliding plane for the research engine can

be seen in appendix A.1.

2.1 Dimensions and Properties

The total clearance (C) between the guide shoe and the guide planes is approximately $0.4mm$. The guide shoe length (L_{shoe}) is $0.700m$ and the width (W_{shoe}) is $0.15m$. The length of the guide plane L_{plane} is $2.9m$. The guide shoe is produced in cast steel and the bearing surface is applied with a $3mm$ layer of white metal (babbit) as bearing surface. The counterpart is made of regular steel which after welding is machined in such a way that the two opposing planes are co-planar. These planes are manufactured with a specified surface quality. The properties of the components can be seen in the production drawings presented in Appendix A.1.

Position of Guide Shoe

The vertical position of the guide shoe, the speed and the acceleration is presented in figure 2.2 for 100 % load (Full load).

Loading of Guide Shoe

A typical normal force is shown in figure 2.3 for a full load situation. Note that TDC denotes the Top Dead Center and BDP the Bottom Dead Center of the stroke. In the following it is assumed that the load is evenly distributed on both guide planes in either maneuver or exhaust side.

Lubrication of Guide Shoe

The guide shoe is lubricated from the cross head. The lubricant is supplied through the cross head via a circumferential channel in the cross head pin. Since the oil is fed to the cross head through a telescope pipe the pressure varies during one stroke. The pressure variation is caused by the volumetric change of the telescope pipe, the inertia of the system and the feed rate from the oil supply pump. The four oil grooves are machined into the bearing surface. Only the two central ones are fed with the oil from the telescope pipe. A typical pressure history in the oil supply system is shown in figure 2.4 showing large differences in oil supply pressure over time.

2.2 Service Experiences

The list of problems with this bearing type is short. Only very few problems have been encountered with this bearing type compared to the large number of guide shoe bearings

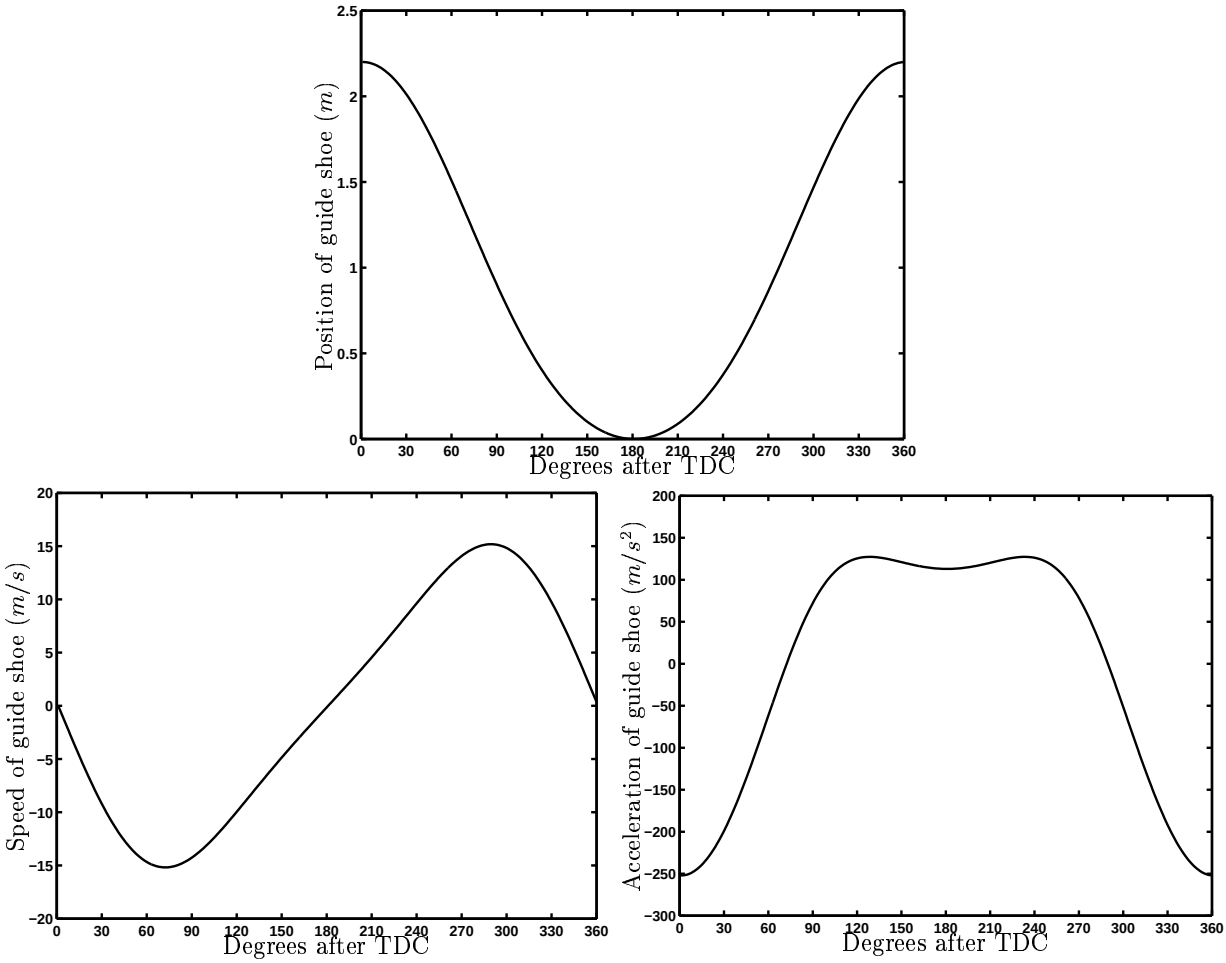

Figure 2.2: Position, speed and acceleration for the full speed condition (123 rpm).

installed (more than 6000 engines have been manufactured with this design). The usual service problems observed are production related. Having this in mind a tool for generating characteristic data for this bearing will be valuable in designing new optimal guide bearings.

2.3 Frictional Losses in Guide Shoe Bearing

So far purely theoretical considerations concerning frictional losses for this bearing have been carried out. As mentioned in the introduction an expected frictional loss of approximately 1% is expected. This quantity is to be verified theoretically and experimentally.

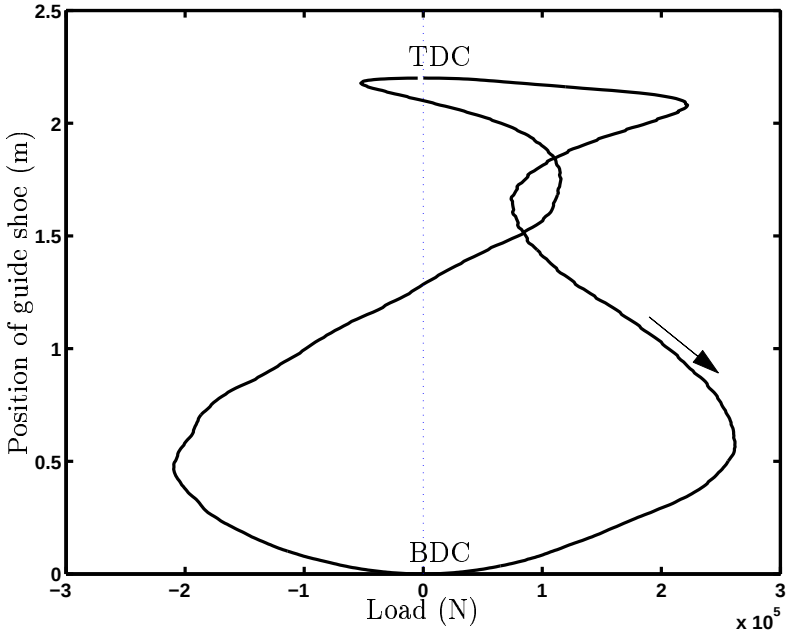

Figure 2.3: Normal load acting on both guide shoes for 100 % Load

2.4 Requirements for Calculation of Guide Shoe Characteristics

The service experiences consolidates the belief that the bearing is acting in the fluid lubrication regime.
The characteristics for this kind bearing are the oil film thickness distribution, the pressure distribution, the temperature and of course the frictional loss. All of these quantities are related to the solution of Reynolds equation for establishing the characteristics. Full separation is expected to be present in the bearing so that Reynolds equation for smooth surfaces is expected to be adequate. Since this bearing is subjected to alternating sliding speed from $+u$ to $-u$ and the normal load shifts direction in one operation cycle cavitation is likely to occur in the bearing. Focusing on the guide planes on which the guide bearing is sliding raises a new question, namely how the deformations of the guide planes influence the guide shoe characteristics. Furthermore, the assembly procedure of the guide planes suggest for initially deformed guide planes which the guide shoe must adapt to.

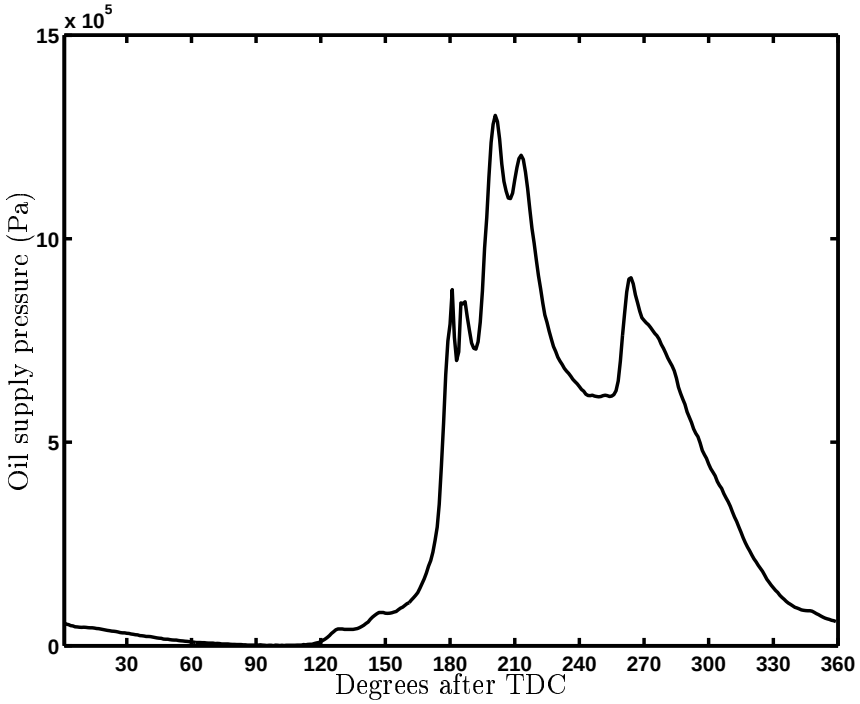

Figure 2.4: Oil supply pressure history

Chapter 3

Piston Assembly Presentation

The piston is mounted on top of the piston rod. A side view of the engine was presented in figure 1.2. The piston is seen in figure 3.1.

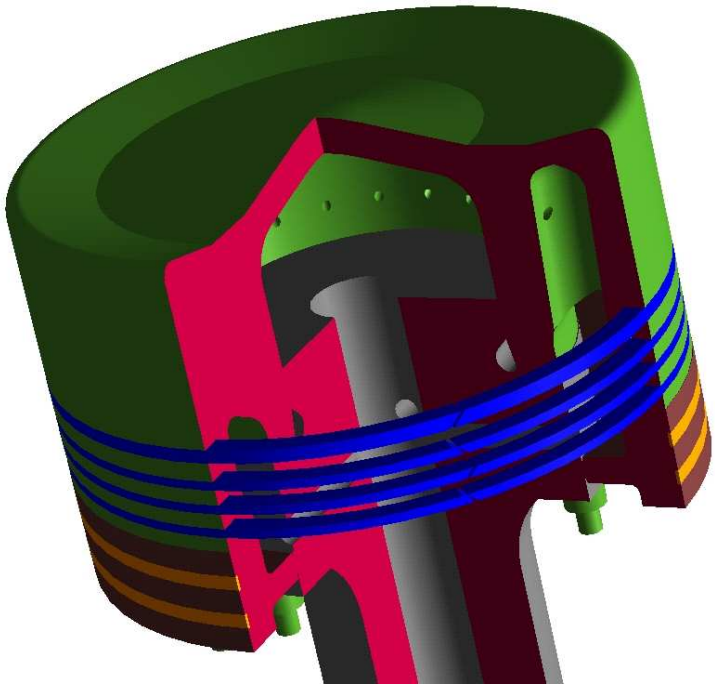

Figure 3.1: Piston mounted with piston skirt and four piston rings

3.1 Description of Characteristics Four Stroke vs. Two Stroke

A lot of studies concerning piston characteristics have been carried out. This for instance concerns:

1. Position of piston in liner

2. Movement of piston ring
3. Oil Film Thickness (OFT)
4. Wear

However, the majority of these studies have been carried out on small 4 stroke engines. There is quite a difference in operating conditions between a large two stroke diesel engine and a small 4 stroke diesel/gasoline engine. The piston diameter ratio is about 5 - 10 and the engine speed about a factor of 20-30 smaller. Furthermore, the lubricant is supplied through the piston for a four stroke engine and distributed by the oil control ring. For a two stroke marine engine oil is supplied from the liner at a discrete position. This means that the piston rings must run in the oil supplied at this particular position. This gives another OFT history than for four stroke engines. A significant issue is that two stroke engines fires at every stroke and that reduces the amount of time for a new oil film to build up.
Another issue is wear. With a total life time of 4000-6000 hours for most four stroke automotive engines the manufactures have been able to promote a strategy where part replacement is not necessary. However, for a two stroke marine diesel engine the first service overhaul is performed after 8000 hours. At that time a the wear is measured and the piston rings are be replaced if necessary. Usually this is done after 12000 hours of operation. This fact gives a completely changed focus with other requirements to materials and surface finish. Further a cylinder liner for a K90MC engine weighs about 8 tons and therefore production costs and handling are also an issue.

Piston Crown and Skirt

A typical piston crown is forged and afterwards the piston ring grooves are applied with an anti wear layer (Typically Chrome layer). The piston is cooled by cooling oil, which is circulating in the interior of the piston. The oil is supplied through the piston rod via the telescope mechanism.
The piston skirt is made from cast iron and is fitted with two stationary bronze rings in order not to provoke scuffing in the low load regime if side forces occur.

Piston Rings

A typical piston for a 2 stroke engine is mounted with 4 piston rings made of cast iron. These may be coated with a running in layer. The wear rate is approximately $0.05 - 0.1\frac{mm}{1000h}$. The piston rings have a very open surface structure due to the graphite in the cast iron.
The function of the piston rings is to seal the gas inside the combustion chamber from the gas trapped below the piston. Several rings are used in order to get a controlled pressure drop over each ring and to reduce the wear on the components.

As it is shown in figure 3.1 there are at present 4 piston rings. The top ring is a CPR-ring(Control Pressure Ring). This means that the pressure drop over the first ring is controlled in the whole lifetime of the ring - not illustrated. The three other rings are traditional oblique cut rings. The rings have a continuously changing geometry because of wear. However, each ring has approximately the same shape on the running surface after running in. Changes is observed in the ring tension which grows smaller as the rings grows thinner in radial direction. In the following it is assumed that the roughness of the ring at time t where $t > t_{runintime}$ stays the same in the larger part of the lifetime of the ring. It is assumed that the surface roughness pattern also stays the same.

Cylinder Liner:

The cylinder liner is usually made of cast iron and is afterwards machined in a certain matter so that the wear rate is kept as low as possible - at least in the early stages of its lifetime.

The liner is also subjected to wear, however not so significantly as the ring (the lifetime is substantially longer). The surface roughness of the liner is assumed to follow the same pattern as the piston ring where the surface roughness stays the same after running in.

Wave Cut

Wave cut is present in the liner. This means that the liner is machined such that the surface consists of a wavy pattern. This wave cut is eventually worn away since the depth is limited. The reason for introducing wave cut is the ability of the liner to have a small storage for oil such that wear is reduced. An analysis by Saburi et al. [1995] has been carried out in a two stroke engine but with a simple / ideal profile of the ring. No wear was subjected to the liner which meant that the profile of the liner was that of the production drawings. This is not the case since the wave cut is worn away especially near TDC and BDC.

Wave cut is not implemented in the current work since the experimental setup was not applied with such a feature.

3.2 Dimensions and Properties

The overall dimensions of the components in focus are listed in table 3.1.

Bore	D_{piston}	500	mm
Ring Width	W_{ring}	$9.5 - 12.5$	mm
Middle Induced pressure	MEP	18	bar
Max Cylinder pressure	$p_{comb,max}$	160	bar
Lube oil consumption		0.45-1.0	$g/BHPh$
Piston ring rotation speed (Estimate)		0.05	rpm

Table 3.1: Characteristic dimensions of piston assembly

Position of Piston

The piston slides in the cylinder liner according to the connecting rod mechanism. The vertical position, velocity and acceleration can be seen in figure 2.2.

Loading of Piston

The piston is subjected to the combustion pressure and carries the load generated by the combustion process to the cross head pin.
Typical combustion and interring pressures are shown in figure 3.2 for the research engine.

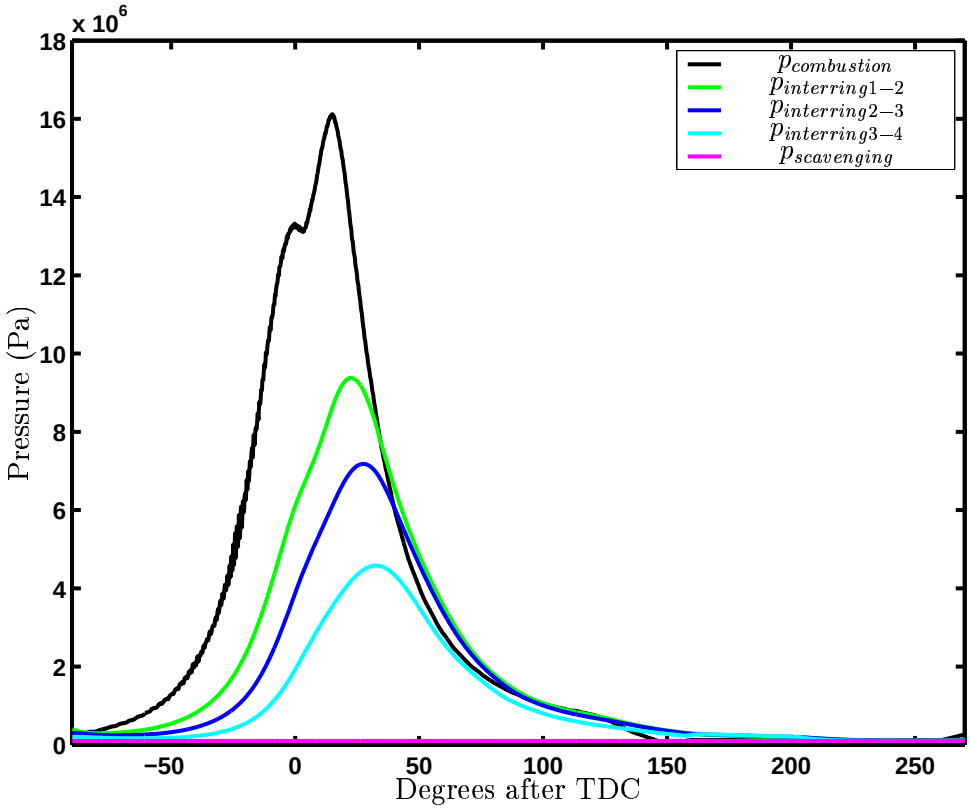

Figure 3.2: Pressure in piston ring package

Lubrication of Piston Rings

The piston rings are lubricated from the liner. The lubricant is supplied through channels machined in the liner surface. The oil is fed at an adjustable time and rate.

3.3 Service Experiences

For engines in general the list of problems with piston ring/liner is long. This is due to the fact that wear is present in this system due to solid contact between the moving parts and the liner. Therefore reduction of the wear is always the aim of work. The service experiences and tests carried out by MBD are often not very clear since there are so many parameters influencing the lubrication condition that it is hard to get good statistical data. Another factor influencing this is that the wear rate is low - typically below $0.1mm$ per $1000h$. This makes is hard to test a low of new alternatives because of the long lasting experiments.

3.4 Requirements for Calculation of Piston Ring Characteristics

The service experiences for the piston ring / cylinder liner contact states the fact that the bearing is acting in the partial lubrication regime.
The characteristics for this bearing are the oil film thickness distribution, the pressure distribution, the temperature and of course the frictional loss.
All of these quantities are related to the solution of Reynolds equation applied to the problem. Since partial lubrication is expected to be present in the bearing Reynolds equation for rough surfaces is expected to be adequate. Since the bearing is subjected to alternating sliding speed from +u to -u along with the pressure drop in the ring package cavitation is likely to occur in the ring. Due to the low speed near TDC and BDC and high load partial lubrication and asperity interaction is likely to occur.

Chapter 4

Lubrication Theory

In the current chapter the different lubrication models used in the current study are presented. The derivations shown in the following are based on two surfaces moving relative to each other with the coordinate systems shown in figure 4.1. u, v denotes the sliding speed of the surface.

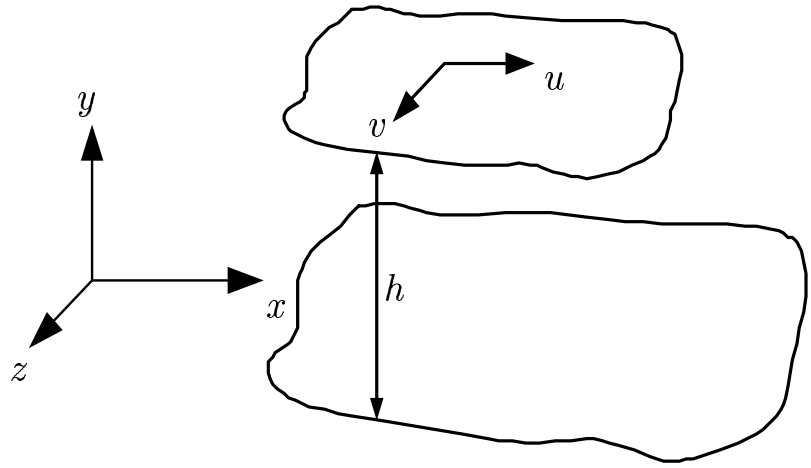

Figure 4.1: Coordinate system definition

Since the space in between the two surfaces are filled with fluid and there is a relative motion between them a pressure will build up according to Navier-Stokes equations.

4.1 Lubrication and Friction of Smooth Surfaces

One of the reduced forms of Navier-Stokes equations is Reynolds equation. There is a list of assumptions used in order to get a simple representation of the problem - and a simple solution.

- Inertial properties of the fluid film are neglected

- Fluid is assumed to be iso-viscous
- Film thickness (h) << width (W) and length (L) of bearing (2D solution)
- Iso-thermal conditions assumed
- Laminar flow
- No slip at surfaces

The general Reynolds equation is presented in equation 4.1. See for instance Hamrock [1994] for a derivation of Reynolds equation.

$$\frac{\partial}{\partial x}\left(\frac{\rho h^3}{12\eta}\frac{\partial p}{\partial x}\right)+\frac{\partial}{\partial z}\left(\frac{\rho h^3}{12\eta}\frac{\partial p}{\partial z}\right)=\frac{\partial}{\partial x}\left(\frac{\rho(u_a+u_b)h}{2}\right)+\frac{\partial}{\partial z}\left(\frac{\rho(v_a+v_b)h}{2}\right)+\frac{\partial}{\partial t}\left(\rho h\right) \quad (4.1)$$

Some of the terms in equation 4.1 may be cancelled out. The pressure variations are relatively small such that any changes in ρ are negligible. The movement of the bearing parts are often in one direction only and that states that $\frac{\partial}{\partial z}\left(\frac{\rho(v_a+v_b)h}{2}\right)=0$. Furthermore, it is assumed that only one of the surfaces are moving such that $u_a=0$. The result of these considerations can be shown in equation 4.2.

$$\frac{\partial}{\partial x}\left(\frac{h^3}{12\eta}\frac{\partial p}{\partial x}\right)+\frac{\partial}{\partial z}\left(\frac{h^3}{12\eta}\frac{\partial p}{\partial z}\right)=\frac{u}{2}\frac{\partial h}{\partial x}+\frac{\partial h}{\partial t} \quad (4.2)$$

The equation is the reduced form of Reynolds equation. For a given bearing fulfilling the requirements this differential equation can be solved. The solution to the system (the pressure distribution) can be found by the use of either analytical or numerical means depending on the problem.

4.1.1 Bearing Characteristics Smooth Surfaces

When the two surfaces are fully separated by fluid and the surface roughness is small compared to the distance between the surfaces Reynolds equation may be used in its reduced form (equation 4.2). The interesting bearing characteristics are individual depending on the aim of the study. Usually the bearing has to match some sort of external parameter. This may be an external load, a given film thickness or maybe a certain speed. A calculation is issued in order to verify a quantitative parameter.
In this thesis frictional behavior is important, therefore information about running conditions of the bearing are the aim of this study. Since the bearing in this study is loaded with a well defined external load (for example force F_{ext} and moment M_{ext}) the pressure distribution and oil film thickness are determined by solving Reynolds equation for smooth surfaces and integrated for the wanted properties. Equation 4.3 shows an example of this. The pressure

is integrated over the bearing area in order to retrieve the force and moment generated by the oil film distribution.

$$F_{oil} = \int\int p dx dz$$
$$M_{oil} = \int\int p x dx dz \tag{4.3}$$

The calculated load carrying capacity is checked for equilibrium with the external loading. Once this is established by adjusting the degrees of freedom - usually the oil film thickness, a new calculation step may be issued if the bearing is dynamically loaded. The procedure for dynamically loaded bearings is presented in chapter 6.

4.1.2 Friction for Smooth Surfaces

The frictional loss for relative movement of bearing surfaces relative to each other in sliding direction x may be calculated by equation 4.4.

$$F_{fric,oil} = \int\int \tau dx dz \tag{4.4}$$

Where the shear stress is defined as :

$$\tau = \frac{h}{2}\frac{\partial p}{\partial x} + \eta\frac{u}{h} \tag{4.5}$$

4.2 Lubrication and Friction of Rough Surfaces

In some bearings the minimum oil film thickness compared to the surface roughness is small. If the oil film thickness is of the same order as the surface roughness - local effects arising from the surface pattern may have impact on the lubrication condition. An example of this kind of lubrication condition can be seen in figure 4.2. A natural extension of that is to take into account surfaces that are not necessarily smooth and implement these into the lubrication model . Such a model has been suggested by Patir and Cheng [1978]. The Average Reynolds equation is introduced and applied to rough surfaces. An application of this is given in Patir and Cheng [1979]. This modified Reynolds equation is presented in equation 4.6. The implementation of roughness effects in Reynolds equation introduces flow factors ϕ_i, which are dependent on the surfaces appearance of the bearing. In the following isotropic, homogeneous surface roughnesses are assumed.

$$\frac{\partial}{\partial x}\left(\phi_x \frac{h^3}{12\eta}\frac{\partial \overline{p}}{\partial x}\right) + \frac{\partial}{\partial z}\left(\phi_z \frac{h^3}{12\eta}\frac{\partial \overline{p}}{\partial z}\right) = \frac{u}{2}\frac{\partial \overline{h}_T}{\partial x} + \frac{u}{2}\sigma\frac{\partial \phi_s}{\partial x} + \frac{\partial \overline{h}_T}{\partial t} \tag{4.6}$$

As shown in equation 4.6 numerous new terms are present.

The term h_T denotes the local film thickness and is defined by the the nominal film thickness h and the local roughness amplitude δ_i, shown in equation 4.7 and in figure 4.2. The dotted lines in the figure represents the mean value.

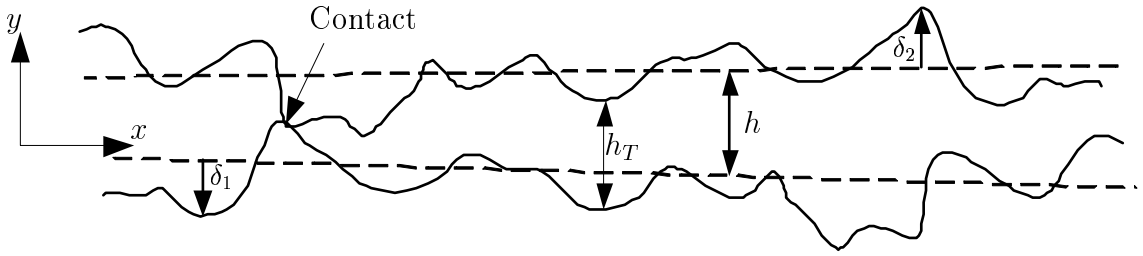

Figure 4.2: Coordinate system

$$h_T = h + \delta_1 + \delta_2 \tag{4.7}$$

Since the local roughness is a statistical value the value for $\overline{h}_T$ the average separation may be determined by equation 4.8 - see Hamatake et al. [2001].

$$\overline{h}_T = \int_{-h}^{\infty} (h + \delta) f(\delta) d\delta \tag{4.8}$$

In this context δ is the combined roughness of both bearing surfaces. $f(\delta)$ denotes the probability density of the roughness (Gaussian surfaces appearance assumed in this case and σ_i is the the standard deviation).

The result of this integration gives equation 4.9

$$\overline{h}_T = \frac{h}{2}\left(1 + erf(\frac{h}{\sqrt{2}\sigma})\right) + \frac{\sigma}{\sqrt{2}\pi} e^{\frac{-h^2}{2\sigma^2}} \tag{4.9}$$

The term σ is the standard deviation of the combined surface roughness (approximately 10% larger than the R_a value according to Ruddy et al. [1981]). The relation between H_T and H_m (defined as :$H_T = \frac{\overline{h}_T}{\sigma}, H_m = \frac{h}{\sigma}$) are plotted in figure 4.3.

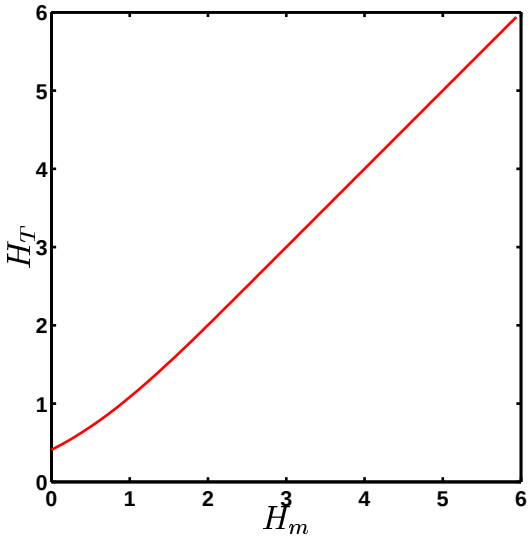

Figure 4.3: The average local film thickness H_T as function of the nominal film thickness H (Normalized)

As seen in the figure the difference between the local and the nominal film thickness are asymptotically closing in on the value for h as the nominal film thickness h increases. This is a natural extension since local effects are not relevant once the separation between the surfaces is large.

Using the relation of $\overline{h}_T$ and h and inserting into 4.6 gives equation 4.10.

$$\frac{\partial}{\partial x}\left(\phi_x \frac{h^3}{12\eta}\frac{\partial \overline{p}}{\partial x}\right) + \frac{\partial}{\partial z}\left(\phi_z \frac{h^3}{12\eta}\frac{\partial \overline{p}}{\partial z}\right) = C\frac{u}{2}\frac{\partial h}{\partial x} + \frac{u}{2}\sigma\frac{\partial \phi_s}{\partial x} + C\frac{\partial h}{\partial t} \tag{4.10}$$

,where $C = \frac{1}{2}\left(1 + erf(\frac{h}{\sqrt{2}\sigma})\right)$

The three flow terms introduced into Reynolds equation are pressure flow factors ϕ_x, ϕ_z and shear flow factors ϕ_s. The derivation can be seen in Patir and Cheng [1978]. ϕ_s is denoted the shear flow factor and can be approximated by equation 4.11 for Gaussian isotropic surfaces. The factor describes the additional flow due to sliding in a rough bearing.

$$\phi_s = \begin{cases} 1.899 H_m^{0.98} e^{-0.92 H_m + 0.05 H_m^2} & H_m \leq 5 \\ 1.126 e^{-0.25 H_m} & H_m > 5 \end{cases} \tag{4.11}$$

The shear flow factor is shown in figure 4.4, and it is obvious that the roughness effect on the shear flow factor is significant only in the small film regime.

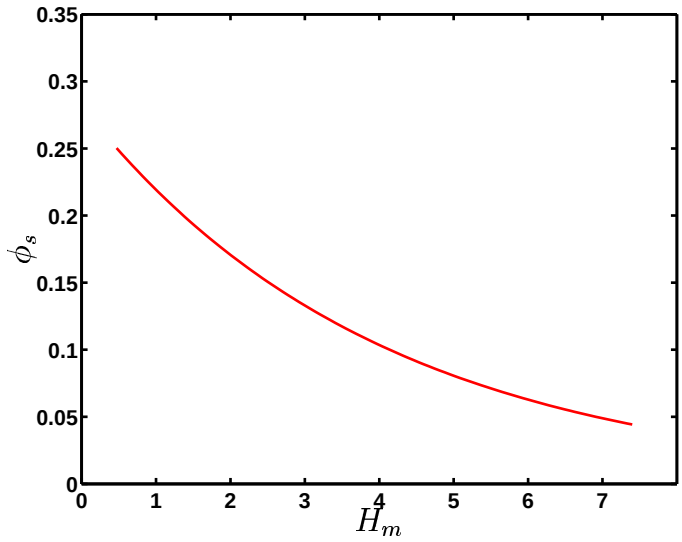

Figure 4.4: Shear flow factor

ϕ_x is denoted the pressure flow factor and can be approximated as shown in equation 4.12 for Gaussian isotropic surfaces. This factor ϕ_x compares the average pressure induced flow for a rough bearing to that of a smooth bearing.

$$\phi_x = \frac{1 - 0.90e^{-0.56H_m}}{12} \text{ for } H_m > 0.5 \tag{4.12}$$

The pressure flow factor is pictured in figure 4.5.

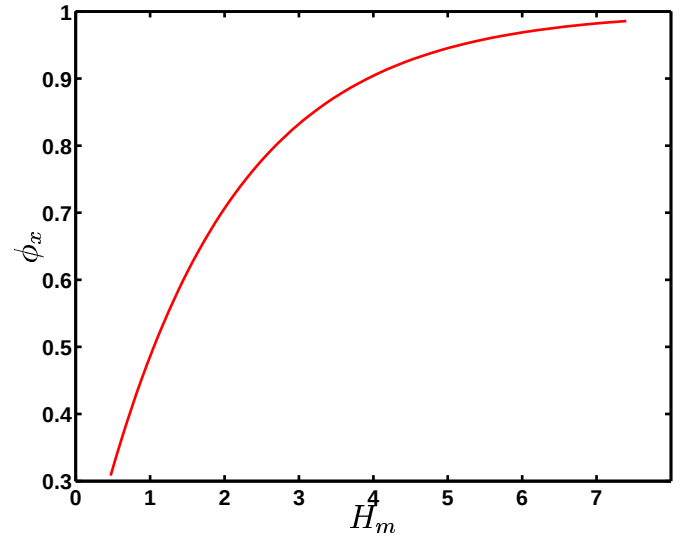

Figure 4.5: Pressure flow factor

The Reynolds equation for rough surfaces asymptotically turns into Reynolds equation when $H_m \to \infty$. That is a natural extension of the model proposed by Patir and Cheng [1978].

4.2.1 Bearing Characteristics Rough Surfaces

The load carrying capacity may now be established in the same way as for the smooth surfaces seen in equation 4.3, since no new components are introduced by the new model, except for slightly changed load carrying capacity due to altered pressure distributions. An implementation on piston rings has been given by for instance Sanda et al. [1997] or Priest et al. [2000].

4.2.2 Friction for Rough Surfaces

The frictional loss may be calculated by equation 4.4. But note that the shear stress definition is altered due to the introduction of flow factors. The new definition is shown in equation 4.13. The derivation can be seen in Patir and Cheng [1978].

$$\tau = \phi_{fp}\frac{h}{2}\frac{\partial \overline{p}}{\partial x} + (\phi_f + \phi_{fs})\frac{u\eta}{h} \tag{4.13}$$

Three new flow factors are introduced relating to she shearing of the bearing. ϕ_{fp} is the mean pressure flow factor component of the shear stress - shown in figure 4.6.

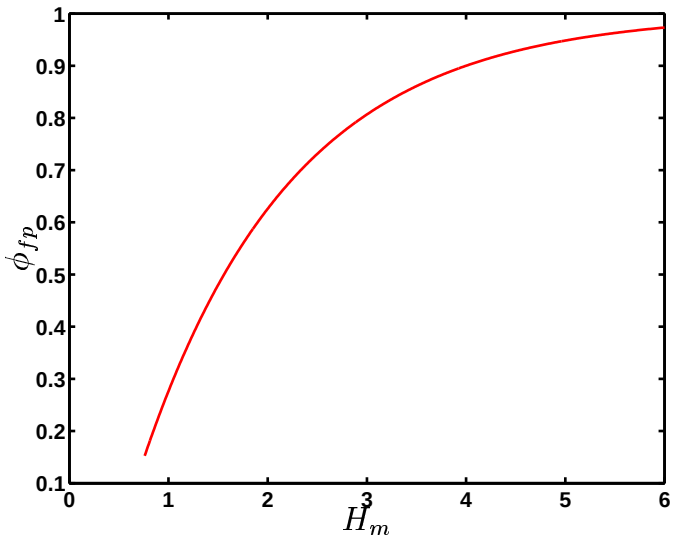

Figure 4.6: Shear stress flow factor

ϕ_f is the mean sliding velocity component of the shear stress. This can be obtained by equation 4.14. This equation requires a numerical integration. However, the solution may be approximated by equation 4.15, the dependence of h is shown in figure 4.7.

$$\phi_f = h\int_{-h}^{\infty}\frac{f(\delta)}{h+\delta}d\delta \tag{4.14}$$

$$\phi_f = \begin{cases} \frac{35}{32} z \left[(1-z^2)^3 ln \frac{z+1}{\epsilon^*} + \frac{1}{60} \left(-55 + z(132 + z(345 + z(-160 + z(-405 + z(60 + 147z)))))) \right) \right] \\ \text{for } H_m \leq 3 \\ \frac{35}{32} z \left[(1-z^2)^3 ln \frac{z+1}{z-1} + \frac{1}{15} \left(66 + z^2(30z^2 - 80) \right) \right] \\ \text{for } H_m > 3 \end{cases} \tag{4.15}$$

where $z = \frac{H_m}{3}$ and $\epsilon^* = \frac{1}{300}$

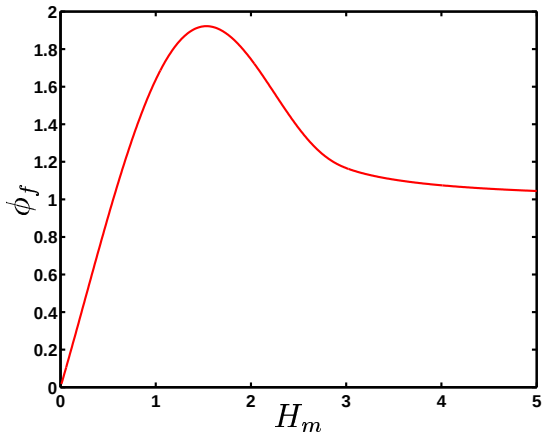

Figure 4.7: Shear flow factor ϕ_f as a function of H_m

ϕ_{fs} is the mean sliding velocity component of the shear stress. This can be obtained by equation 4.16. The term is only active if the two surfaces roughness's are different, otherwise this term vanishes. The dependence of h is shown in figure 4.8.

$$\Phi_{fs} = 11.1 H_m^{2.31} e^{-2.38 H_m + 0.11 H_m^2} \tag{4.16}$$

$$\phi_{fs} = V_{r1} \Phi_f s(H_m, \gamma_1) - V_{r1} \Phi_f s(H_m, \gamma_2) \tag{4.17}$$

Where $V_{r1} = (\frac{\sigma_1}{\sigma})^2$ and $V_{r2} = (\frac{\sigma_2}{\sigma})^2 = 1 - V_{r1}$. γ denotes the orientation of the asperities - $\gamma_i = 1$ for isotropic surfaces, for other cases see Patir and Cheng [1978] and Patir and Cheng [1979].

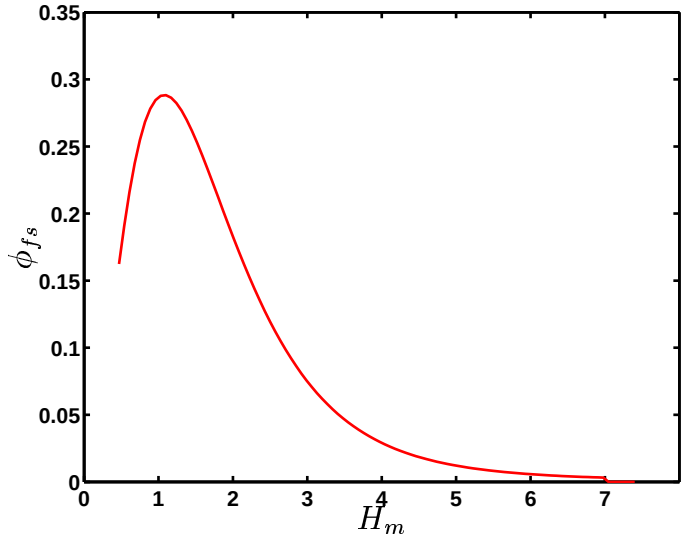

Figure 4.8: Shear flow factor ϕ_{fs} as a function of H_m

This concludes the description of the new terms in equation 4.10. As shown in the flow factors the surface roughness is important once the film thickness is small. For large film thickness h equation 4.13 reduces to equation 4.5. Since this is statistically based some of the surface peaks will be in contact with each other as shown in figure 4.2. Therefore a natural extension of this is to include the asperity interaction in the lubrication model.

4.3 Asperity Contact Model

In the current section the asperity contact model introduced by Greenwood and Tripp [1971] is used.

4.3.1 Surface Appearance

The surfaces of the sliding contacts are important for the asperity interaction model. The amount and size of the asperities strongly depends on the interacting components. In the current study only components that have been run in are considered - which means that the statistical surface appearance is not altered with time although solid to solid contact is present. The size, shape, orientation and distribution of asperities are also important in asperity models.
In the following it is assumed that the distribution is a Gaussian distribution as proposed in Patir and Cheng [1979], which is also the assumption used in the previous section concerning the lubrication of rough surfaces.
The orientation of the asperities is also important. The orientation refers to whether the asperities are mainly aligned in one direction or not. In this case an isotropic asperity orientation is assumed.

Furthermore, the r.m.s. values σ_i are needed along with the elasticity modulus of the surfaces. The r.m.s. value is approximately 10 percent larger than R_a for a surface with a Gaussian distribution - see Ruddy et al. [1981].
The r.m.s. values are statistically used to determine at what distance asperity contact is present. An averaged surface roughness and σ is denoted as the variance of this quantity, shown in equation 4.18.

$$\sigma = \sqrt{\sigma_1^2 + \sigma_2^2} \tag{4.18}$$

Furthermore, β and η_s which are two surface parameters are required. β describes the average radius of curvature of the single asperity peak and η_s describes the surface density of the peaks.
The load carried per unit width can be described by equation 4.19, taken from Greenwood and Tripp [1971]. The equation is based on the assumption that the contact is elastic, and represents the approximate Hertzian solution for contact of two paraboloids.

$$W_C = \frac{16\sqrt{2}}{15}\pi(\eta_s\beta\sigma)^2 E' \sqrt{\frac{\sigma}{\beta}} \int F_{\frac{5}{2}}(\frac{h}{\sigma})dx \tag{4.19}$$

E' is the composite modulus of elasticity of both surfaces.
The last unknown $F_n(H_m)$ is the asperity contact function, which depends on the statistical distribution of asperities. The equation 4.20 shows the equation for the Gaussian distribution.

$$F_n(H_m) = \frac{1}{\sqrt{2\pi}} \int_{H_m}^{\infty} (x - H_m)^n e^{-\frac{x^2}{2}} dx \tag{4.20}$$

This integration is pictured in figure 4.9 as a function of H_m for two values of n.

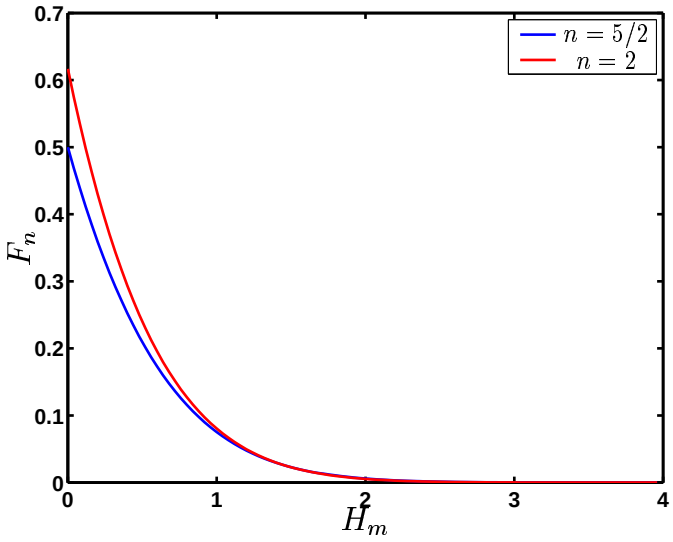

Figure 4.9: F_n as a function of H_m

For practical applications this equation, which requires numerical integration can be replaced by analytical means if the approximation proposed by Rohde and Kong [1975] is used. This can be done if the surface distribution is assumed to be Gaussian.

$$F_{\frac{5}{2}} = \left\{ \begin{array}{lll} f_1 e^{f_2 ln(H_m^* - H_m) + f_3 (ln(H_m^* - H_m))^2} & if & H_m \leq 3.5 \\ f_1^H e^{(H_m^* - H_m)^{f_2^H}} & if & 3.5 \leq H_m \leq H_m^* \\ 0 & if & H_m^* \leq H_m \end{array} \right\} \tag{4.21}$$

The coefficients are shown in equation 4.22.

$$\begin{aligned} f_1 &= 1.705 \cdot 10^{-4} \\ f_2 &= 4.05419 \\ f_3 &= 1.37025 \\ f_1^H &= 8.8123 \cdot 10^{-5} \\ f_2^H &= 2.1523 \\ H_m^* &= 5 \end{aligned} \tag{4.22}$$

4.3.2 Including Asperities in a Lubrication Model with Cavitation

Including asperities into a lubrication model, is like including microscopic effects on a macroscopic problem. However, a question naturally arises in this content. Is each asperity acting like a small bearing or is an asperity not important compared to the application of Reynolds equation in this context? Should the surface be modeled as perfectly smooth (Reynolds equation) or should the oil film model be altered such that the lubrication of each asperity is included? This last physical interpretation has been made by Patir and Cheng [1978]. However, considerations about cavitation and asperity interaction is not presented. In the following it is assumed that cavitation can occur and that the asperities will not act like small bearings viewed from a global point of view which means that Reynolds equation is fulfilled in large scale. This is based on the fact that the asperity is a statistical quantity incorporated in Reynolds equation and therefore it is also seems valid to include this quantity in the cavitation area of the contact.

4.3.3 Bearing Characteristics Rough Surfaces with Asperity Interaction

The load carrying capacity is similar to the one calculated for rough surfaces except with the new term arising from the contact pressure at the contact points. This new term is shown in

equation 4.23.

$$F_{asp} = \int W_C dz \tag{4.23}$$

4.3.4 Friction for Rough Surfaces with Asperities

The friction generated on the bearing surfaces originate from two terms - asperity friction and fluid film friction for the rough lubrication model.
The asperity friction term is presented in equation 4.24 as the shear strength of the surface film.

$$F_{fric,asp} = \alpha F_{asp} + \tau_0 A_C \tag{4.24}$$

Where A_C denotes the area of asperities in contact which is given by 4.25 and τ_0 denotes the shear strength of a boundary film with no normal load (Tabular value).

$$A_C = \pi D_{piston} (\pi \eta \beta \sigma)^2 E' \sqrt{\frac{\sigma}{\beta}} \int_0^{W_r} F_2(\frac{h}{\sigma}) dx \tag{4.25}$$

The determination of $F_2(\frac{h}{\sigma})$ is made using equation 4.20. Alternatively equation 4.21 may be used as an approximation to the integral, which have to be determined by numerical integration. The new coefficients are shown in equation 4.26.

$$\begin{aligned} f_1 &= 2.1339 \cdot 10^{-4} \\ f_2 &= 3.804467 \\ f_3 &= 1.341516 \\ f_1^H &= 1.1201 \cdot 10^{-4} \\ f_2^H &= 1.9447 \\ H_m^* &= 5 \end{aligned} \tag{4.26}$$

The total friction force can be determined by inserting equation 4.13 into equation 4.4 and add equation 4.24 as shown in equation 4.27.

$$F_{fric} = F_{fric,oil} + F_{fric,asp} \tag{4.27}$$

The necessary theory concerning lubrication models have been presented such that they are available depending on the problem to be solved. Models for lubrication have been presented depending on the relative film thickness compared to the surface roughness.

Chapter 5

Cavitation in Bearings

Calculating bearing characteristics by the use of Reynolds equation may create negative pressures. The nature of Reynolds equation does not contain the information about the incapability of the fluid to sustain negative film pressures. Therefore negative pressures can occur in the process of pressure distribution calculations of bearings. This approach is often denoted as the Full Sommerfeld solution. Large negative pressures cannot be present in running bearings. Experiments have shown that the fluid is capable of sustaining only very small negative pressures, and if the pressure drops below a certain limit cavitation occurs. Removing these negative pressures by simply neglecting them in the load carrying capacity calculation is often named the Half Sommerfeld or the Gümbel condition. The problem with this conservative algorithm is that mass flow continuity is not satisfied. The formulation of the Reynolds or the Swift-Steiber boundary condition ensured that flow continuity was present. This approach is the one of the two models used in this study. It is recently used by Priest et al. [1998], who named it Reynolds separation and reformation model, because an extra term is included- namely the ability of the fluid to reform after cavitation. The other approach presented here is noted the open-end cavitation, which states that fluid will be dragged into the bearing to eliminate cavitation - used by for instance by Han and Lee [1998].

5.1 Reynolds Separation and Reformation

5.1.1 Determining The Film Rupture Location

The point where cavitation starts (the film rupture location) can be found if Reynolds boundary condition is applied. This states that $p(x^*) = 0$ and $\frac{\partial p}{\partial x^*} = 0$ at $x = x^*$. The problem is limited to determination of the location x^* where both conditions are fulfilled.
For analytical solutions to Reynolds equation two nonlinear equations with two unknowns are to be solved for a one dimensional problem.
Many techniques are available, one of them is to iteratively modify the solution domain until

the criteria is fulfilled. An example is shown in figure 5.1.

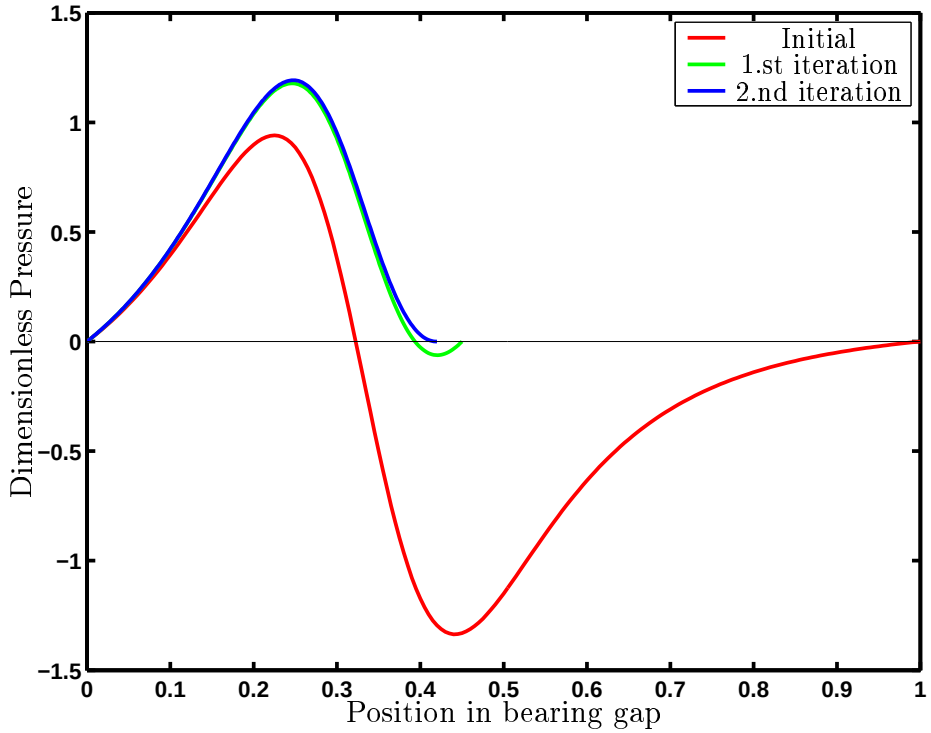

Figure 5.1: Iteration search for $\frac{\partial p}{\partial x} = 0$

5.1.2 Inside The Cavitated Region

The structure of cavitation is not well determined but can perceived as small gaseous bubbles, because the fluid has to compensate for the negative pressures. Another theory is that when cavitation occurs then the oil film turns into oil channels connecting the non-cavitated regions - Thomsen [1975]. In the present analysis the load carrying capacity of the cavitated region is not included in the analysis.

5.1.3 Reformation of The Film

In some bearing configurations the fluid film can reform. The point of cavitation is called x^*, and the point of reformation is called x^{**}

The approach mentioned originates in a flow continuity consideration. The flow into the cavitated region q_{cav} is calculated is set equal to the flow out of the cavitated region. This equality can be used to find x^{**} shown in equation 5.1 - one dimensional assumption.

$$q_{cav} = \frac{u}{2}h(x^*) = -\frac{h(x^{**})^3}{12\eta}\frac{\partial p}{\partial x} + \frac{u}{2}h(x^{**}) \tag{5.1}$$

Hereby three nonlinear equations equation 5.1, $p(x^*) = 0$ and $\frac{\partial p}{\partial x^*} = 0$ at $x = x*$ are to be solved in order to determine these points. An example of a reformation in a bearing subjected to cavitation is shown in figure 5.2. The initial pressure distribution calculated using the full Sommerfeld solution is shown as the curve with label 'Initial'. This curve shows that cavitation occurs in this bearing. The pressure distribution until the point of cavitation is shown as the curve labeled 'Cavitation'. Since the pressure at the exit boundary is > 0 the possibility for reformation of the oil film is present. The point of reformation is determined from iteration. The result is shown as the curve labeled 'Reformation'. The assumption in this case is a parabolic film thickness distribution with an outlet pressure of 0.5.

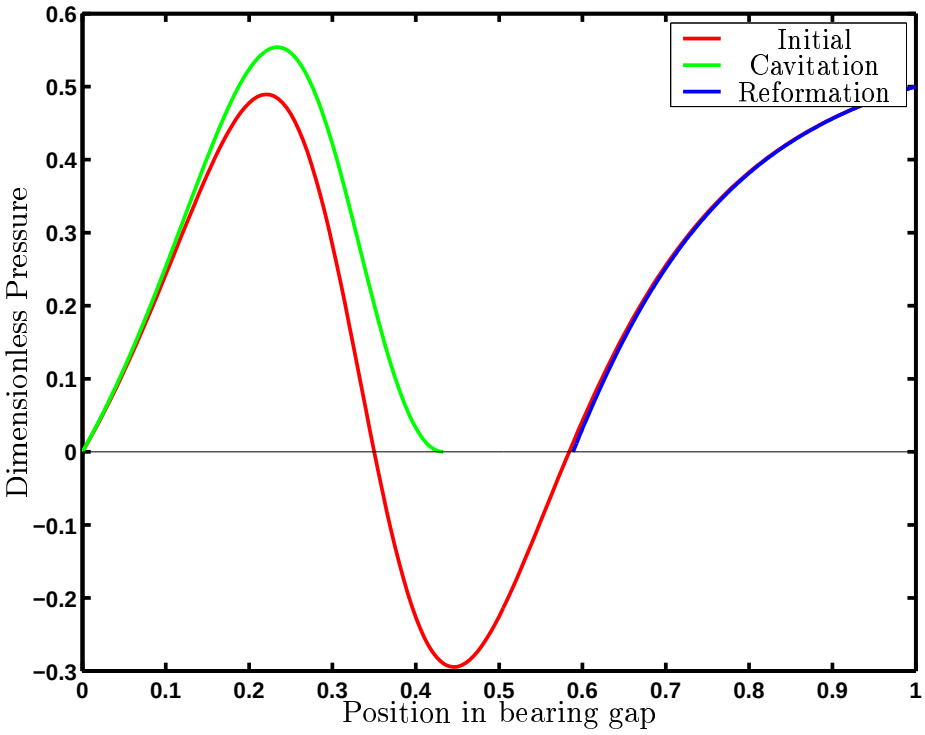

Figure 5.2: Pressure distribution (Cavitation and Reformation)

5.1.4 Application of Cavitation Algorithm

For analytical descriptions of pressure distributions the procedure shown above can easily be incorporated.

An implementation of such a procedure is shown in a flowchart in figure 5.3.

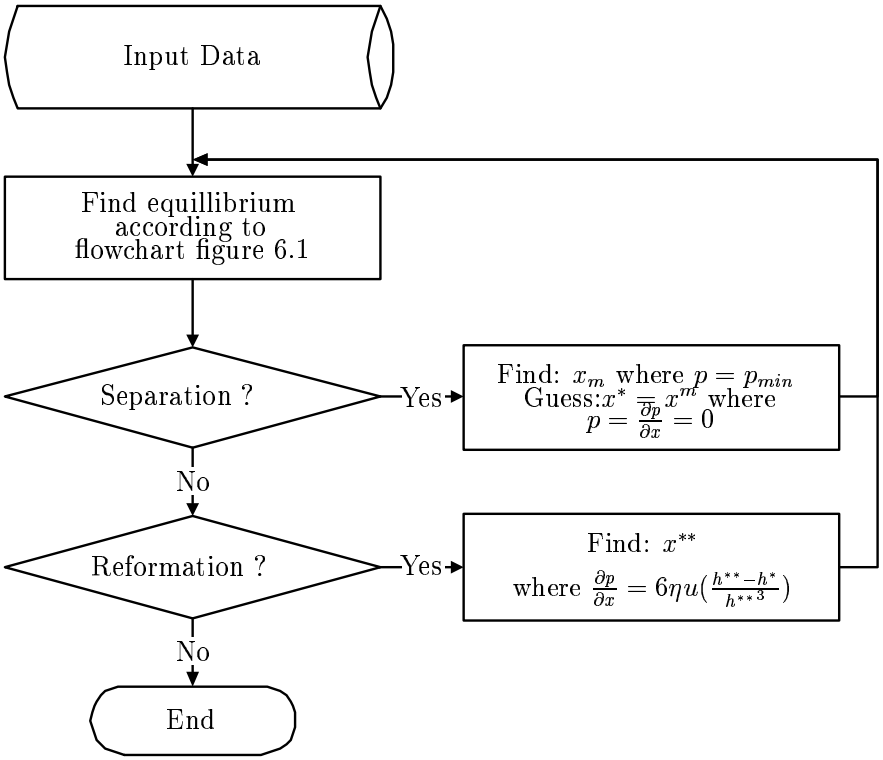

Figure 5.3: Flowchart Reynolds cavitation and reformation algorithm

If the establishment of the solution requires a numerical description the procedure shown above may be time demanding. A larger number of iterations in order to establish the cavitation area may be necessary. Therefore a fast implementation can be useful. A simplified version is applied called the Negative Pressure Elimination Method (NPEM) Saburi et al. [1995], which is more conservative than a traditional Reynolds boundary condition. The method is applied in such a way that the largest negative pressures are removed and a new iteration process is carried out for equilibrium determination. The pressure profile is examined for negative pressures. If negative pressures are present the largest of these are cancelled out and a new search for equilibrium with the external load is initiated. The advantage of this method is that it is a fast implementation compared to the other method used by for instance Priest et al. [2000]. The result is close to the solution where the flow continuity equation is used, but this depends on the discretization of the problem. Working with NPEM it cannot be ensured that the point of cavitation is not within two discretization points without moving these points to locate the exact position. This is no real problem since the discretization is fine - such that the error performed in this assumption is small. Otherwise an assumption of the pressure distribution being described by for instance a 3rd degree polynomial around the cavitation could be implemented in order to check the error - as shown in Thomsen [1975]. The flowchart for cavitation elimination is shown in figure 5.4. The method removes the largest negative pressure in each iteration until no negative

pressures are present. The number of iterations needed for cavitation elimination depends on the discretization of the problem. If for instance there are N_{cav} cavitation points in a infinite bearing this may take no more than $log(\frac{N_{cav}+1}{2})$ iterations. The typical error in this context is that the point where $\frac{\partial p}{\partial x} = 0$ lies within two discretization points, which is no problem if a fine mesh is used.

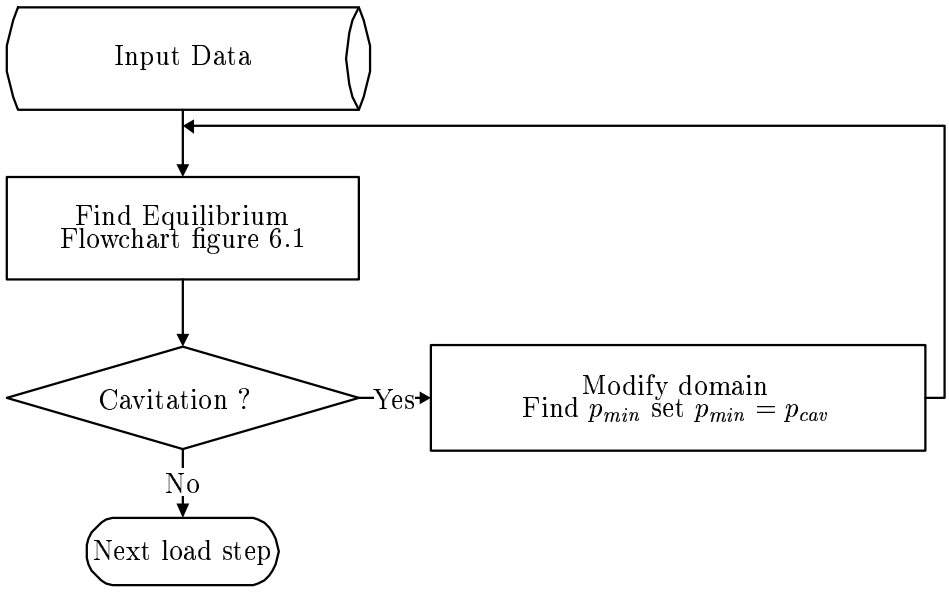

Figure 5.4: Flowchart NPEM algorithm

5.2 Open-end Cavitation

The open-end cavitation states that cavitation does not occur in the bearing. Once the bearing pressure drops below the saturation pressure of the bearing fluid will be dragged in the bearing in order to fill the domain and eliminate the small pressures. See for instance Han and Lee [1998]. An example of this configuration is shown in figure 5.5. The initial pressure profile is shown and the pressure profile for the open-end cavitation is shown. Note that the outlet boundary is moved such that the smallest pressure in the bearing is not smaller than the outlet pressure and $\frac{\partial p}{\partial x^*} = 0$. This point is determined iteratively.

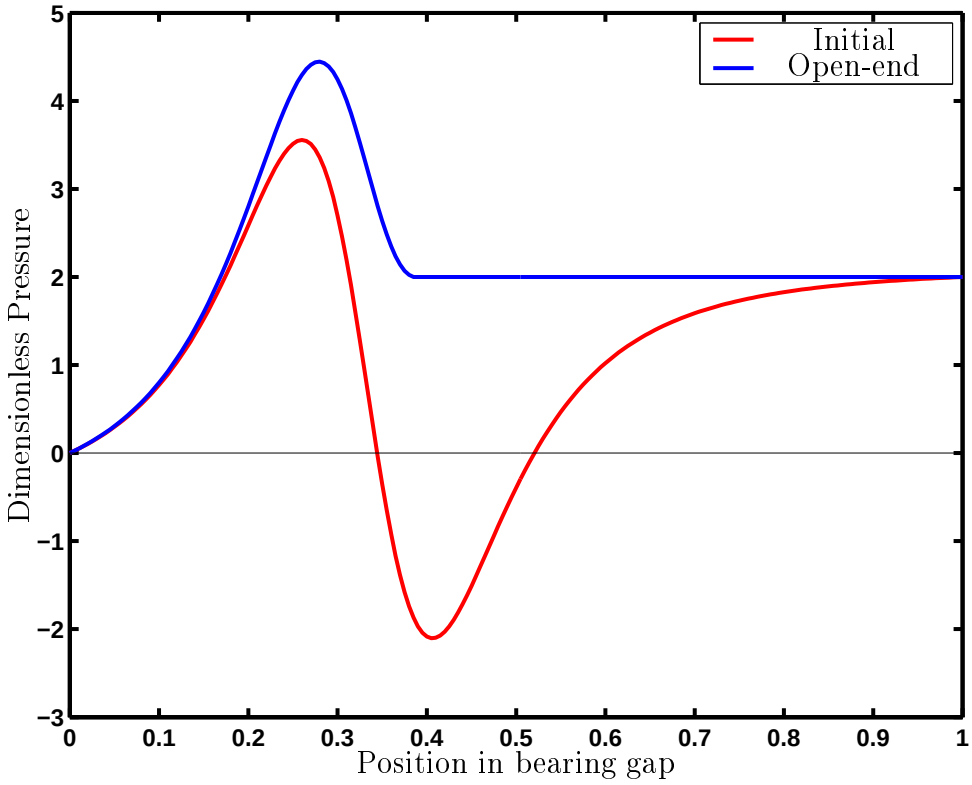

Figure 5.5: Pressure distribution with open end cavitation

5.2.1 Application of Cavitation Algorithm

The flow chart for this type is shown in figure 5.6

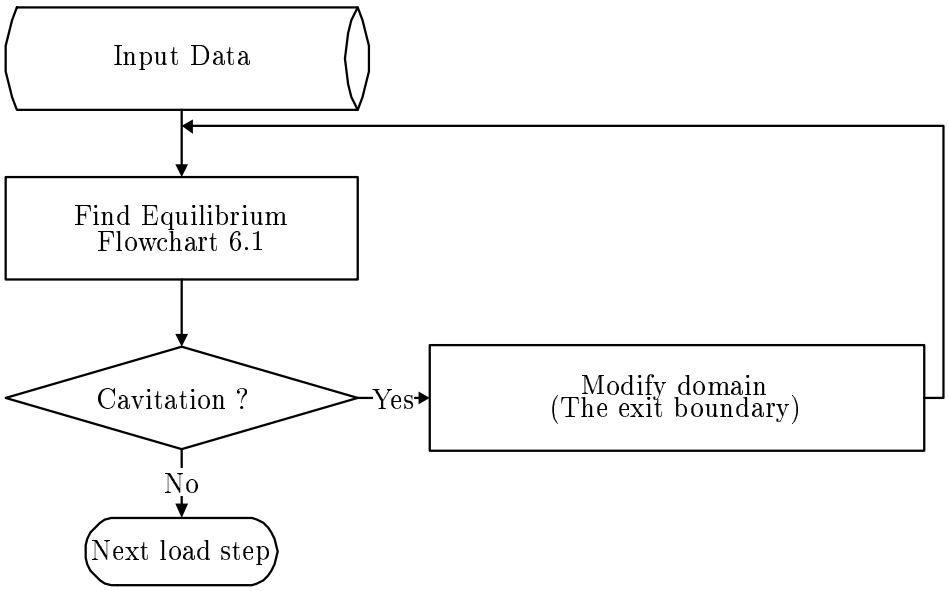

Figure 5.6: Flowchart open-end cavitation

Chapter 6

Time Stepping in Dynamically Loaded Bearings

Bearings subjected to dynamic load move accordingly to these exterior loads. The load may be periodic or not. Periodically loaded bearings are for instance bearings mounted in combustion engines or compressors.

The solution to statically loaded bearings is in most cases pretty straight forward, since the degrees of freedom match the number of equations to be solved simultaneously in order to find equilibrium.

The situation is not so straight forward in dynamically loaded bearings. Since the position is dynamically altered a time dependent equilibrium must be established. But if the bearing is periodically loaded a solution may be found by simple means due to the periodicity in loading and dynamic response of the system. There are a number of different approaches available. The approach chosen for this study originates in stability analysis of rotor journal bearings. The integrated Reynolds equation is the base point of this approach.

6.1 Damping and Stiffness of Rotor Bearings

The damping and stiffness of a bearing subjected to constant load may be important in order to check the stability of the bearing. Stodola [1925] suggested that the dynamic response of a bearing could be represented by stiffness and damping coefficients.

One way to determine the damping coefficients of a bearing is the application of perturbation theory in lubrication suggested by Lund [1968]. Lund [1968] proposed a solution to this problem that could be attained from analytical or numerical means, depending on the solution for the pressure profile for the problem.

The approach originates in Reynolds equation - see also Lund and Thomsen [1978]. The benefit is robustness in determination of damping and stiffness coefficients for the chosen bearing.

6.1.1 Analytical Approach

Some bearings run under such conditions that analytical solutions are available for the determination of bearing characteristics. These characteristics may be pressure, oil film thickness, load carrying capacity frictional loss and so on. A bearing subjected to a static load and a given running speed attains at a static equillibrum position $\overline{v}$ with $\dot{\overline{v}} = \overline{0}$. The load carrying capacity is noted $\overline{T}$. $\overline{T}$ may be a force of a moment depending on the problem. Assuming that the bearing is given a small disturbance denoted $\Delta\overline{v}$ and velocity term $\Delta\dot{\overline{v}}$ the carrying capacity is altered.
The load carrying capacity of the bearing may be Taylor expanded as shown in equation 6.1(1st order terms only). This expansion can be used to determine the change in load carrying capacity for the small disturbance $\Delta\overline{v} \ll \overline{v}$. The correlation between the disturbance and the change in load carrying capacity is presented in equation 6.1.

$$\overline{T} = \overline{T}_0 + \frac{\partial\overline{T}}{\partial\overline{v}}\Delta\overline{v} + \frac{\partial\overline{T}}{\partial\dot{\overline{v}}}\Delta\dot{\overline{v}} \tag{6.1}$$

The term $\frac{\partial\overline{T}}{\partial\overline{v}}\Delta\overline{v}$ describes the change in load carrying capacity due to the disturbance $\Delta\overline{v}$. It is observed that $\frac{\partial\overline{T}}{\partial\overline{v}}$ may be interpreted as the stiffness of the oil - and $\frac{\partial\overline{T}}{\partial\dot{\overline{v}}}$ the damping of the oil.
If an analytical solution for the current problem is present for the load carrying capacity, these terms can be determined analytically - see for instance Vølund and Klit [2000] and Klit and Vølund [2002].
The terms are called the dynamic coefficients $\overline{\overline{K}}$ and $\overline{\overline{B}}$ for the chosen bearing.
These are coefficient matrices with the definitions denoted in equation 6.2 and 6.3.

$$B_{i,j} = \frac{\partial\overline{T_i}}{\partial\dot{\overline{v_j}}} \tag{6.2}$$

$$K_{i,j} = \frac{\partial\overline{T_i}}{\partial\overline{v_j}} \tag{6.3}$$

The system may now be defined as shown in equation 6.4.

$$\overline{T} - \overline{T}_0 = \overline{\overline{K}} \cdot \Delta\overline{v} + \overline{\overline{B}} \cdot \Delta\dot{\overline{v}} \tag{6.4}$$

This system of equations terms relates the coupling between a perturbation Δv_i , $\Delta\dot{v}_i$ and the effect this has on the bearing performance. Note that a perturbation in Δv_i may create disturbances in all the elements of $\overline{T}$.

6.1.2 Numerical Approach

Working with bearings for which the assumptions required for analytical solutions do not hold requires other ways to determine the dynamic coefficients.

For this approach a numerical determination of the dynamic coefficients is useful. The way to do that originates in perturbations around the current state, with the base in Reynolds equation. The advantage of this approach compared to a numerical differentiation of the calculated load carrying terms is that the numerical inaccuracy of the numerical differentiation technique can be eliminated by J.W. Lund's approach - see Lund and Thomsen [1978]. The chosen perturbation is shown in equation 6.5. This is a small 1st order perturbation in the position around position $\overline{v}$.

$$\begin{aligned} \overline{v} &= \overline{v}_0 + \Delta\overline{v} \\ \dot{\overline{v}} &= \dot{\overline{v}}_0 + \Delta\dot{\overline{v}} \end{aligned} \tag{6.5}$$

$\overline{v}$ is a set of variables related to the position of the bearing. $\Delta\overline{v} \ll \overline{v}$ and correspondingly that $\Delta\dot{\overline{v}} \ll \dot{\overline{v}}$.
The perturbation changes the film thickness profile for the bearing $h = h_0 + h(\Delta\overline{v})$.
The perturbation in oil film thickness generates a similar perturbation in the oil film pressure shown in equation 6.6.

$$p = p_0 + p_{\overline{v}}\Delta\overline{v} + p_{\dot{\overline{v}}}\Delta\dot{\overline{v}} \tag{6.6}$$

This perturbation is introduced in Reynolds equation to give equation 6.7.

$$\begin{aligned} \frac{\partial}{\partial x}\left(\frac{(h_0+h(\Delta\overline{v}))^3}{12\eta}\frac{\partial}{\partial x}\left(p_0 + p_{\overline{v}}\Delta\overline{v} + p_{\dot{\overline{v}}}\Delta\dot{\overline{v}}\right)\right) + \frac{\partial}{\partial z}\left(\frac{(h_0+h(\Delta\overline{v}))^3}{12\eta}\frac{\partial}{\partial z}\left(p_0 + p_{\overline{v}}\Delta\overline{v} + p_{\dot{\overline{v}}}\Delta\dot{\overline{v}}\right)\right) = \\ \frac{u}{2}\frac{\partial}{\partial x}\left(h_0 + h(\Delta\overline{v})\right) + \frac{\partial}{\partial t}\left(h_0 + h(\Delta\overline{v})\right) \end{aligned} \tag{6.7}$$

The single terms $(v_i, \Delta v_j, \Delta\dot{v}_k)$ are isolated such that sets of equations are established.
Isolating all original terms generates the system shown in equation 6.8 and Reynolds equation is naturally the result.

$$\frac{\partial}{\partial x}\left(\frac{(h_0)^3}{12\eta}\frac{\partial}{\partial x}\left(p_0\right)\right) + \frac{\partial}{\partial z}\left(\frac{(h_0)^3}{12\eta}\frac{\partial}{\partial z}\left(p_0\right)\right) = \frac{u}{2}\frac{\partial}{\partial x}\left(h_0\right) + \frac{\partial}{\partial t}\left(h_0\right) \tag{6.8}$$

The terms $\Delta\overline{v}$ keeping only 1.st order terms are shown in equation 6.9, where the righthand side $RH_{\overline{x}}$ depends on the actual problem to be solved. The same operations are performed for $\Delta\dot{\overline{v}}$ in equation 6.10. An example a $RH_{\overline{x}}$ is shown in chapter 7 for a slider bearing. Note that appropriate boundary conditions must be applied as well.

$$\frac{\partial}{\partial x}\left(\frac{(h_0)^3}{12\eta}\frac{\partial}{\partial x}\left(p_{\overline{v}}\right)\right) + \frac{\partial}{\partial z}\left(\frac{(h_0)^3}{12\eta}\frac{\partial}{\partial z}\left(p_{\overline{v}}\right)\right) = RH_{\overline{v}} \tag{6.9}$$

$$\frac{\partial}{\partial x}\left(\frac{(h_0)^3}{12\eta}\frac{\partial}{\partial x}\left(p_{\dot{\overline{v}}}\right)\right) + \frac{\partial}{\partial z}\left(\frac{(h_0)^3}{12\eta}\frac{\partial}{\partial z}\left(p_{\dot{\overline{v}}}\right)\right) = RH_{\dot{\overline{v}}} \tag{6.10}$$

As shown is equations 6.8-6.10 the left hand terms are identical, only the right hand side is altered. The advantage of this is that once Reynolds equation is discretized, the lefthand side of the system of equations is the same. This means that the same system is to be solved with several right hand sides whether a solution for the pressures or the perturbed pressures are the objective.
Thereby the solution to each problem can be found and the solution to the pressures, and the perturbation pressures are obtained.
Integrating these perturbation pressures generates the damping and stiffness coefficients for the bearing chosen - shown in equation 6.11 .

$$\begin{aligned} K_{i,j} &= \int\int proj(i) p_{\overline{v}_j} dA \\ B_{i,j} &= \int\int proj(i) p_{\dot{\overline{v}}_j} dA \end{aligned} \tag{6.11}$$

Where $proj(i)$ is the projection of the perturbation pressures on to property i (May be sine or cosine for radial bearings or may be a torque arm for torque calculation terms).
Once the stiffness and damping coefficients are established the stability of the bearing may be examined in a similar manner as for the analytical solution.

6.2 Application to Dynamically Loaded Bearings

Stability is checked for bearings running under steady load - traditionally. The same procedure may be imposed for dynamically loaded bearings. Take for instance a main bearing in a combustion engine. This bearing has a periodic load and thereby a stable orbit, which the center of the shaft follows.
The problem is to determine this orbit since it depends on the time history of the bearing. The procedure for calculating orbits for dynamically loaded bearings with the above mentioned approach is described in the forthcoming paragraph.
To obtain a solution over one period of a dynamically loaded bearing - the external loads $\overline{T}_{ext}$ are discretized in time with time intervals Δt.
An assumption of the position $\overline{v_k}$ at time step k of the bearing within the clearance is made and the load carrying capacity is calculated using estimates for $\dot{\overline{v_k}}$. The calculated load carrying capacity $\overline{T}_{oil_k}$ is checked with the external loading. The problem is to get the right estimates for the unknowns in $\dot{\overline{v_k}}$. This is where the stiffness and damping coefficients are useful. Another problem is that once a correction is presented for one of the elements in $\dot{\overline{v}}_k$, this has a potential effect in all the terms of the load carrying capacity of the bearing.
The stiffness and damping coefficients represent this cross coupling effect in two matrices: $\underline{\underline{K}}$ and $\underline{\underline{B}}$. Where $K_{i,i}$ determines the stiffness in direction i for a perturbation in direction i. $K_{i,j}$ where $i \neq j$ represents the cross coupling terms. The same is the case for the damping terms $B_{i,j}$.
This coupling can be used in order to give good estimates for the dynamic properties.

Once the estimates at iteration i for $\overline{\dot{v}}_{k,i}$ are issued the load carrying capacity $\overline{F}_{oil_{k,i}}$ is determined. The load carrying capacity is inserted into equation 6.12. This system of linear equations is solved for $\Delta\overline{\dot{v}}_{k,i}$. The solution represents the corrections needed for the estimates for $\overline{\dot{v}}_{k,i+1}$ that are used for calculation of the load carrying capacity of the discrete pressures. These pressures are determined by the solution to the system of linear equations used to describe Reynolds equation for the bearing problem.

$$\overline{\overline{B}}\Delta\overline{\dot{v}}_{k,i+1} = \overline{T}_{ext} - \overline{T}_{oil_{k,i}} \tag{6.12}$$

The system is now updated such that the new estimate for $\overline{\dot{v}}$ is:

$$(\overline{\dot{v}}_k)_{i+1} = (\overline{\dot{v}}_k)_i + (\Delta\overline{\dot{v}}_k)_i \tag{6.13}$$

The estimate is inserted into Reynolds equation and the solution is established once more. This procedure is repeated until equilibrium is reached within a certain criteria. See the flowchart for this procedure in figure 6.1.
Once equilibrium is reached at the time step a step forward in time is issued using an appropriate time stepping criteria. A simple formulation is the Euler formulation stating that the new position may be determined from:

$$\overline{v}_{k+1} = \overline{v}_k + \overline{\dot{v}}_k\Delta t \tag{6.14}$$

Where Δt is determined by the resolution of the calculation in time domain. The new search for equilibrium is issued once more and this continues until the locus curve represents a closed loop as expected for the periodically loaded bearing. This procedure is shown in figure 6.2.

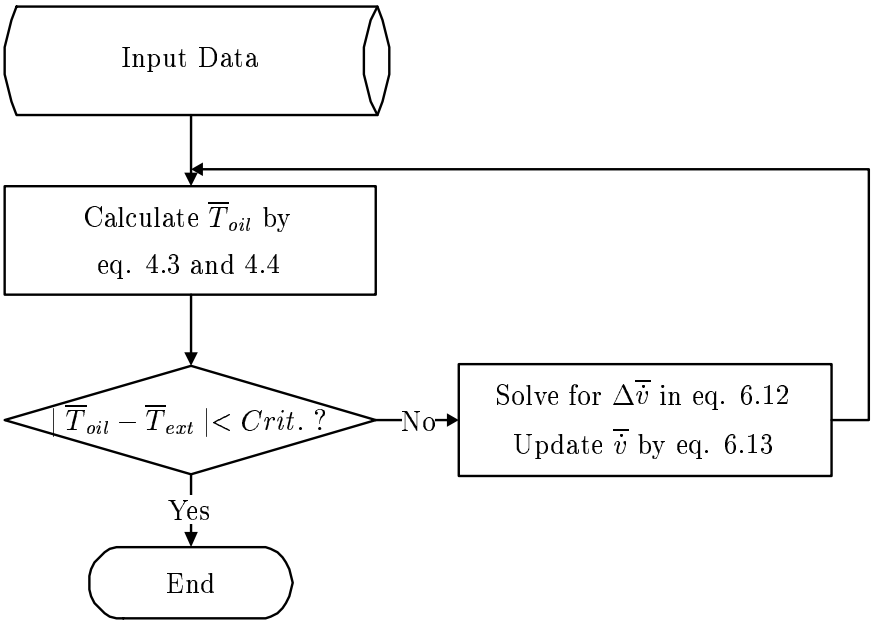

Figure 6.1: Flowchart for equilibrium search

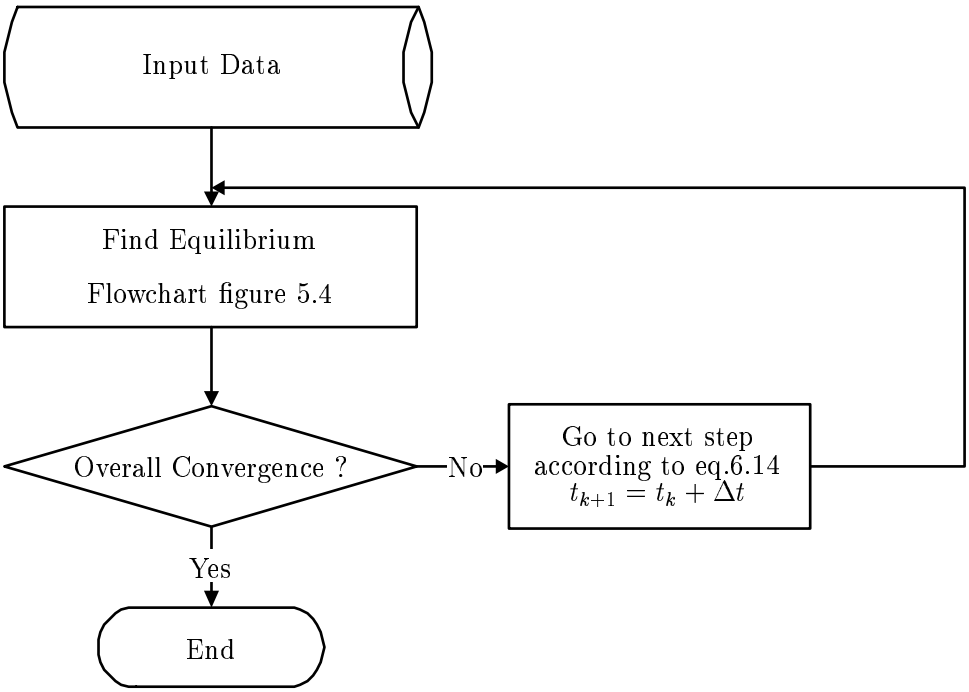

Figure 6.2: Flowchart for time stepping

Chapter 7

Calculation of Guide Shoe Characteristics

In the present chapter analytical and numerical models for frictional loss are presented for the guide shoe bearing. Since the frictional loss is directly correlated with the oil film thickness a natural aim of this analysis is to generate a model of the oil film properties in the bearing. The models described in this chapter start out very simple and are gradually applied with more features in order to describe the problem and its solution better. The assumptions for fulfilling Reynolds equation are assumed to be valid in the entire scope of the analysis' presented. The reason for the gradual refinement of the models is to examine the terms having significant influence on the bearing performance.

7.1 Analytical Models

Analytic descriptions exist for bearings with simple and well defined geometries. For instance the pressure distribution in some journal bearings can be described by analytical means Hamrock [1994] and Klit and Vølund [2002].

7.1.1 Two examples: Short and Infinite Width Journal Bearings

If the journal bearing is short relative to the circumferential length ($\frac{Diameter}{Width} > 2$) - short width bearing theory can be applied, see for instance Hamrock [1994]. In short width journal bearing theory the Poiseuille flow in circumferential direction ϕ is assumed to be negligible compared to the Couette flow. This assumption implies that the flow in axial direction is more significant than the circumferential flow. This simplifies Reynolds equation such that an analytical solution can be deduced. This reduced Reynolds equation is shown in equation 7.1.

$$\frac{\partial}{\partial z}\left(\frac{h^3}{12\eta}\frac{\partial p}{\partial z}\right) = \frac{\omega}{2}\frac{\partial h}{\partial \phi} + \frac{\partial e}{\partial t}cos(\phi - \Phi) \tag{7.1}$$

If the width of the bearing is large ($\frac{Diameter}{Width} < \frac{1}{2}$) the pressure gradient in the axial direction z can be neglected and that reduces Reynolds equation to a one dimensional description, as shown in equation 7.2 - see Hamrock [1994].

$$\frac{1}{r^2}\frac{\partial}{\partial\phi}\left(\frac{h^3}{12\eta}\frac{\partial p}{\partial\phi}\right) = \frac{\omega}{2}\frac{\partial h}{\partial\phi} + \frac{\partial h}{\partial t}cos(\phi - \Phi) \tag{7.2}$$

Therefore an analytical description can be reached. The same considerations can be imposed if the bearing components are flat.

7.2 Analytical Rectangular Squeeze Bearing

The model used in this analysis is presented in figure 7.1, where x denotes the sliding direction, z denotes the width and y the height.

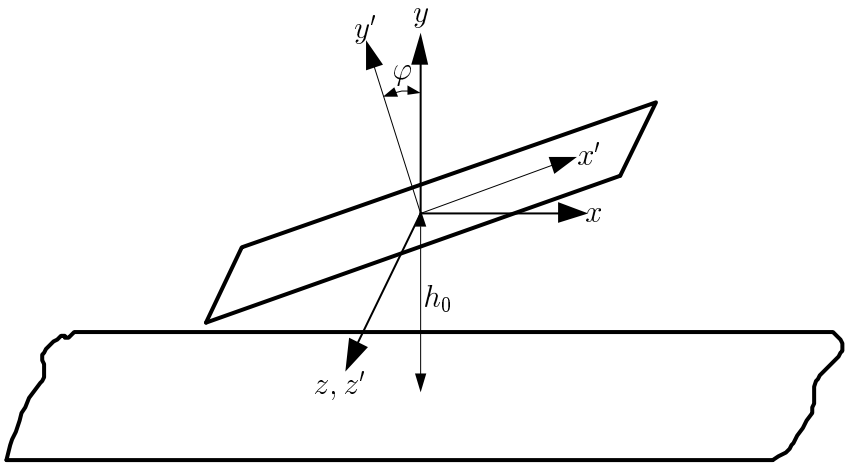

Figure 7.1: Definition of slider bearing

The degrees of freedom for the analysis' presented are the central film thickness h_0 and the attitude angle φ and of course the dynamic components. Reynolds equation applied to this problem is presented in equation 7.3.

$$\frac{\partial}{\partial x}\left(\frac{h^3}{12\eta}\frac{\partial p}{\partial x}\right) + \frac{\partial}{\partial z}\left(\frac{h^3}{12\eta}\frac{\partial p}{\partial z}\right) = \frac{u}{2}\frac{\partial h}{\partial x} + \frac{\partial h}{\partial t} \tag{7.3}$$

Reynolds equation can be simplified if the theory for short width or infinite width bearing theory is applied, which is presented in the following section.
Since the integrated form of Reynolds equation is needed for the force balance a representation of the oil film as presented in figure 7.2 can be used for the understanding of the problem and its solution.

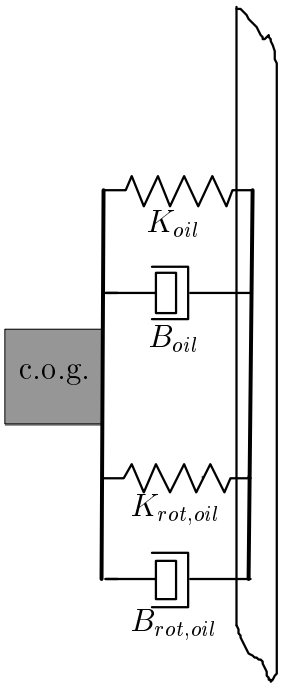

Figure 7.2: Definition of dynamic system

The problem is reduced such that a solution to the forced harmonic system is wanted. The only modification from a traditional simple dynamic system is that the stiffness and damping terms depends on the oil film thickness distribution and are highly nonlinear. The loading of the guide shoe is a normal force F_{ext} acting in the y direction according to the definition in figure 7.1. Furthermore, an external moment is applied M_{ext} which is acting around the z axis - The quantity is set =0 in this context.

7.2.1 Infinitely Wide Guide Bearing

Suppose the guide shoe system can be viewed as an infinitely wide slider. Furthermore, neglecting the oil grooves gives rise to a simple representation of the problem. Reynolds equation is reduced to a one dimensional equation in space, see equation 7.4.

$$\frac{\partial}{\partial x}\left(\frac{h^3}{12\eta}\frac{\partial p}{\partial x}\right) = \frac{u}{2}\frac{\partial h}{\partial x} + \frac{\partial h}{\partial t} \tag{7.4}$$

No Inclination $\varphi = 0$

The first approach chosen for this study is based on the analysis made by Abanteriba [1995], who performed an analysis of a cross head bearing by this approach, the design however was quite different from the one presented here. The presentation given in equation 7.4 requires that the bearing can be viewed as a bearing with infinite width. Furthermore, requiring

that the shoe cannot rotate causes the sliding term in equation 7.4 to vanish. This reduces Reynolds equation to equation 7.5 and an analytical solution can be established by simple means. The pressure distribution is presented in equation 7.6. This implies that only squeeze motion can take place and therefore the dynamic system is like it is pictured in figure 7.2, with the modification that only the linear damper is active in the system - no stiffness, rotational stiffness and rotational damping.

$$\frac{\partial}{\partial x}\left(\frac{h^3}{12\eta}\frac{\partial p}{\partial x}\right) = \frac{\partial h}{\partial t} \tag{7.5}$$

$$p(x, h, \frac{\partial h}{\partial t}) = \frac{12\eta}{h^3}\left(\frac{1}{2}\frac{\delta h}{\delta t}x^2 + Ax + B\right) \tag{7.6}$$

In the equation presented above A and B are integration constants.
Using boundary conditions $p = 0$ at $x = \pm\frac{L_{shoe}}{2}$ determines the integration constants A and B to be : $A = 0$ and $B = -\frac{12\eta}{h^3}\left(\frac{1}{8}L_{shoe}^2\right)\frac{\partial h}{\partial t}$ Thereby the complete description of the pressure profile can be given as a parabolic description in equation 7.7.

$$p(x, h, \frac{\partial h}{\partial t}) = \frac{6\eta}{h^3}\frac{\delta h}{\delta t}\left(x^2 - \frac{L_{shoe}^2}{4}\right) \tag{7.7}$$

Equation 7.7 is integrated to get the load bearing capacity 7.8.

$$F(h, \frac{\partial h}{\partial t}) = -\frac{\eta}{h^3}\frac{\partial h}{\partial t}L_{shoe}^3 W_{shoe} \tag{7.8}$$

The system presented in figure 7.2 can be written as shown in equation 7.9. The locus curve is found by solving the ordinary differential equation presented below (Inertia effects neglected). A 4th-order Runge Kutta method was chosen for time stepping control.

$$F_{ext} = B_{oil}\frac{\partial h}{\partial t} \tag{7.9}$$

where B_{oil} is the nonlinear damper given by $B_{oil} = -\frac{\eta L_{shoe}^3 W_{shoe}}{h^3}$. The load condition is chosen to be the load for 100% load (Full Load) for the test engine. This load curve can be seen in figure 7.3. This normal load is generated by the measured values for acceleration and combustion pressure. These terms are used for the determination of the normal load acting in the guide shoe bearing. The solution to this problem using the boundary conditions described above is presented in figure 7.4. The axes are normalized such that the Y-axis is normalized with respect to the stroke (S) and the X-axis with respect to the clearance($C = 400 \cdot 10^{-6} m$). The figure shows the center of gravity's (COG.) movement within the clearance of the guide planes as a function of the stroke. The position where $1/2 - h/C = 0$ is the position where the guide shoe is positioned in the center of the clearance.

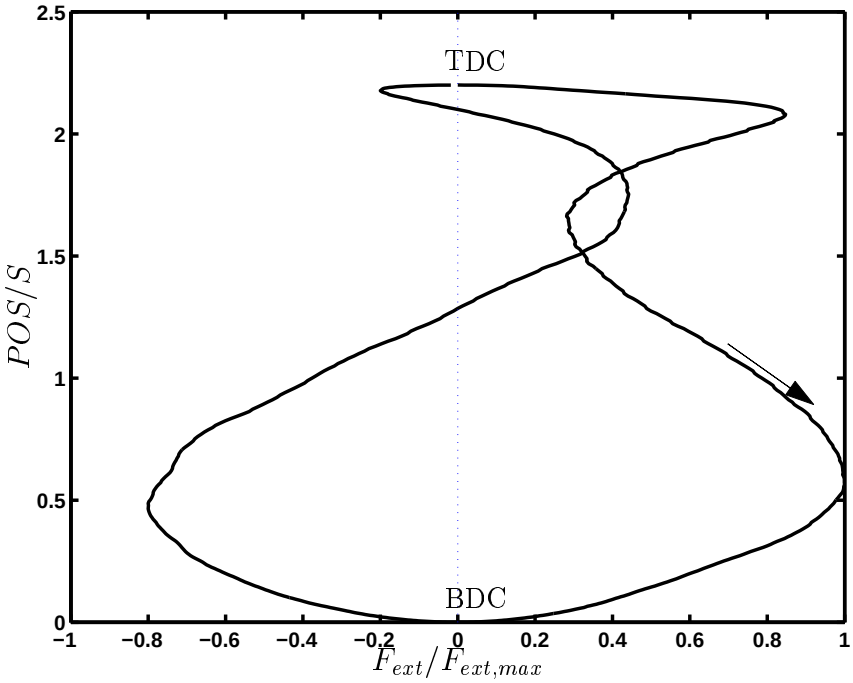

Figure 7.3: Normal force on the infinite bearing problem

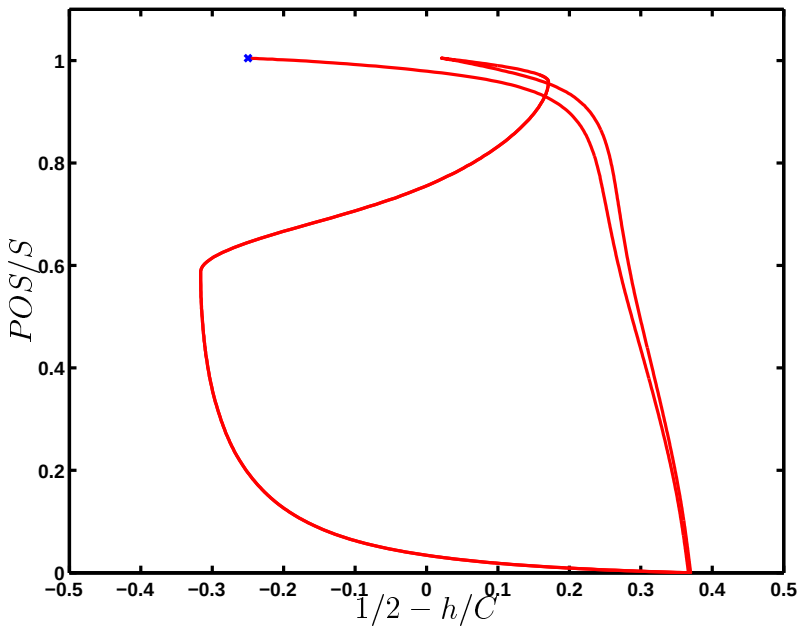

Figure 7.4: Solution to the infinite bearing problem with co-planar baring parts

The starting point is at the position marked with the 'x' in the figure. It can be observed that the overall convergence is obtained after about 1.5 cycles, for almost arbitrary starting point.

7.2.2 Infinitely Wide Slider with Inclination

Adding an extra degree of freedom to the problem namely the shoe inclination changes the system. For the infinitely wide slider (Pressure is independent of the width) it is possible to evaluate the coefficients analytically in each step in the iteration process - see Vølund and Klit [2000]. This system is equal to the dynamic system presented in figure 7.2. The oil film thickness is still assumed to be independent of z. The oil film is described by equation 7.10, where the attitude angle φ and the central oil film thickness h_0 are the degrees of freedom. Equation 7.12 describes the attitude angle and accordingly the variation in film thickness. Equation 7.11 describes the squeeze term. The oil film description is inserted into equation 7.3 - integrating twice gives equation (7.13).

$$h = h_0 + \varphi x \tag{7.10}$$

$$\frac{\partial h}{\partial t} = \frac{\partial h_0}{\partial t} + \frac{\partial x}{\partial t}\varphi + \frac{\partial \varphi}{\partial t}x = w - u\varphi + \dot{\varphi}x \tag{7.11}$$

$$\frac{\partial h}{\partial x} = \varphi \tag{7.12}$$

The pressure distribution is expressed as a function of h for a simple representation of the system.

$$p\left(h\right) = \left(-6\eta\frac{u}{\varphi} + 12\eta\frac{w}{\varphi^2}\right)\left(\frac{h_0}{2h^2} - \frac{1}{h}\right) + 6\eta\frac{\dot{\varphi}}{\varphi^3}\left(ln\left(h\right) + \frac{2h_0}{h} - \frac{h_0^2}{2h^2}\right) - \frac{12\eta A}{2\varphi h^2} + B \tag{7.13}$$

The coefficients A and B are given as: (note that h_1 and h_2 are the film thickness' at $x = -\frac{L_{shoe}}{2}$ and $x = \frac{L_{shoe}}{2}$ respectively and that h_0 is the central oil film thickness.

$$A = \left(-u + \frac{2w}{\varphi}\right)\frac{\left(h_1 - h_2\right)^2}{8h_0} + \left(\frac{\dot{\varphi}}{\varphi^2}\right)\left[\left(h_1^2\frac{h_2^2}{h_2^2 - h_1^2}\right)ln\left(\frac{h_1}{h_2}\right) + \left(h_1h_2 - \frac{h_0^2}{2}\right)\right]$$

$$B = 6\frac{\eta}{\varphi h_2^2}A - \left(-6\eta\frac{u}{\varphi} + 12\eta\frac{w}{\varphi^2}\right)\left(\frac{h_0}{2h_2^2} - \frac{1}{h_2}\right) - 6\frac{\eta\dot{\varphi}}{\varphi^3}\left(ln\left(h_2\right) + 2\frac{h_0}{h_2} - \frac{h_0^2}{2h_2^2}\right)$$

These coefficients are determined from the boundary conditions where $p = 0$ at $x = \pm\frac{L_{shoe}}{2}$. The inclination of the slider generates a non-symmetric pressure profile which introduces a torque term. This generates a system of equations shown in equation 7.17. The load carrying capacity, equation 7.14, is found by integrating the pressure over the slider.

$$\begin{aligned} F_{oil} = {} & \eta\left(-6\tfrac{u}{\varphi^2} + 12\tfrac{w}{\varphi^3}\right)\left[ln\left(\tfrac{h_1}{h_2}\right) + \tfrac{h_0}{2}\left(\tfrac{1}{h_1} - \tfrac{1}{h_2}\right)\right] + \tfrac{6\eta A}{\varphi^2}\left(\tfrac{1}{h_2} - \tfrac{1}{h_1}\right) + \tfrac{B}{\varphi}\left(h_2 - h_1\right) \\ & + 6\eta\tfrac{\dot{\varphi}}{\varphi^4}\left[\left(2h_0 + h_2\right)ln\left(h_2\right) - \left(2h_0 + h_1\right)ln\left(h_1\right) - \tfrac{h_0^2}{2}\left(\tfrac{1}{h_1} - \tfrac{1}{h_2}\right) + h_1 - h_2\right] \end{aligned} \tag{7.14}$$

The torque, equation 7.15, is generated by the non-symmetric pressure distribution on the guide shoe.

$$\begin{array}{l} M_{oil} = \eta\left(-6\frac{u}{\varphi^3}+12\frac{w}{\varphi^4}\right)\left[\frac{h_0}{2}ln\left(\frac{h_2}{h_1}\right)+h_1-h_2\right]-\frac{6\eta A}{\varphi^3}ln\left(\frac{h_2}{h_1}\right)+\frac{B}{2\varphi^2}\left(h_2^2-h_1^2\right) \\ +6\eta\frac{\dot{\varphi}}{\varphi^5}\left[\frac{-3}{4}\left(h_1^2-h_2^2\right)-\frac{h_1^2}{2}ln\left(h_1\right)+\frac{h_2^2}{2}ln\left(h_2\right)+\frac{h_0^2}{2}ln\left(\frac{h_1}{h_2}\right)\right]-\frac{h_0F_{oil}}{\varphi} \end{array} \tag{7.15}$$

Another torque term is introduced namely the torque generated by the friction force of the system. This friction force is calculated by equation 4.4. The result is shown in equation 7.16.

$$\begin{aligned} M_{fric} =& D_{shoe}[\left(-6\eta\frac{u}{\varphi}+12\eta\frac{w}{\varphi^2}\right)\left(\frac{h_0(h_1-h_2)}{2h_1h_2}+\frac{1}{2}ln(\frac{h_2}{h_1})\right)+ \\ & 6\eta\frac{\dot{\varphi}}{\varphi^3}\left(\frac{h_2-h_1}{2}+h_0ln(\frac{h_2}{h_1})-\frac{h_0^2(h_1-h_2)}{2h_2h_1}\right)- \\ & \frac{6\eta A}{\varphi}(\frac{1}{h_2}-\frac{1}{h_1})+\frac{\eta u}{\varphi}ln(\frac{h_2}{h_1})] \end{aligned} \tag{7.16}$$

These equations are inserted into the force and torque equations established for the system 7.17.

$$\begin{aligned} M\frac{d^2y}{dt^2} &= F_{oil}-F_{ext} \\ J\frac{d^2\varphi}{dt^2} &= M_{oil}-M_{fric}+M_{ext} \end{aligned} \tag{7.17}$$

These equations are solved in time domain with respect to h, φ, $\frac{\partial h}{\partial t}$ and $\frac{\partial \varphi}{\partial t}$. The procedure for solving this system is presented i Chapter 6.
At time $t = t_k$the guide shoe has coordinates h_k and φ_k and acceleration $\ddot{h}_k$ and $\ddot{\varphi}_k$ relative to the guide plane. In the j'th iteration the speeds are estimated to $(w_k)_j = \frac{\partial h}{\partial t}_j$ and $(\dot{\varphi}_k)_j$. These speeds are given increments Δw_j and $\Delta\dot{\varphi}_j$ and the corresponding change in the hydrodynamic forces may be expressed as equation 7.18

$$\begin{aligned} &\left\{\begin{array}{cc} (B_{yy})_j & (B_{y\varphi})_j \\ (B_{\varphi y})_j & (B_{\dot{\varphi}\dot{\varphi}})_j \end{array}\right\}\left\{\begin{array}{c} \Delta w_j \\ \Delta\dot{\varphi}_j \end{array}\right\}= \\ &\qquad\left\{\begin{array}{l} M\frac{d^2y}{dt^2}+(F_{ext})_j-F_{oil}\left(y_k,\varphi_k,(w_k)_j,(\dot{\varphi}_k)_j\right) \\ J\frac{d^2\varphi}{dt^2}-M_{oil}\left(y_k,\varphi_k,(w_k)_j,(\dot{\varphi}_k)_j\right)-M_{fric}\left(y_k,\varphi_k,(w_k)_j,(\dot{\varphi}_k)_j\right) \end{array}\right\} \end{aligned} \tag{7.18}$$

Where

$$\begin{aligned}
(B_{yy})_j &= \left(\tfrac{\partial F_{oil}}{\partial w}\right)_{y_k,\varphi_k,(w_k)_j,(\dot{\varphi}_k)_j} \\
(B_{y\varphi})_j &= \left(\tfrac{\partial F_{oil}}{\partial \dot{\varphi}}\right)_{y_k,\varphi_k,(w_k)_j,(\dot{\varphi}_k)_j} \\
(B_{\varphi y})_j &= \left(\tfrac{\partial M_{oil}}{\partial w}\right)_{y_k,\varphi_k,(w_k)_j,(\dot{\varphi}_k)_j} \\
(B_{\varphi\varphi})_j &= \left(\tfrac{\partial M_{oil}}{\partial \dot{\varphi}}\right)_{y_k,\varphi_k,(w_k)_j,(\dot{\varphi}_k)_j}
\end{aligned} \tag{7.19}$$

The perturbation coefficients (B_{ij}) are found analytically for an infinitely wide slider. Taking the derivatives of equation 7.14 and (7.15) as specified in equation 7.19 gives expressions for the damping coefficients equation 7.20),(7.21) and (7.22).

$$B_{yy} = \frac{\partial F_{oil}}{\partial w} = 12\frac{\eta}{\varphi^3}\left[ln\left(\frac{h_1}{h_2}\right) + \frac{2h_0 - h_1}{4h_2} - \frac{2h_0 - 5h_2}{4h_1} + \frac{2h_2 - h_1}{2h_0} - \frac{h_2^2}{2h_0 h_1} - 1\right] \tag{7.20}$$

And

$$B_{\varphi y} = \frac{12\eta}{\varphi^4}\left(\frac{h_0}{2}ln\left(\frac{h_2}{h_1}\right) + h_1 - h_2\right) - \frac{6\eta}{\varphi^3}\frac{\partial A}{\partial w}ln\left(\frac{h_2}{h_1}\right) + \frac{\partial B}{\partial w}\frac{h_2^2 - h_1^2}{2\varphi^2} - \frac{h_0}{\varphi}\frac{\partial F_{oil}}{\partial w} \tag{7.21}$$

$$\begin{aligned}
B_{\varphi\varphi} =& \frac{6\eta}{\varphi^5}\left[\frac{-3}{4}\left(h_1^2 - h_2^2\right) - \frac{h_1^2}{2}ln\left(h_1\right) + \frac{h_2^2}{2}ln\left(h_2\right) + \frac{h_0^2}{2}ln\left(\frac{h_1}{h_2}\right)\right] \\
&- \frac{6\eta}{\varphi^3}\frac{\partial A}{\partial \dot{\varphi}}ln\left(\frac{h_1}{h_2}\right) + \frac{\partial B}{\partial \dot{\varphi}}\frac{h_2^2 - h_1^2}{2\varphi^2} - \frac{h_0}{\varphi}\frac{\partial F_{oil}}{\partial \dot{\varphi}}
\end{aligned} \tag{7.22}$$

where $\frac{\partial A}{\partial w} = \frac{1}{\varphi}\left(\frac{(h_1-h_2)^2}{4h_0}\right)$, $\frac{\partial A}{\partial \dot{\varphi}} = \frac{1}{\varphi^2}\left[\frac{h_1^2 h_2^2}{h_2^2-h_1^2}ln\left(\frac{h_1}{h_2}\right) + h_1 h_2 - \frac{h_0^2}{2}\right]$, $\frac{\partial B}{\partial w} = \frac{6\eta}{\varphi h_1^2}\frac{\partial A}{\partial w} - 12\frac{\eta}{\varphi^2}\left(\frac{h_0}{2h_1^2} - \frac{1}{h_1}\right)$ and $\frac{\partial B}{\partial \dot{\varphi}} = \frac{6\eta}{\varphi h_1^2}\frac{\partial A}{\partial \dot{\varphi}} - \frac{6\eta}{\varphi^3}\left[\frac{-h_0^2}{2h_1^2} + 2\frac{h_0}{h_1} + ln\left(h_1\right)\right]$

Some algebraic manipulation of the equations verifies that $B_{\varphi y} = B_{y\varphi}$.

The solution to the presented problem can be seen in figure 7.5. This figure shows the position of the center of gravity within the clearance space and the inclination of the shoe.

Since the bearing is not of infinite width a correction must be applied to compensate for that. This has been done by Abanteriba [1995], who established load correction factors for the current problem - these are included in the simulations. These correction factors were established with the assumption that no inclination of the shoe is present - see figure 7.6.

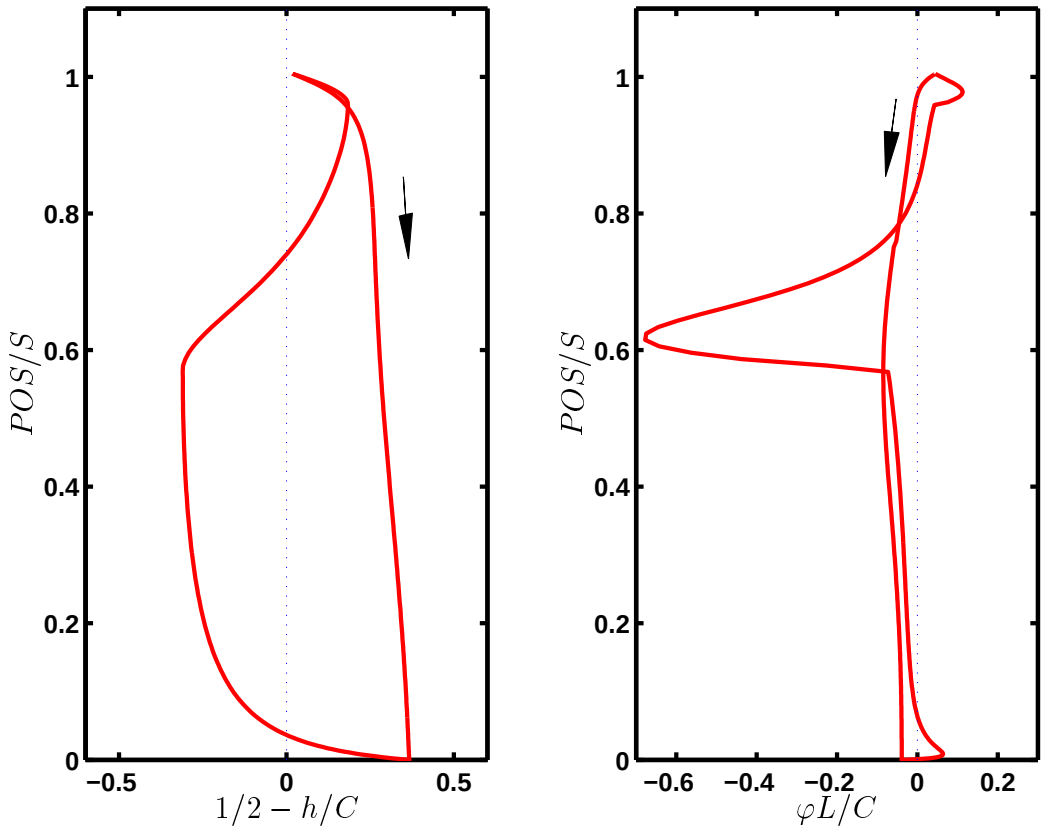

Figure 7.5: **Left:**C.O.G movement in clearance **Right:** Attitude angle of shoe

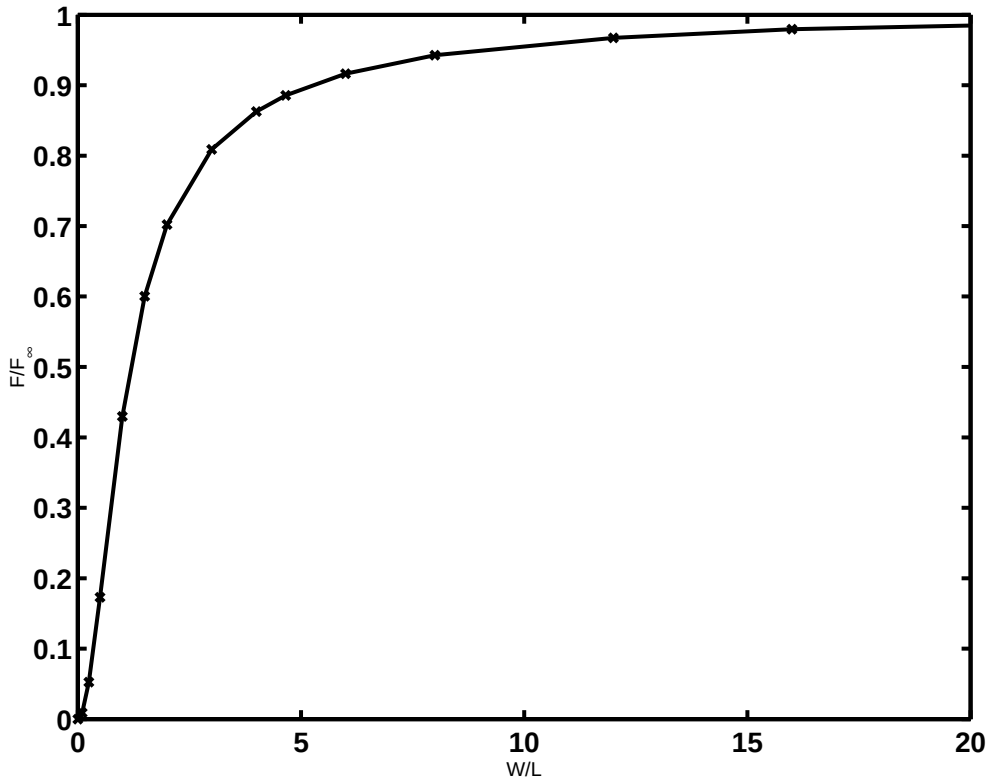

Figure 7.6: Correction factor for F_{oil}

These factors are derived using a numerical model of a plane squeeze bearing with finite width and an analytical description of an infinite bearing with the same properties .

7.2.3 Infinitely Wide Slider and Flexible Components

Since the guide bearings absorb the horizontal forces generated by the connecting rod the forces from the oil acting on the structure and the guide shoe are large. The flexibility of the components have been examined by issuing a contact analysis of the interacting components. For instance see one calculation result in figure 7.7. It was established that the deflection could be as large as the magnitude of the oil film thickness.

Once again the system can be viewed as a forced harmonic system presented in figure 7.8. An average stiffness of the guide plane were used in generating the results. The guide shoe was assumed to be rigid. As shown in figure 7.9 the global position of the guide shoe is changed significantly compared to figure 7.4. But viewed in a local coordinate system placed on the surface of the guide shoe the oil film thickness is not altered. Since no inclination is present and only one bearing is present the characteristics for the guide shoe system has not changed seen from an oil film viewpoint due to the uniform stiffness and the missing degree of freedom in the attitude angle of the guide shoe.

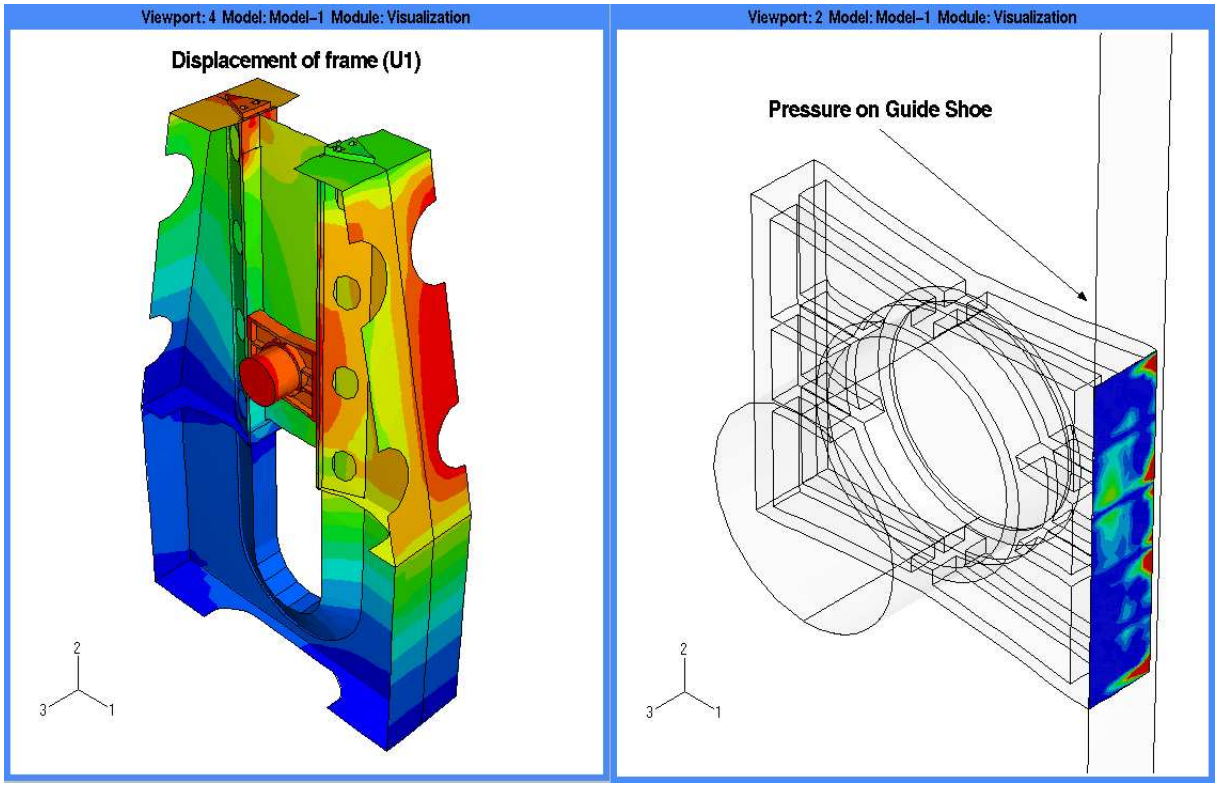

Figure 7.7: Flexible investigation of frame box

7.2.4 Slider with Finite Width and Length, Inclination and Flexible Components, Two Bearings

Adding a new feature to the problem namely the width of the bearing complicates the solution significantly. This system cannot be solved analytically. To solve this kind of problem a numerical description is necessary. Furthermore, introducing the second bearing surface (The opposite side of the guide shoe) an extra frictional term is introduced. This term has shown to be significant in friction calculations.

7.3 Numerical Models of The Guide Shoe Problem

In the present section a description of the guide shoe problem is presented using numerical modelling techniques. Since the guide shoe with finite width running in rigid environment will be the natural extension of the analytical models this is presented in the following.

7.4 Guide Shoe with Finite Width and Inclination

As mentioned in the previous section the solution to Reynolds Equation for a 2D formulation of the bearing problem is not possible by analytical means and therefore a numerical

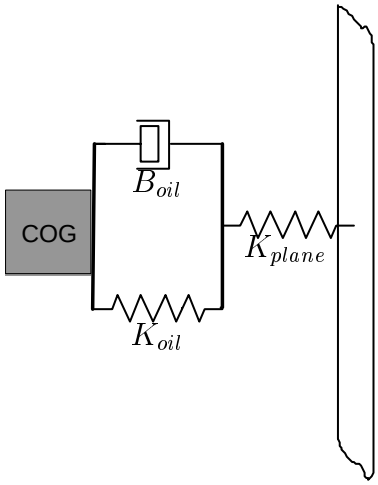

Figure 7.8: Flexible component interaction with oil film

implementation is necessary.

For the chosen configuration it is assumed that the guide shoe consists of two bearing pads running on rigid co-planar guide planes. The degrees of freedom for this system is the central film thickness h_0 and the inclination φ.

7.4.1 Finite Difference Formulation of Reynolds Equation

A finite difference formulation is chosen to solve this problem. The discretization is done using a $\frac{1}{2}$ point discretization technique using central differences. The bearing area is discretized in the way presented in figure 7.10. The notation N_{length} refers to the number of divisions in the sliding direction of the bearing and N_{width} refers to axial divisions.

The result of this formulation is a system of $NN \times NN$ linear equations where $NN = (N_{width} + 1)(N_{length} + 1)$.

$$\underline{\underline{A}}_{NNxNN} \times \underline{p}_{NNx1} = \underline{RH}_{NNx1} \tag{7.23}$$

Every point in the discretization corresponds to one row in the general oil film system of equations shown in equation 7.23.

7.4.2 Newton's 2'nd Law

Equilibrium is obtained when Newton's laws of motion are fulfilled. The relevant equations are shown in equation 7.17.

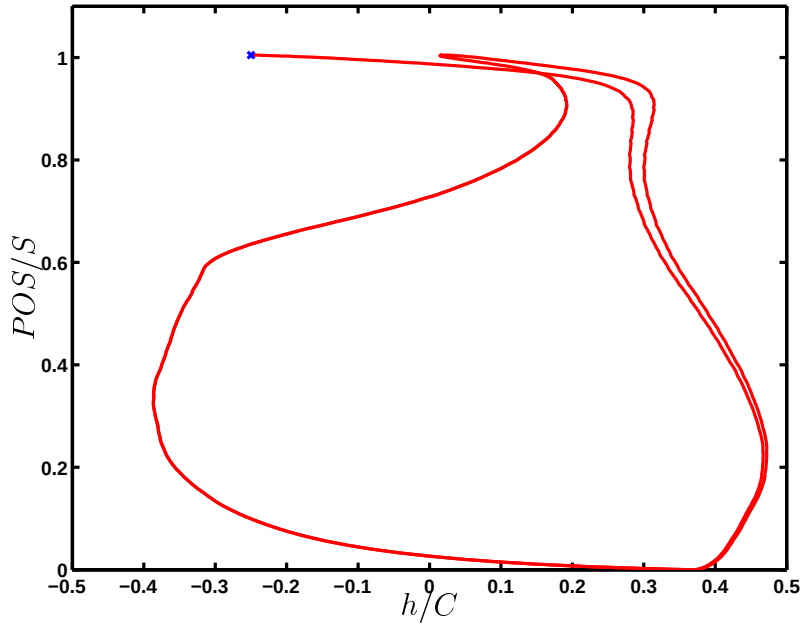

Figure 7.9: Solution to the infinite bearing problem with coplanar baring parts

7.4.3 Searching for Equilibrium

The method for determining equilibrium presented in Chapter 6 is adopted. To find the necessary damping coefficients the perturbation technique shown in Chapter 6 is applied to the current problem.

The perturbation coefficients (B_{ij}) are generated by a perturbation of Reynolds equation - result seen in equation 7.24 and 7.25 and a successive numerical integration as described in chapter 6. For this problem the perturbed Reynolds equations are shown in equation 7.24 and 7.25. The boundary conditions are chosen such that the damping properties of the oil is set equal to zero at the boundaries and in the cavitated area.

$$\frac{\partial}{\partial x}\left(\frac{h^3}{12\eta}\frac{\partial p_{\Delta w}}{\partial x}\right)+\frac{\partial}{\partial z}\left(\frac{h^3}{12\eta}\frac{\partial p_{\Delta w}}{\partial z}\right)=1 \tag{7.24}$$

$$\frac{\partial}{\partial x}\left(\frac{h^3}{12\eta}\frac{\partial p_{\Delta \dot{\varphi}}}{\partial x}\right)+\frac{\partial}{\partial z}\left(\frac{h^3}{12\eta}\frac{\partial p_{\Delta \dot{\varphi}}}{\partial z}\right)=x \tag{7.25}$$

Equation 7.24 and 7.25 are solved to find the perturbed pressure these are integrated according to equation 6.11. This results in the system of equations presented in equation 7.18.

When equation 7.17 is close to be fulfilled - the change from one iteration to the next becomes sufficiently small - the new position of the guide shoe is determined by explicit time stepping using a second order Adam-Bashforth method - see equation 7.27.

The error term is defined as shown in equation 7.26.

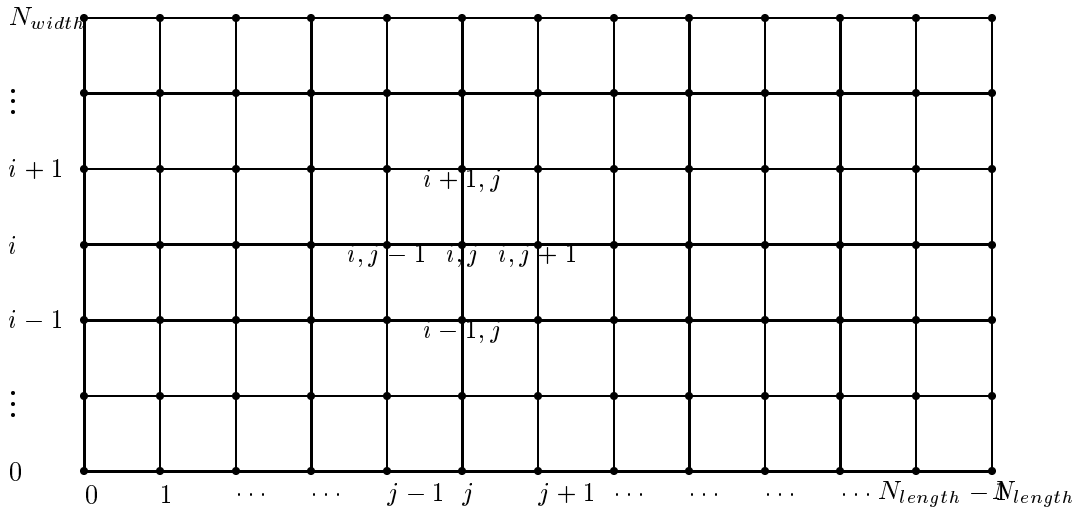

Figure 7.10: Discretization of bearing for oil film calculation

$$Err = \sqrt{\left(\frac{F_{oil} - F_{ext}}{F_{ext}}\right)^2 + \left(\frac{M_{oil} + M_{fric} - M_{ext}}{M_{ext}}\right)^2} \tag{7.26}$$

The step is accepted when $Err \leq Err_{crit}$, (usually in the neighborhood of 10^{-4})

$$\begin{aligned} y_{k+1} &= y_k + \tfrac{\Delta t}{2}\left(3w_k - w_{k-1}\right) \\ \varphi_{k+1} &= \varphi_k + \tfrac{\Delta t}{2}\left(3\dot{\varphi}_k - \dot{\varphi}_{k-1}\right) \end{aligned} \tag{7.27}$$

The process proceeds until the guide shoe follows the same path in consecutive strokes.

7.5 Cavitation in Guide Shoe Bearing

In periods of the stroke the pressure is negative if no action is taken to counteract for that, especially when the second bearing is introduced. The fluid cannot sustain the large negative pressures and therefore cavitation occurs. The model used here is the one described as the Negative Pressure Elimination Method (NPEM). The flowchart for cavitation elimination is shown in figure 5.4.

Although no bearing capacity is present a fraction of the remaining fluid is still shearing and therefore contributing to the total friction of the guide shoe system. It is assumed that the fluid will still have contact to both bearing surfaces, but no longer to its full extent. A similar approach as for example in Priest et al. [1998].

A volumetric approach is used for the determination of the fraction of shearing fluid within the area of cavitation. The algorithm is as follows.

Store the full information of the oil film thickness distribution for the non-cavitated bearing in $\underline{\underline{h}}_{FULL}$ at the current load step. Step forward in time. If cavitation is present in point i, j

calculate the filling ratio in this point by the formula:

$$FILL_{i,j} = \frac{h_{FULLi,j}}{h_{i,j}} \tag{7.28}$$

If no cavitation is present set $h_{FULLi,j} = h_{i,j}$. Multiply this matrix element by element when calculating the shearing term. The matrix $\underline{\underline{FILL}}$ has values in the range from 0 to 1. When an element in $FILL_{i,j}$ is equal to 1 the space is completely filled with oil and is shearing to its full content. This shearing ability drops if the filling ratio is lowered ($FILL_{i,j} < 1$).

7.5.1 Solving for Pressures in Equation 7.23

The system can be solved using direct solving methods (LU-factorization method) or iterative methods.
A LU-factorization method was chosen because of the numerous solving attempts on the system with the same matrix, but with changed righthand side, which means that the factorization needs only to be performed once and the back substitution for each righthand side which is attempted in order to find the solution. Furthermore, a technique for limiting the total number of calculations were used. The chosen technique was based on the solution of banded linear equations. These methods are further described in Press et al. [1996].

7.6 Verification of Oil Film Model

The numerical model was subjected to different load situations and configurations in order to verify the model. The engine was run both ways around and checks for symmetric results were performed. This was to verify that the two oil films were functioning in the same manner. A calculation using symmetry boundary conditions in the width direction along with no oil grooves was issued and checked with the analytical results. Furthermore, a textbook example of a rectangular squeeze bearing was modeled and the results were compared with textbook examples - the Raleigh step glider and squeeze bearings - see for instance Hamrock [1994]. Another example is the infinite inclined slider bearing which also was modeled and compared. Good correlation were found in all cases.

7.7 Elasticity in Guide Shoe Bearing

As mentioned in the introduction to the current chapter elastic deformation of the bearing components are so significant that the bearing characteristics are changed once this feature is included.
The guide bearing system can be viewed as a damped harmonic system. This system is presented in figure 7.11. COG denotes the center of gravity of the guide shoe.

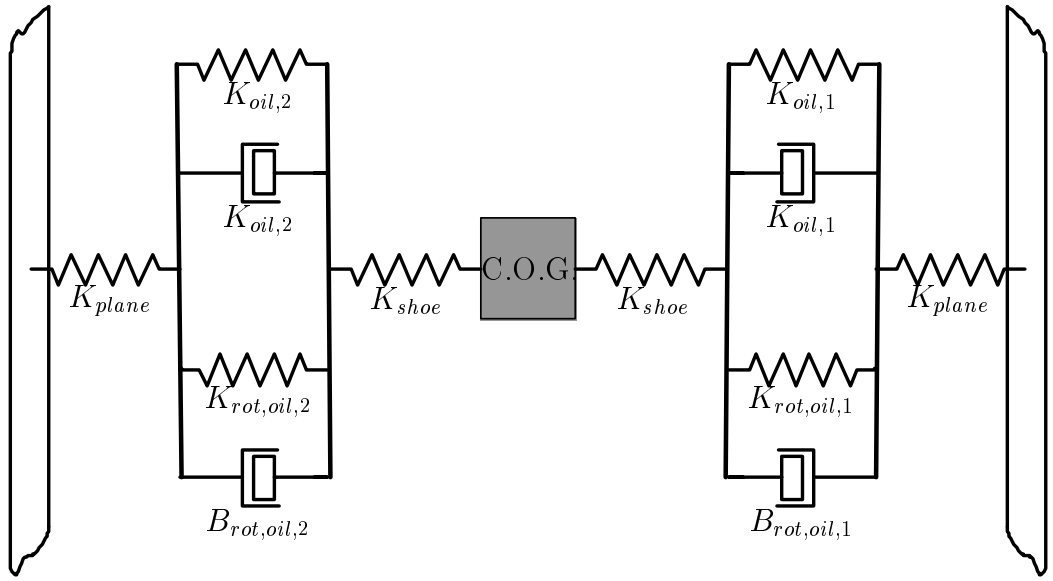

Figure 7.11: Dynamical description of Guide Shoe <> Oil Film <> Frame Box

$B_{oil,i}$ and $K_{oil,i}$ present damping and stiffness of the oil in bearing i and are functions of the transient position and are therefore highly nonlinear. The terms $B_{rot,oil,i}$ and $K_{rot,oil,i}$ represent the rotational damping and stiffness of the oil. The elasticity of the guide plane and guide shoe is presented by K_{plane} and K_{shoe} and are the same for both sides of the bearing.

For the system shown in figure 7.11 the inertial properties are neglected which means that the solution can be established as the solution to 3 discrete systems. Two flexibility systems (One for the frame box and one for the guide shoe) and one oil film system. Since the stiffness of the plane is a function of the shoe position relative to the guide plane (vertical direction) uniform stiffness is not present and a cross coupling between the two guide planes exist.

Furthermore, the guide plane is subjected to pre-tension. The tightening of the stay bolts originating from the assembly of the entire engine generates a global deflection of the frame box which is reflected on the guide planes. These may no longer be considered to be planar surfaces. This means that the damping and stiffness of the oil film also depends on the position of guide shoe relative to the guide plane.

7.8 Finite Element Modelling

The frame box and the guide shoe surface are flexible. Since the load is relatively high the guide plane and the guide shoe deflect due to the load absorbed in the bearing. In order to compensate for that finite element models of one cylinder unit and one guide shoe were established. This generated two systems of equations shown in equation 7.29 - one for each

component.

$$\begin{aligned} \underline{\underline{K}}_{shoe} \cdot \underline{\Delta h}_{shoe} &= \underline{F}_{shoe} \\ \underline{\underline{K}}_{plane} \cdot \underline{\Delta h}_{plane} &= \underline{F}_{plane} \end{aligned} \tag{7.29}$$

Interpolating the pressure from the oil film to the plane and the shoe generates $\underline{F}_{shoe}$ and $\underline{F}_{plane}$. The solution $\underline{\Delta h}_i$ to equation 7.29 is interpolated to the oil film and inserted into the discretized Reynolds equation as (Δh_i). A linear interpolation technique in two dimensions (x and z) was used to convert the pressures acting on the structural parts from the oil. This linear interpolation was the same as the shape functions for the elements.

7.8.1 Finite Element Model of Frame

The finite element model of the frame is generated from solid, shell and shell-to-solid elements - Ansys [1999]. Only one section of the entire engine was modeled, this was half of the 2nd cylinder and half of the 3rd cylinder in the research engine. This is presented in figure 7.12. The cylinder section was applied with symmetry boundary conditions (The blue arrows shown in figure 7.12). In order to get a good accuracy of the model a large number of elements were used, which resulted in 300000 degrees of freedom (DOF). The guide plane surfaces contained approximately 1000 nodes on each surface. Since the guide plane is machined before assembly the shape of the bearing surface is no longer co planar once the entire engine is assembled. This feature is included by issuing a calculation of the assembled bed frame, frame box and cylinder frame. The three components are held together by stay bolts, whose pre-tension force have been used for the numerical model. The result of the calculation can be seen in figure 7.13. The figure reveals that the initially co-planar guide planes can no longer be considered plane in this context. The deformation (U_x) ranges from $-30\mu m$ to $+40\mu m$, which is in the same level as the smallest oil film thickness for the case with rigid components. Therefore this effect is significant in the determination of the guide bearing characteristics.

7.8.2 Finite Element Model of Guide Shoe

The finite element model of the shoe is generated from solid elements. The model is presented in figure 7.14.
The guide shoe was constrained against movement in the pin hole (The blue arrows shown in figure 7.14). In order to get a good accuracy of the model a 36.000 DOF were estimated to be necessary. The bearing surface had approximately 500 nodes on each bearing surface.

7.8.3 Condensing The FE-Models

The large number of degrees of freedom in the frame box (approximately 300.000) increases the computing time with several orders of magnitude because the size of the stiffness matrix

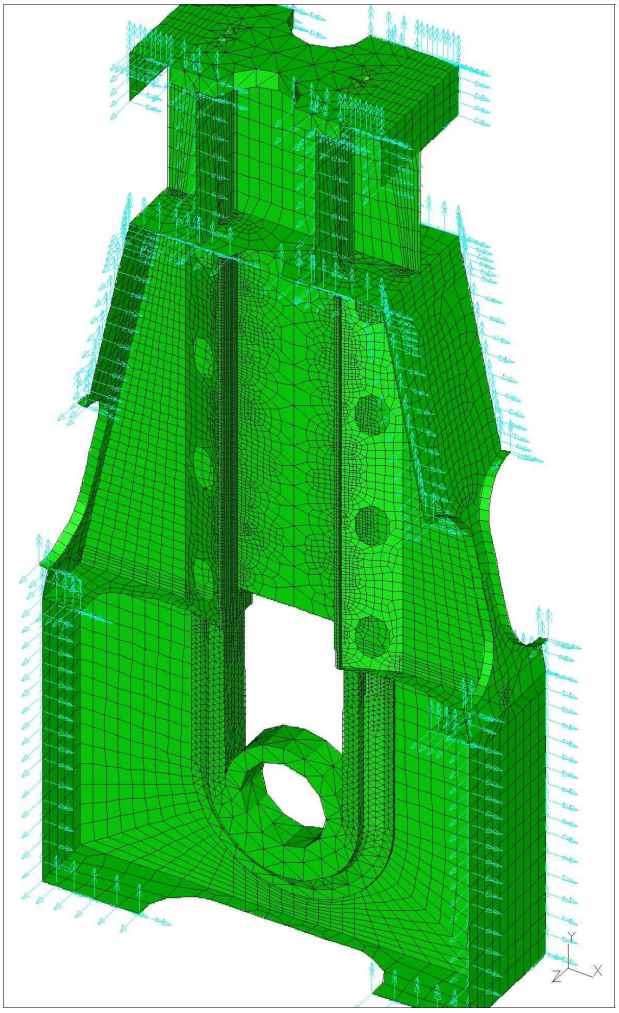

Figure 7.12: Finite Element Model of frame box

is very large K_{plane}. Condensing the finite element model reduces the number of active degrees of freedom. The active number of DOF are chosen such they are directly related to the deformation and loading of the guide plane. This is applied in a simple way by setting up a super element. The commercial Finite Element software ANSYS were used for that - see Ansys [1999]. The reduction in DOF for the frame box (Figure 7.12) were large - from approximately 300000 to only 2000. On the guide shoe (Figure 7.14) the number of DOF was reduced from 36000 to 1000. This speeds up the entire calculation process tremendously. The disadvantage of this process is that the super elements have to be unpacked if information about the stiffness properties in the rest of the FE-model is needed, a rather slow process.

Both system of equations 7.29 contains a characteristic matrix - the stiffness matrix. The stiffness matrix for both finite elements were inverted to get the flexibility matrix for each system. The advantage of working with flexibility matrices is that it much faster to multiply by the interpolated forces (the integrated pressures) in order to get the deflections $\underline{\Delta h}_i$ seen

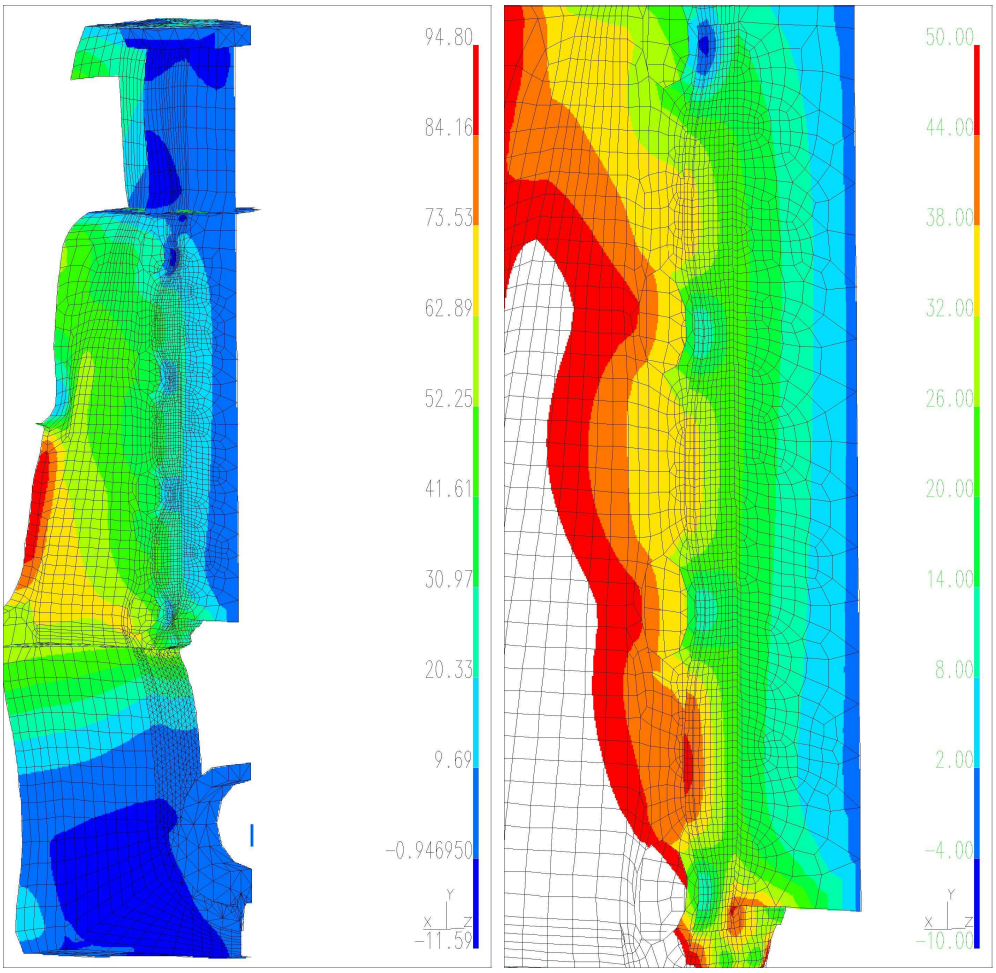

Figure 7.13: Calculation result of predeformed guide plane. **LEFT:** Calculation result for half a cylinder unit. **RIGHT:** Closer view of calculation result

in equation 7.30.

$$\begin{aligned} \underline{\Delta h}_{shoe} &= \underline{\underline{K}}^{-1}_{shoe} \cdot \underline{F}_{oil} \\ \underline{\Delta h}_{plane} &= \underline{\underline{K}}^{-1}_{plane} \cdot \underline{F}_{plane} \end{aligned} \tag{7.30}$$

The latter of these procedures is still one of the major time consumers in the process of establishing the characteristics of the guide shoe. This could be further reduced by choosing the domain of active degrees of freedom such that the active number of DOF could be further reduced, letting the flexibility matrix of the frame box follow the guide shoe position. The problem by doing this is that that requires a lot of stiffness matrices because of the domain change between each load step calculation. That would require a large number of stiffness matrices one for each calculation step(or at least every second if uniform step size is used), and thereby take up a lot of space and may slow down the process because the large number of I/O communication. One flexibility matrix was used and continuously interpolated in

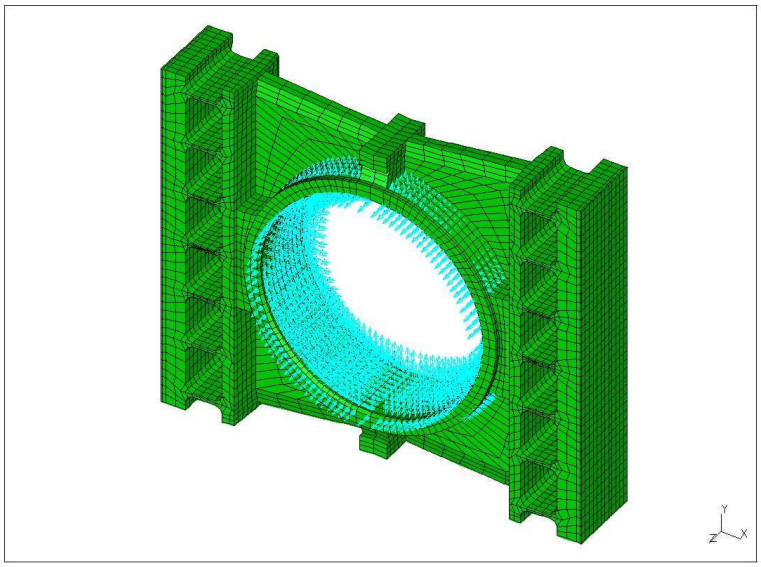

Figure 7.14: Finite Element Model of guide shoe

order to retrieve the local flexibility.

7.8.4 The Coupling Between Solid and Fluid

Since the pressure in the oil film depends on the film thickness and the film thickness is determined from the initial gap and deformation of the surfaces involved in the bearing a coupling is present, as shown in equation 7.31.

$$h = h(x, t, \varphi) + \Delta h_{shoe} + \Delta h_{plane} \tag{7.31}$$

For this reason an iterative scheme is implemented. An under-relaxation technique similar to the one used by Fillon et al. [1994] is applied in order to solve the solid-fluid-solid system. The technique is shown in equation 7.32. The deformation calculated at the current step is noted $\Delta h_{calc} = \Delta h_{plane} + \Delta h_{shoe}$ see equation 7.30 and the result from the previous calculation is denoted $\Delta h_{calc,old}$. This equation ramps the deformations using under-relaxation technique in order to ensure convergence.

$$\Delta h_{new} = (1 - a)\Delta h_{calc,old} + (a)\Delta h_{calc} \tag{7.32}$$

In the current situation $a = 0.06$ is chosen. The value has been established by solution attempts for varying values. This indicates a rather strong coupling between solid and fluid, meaning that the elasticity has large influence on the local oil film thickness,. The values for Δh_{new} is afterwards copied to $\Delta h_{calc,old}$.
These deformations are incorporated into Reynolds equation from cycle to cycle.
The flowchart is shown in figure 7.15.

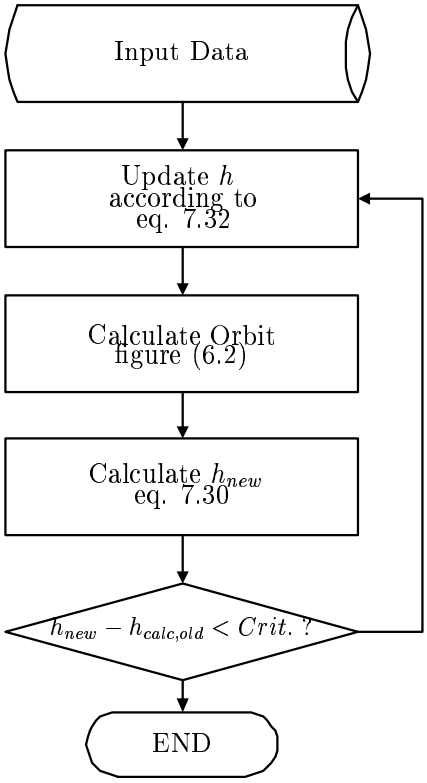

Figure 7.15: Flowchart of solid-fluid-solid interaction

Once these are converged a complete calculation has been performed for the chosen problem. Post-procession can be carried out regarding the desired parameter for investigation.

7.8.5 Simulation Result - Test

Calculating the bearing characteristics showed that the pressure profiles depends on the elasticity of the bearing components. Three simulations where the elasticity was included or not revealed this. The intermediate simulation including only the pre-tension of the frame box. The pressure profile for the simulation for 145 degrees after TDC (Full load 100 %), for all three simulation cases are shown in figure 7.16. The film thickness is found to deviate from the rigid case with co planar guide planes to the full flexible case. The same difference is also spotted for the pressure profiles in figure 7.17.

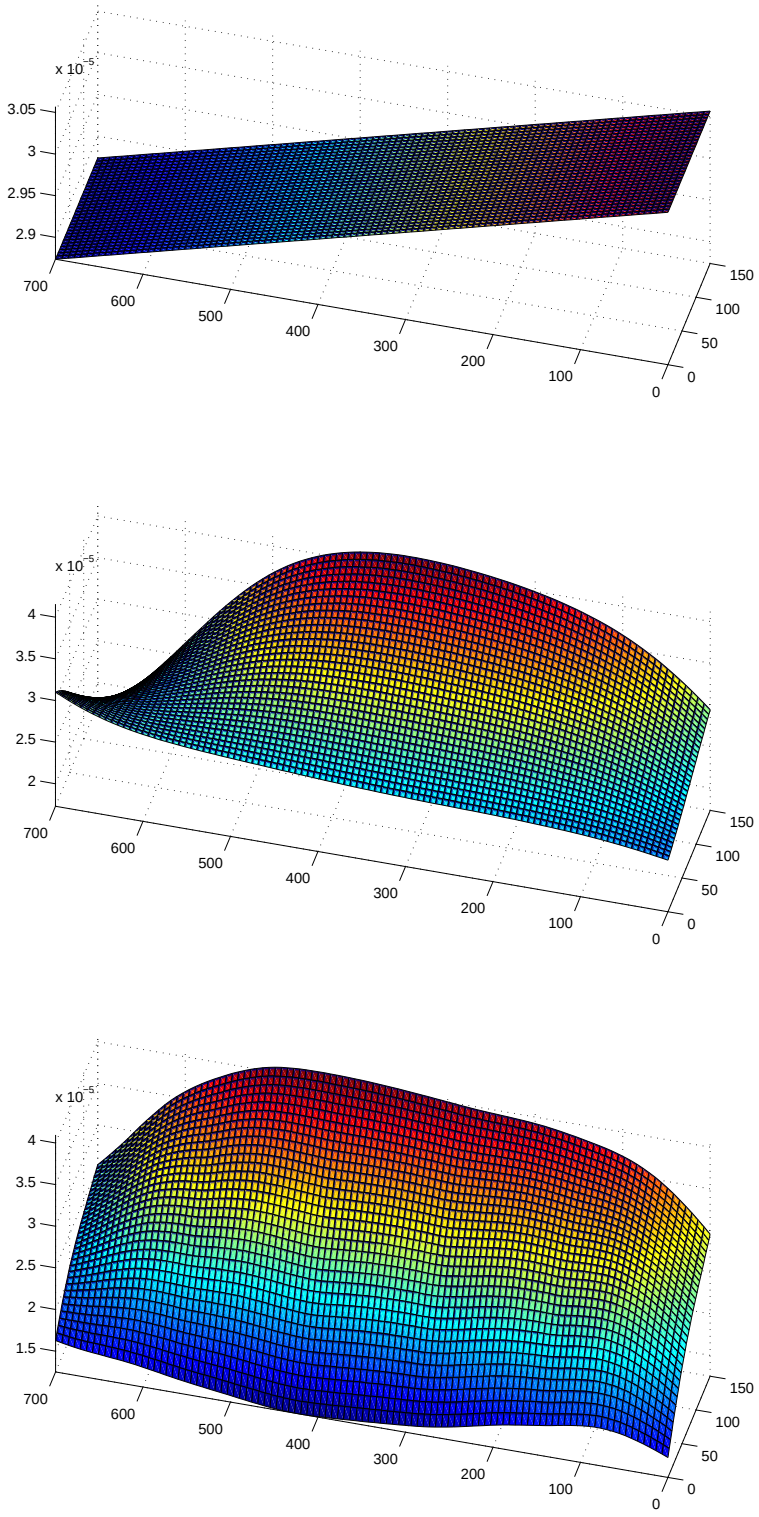

Figure 7.16: Oil film thickness on bearing surface (m) as a function of the width and length of guide shoe. UP: Oil Film Thickness STIFF
CENTER : Oil Film Thickness PRETENSION only
DOWN : Oil Film Thickness FLEX + PRETENSION

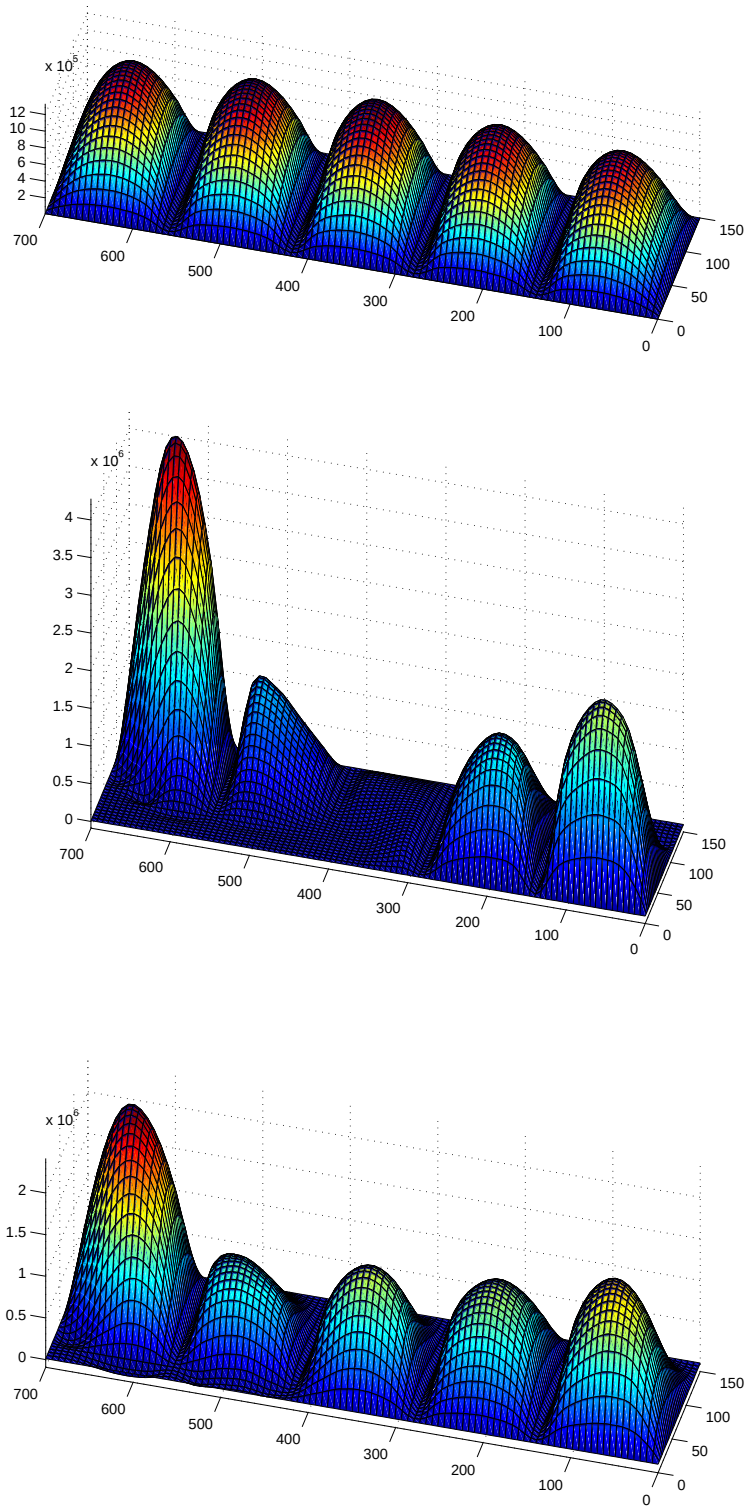

Figure 7.17: Pressure in bearing (Pa) as a function of the width and length of guide shoe.
UP: Pressure STIFF
CENTER : Pressure PRETENSION only
DOWN : Pressure FLEX + PRETENSION

As seen in the figures of the differences in both pressure and oil film profiles are significant. The flexible bearing is carrying the load in a different manner than the stiff bearing for the chosen time step. One reason for this is the nature of the guide plane deflections in time domain due to loading and pre-tension. The pre-tension deformations originate from the assembly procedure and the load dependent deformations from the normal load absorbed in the guide shoe bearing.

Chapter 8

Calculation Results Guide

In the following the results for the calculations of the guide shoe characteristics are presented including full elasticity in both bearing components. These are analogous to Vølund [2001].

8.1 Simulations

The guide shoe characteristics were established for the same conditions as the measured conditions which were according to load points on the propeller curve. The load points were 0,25,50,75 and 100 % Load.

Motoring 0 % Load, 123 rpm

For this loading condition the engine is running with no load but with full speed, which means that only inertia forces form the components are acting on the guide shoe system.

Propeller Loads 25, 50, 75 and 100 % Load

These loads are standard load points when running experiments on the test engine, which is the main reason for choosing these load points.

8.2 Inputs

Since measurements were performed the measured values were used as input for the simulations if they were available.

8.2.1 Oil Supply Pressure

The measured values were used see the data in figure 9.13 in chapter 9

8.2.2 Speed

The speed was applied directly from the measurements.

8.2.3 Normal Load

The normal load was calculated by using the measured pressure values and accelerations of the guide shoe to generate the normal force acting on the bearing - see chapter 9. The result of this calculation is shown in figure 8.1.

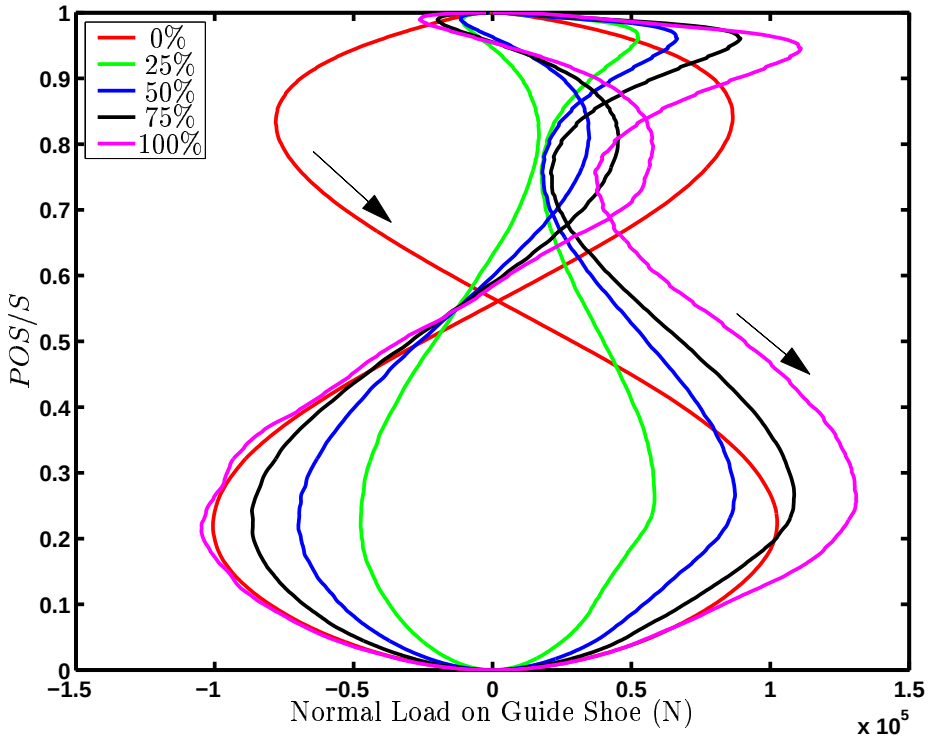

Figure 8.1: Bearing load

8.2.4 Viscosity

The measured temperatures were used for viscosity determination by equation 8.1. Average temperature values between shoe and plane were used for input.

$$\eta(TT) = \frac{e^{e^{(\alpha_{oil} TT + m)}} - 0.6}{\rho} \tag{8.1}$$

The values for α_{oil} and m are correlated to the chosen viscosity grade of the oil.

8.3 Characteristics

The characteristic data for the simulation are the oil film orbit, the maximum guide shoe pressure, the oil film thickness and the friction

8.4 Results

Selected simulation results are presented below. For each case the global position and attitude angle of the guide shoe are presented. Furthermore, the frictional term is presented as well as the pressure and film profiles at different locations during the stroke. The maximum film pressure and minimum oil film thickness curves are plotted as well.

8.4.1 Orbits for Guide Shoe Bearing

In the following section the simulated orbits for all the load configurations are presented. See figures 8.2 - 8.6. In the figures the COG is plotted within the nominal clearance for both degrees of freedom - translation h and rotation φ. On the left the orbit of the COG is shown and on the right the attitude angle.

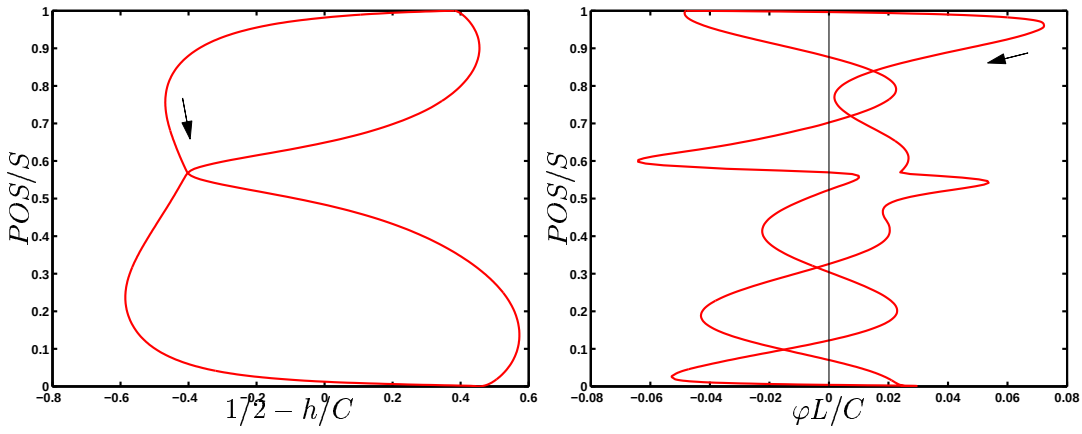

Figure 8.2: Orbit of bearing (Motoring)

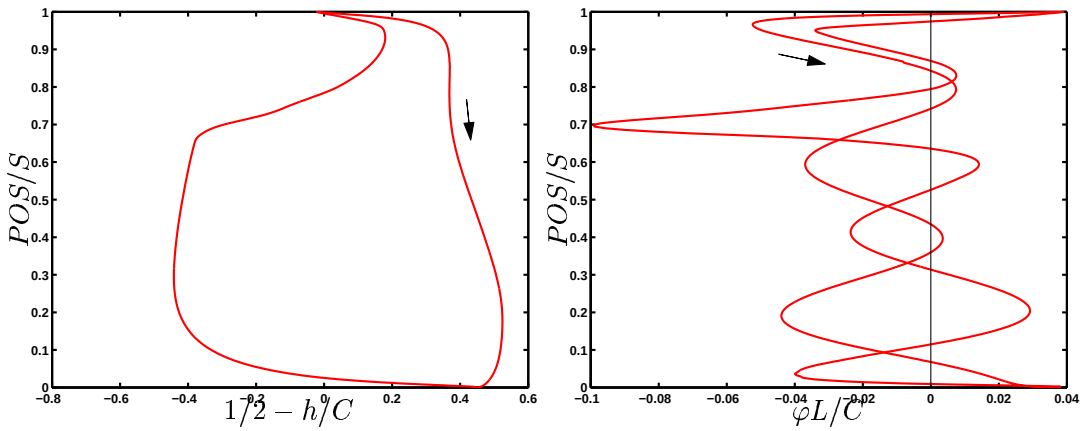

Figure 8.3: Orbit of bearing (25% Load)

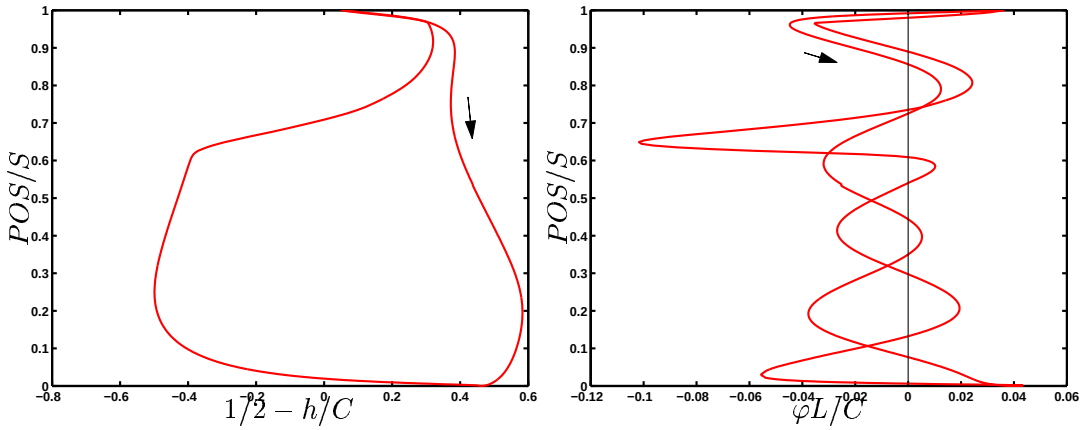

Figure 8.4: Orbit of bearing (50% Load)

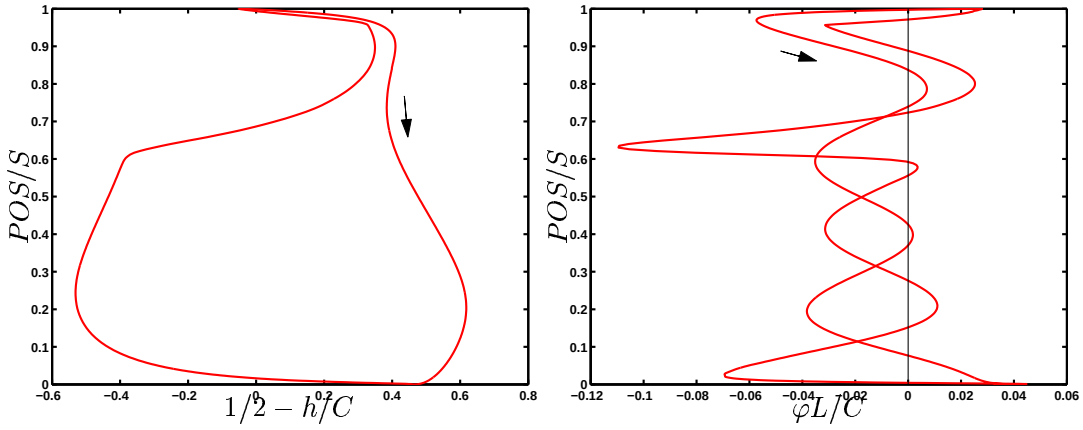

Figure 8.5: Orbit of bearing (75% Load)

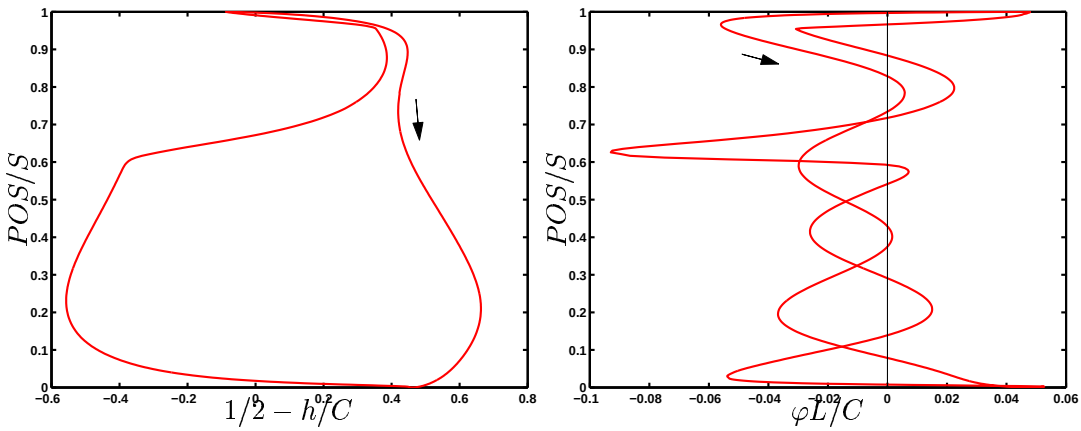

Figure 8.6: Orbit of bearing (100% Load)

In the figures 8.2-8.6 it is revealed that the film thickness and the attitude angle is greatly influenced by the normal load and the running condition of the engine. In all simulations the attitude angle is revealed to follow a mirrored pattern on the up stroke and the down stroke. The reason for this behavior originates in the initially deformed guide planes generated by the pre-tension of the stay bolts - shown in figure 7.13. Furthermore the orbit increases with increased load. The magnitude increases due to the relative larger normal load acting in the bearing. Compare for instance figure 8.3 and 8.6, which reveals this effect. Great influence is observed by the comparison of the left curves $1/2 - h/C$ and only smaller effects on the attitude angle. The relative larger amplitudes originate from the larger deformations and smaller film thickness' generated by the larger normal load.

8.4.2 Selected Pressure and Film Profiles for 100 % Load

Some characteristic plots of the point of minimum oil film thickness and maximum pressures are presented in figure 8.7 and 8.8 for 3 different crank angle degrees. Figure 8.7 reveals that the distribution of the oil film thickness on the bearing surface depends of the deformation of the guide planes and the load acting at the current crank angle. The same is observed for the pressure profiles for the three crank angles.

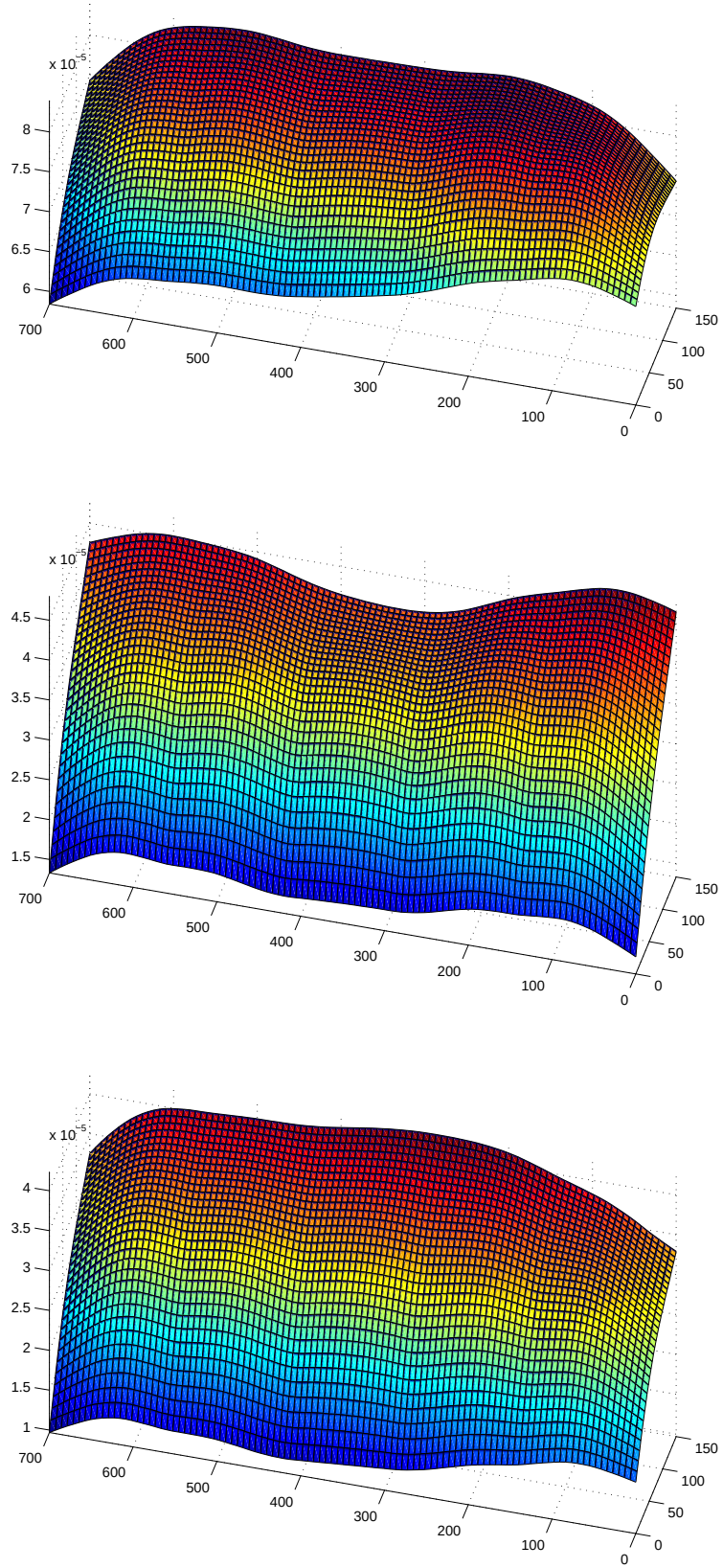

Figure 8.7: Oil film thickness distribution (m) on bearing surface for 3 different crank angles
UP: Oil Film Thickness 25 deg.
CENTER : Oil Film Thickness 105 deg.
DOWN : Oil Film Thickness 125 deg.

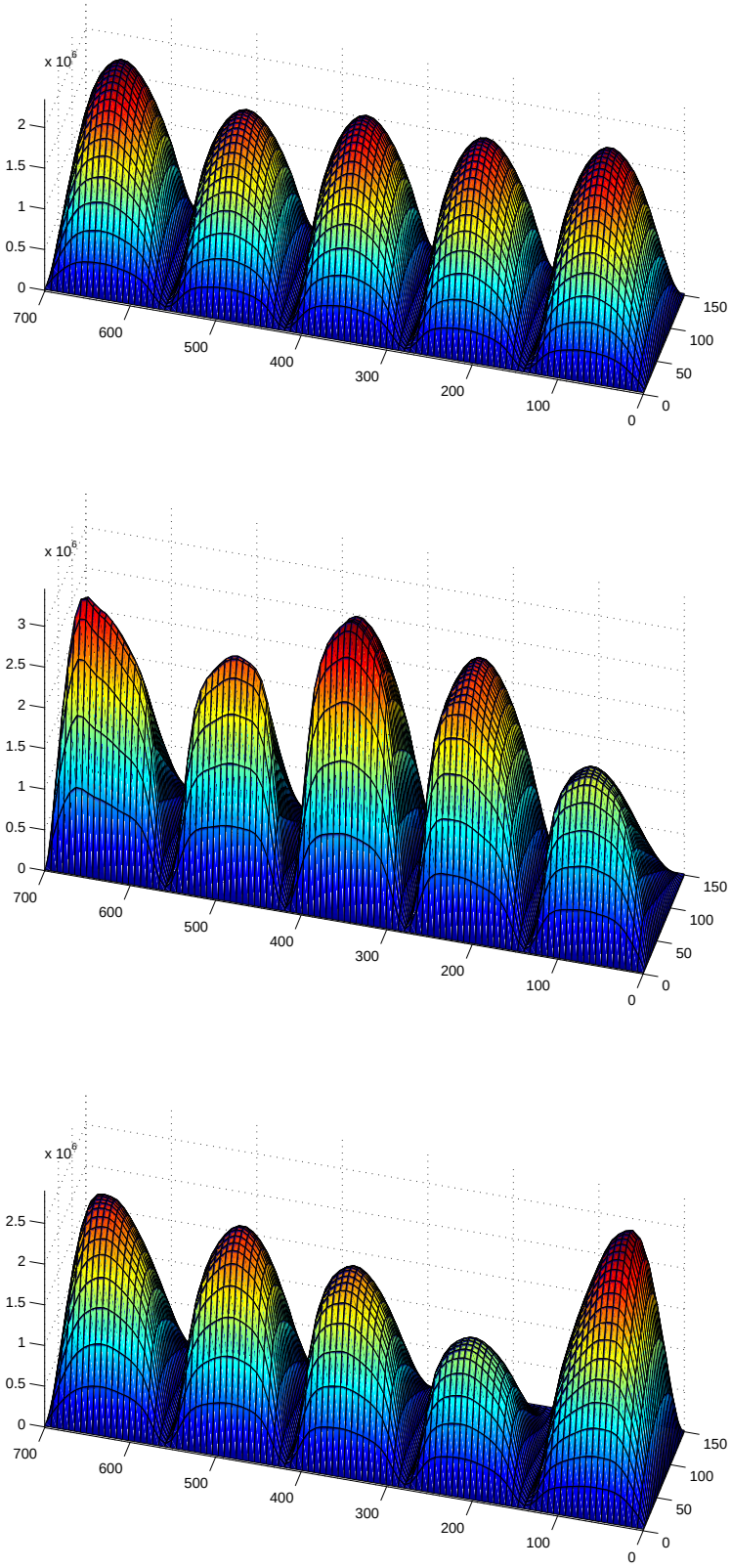

Figure 8.8: Pressure distribution (Pa) on bearing surface for 3 different crank angles
UP: Pressure 25 deg.
CENTER : Pressure 105 deg.
DOWN : Pressure 125 deg.

The minimum oil film thickness plotted as a function of the crank angle can be seen in figure 8.9 and the maximum pressure in figure 8.10.

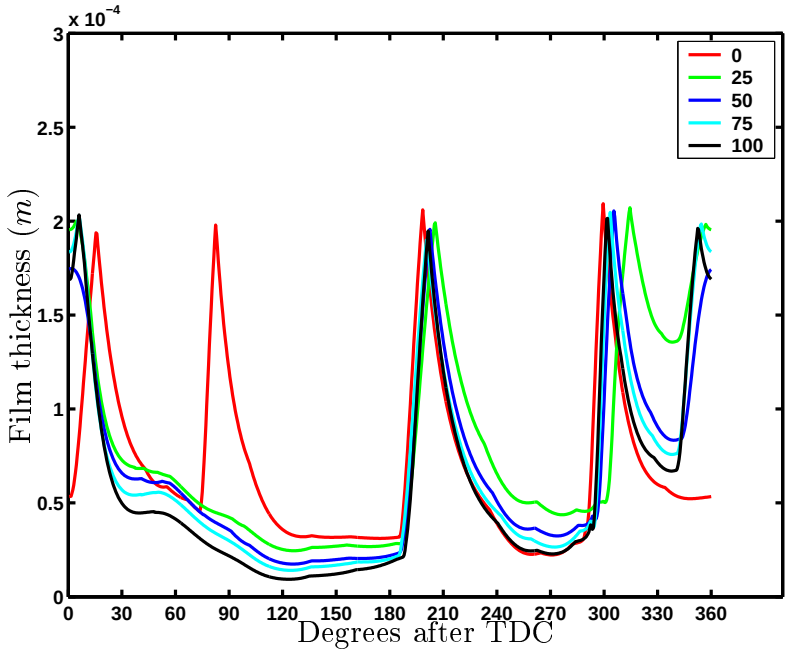

Figure 8.9: Minimum oil film thickness for all simulations

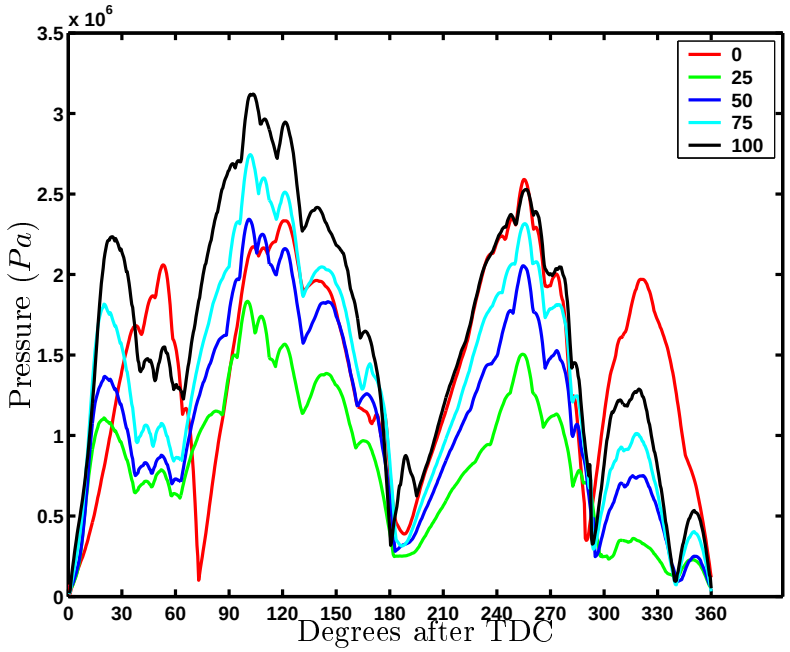

Figure 8.10: Maximum pressure for all simulations

8.4.3 Friction Losses Calculated in Simulations

Integrating the shear acting on the surface of the bearing results in the friction force acting of the bearing surface of the guide shoe. The results for all 5 simulations are presented in chapter 10 along with the measured values.

8.4.4 Power Losses for Simulations

In table 8.1 the total power loss is presented for the bearing along with the minimum oil film thickness and the maximum pressure. The power loss history can be seen in figure 8.11.

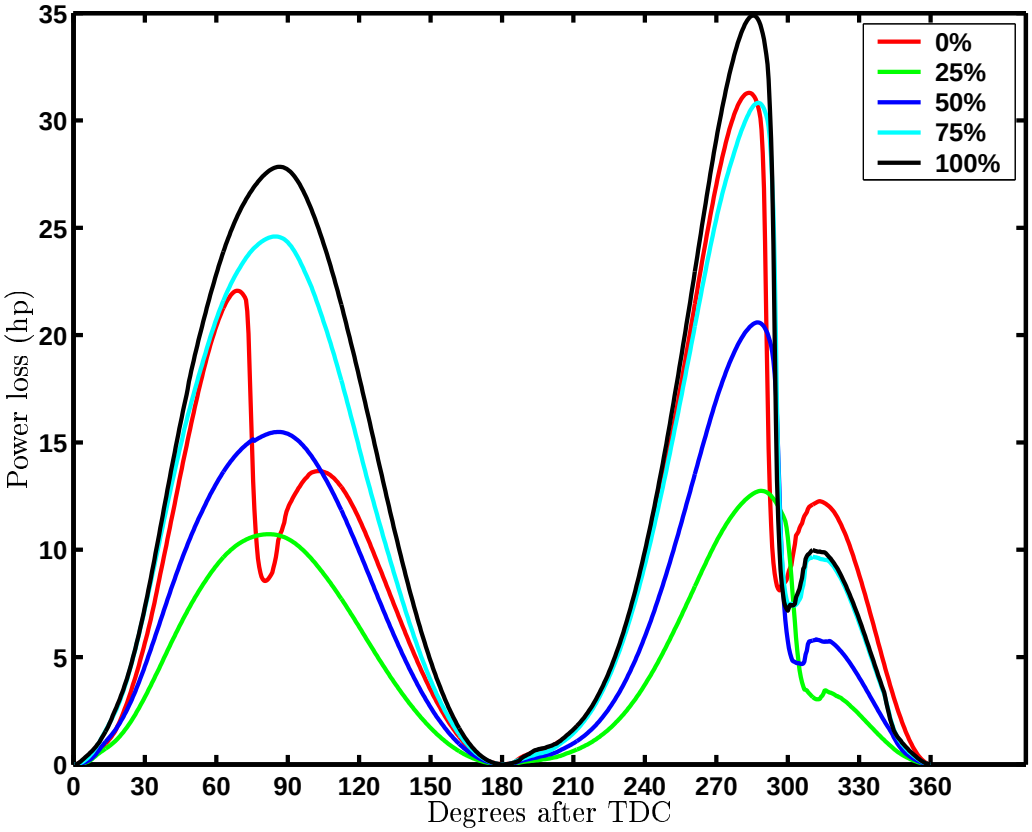

Figure 8.11: Power loss shown for all simulations

As seen in the figure the power loss increases with the load as expected. The table reveals that the minimum oil film thickness decreases for rising load and increased maximum pressures. The minimum oil film thickness is $9.3\mu m$ at 124 degrees after TDC for the full load condition and the maximum pressure occurs at 103 degrees after TDC and reached $31.3bar$.

Case No.	Load %	h_{min} μm	p_{max} Bar	Lost Power hp
1	00	22.2	23.4	9.5
2	25	24.1	18.1	4.7
3	50	17.4	23.4	7.1
4	75	14.1	27.4	10.8
5	100	9.3	31.3	12.1

Table 8.1: Characteristic values for all simulations for 1 guide shoe

8.5 Summary

In the current chapter 5 different simulation results for the bearing were presented. The characteristic parameters such as oil film thickness, pressure, friction loss and power loss were presented. All the inputs for the calculations were if possible generated using the measured quantities. It was revealed that the attitude angle of the shoe is important along with the elastic behavior of the components. The attitude angle was found to give film thickness variations of $28\mu m$ across the guide shoe. The oil film thickness was found to be as low as $9.3\mu m$. The overall loss for the bearing calculated at full load was found to be 1.1% of the generated power.

Chapter 9

Guide Shoe Measurements

9.1 Introduction

In order to gain knowledge about the important parameters controlling / affecting friction an experimental study was conducted. The experimental part of this study was conducted with the aid of people employed at the research laboratory located at MBD. The aim of the experiments were to verify and adjust the numerical model and to gain knowledge about the guide shoe characteristics - a new area of investigation at MBD.

9.2 The Experimental Apparatus

The frictional behavior of the guide shoe is controlled by the interference between the guide planes and the guide shoes as shown in the theoretical part of this thesis. Since the separating media is oil the friction behavior will be controlled by the lubrication condition of the guide shoe bearings. Therefore the measurements are focused on measuring the input/outout parameters which characterize the lubrication condition for the theoretical model. Relevant measurable parameters are listed below.

- Viscosity of the oil
- Oil supply pressure
- Applied normal load
- Pressure in bearing
- Oil film thickness
- Friction

9.2.1 Input Parameters

As shown some of these measured parameters may be considered as either input or output parameters for the theoretical description of friction in the bearing.

Viscosity of The Oil

Since the viscosity is very temperature dependent and only to a limited degree pressure dependent a measurement of the temperature of the oil trapped in the bearing gives a good estimate for the viscosity. The temperature of the bearing components are easily established and are used to predict the lube oil temperature. The measurement points for the guide plane can be seen in figure 9.1, and the sensor placement for the guide shoe can be seen in figure 9.12. It is hereafter assumed that the temperature of the oil trapped in the bearing may be expressed as the mean temperature of the two surfaces.

Oil Supply Pressure

The bearing is fed with oil via the telescope arrangement. This arrangement causes oscillating oil supply pressures. The oil supply pressure was measured by placing pressure transducers in the oil supply system in the maneuver side and the exhaust side of the bearing. The sensors were mounted in the oil grooves on each side of the bearing. This was done in order to get as close to the actual inlet position as possible.

Applied Load

The normal load applied is very important in determining the input characteristics for the bearing. This is established by measuring the cylinder pressure and the angular velocity of the engine. Furthermore, the acceleration of the guide shoe was measured in the vertical plane. These measurements all together makes is possible to calculate the normal load. It is assumed that friction can be neglected in this calculation.

9.2.2 Output Parameters

As all ready mentioned some of these measurement points are output parameters (seen form a calculation point of view) and the objective of these measuring points is to verify/adjust the numerical model.

Oil Film Thickness

The oil film thickness is a characteristic output parameter along with the pressure in the bearing. The oil film thickness is measured by capacitive sensors mounted in the guide plane and by inductive sensor mounted on the guide shoe. The placement of the capacitive sensors

can be seen in figure 9.1. The inductive sensors were placed on the guide shoe for oil film thickness measurements, but these results were of diverging quality and are not shown here.

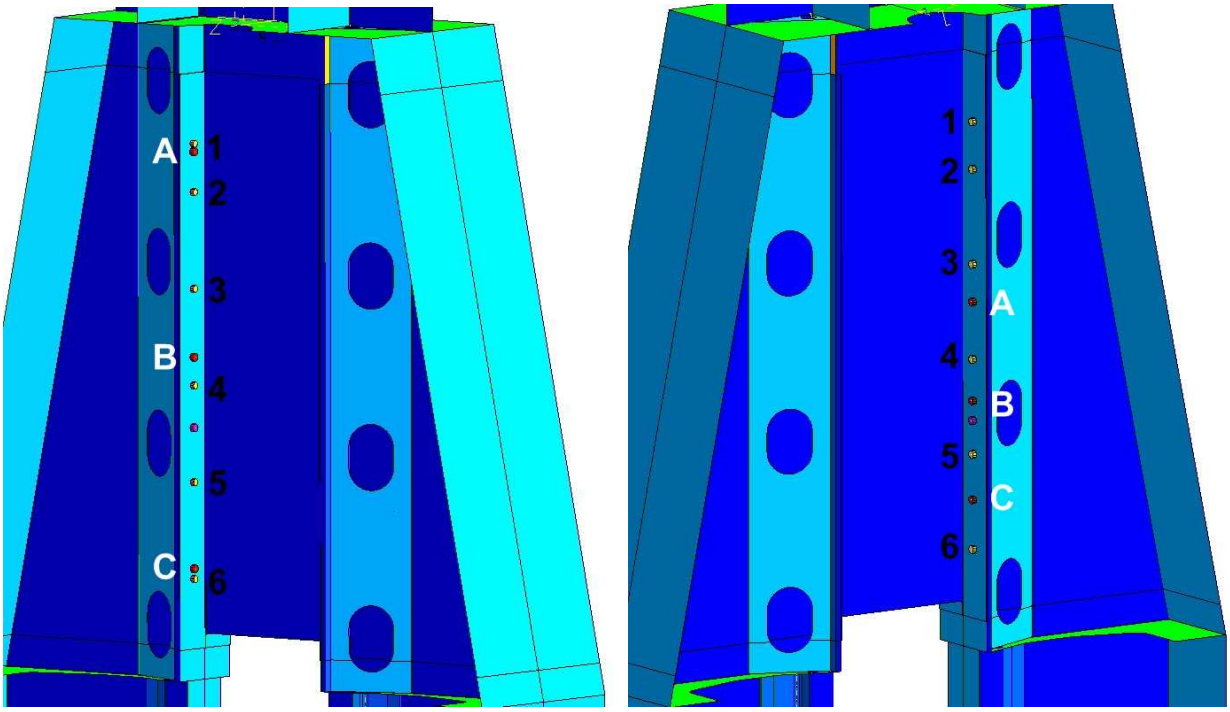

Figure 9.1: Left: Sensors in maneuver side. Right : Sensors in exhaust side. Yellow cylinders(numbers) represent temperature sensors. Red cylinders (characters) represent capacitive sensors.

Friction

Lastly the friction generated by the shearing and squeezing of the oil was measured. This was done by the use of a guide shoe especially designed for the purpose. No sensors were commercially available which could measure friction and at the same time be subjected to a large normal load. Therefore a new guide shoe design was made. The new design criteria of the guide shoe was that the normal stiffness on the running surface of the new design compared to the traditional design should not change too much and at the same time the bearing should be quite flexible in the transverse direction (the shearing direction). A contact calculation was carried out on both the standard design and the new design proposal. The guide shoes were pressed against the guide planes. The result - see figure 9.2- should not generate a higher contact pressure nor significantly shift the area of contact into another location. Several designs were tried before an acceptable solution was found. The result is shown in the result presented in figure 9.2. These kind of contact calculations are often used in the verification of new designs of guide shoe bearings. As shown in the result the contact

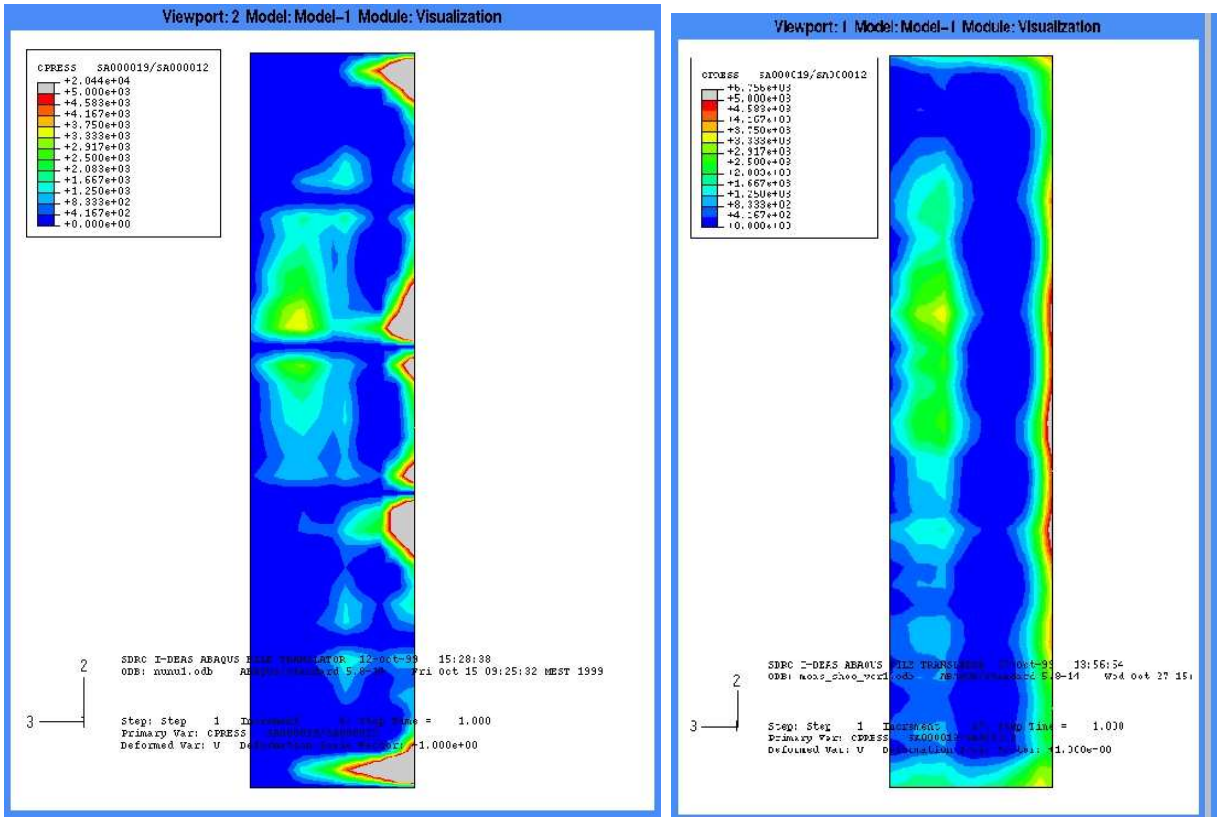

Figure 9.2: Result of contact calculation for guide shoe surface. Left: Original design. Right: Measurement design

pressure is lower for the test shoe than the original design, which is to prefer. The design was verified with people responsible for the design of guide shoe bearings in the R&D department at MBD. The result of the calculation generated a guide shoe design presented in figure 9.3. The figure shows that large stiffness in the normal direction is maintained by the seven ribs. This design of the ribs generates significantly smaller stiffness in the transverse direction than the normal direction. The guide shoe was manufactured and the result can be observed in figure 9.4.

9.3 View of the Measurement Guide Shoe

The shoe can be seen below before assembly in figure 9.4, and the mounted shoe is figure 9.5.

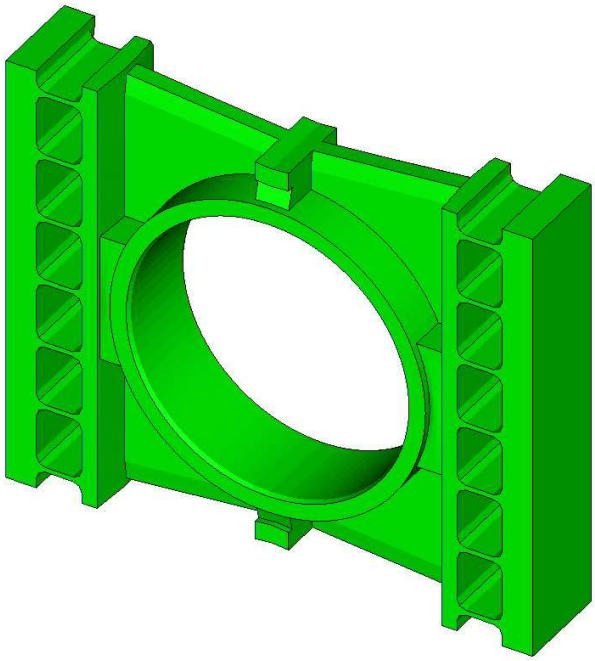

Figure 9.3: Final design of measurement shoe

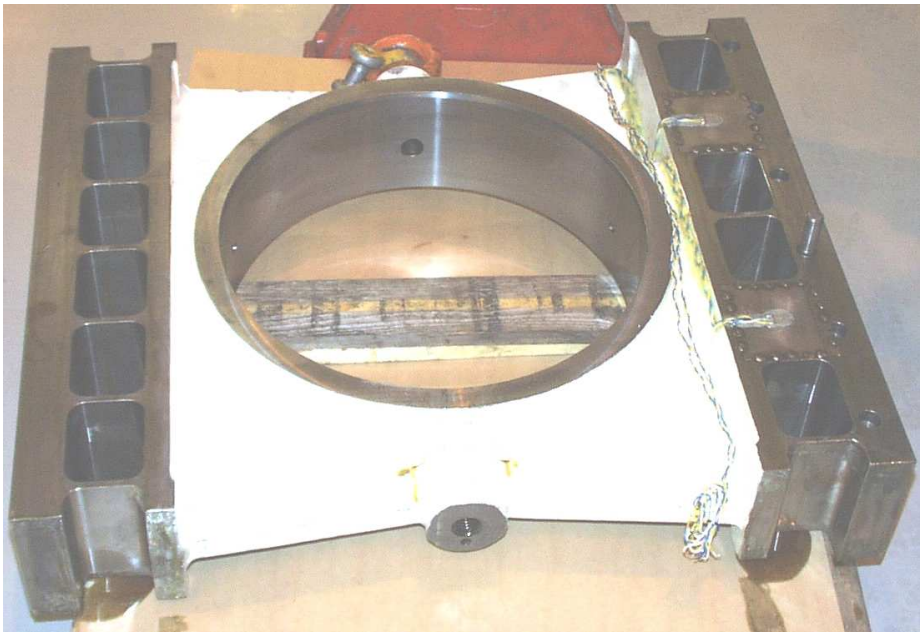

Figure 9.4: View of the measurement guide shoe before assembly

The friction measurement system was calibrated in a hydraulic jack by loading the system with different loads. The loads were applied in the normal loading direction and the transverse direction as well in order to generate a calibration curve. The measuring area for the strain gauges (Shear gauges) was constructed by thin plates welded on the side of the ribs on the

Figure 9.5: Measurement guide shoe installed in engine section

shoe, this can be seen in figure 9.6 and a closeup in 9.7.

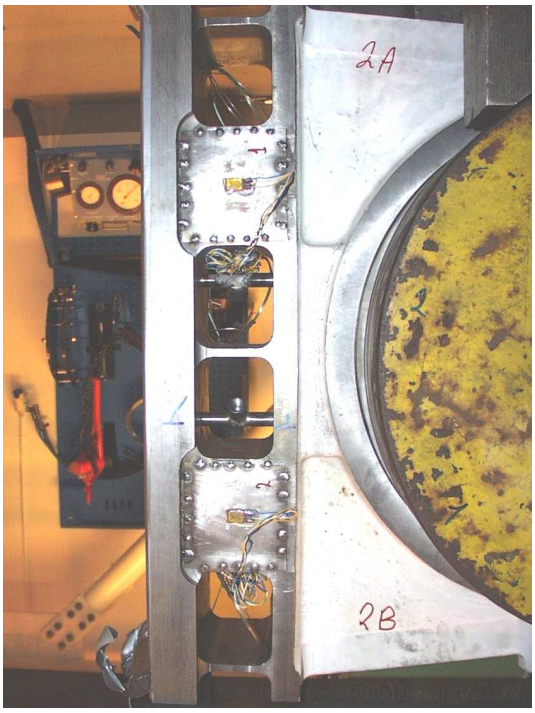

Figure 9.6: View of the strain gauge arrangement for frictional measurements

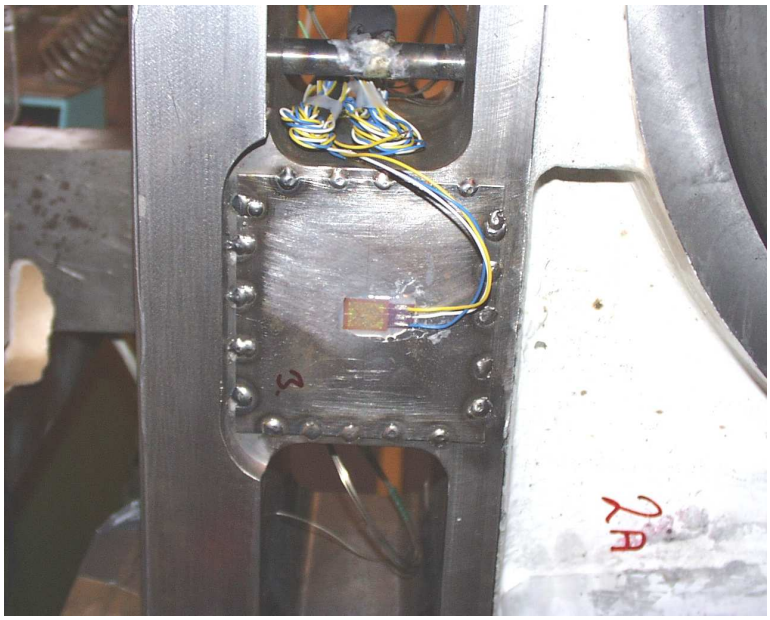

Figure 9.7: Close view of the strain gauge arrangement

Before the measurements were conducted all sensors were calibrated, and the data were used to transform the signal to the corresponding physical parameter (Force, Distance Temperature etc).

9.4 Signal Storing and Analysis

All the sensors mounted in the stationary part (Frame Box) were connected directly to the required amplifiers. The signal from the amplifiers were sent to the data logger equipment (Computer with I/O-board). All sensors mounted on the movable part (the guide shoe) could not be directly connected to the measurement computer. The cables would most likely fail because of the high inertial loads and that limited the size and number of measurement probes. Telemetry was used for transportation of the measurement signal. That required that the amplifiers for the sensors were mounted on the guide shoe and that a wireless signal transmitting device also was installed. The measurement equipment was powered by batteries also attached to the guide shoe. Since the amplifiers were mounted on the shoe a high robustness was required, because the components was subjected to inertial loads from +15 g to -25 g. The signal was transported by the transmitter and picked up by an antenna mounted on the guide planes. That limited the amount of signals that could be transmitted simultaneously. Three signals could be received from the telemetric system at a time. One from the temperature points, one from the acceleration and one from the strain gauge signals. The strain gauge signal channel contained all the strain gauges and the pressure transducers. The signal from the inductive transducers were picked up at another test run, where the signals form the strain gauges were disconnected and the inductive probes connected in stead.

Since only three signals could be received at one time a data switch was incorporated in the hardware. The data switch switched cyclically between all the active measurement channels with a frequency of $30 sec./channel$, which meant that that all strain gauge measurement were recorded as on long string of data. Afterwards the signal had to be chopped in pieces in order to separate the different measurement points. The necessary electronics were produced and tested by people located at the research laboratory at MBD.

Every measurement point was measured with reference to the position of the crank shaft position (angular encoder). Therefore a measurement was initiated every time a signal was received from the angular encoder to the measurement computer. The resolution of this encoded signal was 2048 pulses per revolution. Afterwards the raw data were extracted and ordered such that every measurement point were aligned to the same reference signal from the encoder.

9.4.1 Signal Treatment

After the signal was extracted from the bulk data the signal was processed. Every periodic signal was inspected for periodicity. A FFT-analysis was applied in order to see whether the whole system was subjected to a periodic behavior, other than the one originating from the loading. Since every measurement point had 10-20 revolutions of measured values stored these were averaged in order to filter noise from the signal after checking that the signal was periodic.

Furthermore, a moving least squares data fitting method was applied to the system in order to get continuity in the behavior of the different signals and to cancel out noise. This was only applied to signals where the measurement probe was active during all 360 degrees of one revolution, such as the strain gauge, accelerometer, pressure transducers and the inductive distance signal.

An example is shown below for the entire conversion process. The measurement point is one of the strain gauge measurement points.

9.4.2 Converting the Signal to a Physical Property

The data is converted to its physical property in this section. The chosen example is taken from the strain gauge signal from the maneuver side of the guide shoe.

The raw data is shown for 10 revolutions in figure 9.8 for the example presented above.

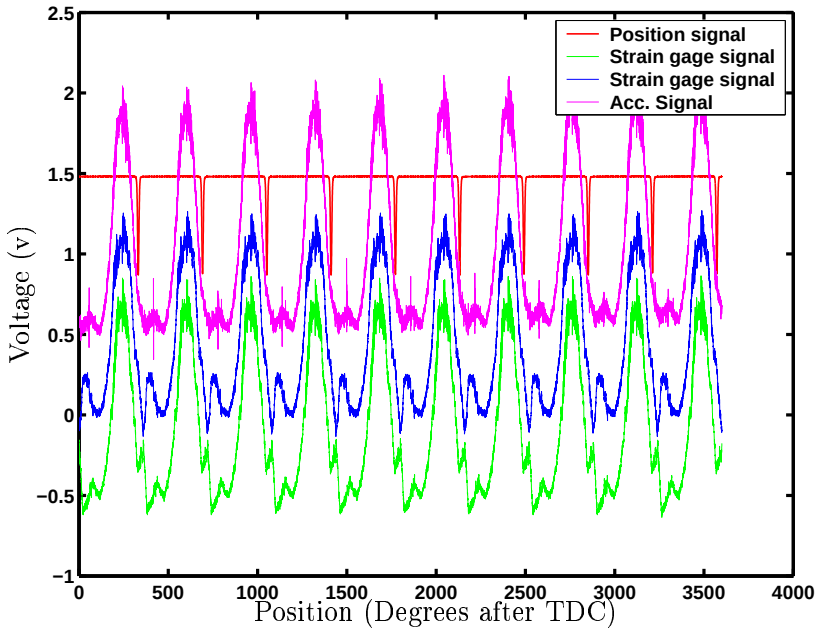

Figure 9.8: 10 revolutions of raw data

These signals are averaged over 10 revolutions and the result is shown in 9.9.

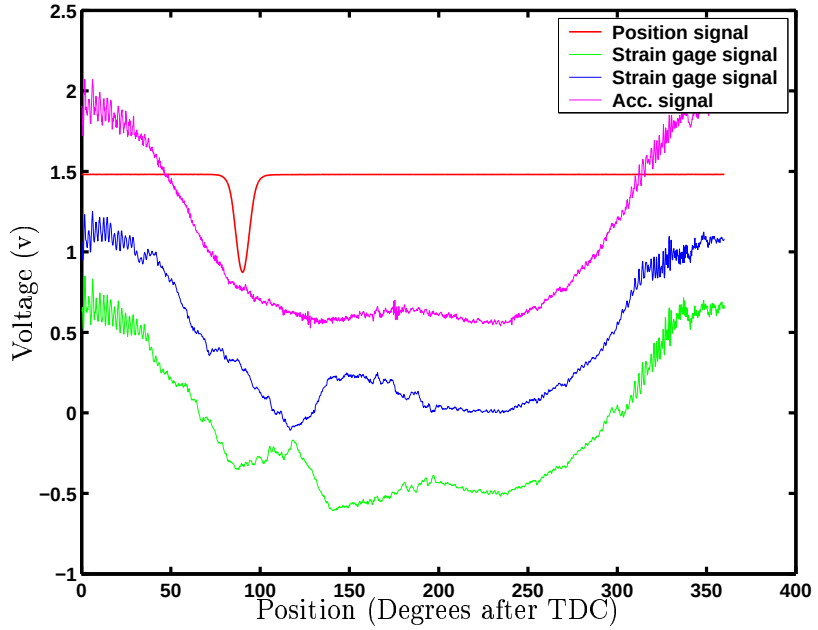

Figure 9.9: Measurement data averaged over 10 revolutions

The friction signal is calculated on this set of data and the result is shown in figure 9.10. This was done using the strain gauge signals and the accelerometer signal in order to extract

the inertial part of the measurement signal.

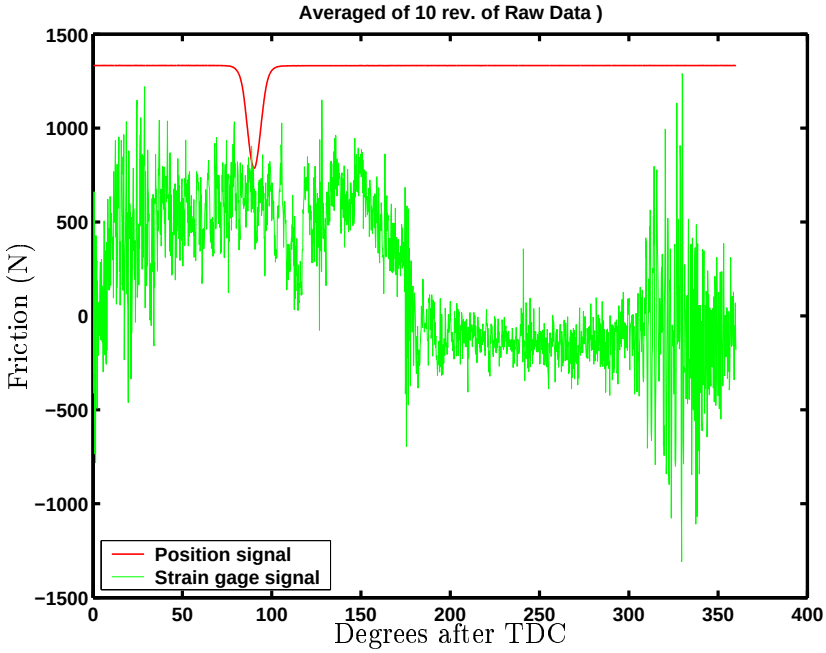

Figure 9.10: Frictional signal calculated from averaged data

The friction signal is calculated by applying least squares method to the signal is shown in 9.10 on this set of data and the result is shown in figure 9.11.

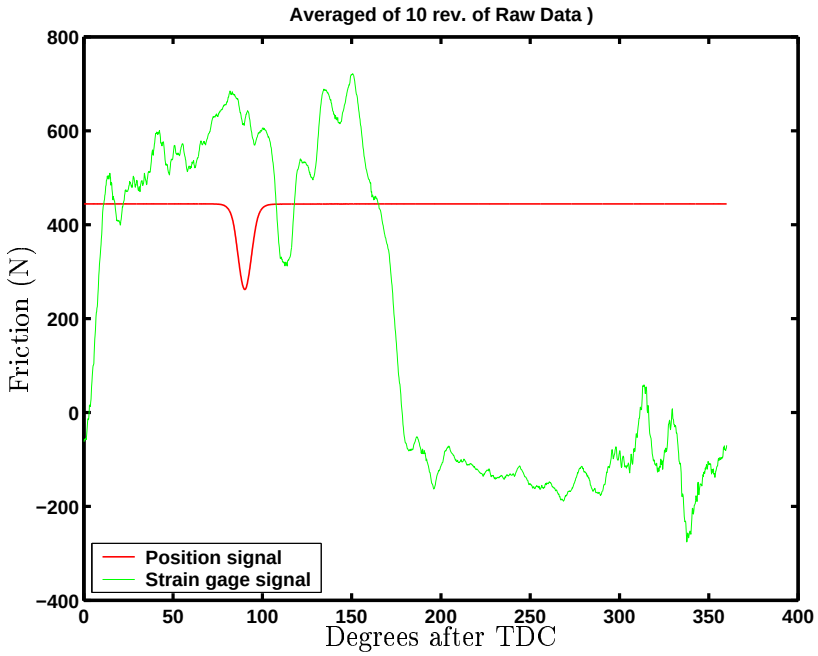

Figure 9.11: Frictional signal (Least Squares Method applied)

9.5 Measurement Programme

After the measurement points were established a measurement programme was decided. An ideal situation would be to adjust one parameter at the time for all parameters. That would however be very time consuming and very expensive.
Since the cost of running the engine is substantial a measurement programme of limited character was chosen. Because this is a friction study of engines built for ships a load diagram for propeller loading was adapted. The engine was run using propeller load at five different points in the load diagram - which is more or less a standard test schedule - see table 9.1.

Test	Load	Speed
1	0 %	123 rpm
2	25 %	77 rpm
3	50 %	98 rpm
4	75 %	112 rpm
5	100 %	123 rpm

Table 9.1: Measurement series

As shown above both the speed and the normal load changes on the guide shoe system as well as the oil supply pressure and therefore this gives rise to a lot of variations within the

programme.

9.6 Measurement Results (Input parameters)

In this section a fraction of the measurement results are presented.

9.6.1 Guide Shoe Temperatures

The temperatures were logged on 6 discrete points (3 on each surface) as shown in figure 9.12 the measured values can be seen in table 9.2.

Load Point	Up MAN	Center MAN	Low MAN	Up EXH	Center EXH	Low EXH
0 %	60	58	61	65	63	68
25 %	58	59	61	57	55	59
50 %	64	63	65	61	59	61
75 %	65	63	67	62	60	59
100 %	65	64	68	63	60	59

Table 9.2: Temperature ($^{\circ}C$) of guide shoe

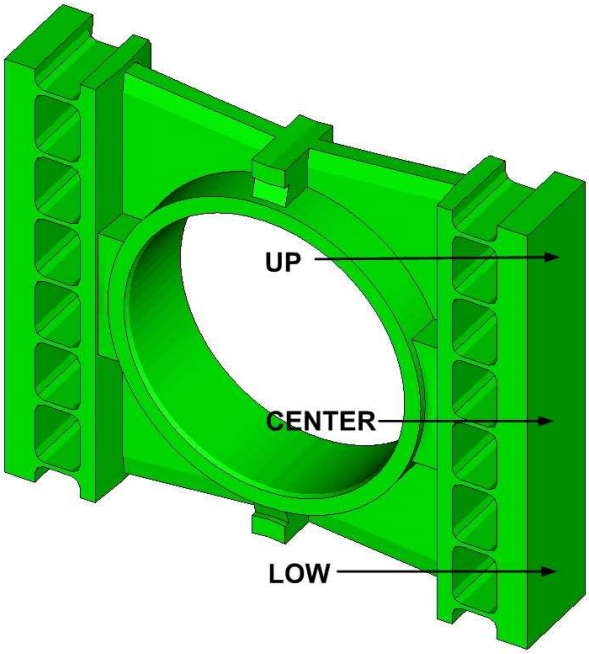

Figure 9.12: Placement of thermo couples on guide shoe

9.6.2 Guide Plane Temperatures

The temperatures were logged on 6 discrete points on each guide plane. These can be seen in table 9.3.

Point	1	2	3	4	5	6	1	2	3	4	5	6
Side	MAN	-	-	-	-	-	EXH	-	-	-	-	-
0 %	53	54	53	52	54	52	53	55	59	60	58	52
25 %	52	53	52	52	52	50	48	47	51	51	50	47
50 %	55	57	57	56	56	55	50	50	54	55	54	50
75 %	56	59	58	56	56	54	51	50	54	56	55	51
100 %	59	61	60	58	59	56	52	52	55	59	58	53

Table 9.3: Temperature ($°C$) of guide plane

The placement of the measuring points can be seen in figure 9.1

9.6.3 Guide Shoe Oil Supply Pressure

Pressures were logged on each run and plotted in figure 9.13.

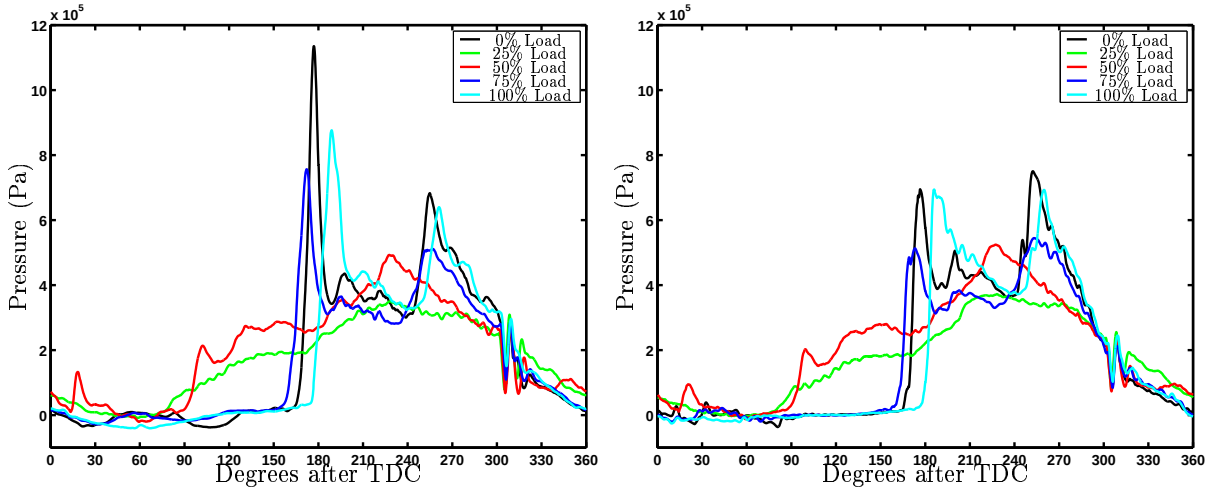

Figure 9.13: Left: Oil supply pressure measured in maneuver side. Right: Oil supply pressure measured in exhaust side

From the figure it can be seen that oil is supplied all the time for the load cases 25 % and 50 %. Upgrading the speed of the engine shows that the telescope oil supply system is no longer able to maintain a flow towards the bearing surface in the entire part of the stroke. This is caused by the volumetric expansion of the telescope, the inertial effects and the feed rate of the oil supply pump are not well adjusted to meet these situations concerning the lubrication of the guide plane during the first part of the expansion stroke.

9.6.4 Normal Load on Guide Shoe

The normal load on the guide shoe could not be measured directly but was established using a measured acceleration signal and the measured combustion pressure. These measurements can be seen below for the complete measuring program.

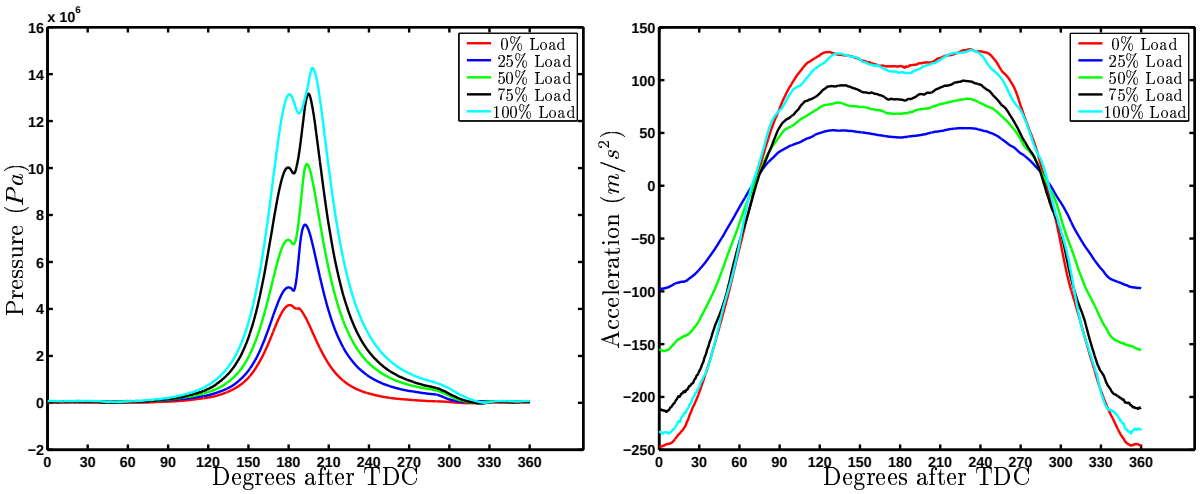

Figure 9.14: Left: Combustion pressure Right: Vertical acceleration of guide shoe

These data are used to generate the normal load input for the guide shoe bearing.

9.7 Measurement Results (Output parameters)

9.7.1 Oil Film Thickness Measurements

For placement of these measurement points see figure 9.1.
For all these measurements the oil film thickness (OFT) for the capacitive sensors were recorded. These are presented in the figures 9.15 - 9.18. The signal for oil film thickness for the 50% load were not recorded due to instrumentation failure.

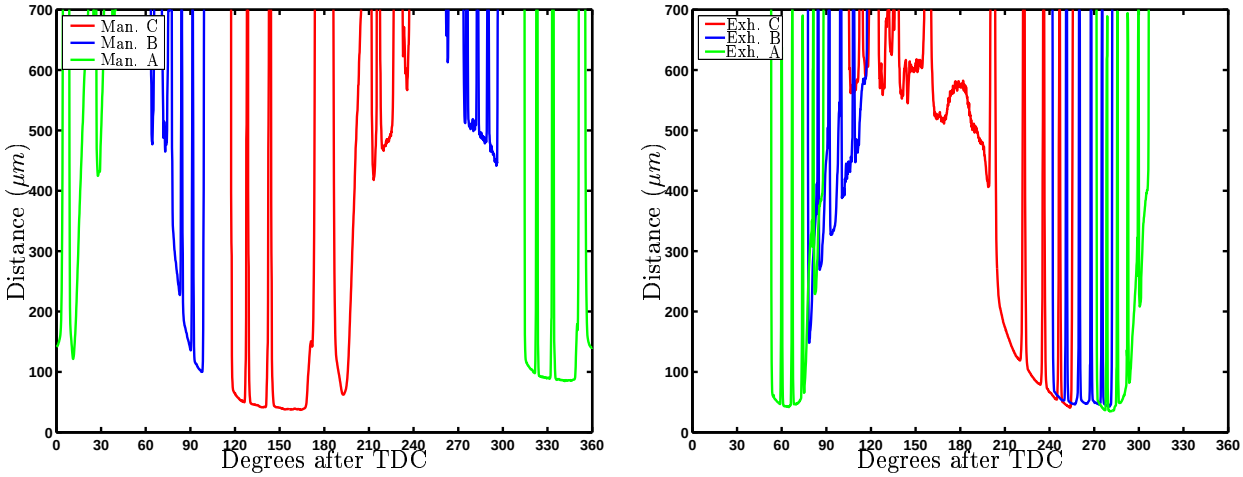

Figure 9.15: Left: Oil film thickness measured in maneuver side Right : Oil film thickness measured in exhaust side (0% Load)

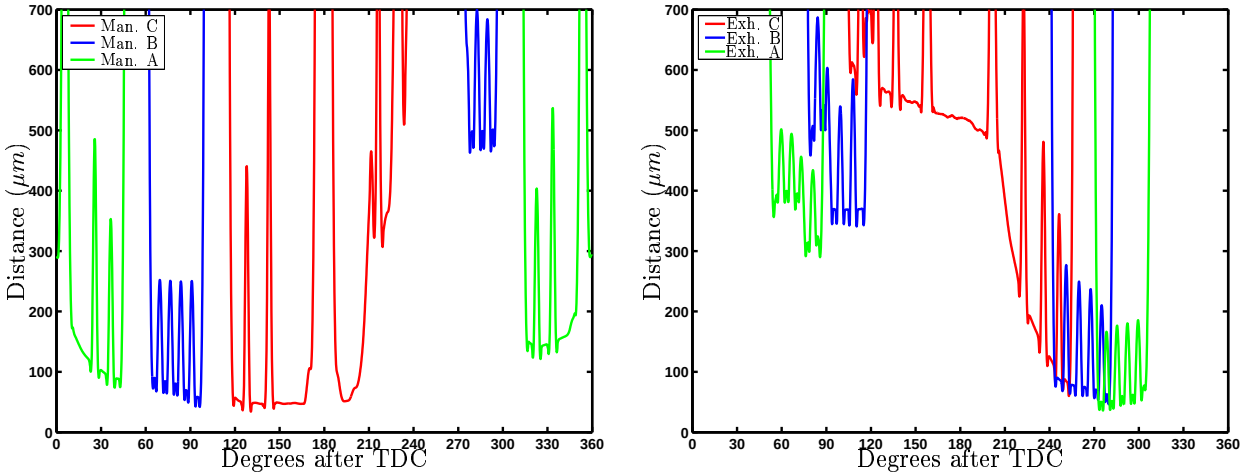

Figure 9.16: Left: Oil film thickness measured in maneuver side Right : Oil film thickness measured in exhaust side (25% Load)

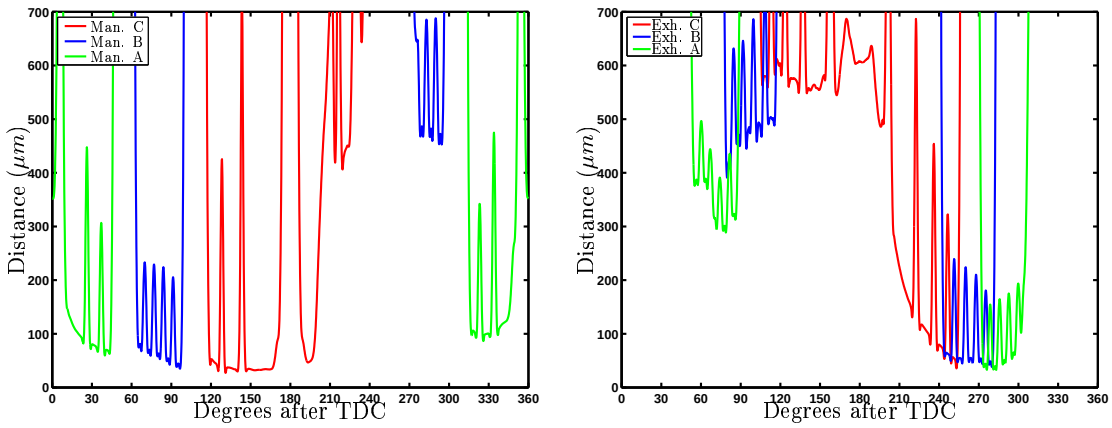

Figure 9.17: Left: Oil film thickness measured in maneuver side Right : Oil film thickness measured in exhaust side (75% Load)

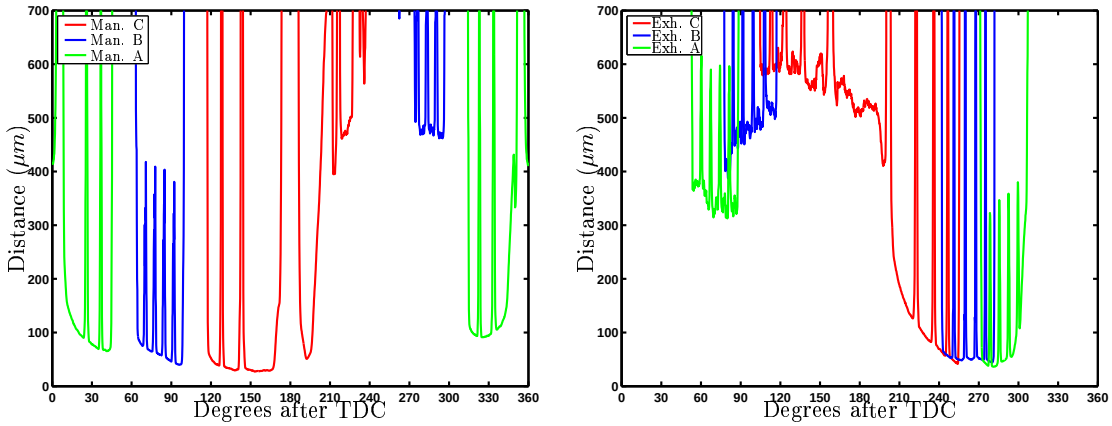

Figure 9.18: Left: Oil film thickness measured in maneuver side Right : Oil film thickness measured in exhaust side (100% Load)

9.8 Guide Shoe Friction

The strain gauge measurements are shown in the current section. Measured frictional values are shown in figures 9.19 - 9.23.

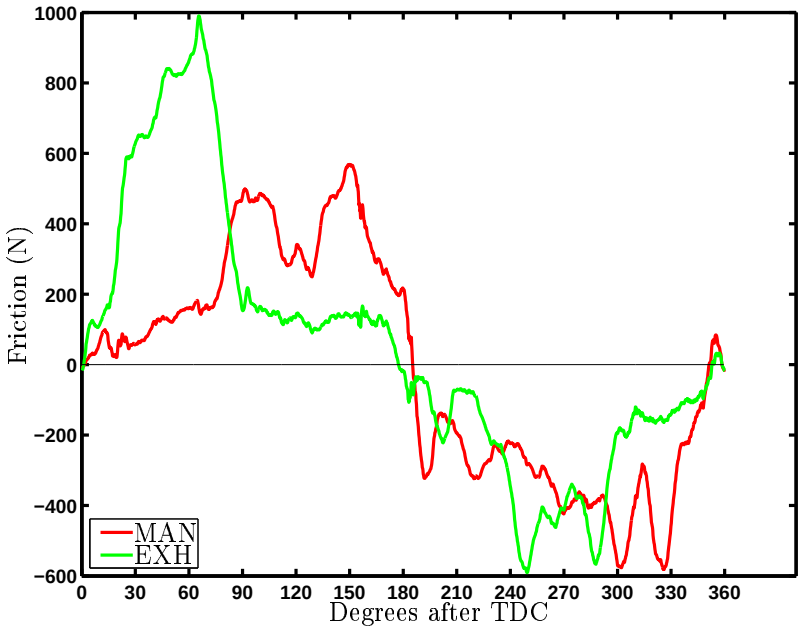

Figure 9.19: Friction for 0% load (Motoring)

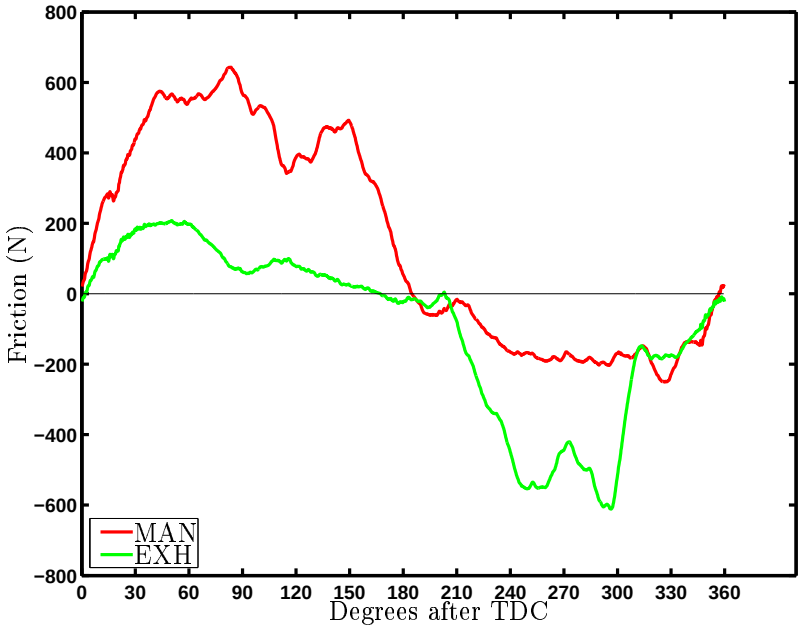

Figure 9.20: Friction for 25% load

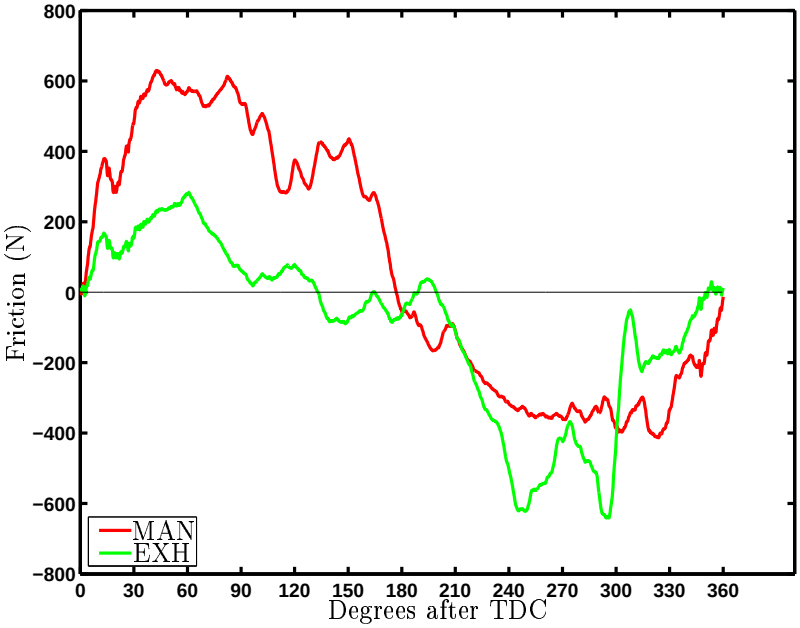

Figure 9.21: Friction for 50% load

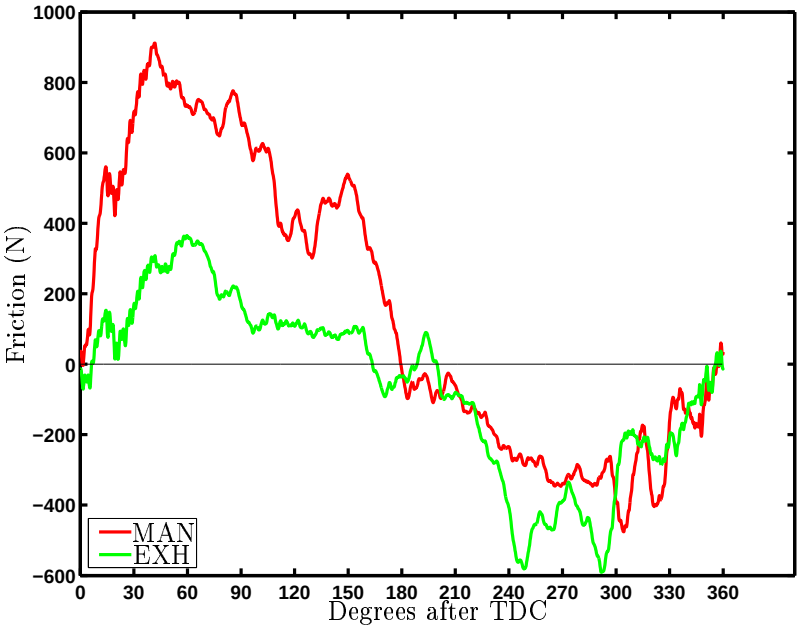

Figure 9.22: Friction for 75% load

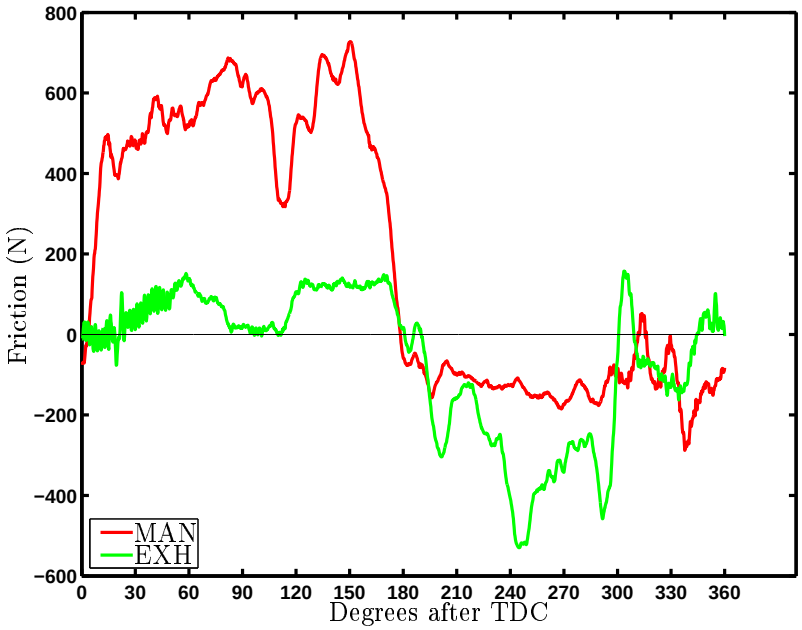

Figure 9.23: Friction for 100% load

All the measured quantities are used for input and post processing for the numerical part of this study in the following chapter.

9.9 Summary

A measurement apparatus for measuring friction, oil film thickness, pressure and temperature was presented. The measurements were conducted with satisfactory result. All though only a limited number of measurements could be done at a time this showed to be no problem since repeatability in the measured quantities were present.

Chapter 10

Calculation = Measurement for Guide Shoe ?

The chapter compares the experimental values with the ones generated from the calculation see also Vølund [2002]. The calculated terms shown in the current chapter are generated using the numerical model. All inputs for the numerical simulation were identical to the running conditions for the experimental apparatus derived in the previous chapter.
Since the main objective of this study is related to the frictional loss these quantities are natural for comparisons - shown in figures 10.1 - 10.5.

10.1 Friction

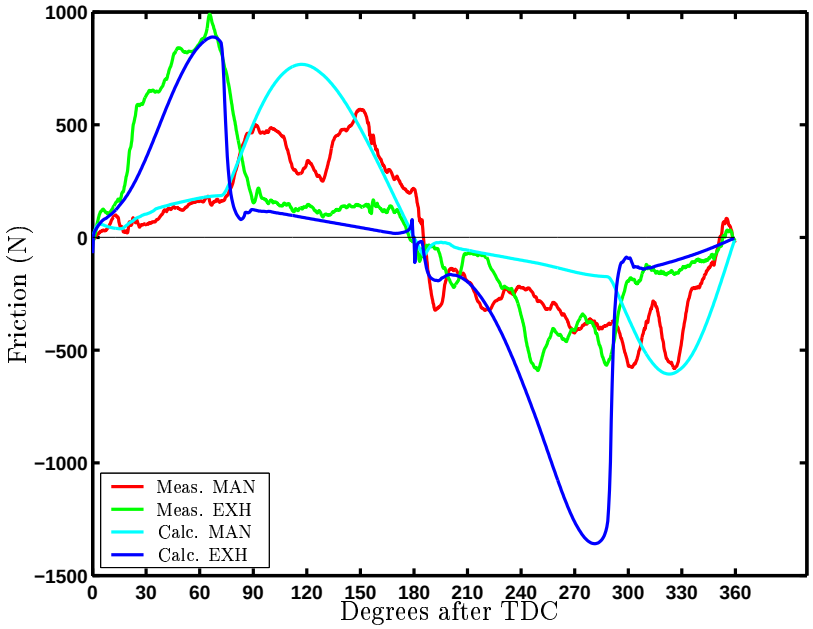

Figure 10.1: Friction 0% load

Focusing on figure 10.1 it is observed that correlation between theory and measurement is present. The frictional history for the first 180 degrees of the stroke shows fine agreement between theory and measurement. In the last 180 degrees the correlation is not so good. From 300 degrees to 360 degrees there is fine correlation again, but in the middle of the up stroke there is a large deviation. This deviation is seen on both signals. It seems as some cross coupling exists between the normal load and the shear term in the measured quantities compared to the theoretical values.

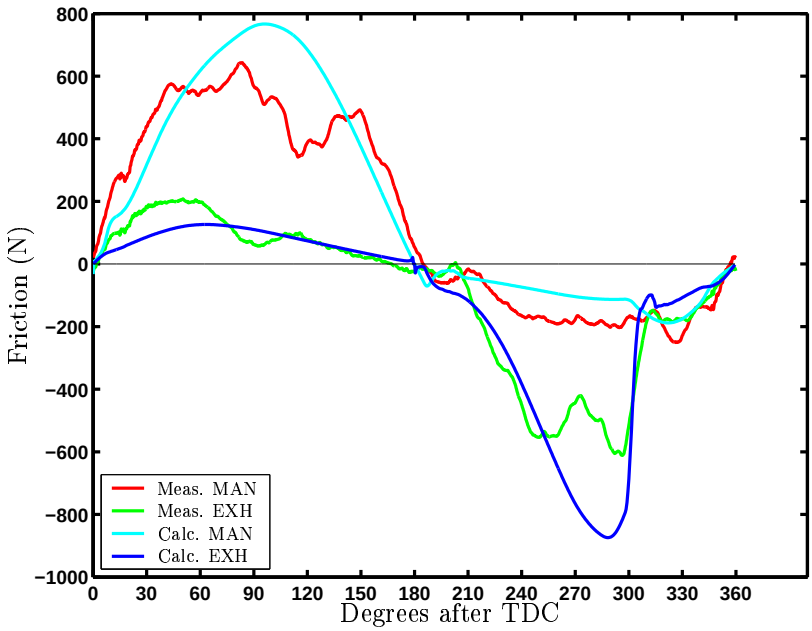

Figure 10.2: Friction 25% load

Focusing on figure 10.2 it is observed that the correlation between theory and measurement is present in the entire stroke. The theoretical values shows smoother distributions than the measured values, but all in all very nice agreement between the two of them.

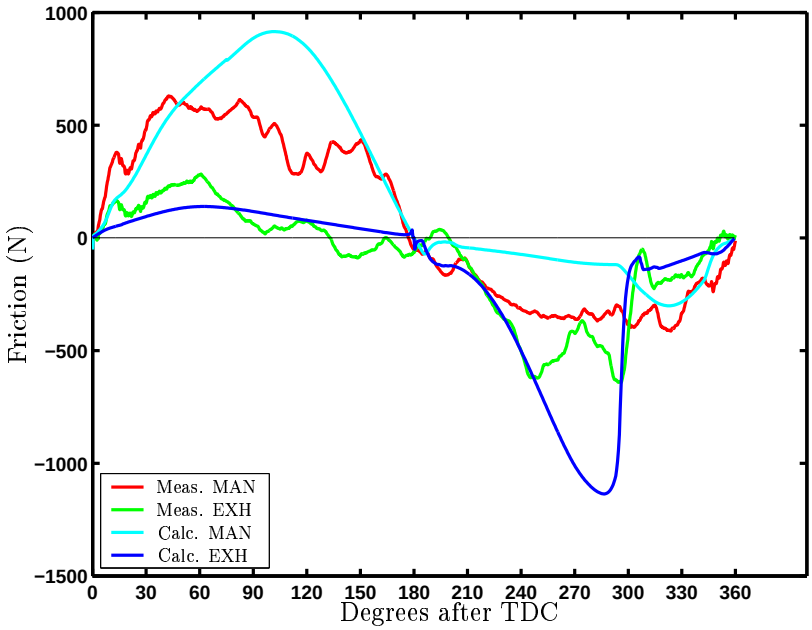

Figure 10.3: Friction 50% load

Figure 10.3 shows acceptable agreement in the first 180 degrees and also fine correlation between the exhaust side signals. The maneuver signal is however diverging some which is more pronounced in the latter part of the stroke.

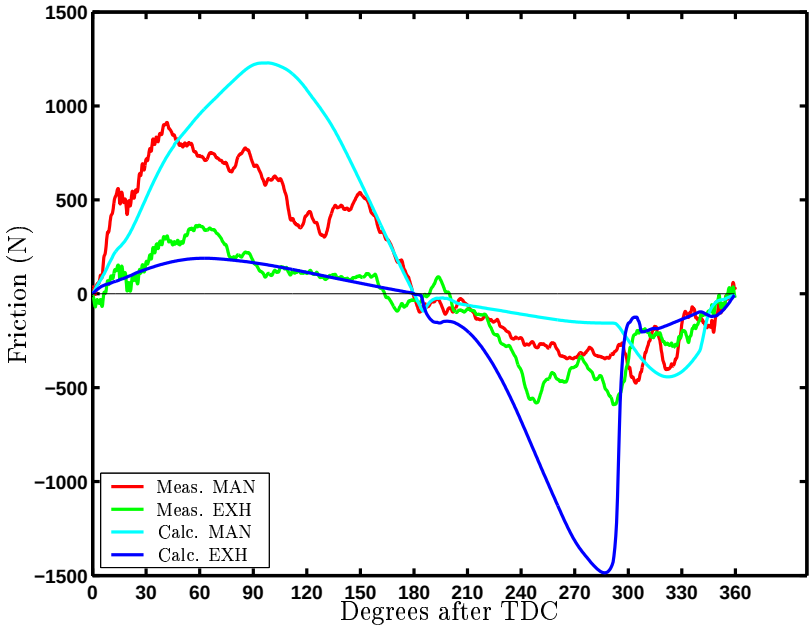

Figure 10.4: Friction 75% load

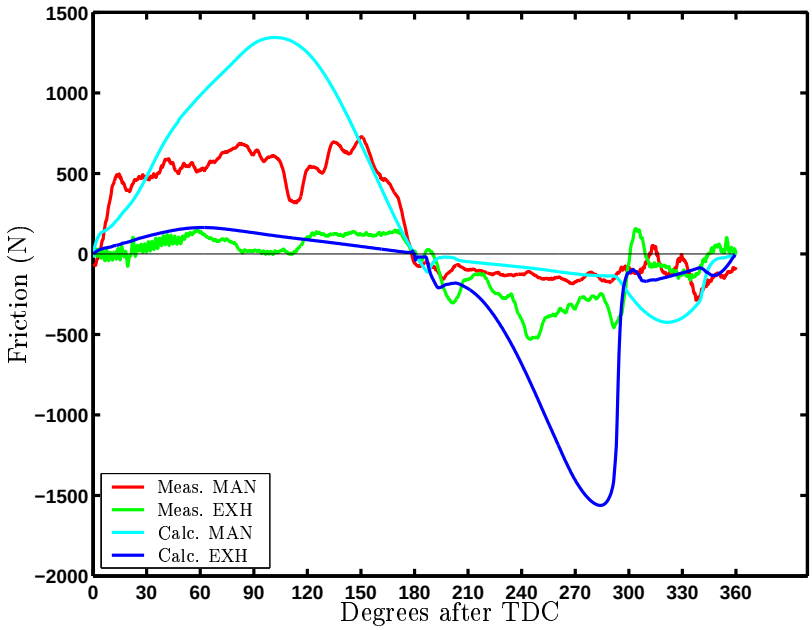

Figure 10.5: Friction 100% load

Focusing on figure 10.4 and 10.5 shows rather acceptable agreement in the lightly loaded sides of the bearing for both cases. For the loaded bearing surfaces the deviation between theory and measurement shows diverging results the more load the more deviation between the two. It seems like a cross coupling effect from the normal load acting on these surfaces is seen. ´The deviations are larger when the nominal load increases. This effect is observed for all configurations.

Discussing these results one should bear in mind that this bearing is subjected to a load which is approximately 50-100 times higher in the normal load direction than the friction force is generating in the other direction, and part of the deviations may be found here. The normal load may generate a cross coupling terms as all ready mentioned. Furthermore, the measured signal in this direction is a combination of mass force and the frictional force acting on it. In this case the mass forces are up to 10 times larger than the frictional force - also a possible source of error. Therefore the sensitivity for the component may not be as is was established by the calibration. Lastly local effects may interfere from the guide plane on to the guide shoe. One should bear in mind that large forces are acting in the bearing and the friction force is only a small quantity in this context.

However, the correlation all together shows reasonable results bearing in mind the possible error causes. Problems with the numerical simulations may also be the cause. The chosen cavitation model may interfere with the area of shearing fluid and thereby generate larger friction forces. The accuracy of the frame box stiffness interferes with the oil film thickness distribution and therefore also the friction force generated. Lastly the assumption of the temperature distribution within the oil film may be too optimistic. Another issue is the ap-

pearance of the guide planes due to thermal expansion which is not included in the model and also the pre-tension appearance of the guide plane compared to the theoretically determined one. The large influence of the pre tensioned guide plane on the oil film distribution was revealed in chapter 7 and inaccuracies between the actual appearance of the guide planes and the theoretically determined appearance will influence the frictional loss.

10.2 Oil Film Thickness

In the numerical problem the oil film thickness values have been extracted for the sensors mounted in the guide plane at approximately the same positions as the placement of the sensors in the experiment. These are shown in figures 10.6 to 10.9.

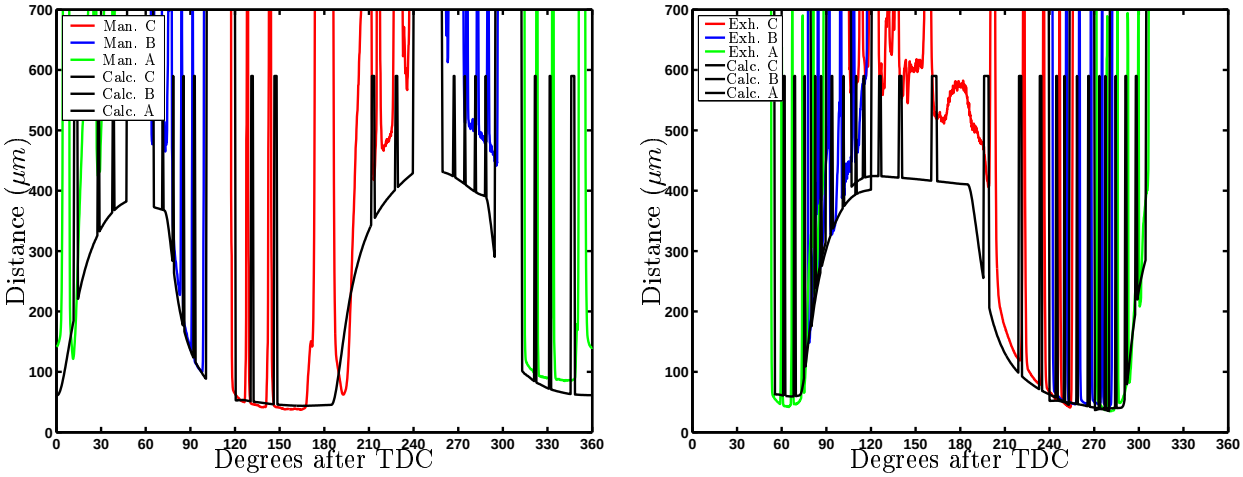

Figure 10.6: Left: Oil film thickness measured in maneuver side. Right : Oil film thickness measured in exhaust side. (0% Load)

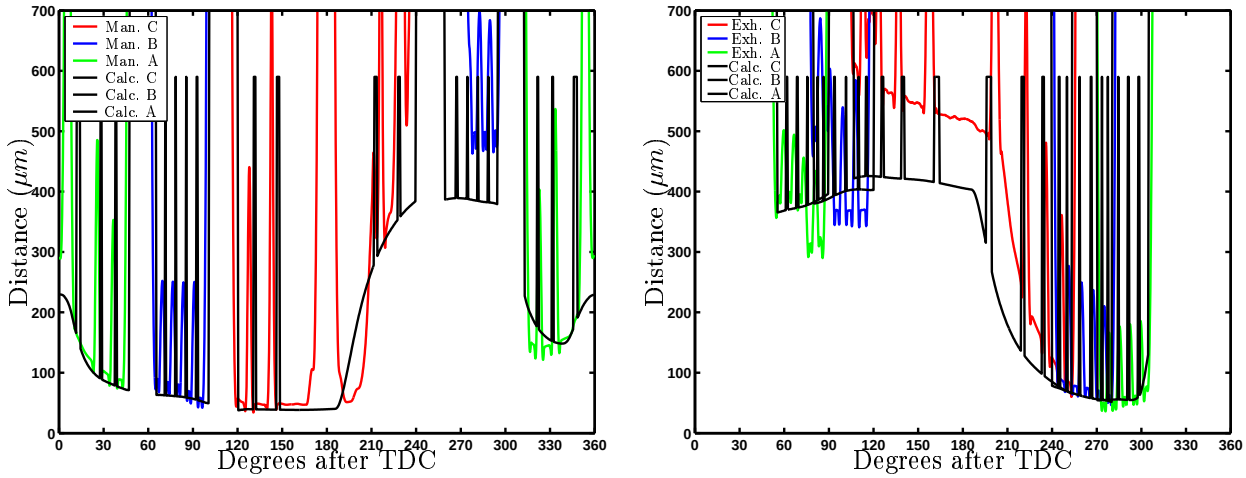

Figure 10.7: Left: Oil film thickness measured in maneuver side. Right : Oil film thickness measured in exhaust side. (25% Load)

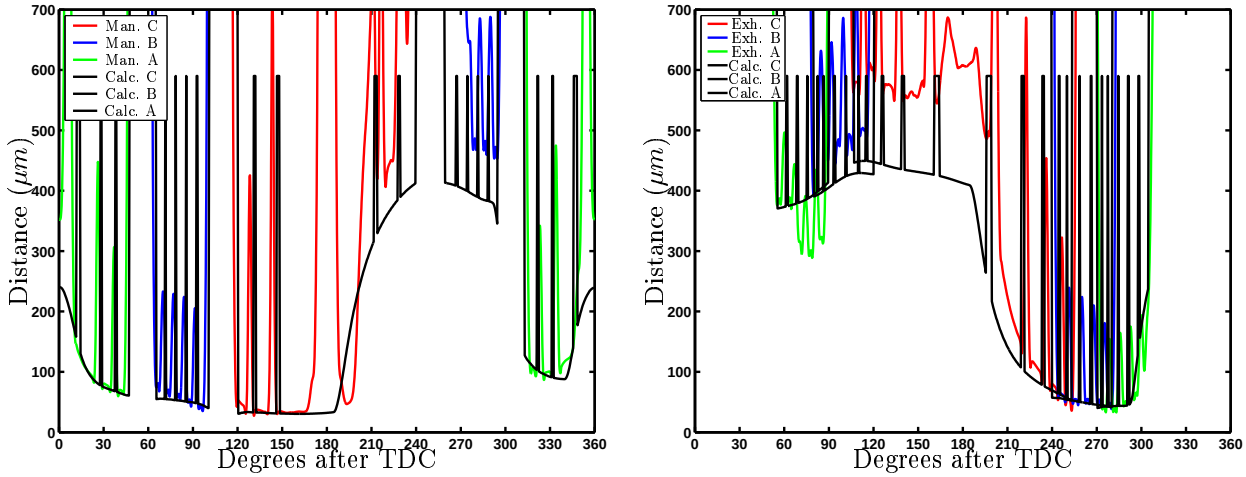

Figure 10.8: Left: Oil film thickness measured in maneuver side. Right : Oil film thickness measured in exhaust side. (75% Load)

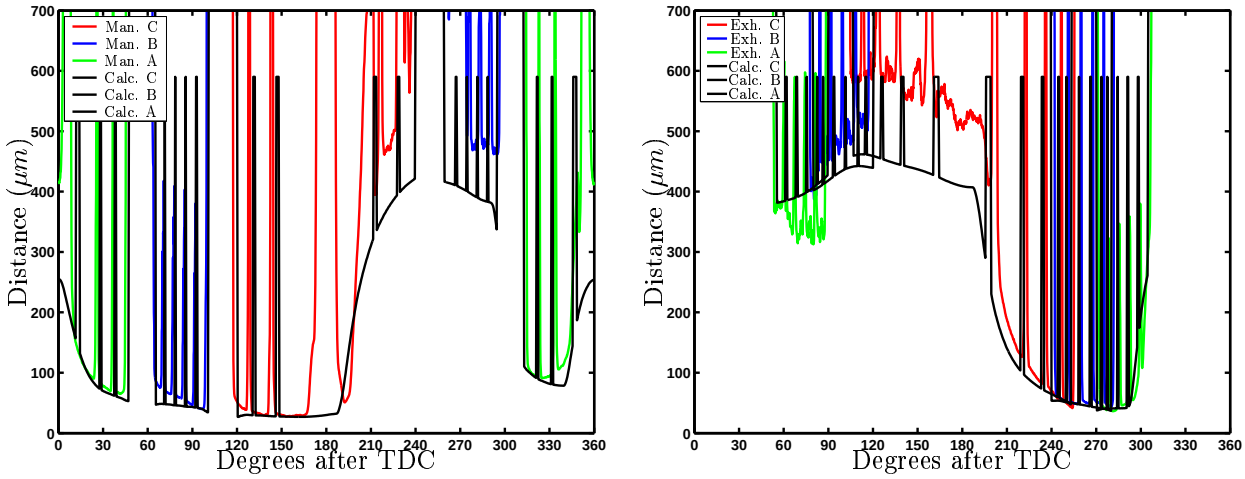

Figure 10.9: Left: Oil film thickness measured in maneuver side. Right : Oil film thickness measured in exhaust side. (100% Load)

As seen in the figures for the oil film thickness reasonable agreement is found between measured and simulated values for guide bearing passing each sensor. The sudden changes in the measurement signal indicates that an oil groove is passing the sensor. A comparison between 0% and 100% load reveals that the characteristics are very sensitive to changes in load history. The overall correlation between measured values and predicted values is quite satisfactory. Figure 10.6 shows good correlation in large parts of the stroke but in other parts there are large deviations. The fluctuating measurement results in these areas originate from cavitation of the bearing see for instance the sensors A,B and C in the exhaust side where cavitation is present when the guide shoe is running mainly on the maneuver plane where the sensors A,B and C in the maneuver plane are placed. The opposite is the case once the shoe shifts to the other guide plane. The same is the case for the results presented in figure 10.9.

10.3 Summary

Comparisons were performed between simulated and measured values concerning oil film thickness and friction force. The measured values for oil film thickness and frictional loss corresponds to an acceptable degree with the simulated values. The deviations are of varying size. The numerical model does to an acceptable degree reflect the true guide shoe characteristics. It is hereby concluded that the established numerical model to a satisfactory degree describes the guide shoe characteristics concerning oil film thickness and friction history. The established numerical model may therefore be utilized in a frictional reduction study.

Chapter 11

Reducing Guide Shoe Frictional Loss

In the present chapter a study concerning reduction of the guide shoe power loss is carried out.
The investigation is initiated in the analytical model. This model is described as a bearing with co-planar bearing surfaces with rigid components. The system is presented in equation 7.3. This seems reasonable since the deviation concerning the frictional loss from the numerical description is small.
The parameters in this model were changed such that the frictional loss was the target for the optimization search process.
Since the guide shoe is running in a two stroke engine there are a number of parameters that cannot be changed. For instance the oil supply pressure cannot be altered. Furthermore, the temperature of the guide planes cannot be changed unless the frictional term is modified and thereby affecting the temperatures of the bearing surfaces. The oil probably can not be changed since this is the system oil and is therefore used for lubrication in the entire engine - the main bearings, the connecting rod bearings, the cam axle system and so on. However, there are still a number of parameters that can be changed. The active degrees of freedom are the width (W_{shoe}) and the length (L_{shoe}) of the bearing. Furthermore, the surface of the bearing can be changed by for instance the number of oil grooves N_{groove} and their appearance and also the clearance (C).
In the first part of the study it is assumed that the bearing surfaces are to remain co-planar and that the oil grooves are locked to be positioned in axial direction. This gives 5 degrees of freedom which are listed below. Isothermal conditions are assumed.

- Number of oil grooves (N_{groove})
- Width (W_{shoe})
- Length (L_{shoe})
- Clearance (C)

- Viscosity (η)

In the following a rule is set such that the minimum oil film thickness compared to the standard design may not be reduced no matter the design chosen. Furthermore, it is assumed that the temperature of the components is constant. The load pattern is chosen to be the 100% load case. The oil supply pressure is assumed to be atmospheric for the analytical models.

11.0.1 Initial Model

The model for the initial analysis is chosen to be the actual bearing. The input values are

- Number of oil grooves :$N_{groove} = 4$
- Width of bearing $W_{shoe} = 0.15m$
- Length of bearing $L_{shoe} = 0.7m$
- Clearance $C = 0.4 \cdot 10^{-3}m$
- Viscosity $\eta = 0.035Pas$

The locus is calculated and the minimum oil film thickness is extracted and the frictional loss is calculated - shown in table 11.1.

Case	L_{shoe} m	W_{shoe} m	C $m \cdot 10^{-6}$	N_{groove} -	h_{min} $m \cdot 10^{-6}$	P_{lost} hp
1	0.7	0.15	400	4	31.5	11.0

Table 11.1: Reference condition (Analytical solution)

For the first analysis is assumed that the clearance C and number of oil grooves (N_{groove}) is constant. Furthermore, it is assumed that the bearing area $L_{shoe}W_{shoe} = 0.105m^2$ is to be kept constant. The reason for this the fact that this is the current design criteria which is based on the size maximum nominal bearing pressure, which may not override 20 bar.
The result is shown below for the case where 4 oil grooves are used as a constant value, the length is varied and the width adjusted such that the bearing area is constant.
As shown in table 11.2 an optimum is actually located at a L_{shoe}/W_{shoe}-ratio which is identical to the reference condition - both regarding lowest friction and minimum film thickness. If then the number of oil grooves are altered such that the total number is halved and they are evenly distributed a new optimum is reached. The results can be seen in table 11.3.
As shown in the table 11.3 above the minimum oil film thickness has increased which opens for the possibility to change the bearing area without altering the bearing capacity compared

Case	L_{shoe} m	W_{shoe} m	C $m \cdot 10^{-6}$	N_{groove} -	h_{min} $m \cdot 10^{-6}$	P_{lost} hp
1	0.5	0.21	400	4	27	12.1
2	0.6	0.175	400	4	30.4	11.3
3	0.7	0.15	400	4	31.5	11.0
4	0.75	0.140	400	4	31.4	11.0
5	0.8	0.131	400	4	31.2	11.1
6	1.0	0.105	400	4	28.6	11.8

Table 11.2: Result ($L_{shoe}W_{shoe} = 0.105m^2$)

Case	L_{shoe} m	W_{shoe} m	C $m \cdot 10^{-6}$	N_{groove} -	h_{min} $m \cdot 10^{-6}$	P_{lost} hp
1	0.5	0.21	400	2	39.8	9.3
2	0.55	0.191	400	2	40.3	9.2
3	0.6	0.175	400	2	40.1	9.2
4	0.7	0.150	400	2	38.5	9.5

Table 11.3: Result 2 grooves ($L_{shoe}W_{shoe} = 0.105m^2$)

Case	L_{shoe} m	W_{shoe} m	C $m \cdot 10^{-6}$	N_{groove} -	h_{min} $m \cdot 10^{-6}$	P_{lost} hp
1	0.45	0.178	400	2	30.8	8.5
2	0.5	0.160	400	2	31.0	8.5
3	0.55	0.145	400	2	30.6	8.6

Table 11.4: Result 2 grooves ($L_{shoe}W_{shoe} = 0.08m^2$)

Case	L_{shoe} m	W_{shoe} m	C $m \cdot 10^{-6}$	N_{groove} -	h_{min} $m \cdot 10^{-6}$	P_{lost} hp
1	0.30	0.217	400	1	29.9	7.1
2	0.35	0.186	400	1	31.3	6.9
3	0.40	0.63	400	1	30.5	7.0

Table 11.5: Result 1 groove ($L_{shoe}W_{shoe} = 0.08m^2$)

Case	L_{shoe} m	W_{shoe} m	C $m \cdot 10^{-6}$	N_{groove} -	h_{min} $m \cdot 10^{-6}$	P_{lost} hp
1	0.35	0.186	400	1	31.3	6.9
2	0.35	0.186	500	1	31.3	6.6
3	0.35	0.186	600	1	31.3	6.4

Table 11.6: Result 1 groove ($L_{shoe}W_{shoe} = 0.065m^2$)

to the reference design. This is done in table 11.4, where the frictional loss is reduced without lowering the minimum oil film thickness.

Taking another step initiates a bearing with only one oil groove and the result is shown in table 11.5 where the bearing area is further reduced without altering the minimum oil film thickness. Doing this reduces the frictional loss even further. Viewing this as a minimum the clearance is altered such that the clearance is increased which reduces the friction a little more - see table 11.6

If another lubrication technique is used the oil grooves can be removed which has been calculated and the result is shown in table 11.7, note that the bearing area is further reduced. Case 2 shown in figure 11.7 has a frictional reduction of 59 % and a bearing reduction of 56 % and this would reduce the fuel consumption with approximately 0.7 g/bhph (130 g/bhph). This situation is not very usable since lubricant is not added to the bearing. However, if the bearing could be externally lubricated that might solve the problem. This could be solved by rethinking the lube system to the guide shoe. Using the lubrication system from the main bearings to apply lubricant to the guide plane with oil from the top of the guide plane and thereby use gravity or maybe spray nozzles to lubricate the entire plane is a solution. Two patents have been filed about this. The first patent Vølund [Filed: 18 may 2002a] denotes the application of the new lubricating mechanism, and the other patent Vølund [Filed: 18 may 2002b] describes the possibility to continually adapt the bearing area to the applied

Case	L_{shoe} m	W_{shoe} m	C $m \cdot 10^{-6}$	N_{groove} -	h_{min} $m \cdot 10^{-6}$	P_{lost} hp
1	0.215	0.215	400	0	30.9	4.88
2	0.215	0.215	600	0	30.9	4.54

Table 11.7: Result 0 grooves ($L_{shoe}W_{shoe} = 0.046m^2$)

external load. The last parameter chosen in this study is the viscosity.

Case	L_{shoe} m	W_{shoe} m	C $m \cdot 10^{-6}$	η $Pa \cdot s$	h_{min} $m \cdot 10^{-6}$	P_{lost} hp
1	0.2	0.2	600	0.045	30.0	5.05
2(REF)	0.215	0.215	600	0.036	30.9	4.54
3	0.23	0.23	600	0.027	30.7	3.93
4	0.25	0.25	600	0.018	30.9	3.20

Table 11.8: Result 0 grooves varying viscosity

As shown in table 11.8 the power loss may be altered if the viscosity is altered - an effect of this is also to modify the bearing area in order to design after h_{min}. A larger area is required if h_{min} is to be kept constant. This adjustment is hard to implement in practice since the oil is used in a lot of different bearing types in the engine, therefore this cannot be altered without examining the effect of this in the rest of the engine. Furthermore, these calculations are performed using the simple analytical models and therefore the local effects are not included - non planar bearing surfaces. A potential is certainly present in optimizing the frictional loss for the given component. These results are obtained by the use of rigid components with co-planar components subjected to squeeze motion to be the load carrying parameter.

It must be examined for the flexible calculation to see whether that is still the case.

11.0.2 Friction Calculation - Flexible Components

The effect of flexible components is examined in the current section. The study conducted originates in the existing design. The solutions presented in the previous section are repeated with the flexible model super imposed. The finite element models are recycled for the analysis. This restriction means that not necessarily the best solution regarding frictional loss is obtained but for an experimental approach this is very usable. The problem of this approach is the the limited width of the guide plane due to the reference design. The optimum however is not too far away from the fixed width solution.

Note that the friction is slightly higher in the case for flexible components and finite width bearings. The results of the different simulations are presented in table 11.9. The simulations were performed using a lower number of oil grooves varying from 4 to 0.

Case	L_{shoe} m	W_{shoe} m	C $m \cdot 10^{-6}$	N_{groove} -	h_{min} $m \cdot 10^{-6}$	P_{lost} hp
FLEX1(REF)	0.70	0.15	400	4	9.3	12.1
FLEX2	0.70	0.15	400	2	13.3	10.1
FLEX3	0.70	0.15	400	1	14.2	9.4
FLEX4	0.70	0.15	400	0	15.5	8.8
FLEX5	0.55	0.15	400	0	9.3	7.8
FLEX6	0.55	0.15	600	0	9.2	7.3

Table 11.9: Result flexible calculation

11.1 Summary

The simulations carried out revealed that a frictional reduction of 59 % and a bearing reduction of 56 % could be obtained theoretically. This would reduce the fuel consumption with approximately 0.7 g/bhph (130 g/bhph). The design required to reach such a large reduction required a wider guide plane, which is not necessarily preferable since this might lengthen the entire engine - a rather expensive matter. Therefore a study concerning a new design fitting inside the existing engine was carried out. This guide shoe can operate with $4.8/12.1 \approx 40\%$ lower friction loss if the guide shoe is fitted for the T50MX test engine. This number could be lowered some if the width of the guide plane could be widened, but this is not possible in the current state. This design has no oil grooves and a 50% increased clearance. The width of the plane should be almost as wide as the length of the guide shoe in order to create the smallest friction loss for this bearing. This is not possible in the current study. Another way to optimize for friction could be obtained by lowering the normal load by increasing the length of the connecting rod, but this is not a parameter for optimization since this would affect other bearing loads and also generates a taller engine - a negative side effect. In all the simulations carried out the temperature has been kept constant. Experimental evaluations of future designs must be conducted to examine whether this is a reasonable assumption in the search for new improved guide shoe designs.

Chapter 12

Calculation of Piston Ring Characteristics

In the present chapter analytical and numerical models for calculating frictional loss in the piston ring package are presented. The frictional loss is directly correlated with the power loss and therefore an oil film model of the bearing is generated. The model described in this chapter start out simple and is gradually applied with more features in order to describe the problem and its solution better. The assumptions for fulfilling Reynolds equation are assumed to be valid in the entire scope of the analysis' presented. The reason for the gradual refinement of the models is to examine the terms which have significant influence on the bearing performance. The major loss in this context arises from the piston rings. Only small shearing is present for the piston skirt due to the small side forces acting here. The definition of the oil film thickness in the bearing can be seen in figure 12.1.

12.0.1 Forces Acting on Piston Ring

Focusing at a single piston ring the forces acting on it is shown in figure 12.2. The ring is subjected to the pressure p_{up} and p_{down} acting in the piston ring package from the combustion process. These pressures may be established either by measurements or by simulation see appendix A.2. The ring is also subjected to a pre-tension term F_{pre} which is the tension from the ring arising from the installation. There is the hydrodynamic load carrying capacity F_{oil} and from the load carried by the asperities F_{asp}. These two terms also have a shearing component due to the movement of the ring. The inertia terms $m\ddot{x}$ and $m\ddot{y}$ and the reaction force from the ring land F_{reac} and its shearing component $F_{fric,reac}$. $F_{press,i}$ denotes the force arising from the pressure acting behind and on top of the ring.
It is assumed that axi-symmetric conditions are present. The friction force in radial direction is assumed to be negligible in the present analysis. Furthermore, the axial force equilibrium is not considered except for the determination of the ring to investigate whether it is resting on one ring land or the other.
Integrating the oil film pressure generated by the motion of the piston ring gives the load

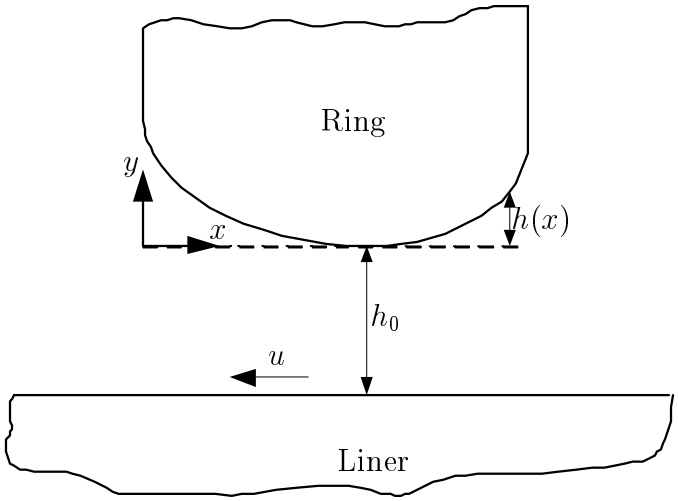

Figure 12.1: Ring profile

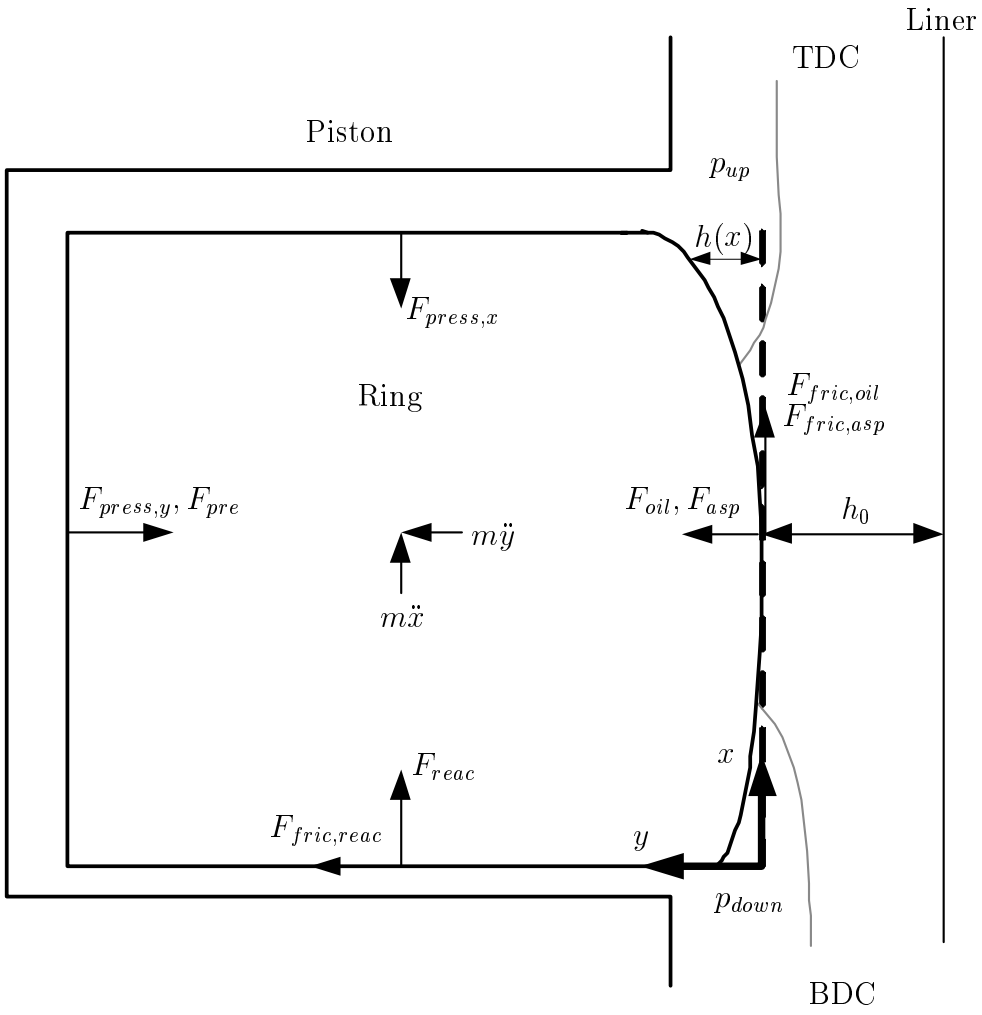

Figure 12.2: Forces acting on piston ring

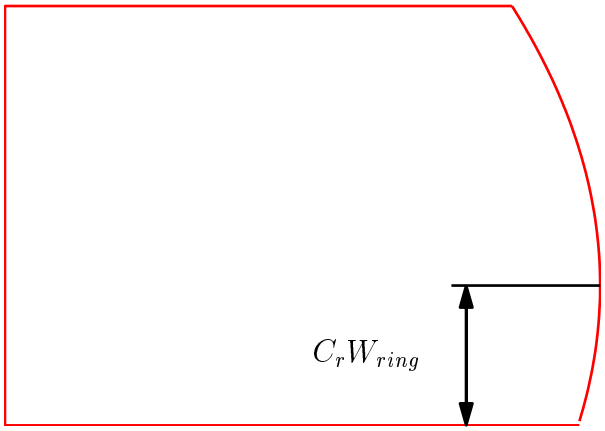

Figure 12.3: Ring profile offset

carrying capacity. Newton's 2'nd law is applied in order to check for a valid solution.

$$\begin{aligned} m\ddot{y} &= F_{asp} + F_{oil} + F_{fric,reac} - F_{press,y} - F_{pre} \\ m\ddot{x} &= F_{fric,asp} + F_{fric,oil} + F_{reac} - F_{press,x} \end{aligned} \tag{12.1}$$

The inertia of the piston ring is assumed to be negligible, which seems reasonable compared to the large load subjected to the ring from the gas pressure in the system.

12.1 Analytical Models

In the current section an analytical model for prediction of piston ring friction and other characteristics will be presented. Focusing on one piston ring the lubrication behavior of this ring can be characterized. Since the ring is subjected to a periodically shifting sliding direction the surface of the ring must be tapered in such a way that an oil film can build up both on the down stroke and the up stroke.

12.1.1 An Analytical Model using a Parabolic Piston Ring Profile

For some ring geometries an analytical description of the solution can be given. It is assumed that the running surface of the ring can be described by a parabolic formulation with an offset. This formulation is chosen out on the basis of numerous studies by for instance Hamrock et al. [August 1998], Sherrington et al. [1991], Yang and Keith [1996a] and Nakai et al. [1996] are some of many. For instance Saburi et al. [1995] uses a circular description combined with a plane centerpiece. In figure 12.3 the definition of the piston ring shape for the following analysis simulations is presented.
The film thickness profile is expressed as shown in equation 12.2.

$$h = h_0 + \frac{1}{r_p}\left(x - C_r W_{ring}\right)^2 \tag{12.2}$$

Since the axi-symmetric approach is used a simplified version of Reynolds equation can be used.

$$\frac{\partial}{\partial x}\left(\frac{h^3}{12\eta}\frac{\partial p}{\partial x}\right) = \frac{u}{2}\frac{\partial h}{\partial x} + \frac{\partial h}{\partial t} \tag{12.3}$$

Integrating once produces equation 12.4

$$\frac{h^3}{12\eta}\frac{\partial p}{\partial x} = \frac{u}{2}h + \frac{\partial h}{\partial t}x + A \tag{12.4}$$

Inserting expression 12.2 into 12.4 gives the expression presented in equation 12.5, where A is a constant of integration.

$$\begin{aligned}\frac{\partial p}{\partial x} =& 12\eta\,(\,\frac{u}{2}\frac{1}{\left[h_0 + \frac{1}{r_p}\left(x - C_r W_{ring}\right)^2\right]^2} + \frac{\partial h}{\partial t}\frac{x}{\left[h_0 + \frac{1}{r_p}\left(x - C_r W_{ring}\right)^2\right]^3} \\ &+ \frac{A}{\left[h_0 + \frac{1}{r_p}\left(x - C_r W_{ring}\right)^2\right]^3}\,)\end{aligned} \tag{12.5}$$

Integrating this expression introduces a new constant of integration B.

$$\begin{aligned}p(x) =& 12\eta[\int_0^x \frac{u}{2}\frac{1}{\left[h_0 + \frac{1}{r_p}\left(\xi - C_r W_{ring}\right)^2\right]^2}d\xi + \int_0^x \frac{\partial h}{\partial t}\frac{x}{\left[h_0 + \frac{1}{r_p}\left(\xi - C_r W_{ring}\right)^2\right]^3}d\xi \\ &+ \int_0^x \frac{A}{\left[h_0 + \frac{1}{r_p}\left(\xi - C_r W_{ring}\right)^2\right]^3}d\xi] + B\end{aligned} \tag{12.6}$$

The integration constants A and B are determined using the boundary conditions.
In order to represent this in a simpler way the different terms are renamed:

$$p(x) = 12\eta\left(I_1(x)\frac{u}{2} + I_2(x)\frac{\partial h}{\partial t} + I_3(X)A\right) + B \tag{12.7}$$

Where :

$$I_1(x) = \int_0^x \frac{1}{\left[h_0 + \frac{1}{r_p}\left(\xi - C_r W_{ring}\right)^2\right]^2}d\xi$$

$$I_2(x) = \int_0^x \frac{\xi}{\left[h_0 + \frac{1}{r_p}\left(\xi - C_r W_{ring}\right)^2\right]^3}d\xi$$

$$I_3(x) = \int_0^x \frac{1}{\left[h_0 + \frac{1}{r_p}\left(\xi - C_r W_{ring}\right)^2\right]^3}d\xi$$

12.1.2 Boundary Conditions

The boundary conditions for the analytical model is chosen to be the pressure at the inlet zone P_{in} and the pressure at the outlet P_{out}. However, cavitation at $x = x^*$ may occur. The Swift-Stieber boundary condition shown in chapter 5 is used for cavitation search.

12.1.3 No Cavitation

Using the first boundary condition at $x = 0$:

$$p(0,t) = p_{in} = 12\eta \left(I_1(0)\frac{u}{2} + I_2(0)\frac{\partial h}{\partial t} + I_3(0)A \right) + B \tag{12.8}$$

The term B may be calculated as $B = p_{in}$. Using the second boundary condition at $x = W_{ring}$:

$$p(W_{ring},t) = p_{out} = 12\eta \left(I_1(W_{ring})\frac{u}{2} + I_2(W_{ring})\frac{\partial h}{\partial t} + I_3(W_{ring})A \right) + B \tag{12.9}$$

$A = \frac{\frac{p_{out}-p_{in}}{12\eta} - I_1(W_{ring})\frac{u}{2} + I_2(W_{ring})\frac{\partial h}{\partial t}}{I_3(W_{ring})}$.
This shows that it is straight forward to determine A and B when cavitation is not present

12.1.4 Cavitation

Introducing the possibility that cavitation may occur at $x = x^*$ and $p = p_{in}$ at $x = x_{in}$ introduces new equations. In equation 12.10 two equations with two unknowns are presented, the system is nonlinear and an iterative solution procedure is used in obtaining the solution. Using the first boundary condition at $x = 0$ is shown in equation 12.8.
Using the second boundary condition at $x = x^*$:

$$\begin{aligned} p(x^*,t) = p_{cav} &= 12\eta \left(I_1(x^*)\frac{u}{2} + I_2(x^*)\frac{\partial h}{\partial t} + I_3(x^*)A \right) + P_{in} \\ \frac{\partial p(x^*,t)}{\partial x} = 0 &= 12\eta \Bigg(\frac{u}{2} \frac{1}{\left[h_0 + \frac{1}{r_p}\left(x^* - C_r W_{ring}\right)^2 \right]^2} \\ &\quad + \frac{\partial h}{\partial t} \frac{x^*}{\left[h_0 + \frac{1}{r_p}\left(x^* - C_r W_{ring}\right)^2 \right]^3} + \frac{A}{\left[h_0 + \frac{1}{r_p}\left(x^* - C_r W_{ring}\right)^2 \right]^3} \Bigg) \end{aligned} \tag{12.10}$$

This gives a system of nonlinear equations. It is assumed that local cavitation is present and that the oil film can rebuild before the outlet region. In the following flow continuity is assumed over the cavitation area. This means that flow continuity is used for determination of $x = x^{**}$

$$\frac{\partial p(x,t)}{\partial x} = 12\eta \frac{u}{2} \left[\frac{h^{**} - h^*}{{h^{**}}^3} \right] \ at\ x^{**} \tag{12.11}$$

Where x^{**} is the reformation point and x^{*} is the starting point of cavitation.
However, in regions where the pressure is elevated the cavitation pressure p_{cav} cannot drop below this elevated pressure. This means that the cavitation pressure will equalize the pressure at the outlet of the bearing, $p_{cav} = p_{outlet}$. The open-end cavitation is used here - see chapter 5. This means that only equation 12.10 is used.
The load carrying capacity is determined by the integration of the pressure distribution. The integration is carried out in equation 12.12.

$$F_{oil} = \pi D_{piston} \int_0^{x_{up}} 12\eta \left[I_1(x)\frac{u}{2} + I_2(x)\frac{\partial h}{\partial t} + I_3(x)A + B \right] dx \tag{12.12}$$

The upper integration limit x_{up} is replaced with W_{ring} if cavitation is not present, otherwise the term is set to x^{*} if cavitation is present.
The other load carrying quantity in this manner is the asperity term F_{asp}. This term is calculated using equation 4.23 at the current problem.
Since the nature of the problem is of the same character as the guide shoe problem concerning the determination of the dynamic behavior the same approach is used here. The degrees of freedom is reduced to one which simplifies the system. Therefore the load carrying capacity is differentiated with respect to $\frac{\partial h}{\partial t}$ in order to get the damping coefficient.

$$B_{oil} = \frac{\partial F_{oil}}{\partial \frac{\partial h}{\partial t}} = \pi D_{piston} 12\eta \int_0^{W_{ring}} \left[I_2(x) + \frac{I_3(x)}{I_3(W_{ring})} I_2(W_{ring}) \right] dx \tag{12.13}$$

Hereby can the system be solved by the methods described as in chapter 6 shown in equation 12.14.

$$B_{oil}\Delta_{\frac{\partial h}{\partial t}} = F_{asp} + F_{oil} - F_{press,y} - F_{pre} \tag{12.14}$$

12.2 Simulation Results

Having mentioned the possible lubrication modes for the purely analytical model simulations have been carried out in order to reveal the difference between the models.

12.2.1 Input Values

The input values for the analytical simulations are presented in table 12.2.1.

Speed	n_{rev}	123 rpm
Height of ring	W_{ring}	12.5 mm
Ring tension	p_{pre}	1.0 bar
Ring Profile	C_r	0.4
Liner Roughness	σ_1	$1.2\mu m$
Ring Roughness	σ_2	$1.0\mu m$
Asperity Fri. chef.	α	0.1
Pressure	$p_{combustion}$	0-160 bar
Viscosity	η	varying

The viscosity is determined from a simulation of the temperature distribution in the research engine. The temperatures of the ring and liner are combined and the viscosity is determined by equation 8.1.

12.2.2 Result Hydrodynamic Lubrication with No Cavitation Criteria

This simulation generated very small oil film thickness. The large negative pressures generated in the cavitation zone by the lack of a cavitation criteria created highly unrealistic running conditions. Film thickness' smaller than $\frac{1}{100}\mu m$ were generated due to the destructive nature of the large negative pressures.

12.2.3 Result Hydrodynamic Lubrication with Cavitation Criteria (Open-end Cavitation)

The simulation where cavitation is included excludes the problems encountered in simulations having no cavitation criteria. The simulation result can be observed in figure 12.4.
As expected the OFT is smallest on the down stroke. The minimum OFT is about $0.1\mu m$ near TDC and the maximum about $25\mu m$. The jump in OFT in the end of the stroke is due to the pressure elimination because the rings are passing the scavenging ports. The corresponding pressure history can be observed in figure 12.5. The frictional loss is depicted in figure 12.6.
This can be converted to lost power for all rings - presented in figure 12.7.

12.2.4 Result Mixed lubrication with Cavitation (Open-end Cavitation)

A simulation was carried out with the mixed lubrication model applied. The simulation result can be observed in figure 12.8.
As for the hydrodynamic model the OFT is smallest on the down stroke. The minimum OFT is about $1\mu m$ near TDC and the maximum about $25\mu m$. The corresponding pressure history

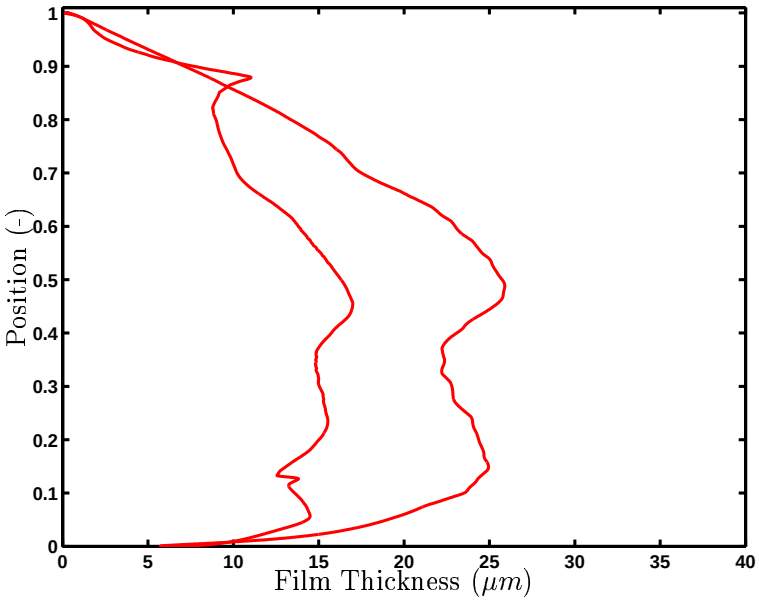

Figure 12.4: Minimum oil film thickness ring 1

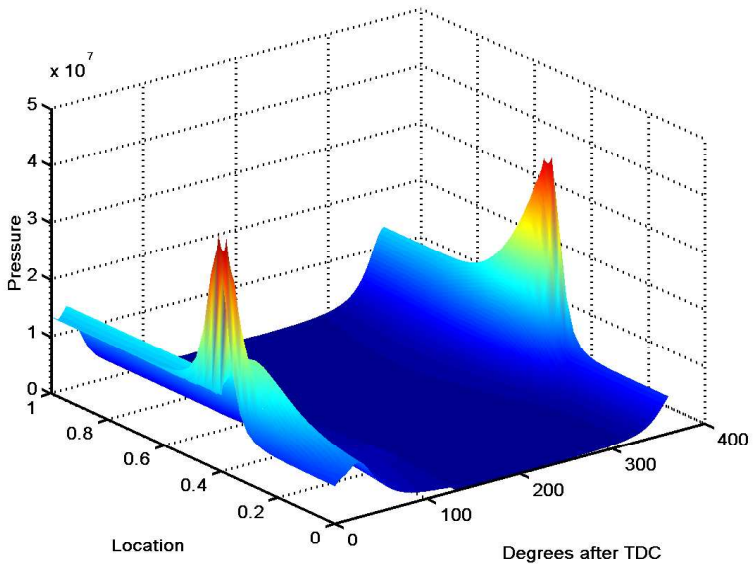

Figure 12.5: Pressure history ring 1

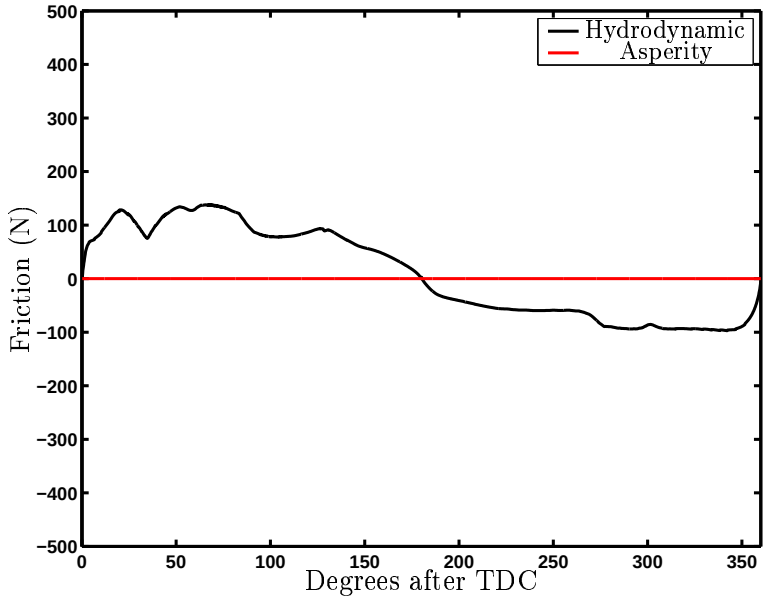

Figure 12.6: Friction ring 1

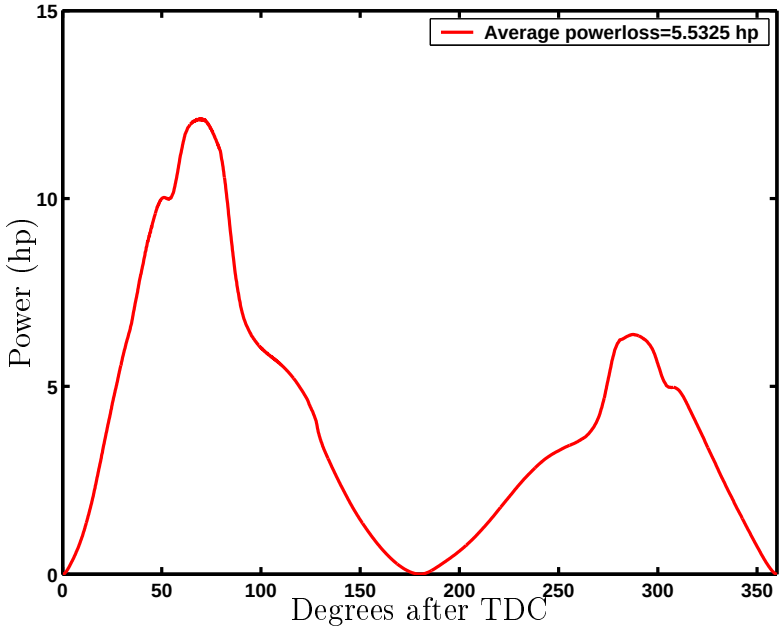

Figure 12.7: Power loss for all rings

can be observed in figure 12.9. The frictional loss is depicted in figure 12.10.
This can be converted to lost power for all rings - presented in figure 12.11.

12.2.5 Discussion

Reviewing all three simulations reveal the importance of including cavitation and asperity interaction in the lubrication model. Furthermore, a significance of the scavenging ports may be important as well as the thermal effects and starvation. The simulated power losses are very small compared to the expected values which consolidates the theory of starved lubrication in the piston ring pack. The mentioned terms call for a numerical description.

12.3 Numerical Models

In this section the basis for calculating oil film thickness using a numerical approach is presented. A general description is presented along with the properties of the calculation tool generated.
The numerical model originates in the analytical results which revealed that asperity interaction and roughness terms are significant. New terms may also be very significant namely the possibility for starvation of the piston ring package.
The model is generated from:

1. 2D-model (Cyclic symmetry)
2. Surface roughness and surface profile
3. Asperity model (Greenwood and Tripp)
4. Cavitation model
5. Starvation model
6. Thermal effects
7. Elastic ring land

12.3.1 2D model

The numerical modelling is carried out using the finite difference technique in the same manner as described in chapter 7. A section of 12 degrees in circumferential direction is modeled. This section size is chosen by the number of scavenging ports, which is 30. This gives the possibility to determine the impact on the characteristics from the scavenging ports.

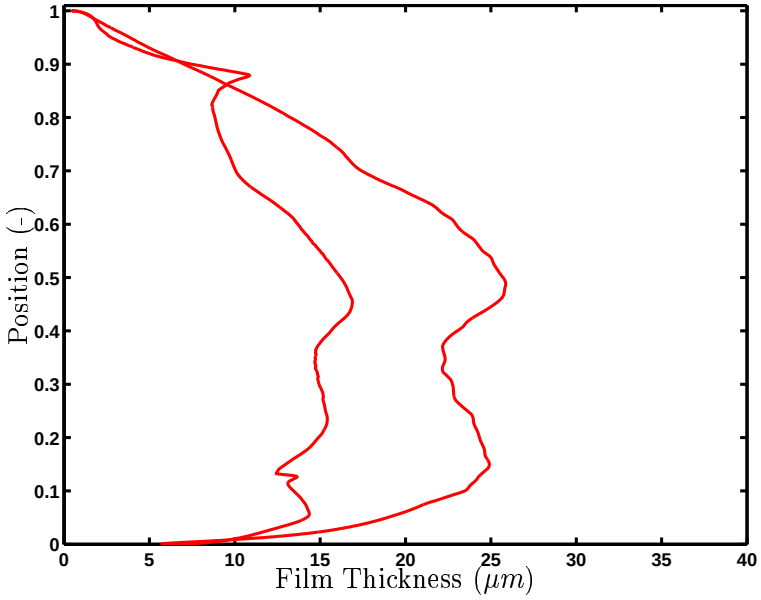

Figure 12.8: Minimum oil film thickness ring 1

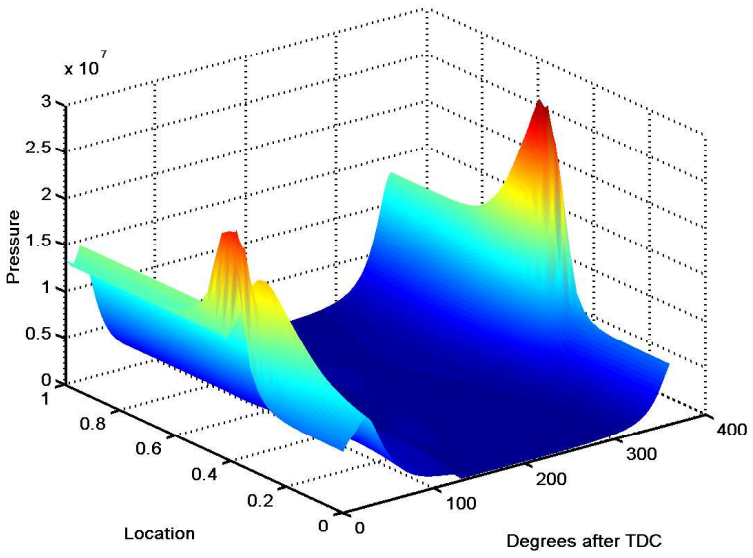

Figure 12.9: Pressure history ring 1

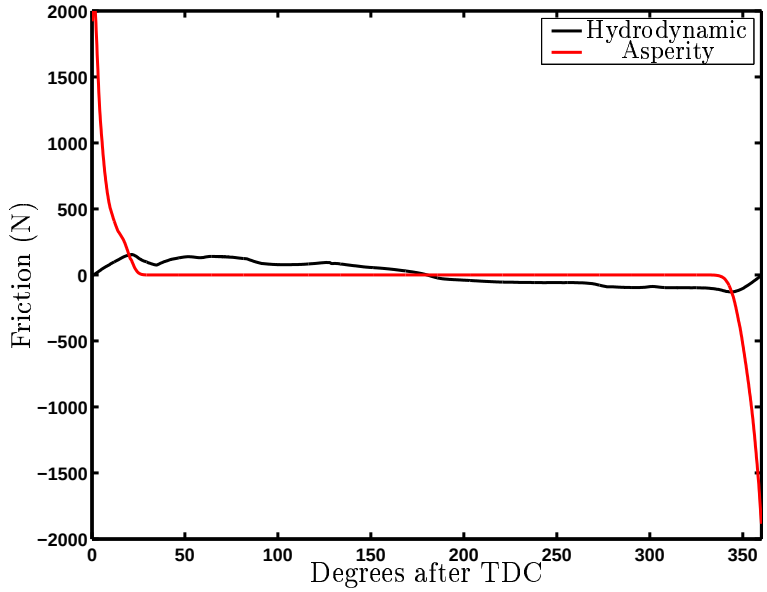

Figure 12.10: Friction ring 1

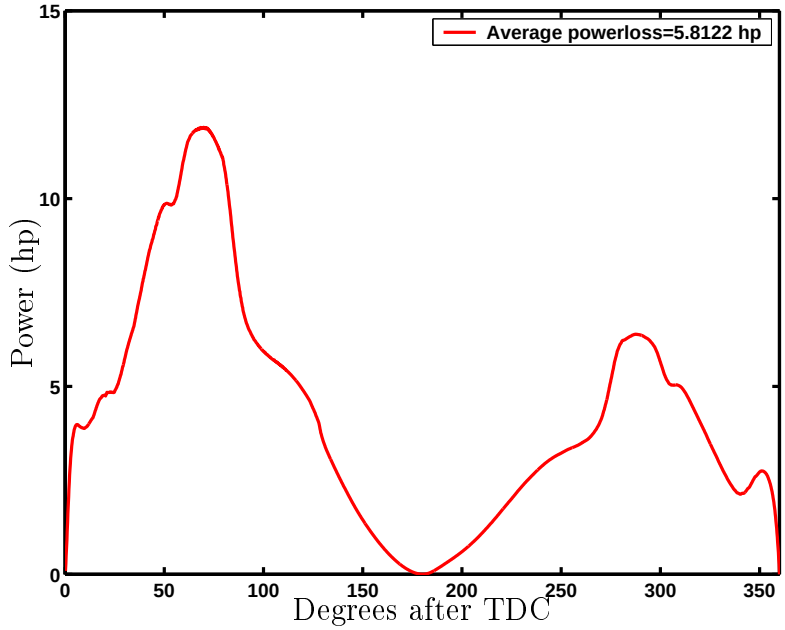

Figure 12.11: Power loss for all rings

12.3.2 Asperity Description

Since the oil film thickness is small solid to solid contact will be present during one cycle. Therefore the surface roughness must be included in the lubrication model as shown in chapter 4. In order to compensate for the surface roughness the asperity contact model is used.

Piston Ring

This ring has a continuously changing geometry because of wear. However, the ring has approximately the same shape after running in. The only thing that changes is that the ring tension grows smaller as the rings grows thinner in radial direction. In the following it is assumed that the roughness of the ring at time t where $t > t_{runintime}$ stays the same in the larger part of the lifetime of the ring. It is assumed that the surface roughness pattern also stays the same.

Cylinder Liner

The liner is also subjected to wear, however not so significantly as the ring (the lifetime is substantially larger). The surface roughness of the liner is assumed to follow the same pattern as the piston ring where the surface roughness stays the same after running in. Wave cut is not implemented in the current model.

12.3.3 Average Reynolds Equation

Since the roughness at part of the stroke is quite large compared to the oil film thickness the model proposed by Patir and Cheng [1978] is implemented. The model using the average Reynolds equation 4.10 seems reasonable, as shown in chapter 4.

12.3.4 Friction

The total frictional force acting on the piston ring can be calculated by equation 4.27

12.3.5 Equilibrium

The method proposed in chapter 6 is used. The force balance shown in equation 12.1 - the equation with $m\ddot{y}$. The perturbation coefficient is determined by solving the system with the perturbed terms shown in equation 12.15 in order to determine the new estimate for $\frac{\partial h}{\partial t}$.

$$\frac{\partial}{\partial x}\left(\frac{h^3}{12\eta}\frac{\partial p_{\Delta\frac{\partial h}{\partial t}}}{\partial x}\right)+\frac{\partial}{\partial z}\left(\frac{h^3}{12\eta}\frac{\partial p_{\Delta\frac{\partial h}{\partial t}}}{\partial z}\right)=1 \tag{12.15}$$

The equilibrium criteria is shown in equation 12.16

$$Err_{crit} < Err = \left|\frac{F_{oil}+F_{asp}-F_{ext}}{F_{ext}}\right| \tag{12.16}$$

The same procedure was shown for the guide shoe problem in chapter 7.

12.3.6 Starvation

Starvation of the piston rings have been implemented by a combination of the methods described by Sanda et al. [1997], and Nakai et al. [1996].

The approach uses the film thickness at an infinite distance h_∞ to determine the location of the inlet h_{in} - see figure 12.12. Flow continuity into the inlet zone is assumed i.e. the pressure gradient is zero. In the derivation the ring is steady and the liner is sliding past the ring. The sliding speed is u. It is assumed that the fluid is attached to the cylinder liner and is moving rigid with the same velocity as the liner.

At the inlet a flow continuity condition is applied, it is assumed that there is no flow out of the ring package at this point. This means that the flow profile is assumed to be in the simplest form - linear and that determines the inlet film thickness to be $h_{in} = 2h_\infty$. The outlet film thickness is described to be the oil film thickness at the point of cavitation. If no cavitation is present the point where $\frac{\partial p}{\partial x} = 0$ is used. The back drafts of this is that flow continuity in the piston ring interface is not necessarily fulfilled.

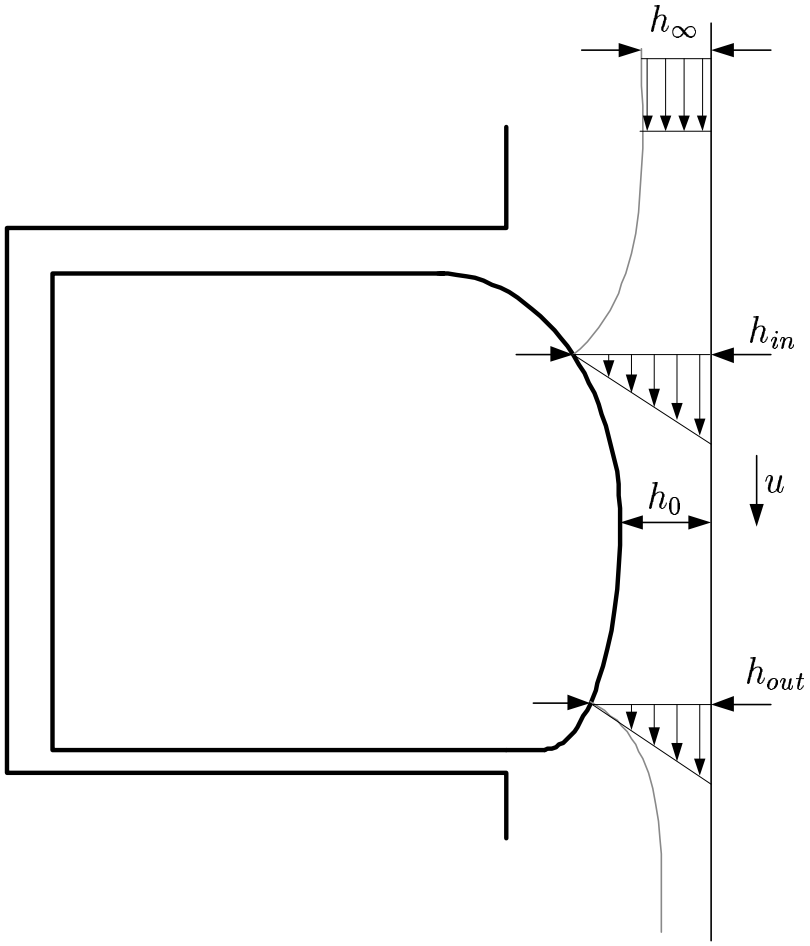

Figure 12.12: Oil formation on piston ring face

Since lubricant in only supplied at every 1st,2nd every 4th or maybe every 10th stroke at a discrete position the rings have to adopt to this situation. The top ring (ring 1) must ride on the oil left by ring 2 on the down stroke. Ring 2 must ride on what was left by ring 3 and so on - and vice versa for the up stroke. The lowest ring is denoted ring 4 and this ring is fully flooded on the down stroke. On the up stroke ring 1 must ride in the oil left by the same ring on the down stroke.
In the numerical model presented this effect is included using the starvation model mentioned and by the use of a technique described by Dowson et al. [1979]. The approach is simple - run the simulation for several cycles and the boundary conditions for every cycle will adjust itself to reach a stable position. Usually this is achieved after 3-4 cycles. The assumption used here is that the lowest ring (Ring 4) is always fully flooded on the down stroke.

12.3.7 Cavitation Model

The topology of the piston ring and liner makes it possible for cavitation to occur.
Different cavitation models have been examined by Priest et al. [1998]. Since the inlet and outlet are not necessarily fully flooded a traditional cavitation model as the approach where cavitation and reformation of the film may appear is not possible within the lubricated area. The model chosen for this study is the open-end cavitation. The implementation of this procedure may be seen in figure 5.6.

12.3.8 Stiffness of Ring Land

The ring land is flexible and deflects dynamically with the load. This can be seen on the wear profiles of the ring. A simple model has been implemented in order to incorporate the effect.
The ring land is modeled by finite elements exploiting cyclic symmetry as shown in figure 12.13, where a partial section of the piston crown for the research engine is modeled using solid tetrahedral elements. The effect of ring land deformation has only minor effect on h_{min}.

12.4 Verification of Oil Film Model

The numerical model was calculated using the conditions for the analytical models described earlier. Similar results were found.

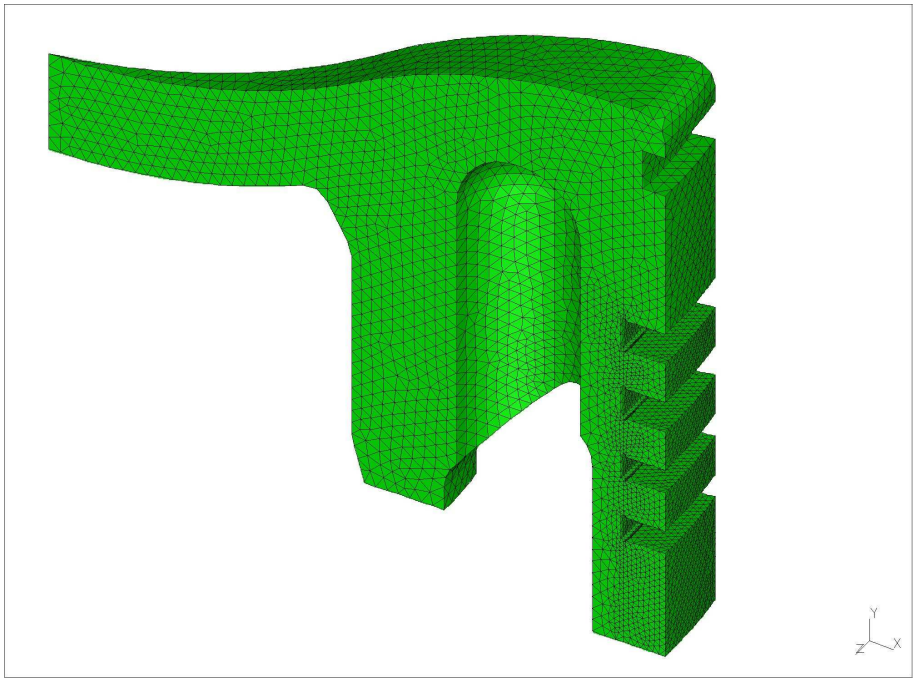

Figure 12.13: FE-model of piston

Chapter 13

Calculation Results Piston

Results for the full load condition is shown in the current section. The engine simulated is the test engine running at full propeller load. Simulated results for measured running conditions will be presented in chapter 15. These measured conditions were quite different from this kind of loading, but in order to gain knowledge about the potential for optimization the size and distribution of oil film thickness and frictional loss is presented at full load in the current chapter.

13.1 Oil Film Thickness History

The result of the calculation can be seen below. All four rings oil film thickness profiles are presented in the figure 13.1.

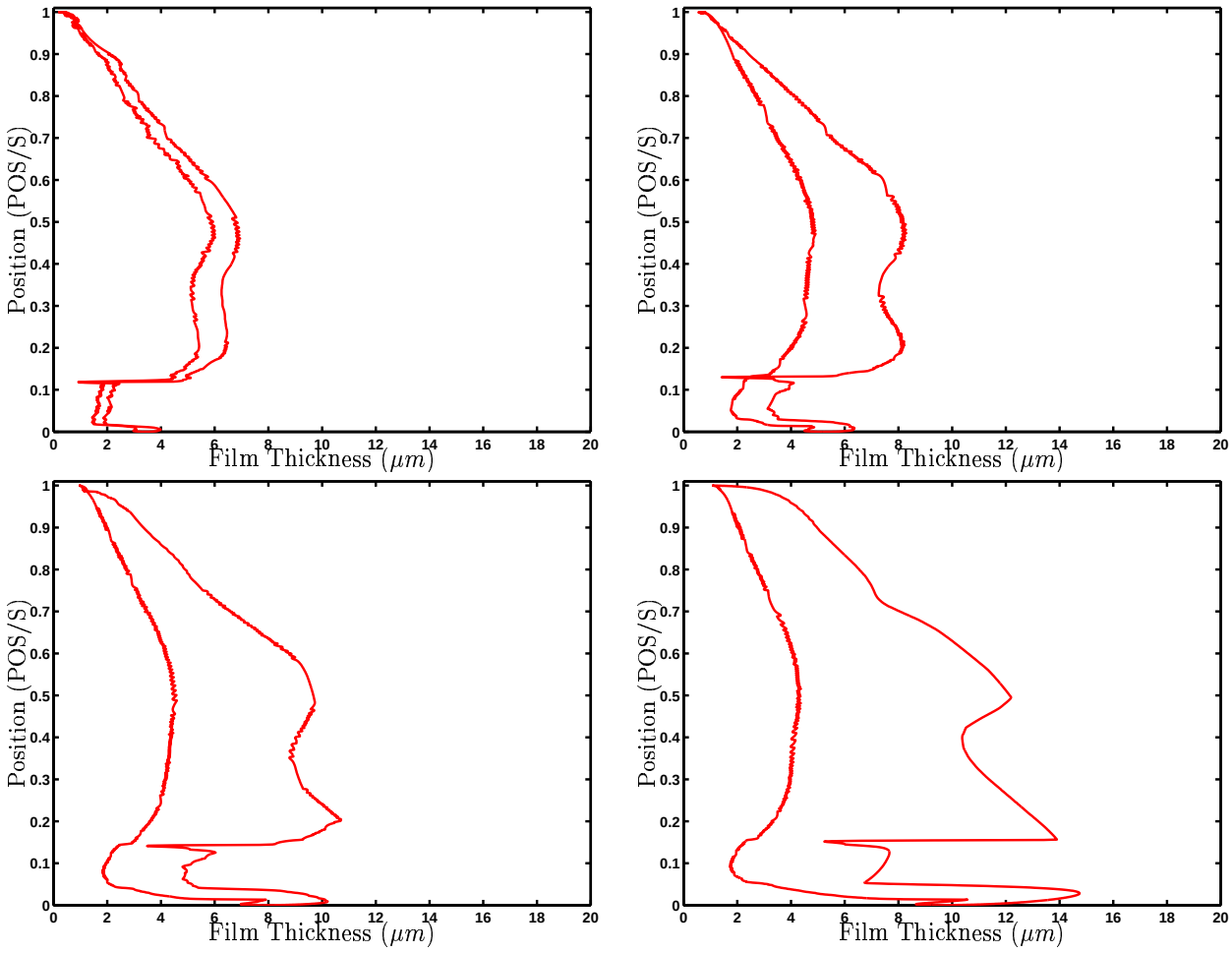

Figure 13.1: Minimum oil film thickness. Upper Left: Ring 1. Upper Right: Ring 2. Lower Left: Ring 3. Lower Right: Ring 4.

The oil film thickness is smallest on the up stroke for all rings. The minimum oil film thickness is about $0.2\mu m$ and the maximum about $15\mu m$. The sudden jump in oil film thickness in the end of the stroke is because of the pressure elimination due to the rings are passing the scavenging ports. The reason why the oil film thickness is smallest on the up stroke is to be found in the starvation boundary condition. The condition stating that ring 4 is fully flooded on the down stroke generates larger oil film thickness' on the down stroke than the up stroke.

13.2 Pressure History

The pressure distribution for all four rings are presented in figure 13.2 for a discrete circumferential position. The position is chosen such that the section passes a scavenging port rib. The pressure peaks around 180 degrees originates in the fact that the piston ring is running on the port ribs which reduces the effective bearing area.

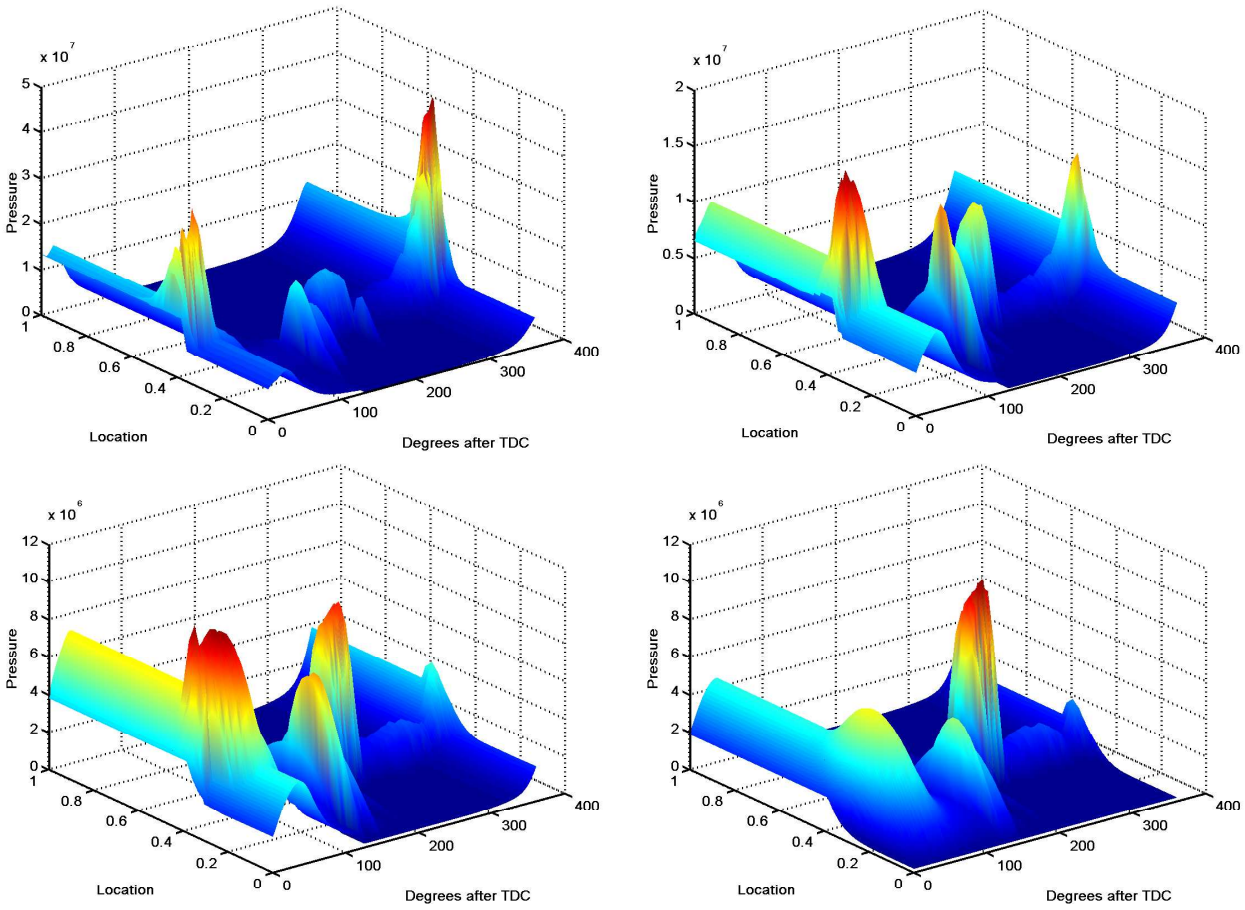

Figure 13.2: Pressure history. Upper Left: Ring 1. Upper Right: Ring 2. Lower Left: Ring 3. Lower Right: Ring 4.

13.3 Cavitation / Starvation of Piston Rings

The lubricated area of the piston ring pack can be seen in figure 13.3. Great variation is seen between the rings and the position in the stroke. The figures reveal that the rings are running under starved conditions. The lubricated area of the ring is in fact only a fraction of the ring width. It is seen that ring 4 is fully flooded on the down stroke - a boundary condition.

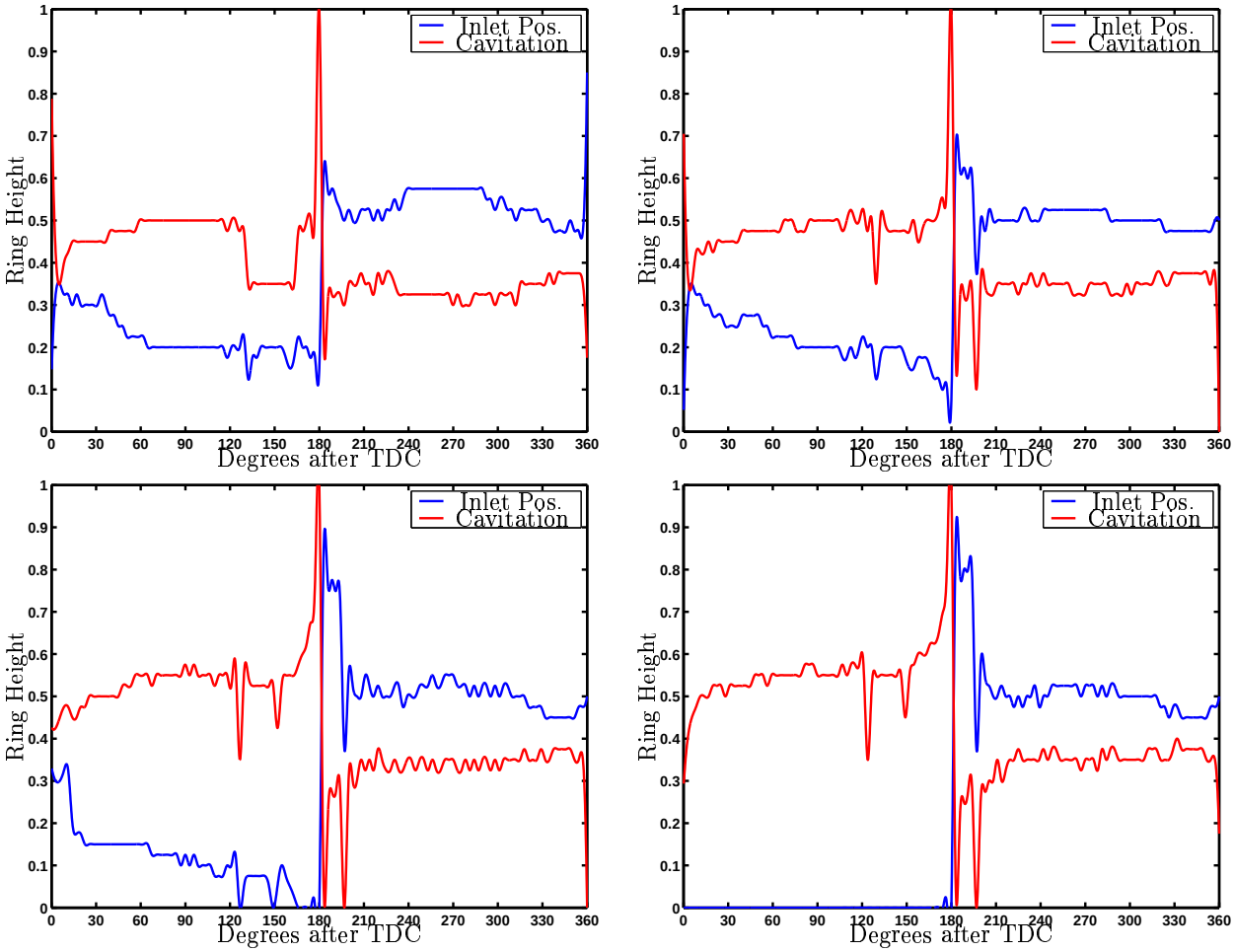

Figure 13.3: Location of cavitation/inlet position. Upper Left: Ring 1. Upper Right: Ring 2. Lower Left: Ring 3. Lower Right: Ring 4.

13.4 Friction History

For each ring the friction contribution from hydrodynamic and asperity friction has been calculated. This can be seen in figure 13.4.

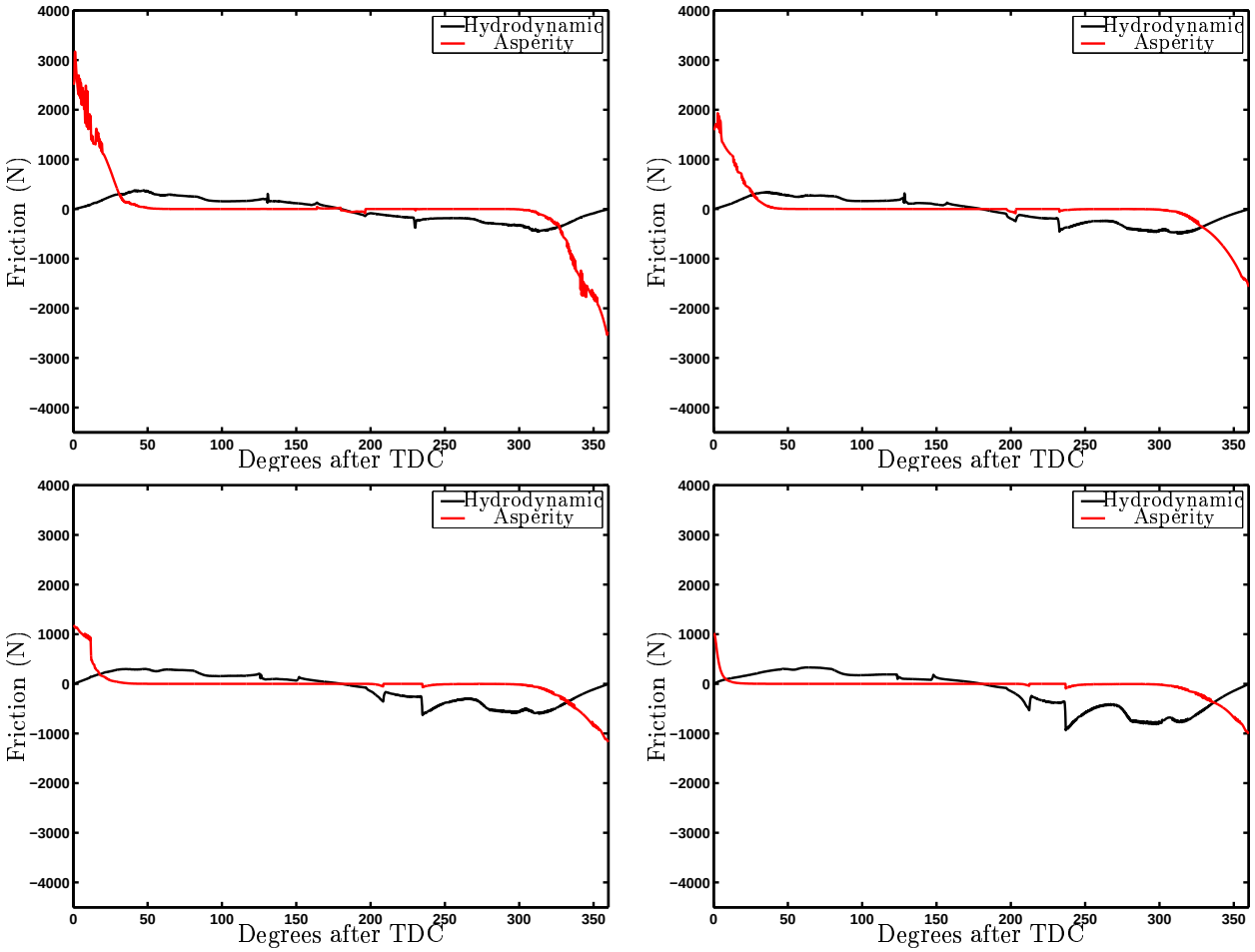

Figure 13.4: Upper Left: Friction for ring 1. Upper Right: Friction for ring 2. Lower Left: Friction for ring 3. Lower Right: Friction for ring 4.

Collecting all the contributions gives the total friction from the piston and this is presented in figure 13.5. This can be converted to lost power - presented in figure 13.6. Reviewing these simulation results clearly reveals the importance of starvation considerations in the ring package. The power loss determined using the fully flooded condition compared to the starved condition reveals that there is a factor of approximately 4 in difference between the two simulations - figures 12.11 and 13.6. As presented in the figure the total power loss is calculated to be $19.5hp$ which corresponds to $\approx 80hp$ for a complete 4 cylinder engine. That

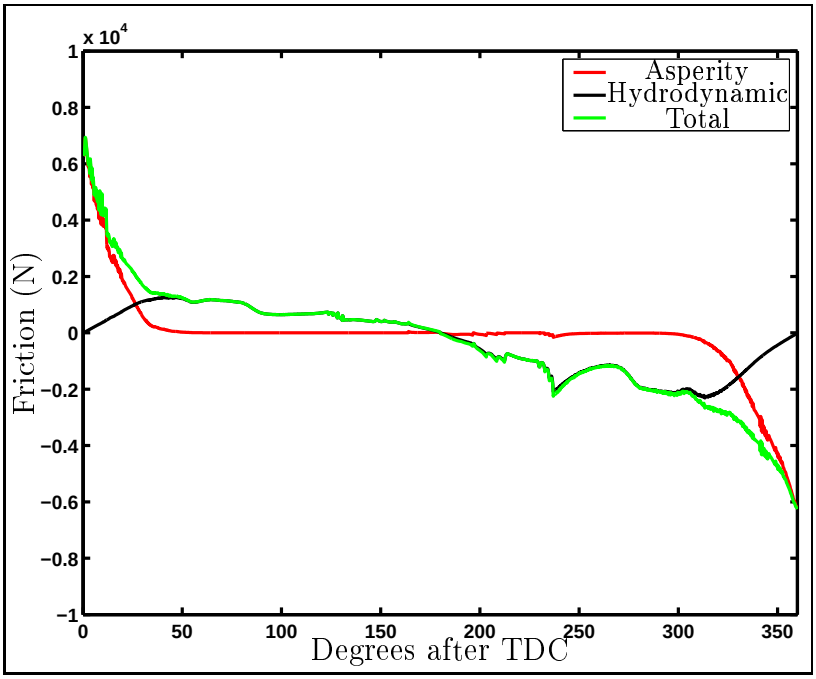

Figure 13.5: Total friction for all rings

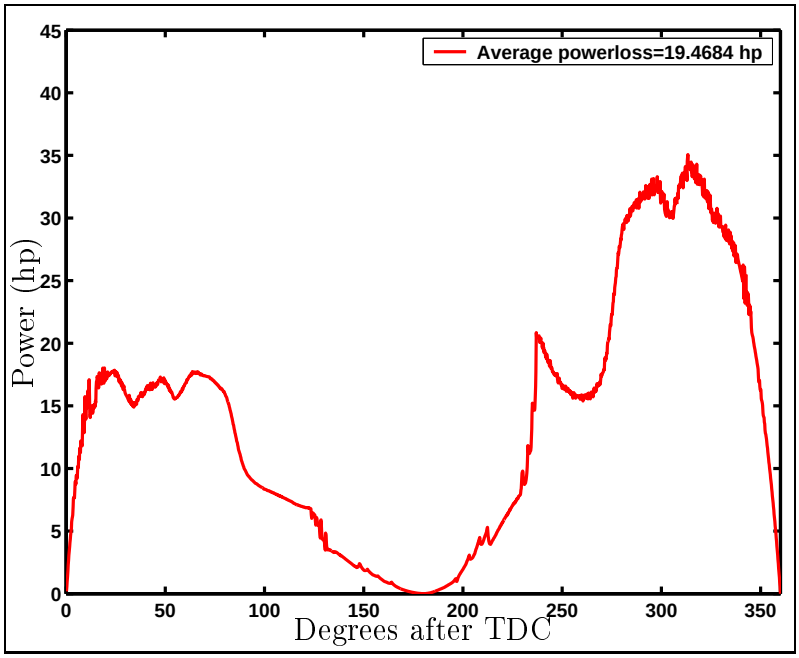

Figure 13.6: Power loss for all rings

is 0.9% of the total generated power.

13.5 Summary

A numerical model for predicting the oil film thickness, pressure distribution and frictional loss in the piston ring package was established. The calculations carried out revealed the overall loss in the piston rings was 0.9% of the generated power. As expected this is a rather large quantity - which verified the optimization potential regarding frictional loss. The choice of lubrication model is however also very influencing on the result if the results from the fully flooded conditions in figure 12.10 are compared to the starved lubrication model in figure 13.4, ring 1. It appears that the starved lubrication model needs more refinement such that flow continuity is satisfied. The condition that ring 4 is fully flooded on the down stroke controls the lubrication condition of all rings, and is therefore an aim for future work.

Chapter 14

Piston Ring Measurements

14.1 Introduction

The objective of the study was to build a model for determining the friction in the piston ring assembly. In order to gain knowledge about the important parameters who control / affect friction an experimental study was conducted and is presented in the current chapter.

14.2 The Experimental Apparatus

The objective of the measurements was to verify and generate input for the numerical models. The frictional behavior of the piston assembly is controlled by the interference between piston rings and cylinder liner. Since the contact is lubricated the frictional behavior will be controlled by the lubrication condition. Therefore measurements will be focused on measuring the input/output parameters which characterize the lubrication condition in the theoretical model. Relevant measurable parameters are listed below.

- Viscosity of the oil
- Piston inter ring pressure
- Oil film thickness
- Friction
- Roughness
- Ring profile

14.3 Input Parameters

As shown above some of these measurement points are input parameters and some are output parameters for the numerical model.

Viscosity of the oil

The viscosity of the oil is a very important parameter since this is to some extent proportional to the load carrying capacity of the bearing at a given oil film thickness.
Since the viscosity is very temperature dependent and only in limited degree pressure dependent in the interesting pressure range a measurement of the temperature of the oil trapped in the bearing gives a good description of the viscosity. It is assumed that the temperature of the oil trapped in the bearing can be expressed as the mean temperature of the two surfaces and the viscosity may be determined by equation 8.1. The placement of the sensors can be seen in figure 14.1.

Pressure Drop in Ring Package

The pressure in the surroundings of the piston ring generates the load acting on piston ring. The load acting on the individual piston rings is established by measuring the inter ring pressure. The transducers are mounted in the piston between the rings.

Roughness

The roughness of the components determines how much asperity contact that may occur in the contact. The roughness may be establishes using a roughness measurements.

Ring Profile

The profiles of the rings control the formation of the oil on rings. These profiles can be determined by profile measurements.

14.4 Output Parameters

Some of these measurement points are output parameters and these measuring points are supposed to verify/correct the numerical models.

14.4.1 Oil Film Thickness

The oil film thickness is a very characteristic output parameter from the theoretical models along with the pressure in the piston rings. The oil film thickness is measured by capacitive sensors mounted in the liner. The placement of these sensors can be seen in figure 14.1. The sensors were placed at the fore end of the engine in order not to have any disturbance from side forces that may be generated by the guide shoe mechanism.

14.4.2 Friction

Lastly the friction generated by the shearing and squeezing of the oil and asperity interaction was measured.

Measuring friction in the piston ring package is a delicate matter. Since the friction is approximately in the order of $1-3\%$ of the applied load and acting in the same plane as the combustion pressure on the piston - this requires accurate measurements. One way to measure friction is to measure the combustion pressure very accurately and measure the force absorbed in the piston rod below the piston ring pack. This has been done for instance by Mehmet and Patterson [1984] with limited success. This measurement method was tested on the research engine. The piston rod was equipped with strain gauges and pressure transducers were installed in the combustion chamber. The measurement results showed that it was not possible to determine the frictional loss in this way by the experimental apparatus . It was not possible to determine what was friction and what was not in the individual tests. Therefore another method was required. A study revealed that two measurement principles could be applied to the system. Due to practical problems with one of the methods the floating liner principle was adopted and applied to the current problem. A sketch of the system is presented in figure 14.2.

The left part of the figure is divided into two parts. On the left side of the center line the original layout of the piston assembly is presented and on the right the modified design. The system on the right differs in such a way that the liner is 'floating'. The liner is not subjected to pre-tension from the cylinder studs. The liner is positioned on top of 4 force transducers - shown on the enlarged picture on the lower right. In order to keep down the cylinder cover a new cooling jacket for the top part of the cylinder liner was designed such that the cylinder cover will be held down via this arrangement. This makes is possible to measure frictional loss in the engine under firing conditions. The enlarged picture on the upper right shows the sealing arrangement whose purpose is to keep the large gas pressures away from the cylinder liner.

The possibility for a failure in an experiment running on a full size engine with components weighing several tons required a preliminary experiment. The preliminary experiment included the measurement of friction lost in the piston ring package under controlled circumstances. This experiment was conducted with the cylinder cover not installed. This eliminated the large loading on the piston from the combustion gas. This was a safety precaution which was preferred before testing the friction setup in a firing cylinder. Running the cylinder by pure motoring did not generate any significant loading on the liner and therefore an arrangement where the piston rings could be loaded without introducing large forces from a combustion was constructed. A tripod stand was created to be positioned on top of the piston - see figure 14.3.

The tripod was connected to the frame box using a linkage arrangement. This linkage arrangement carried a pneumatic hose filled with air. The hose was attached to the piston and

via channels drilled in the piston the air was led out in the middle of the piston ring package between ring 2 and 3. The air supplied originated from a compressor arrangement that normally is used to startup the engine. The system contained pressurized air at approximately 30 bar. The air was controlled by an electronic valve coupled to an angular encoder of the engine. The advantage of this tripod arrangement was the ability to load the piston rings all though no load in the axial direction was generated. This eliminated any normal loading of the force transducers other than friction and vibrations originating from other parts of the engine. Another advantage of attaching the tripod was the simple transportation of the measurement signals from the sensors mounted in the piston to the data logger equipment. Due to manufacturing problems and heavily booked test schedule of the research engine the main experiment have been delayed so much, that the experiment have not been conducted at the delivery of this report. However, the initial experiment which were to examine the possibility for measuring frictional loss under controlled circumstances were conducted by the use of the experimental apparatus just described.

14.5 View of Experimental Apparatus

The parts shown above were manufactured and are presented in the current section.
The majority of these parts are similar to the ones that are to be used for the final experiment to be conducted at a later stage. The liner is similar to the one that were manufactured for the frictional experiment with firing in the cylinder. The liner can be seen in figure 14.4.
The measurement probes installed in the liner consisted of thermo couples and oil film thickness sensors.
The liner was placed on top of the lower cooling jacket and was positioned on four force transducers whose function was to measure the friction forces acting in the bearing. Accelerometers were placed on top of the liner in order to see whether vibration not related to the friction forces were acting on the weighing cell system.
The piston, shown in figure 14.5 was instrumented with pressure transducers, thermo couples and an accelerometer such that all the characteristic parameters could be measured.
The parts were installed in the engine and can be seen in figures 14.6, 14.7 and 14.8.
The installed force transducers can be seen in figure 14.9 and 14.10

14.6 Measurement Programme

The measurement programme is shown in table 14.1
As in the table both speed and normal load was changed in the system as well as the oil supply amount and therefore this gives rise to many variations within the programme. The measurements were logged at 4096 locations per cycle by use of an angular encoder as trigger pulse for measurements.

14.7 Measurement Results (Input parameters)

14.7.1 Liner Temperatures

The temperatures were logged on 16 discrete points. The temperature profiles for these measurements can be seen in figure 14.11 for three tests.

14.7.2 Piston Temperatures

The temperatures were logged on the piston, the temperatures to the corresponding loading condition can be seen in table 14.2.

14.7.3 Piston Ring Pressure

The pressure behind the piston rings was recorded and a fraction of the measurements can be seen in figure 14.12 for the same test as shown above.

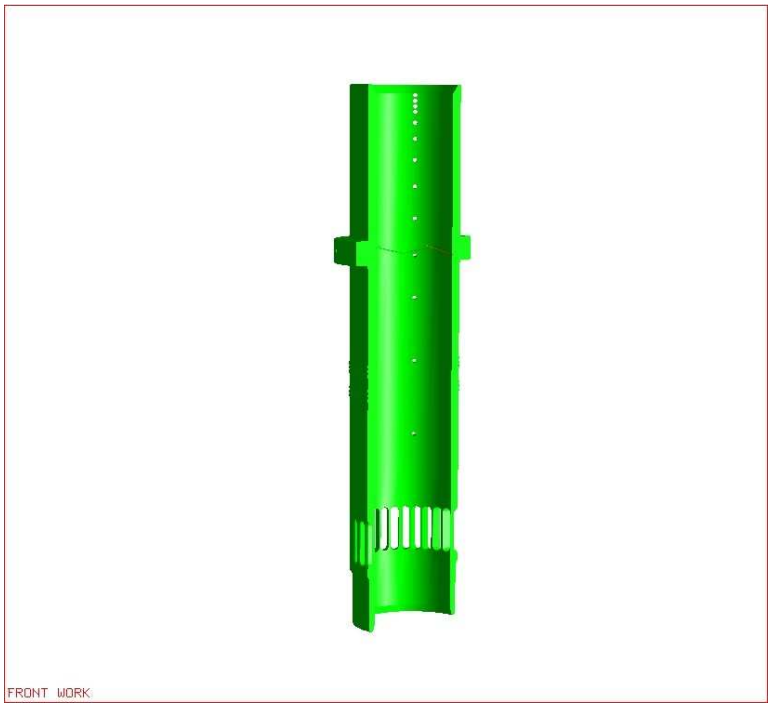

Figure 14.1: Measurement positions of oil film thickness and temperature in liner denoted by the white cylinders

Test	N_{ring}	Speed	Load	Lube Oil
1	4	30 rpm	vary	vary
2	4	50 rpm	vary	vary
3	4	70 rpm	vary	vary
4	2	30 rpm	vary	vary
5	2	50 rpm	vary	vary
6	2	70 rpm	vary	vary

Table 14.1: Measurements

Test	T (Degree Celsius)
Start	33
Half	51
Max	72

Table 14.2: Piston temperatures (70 rpm)

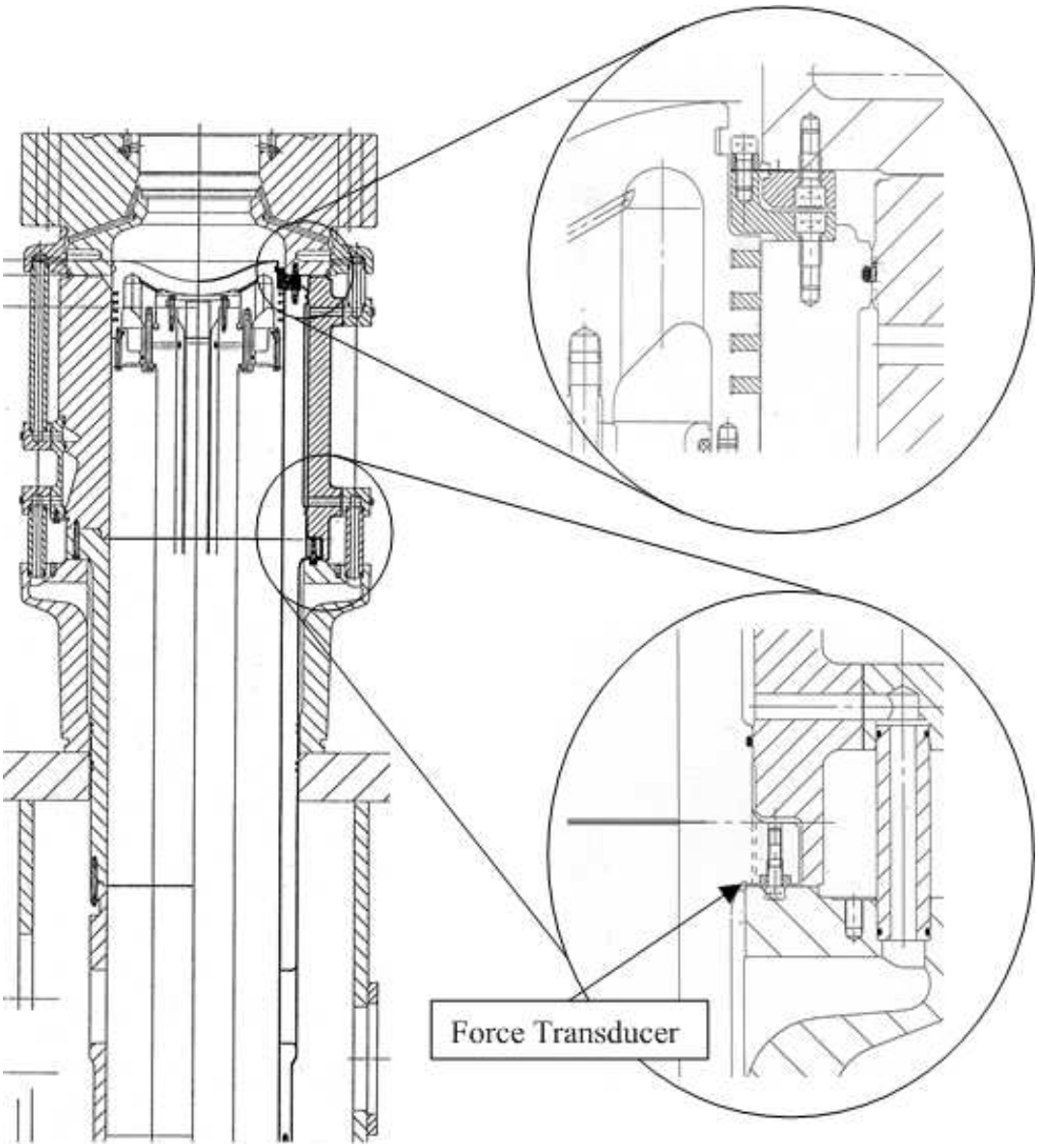

Figure 14.2: Drawing of experimental setup

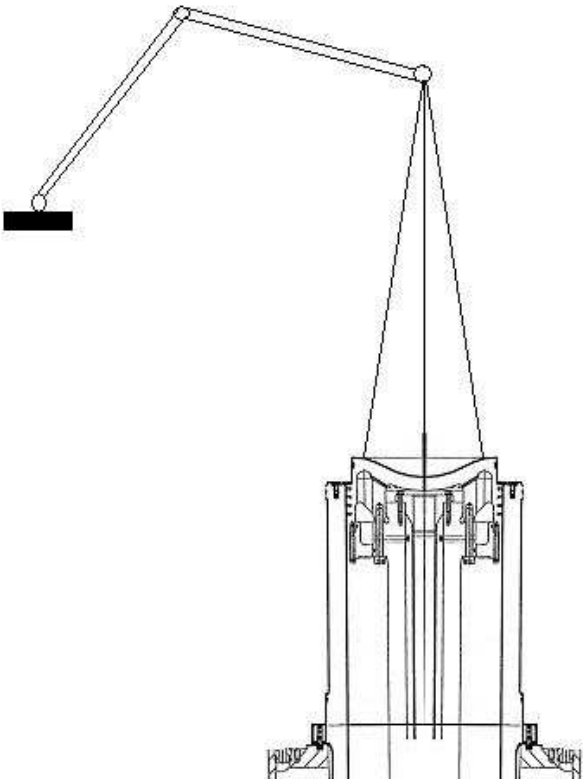

Figure 14.3: Linkage arrangement for experimental setup

Figure 14.4: Liner before installation

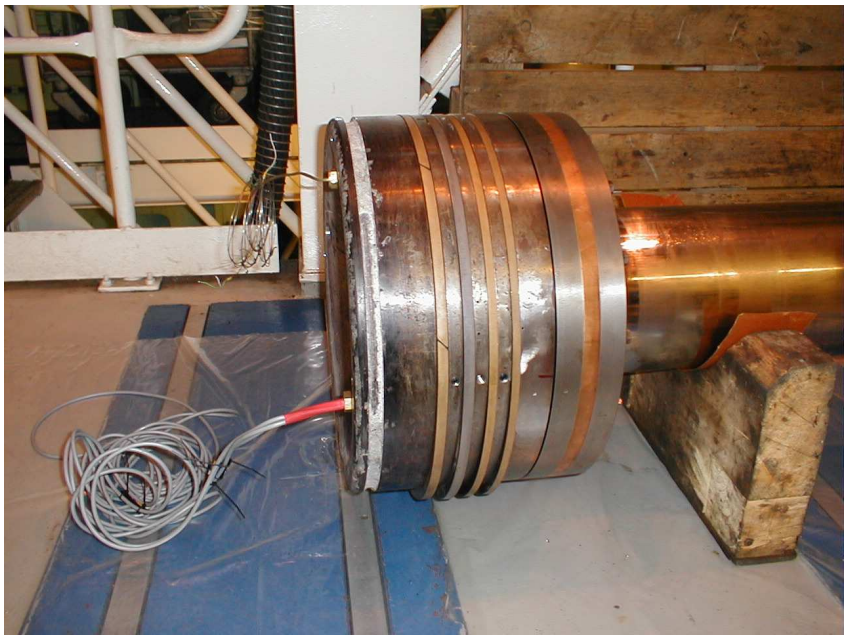

Figure 14.5: Piston before installation

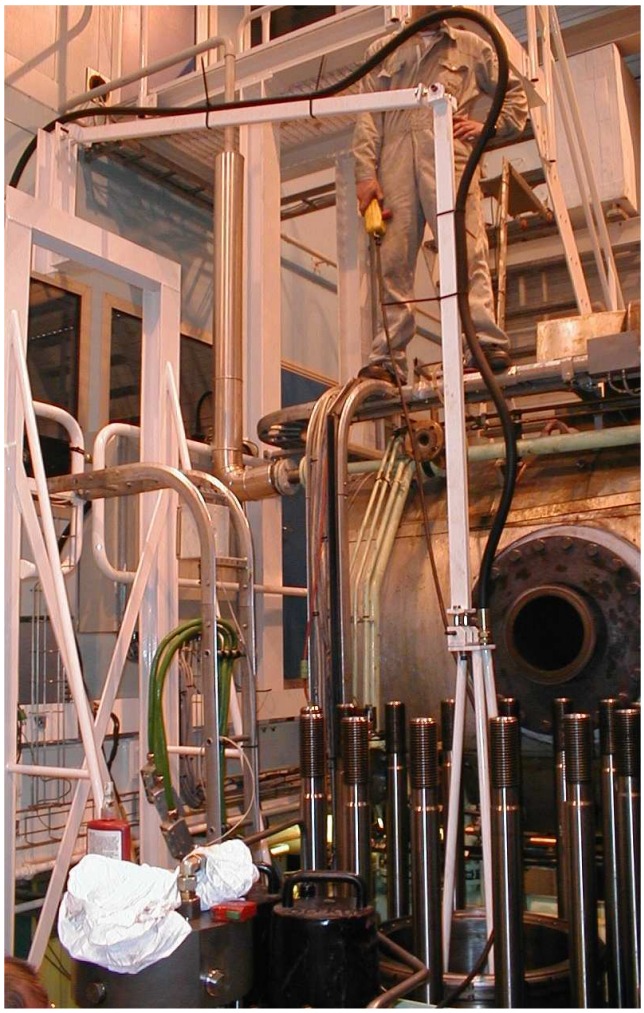

Figure 14.6: Overall view of tripod arrangement

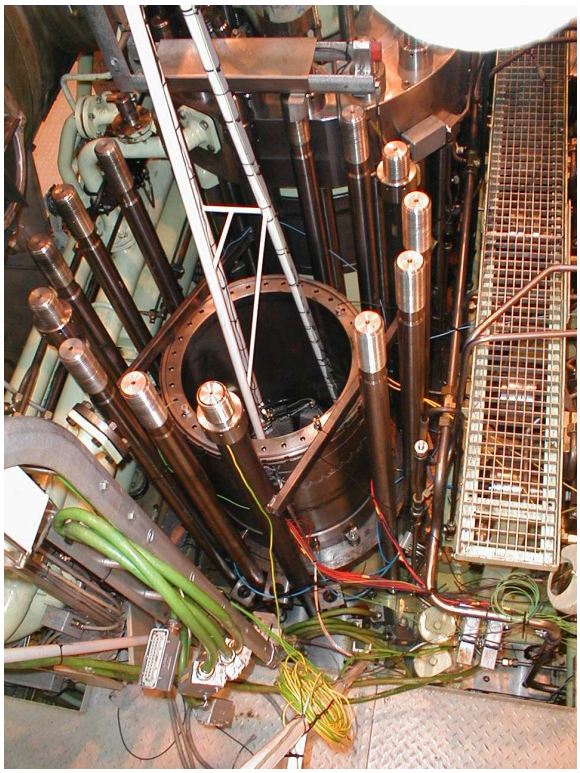

Figure 14.7: Closer view of tripod arrangement

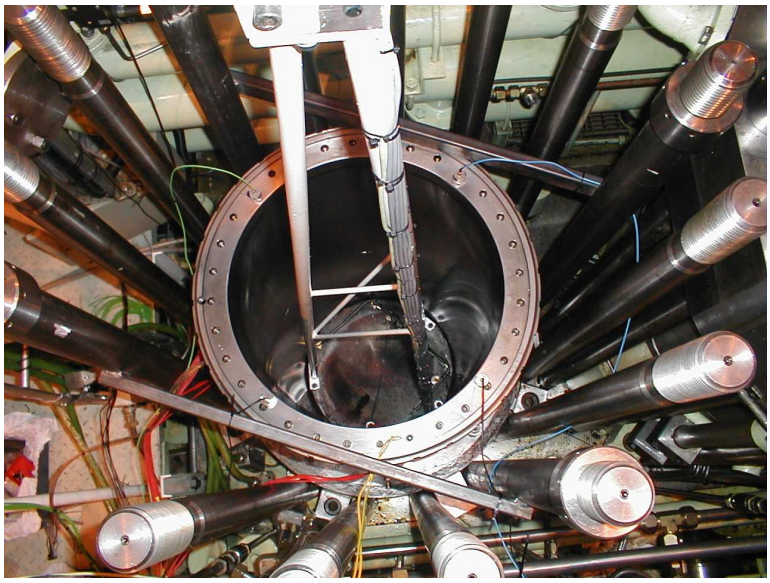

Figure 14.8: Downward view of tripod arrangement

Figure 14.9: Location of force transducer

Figure 14.10: Force transducer

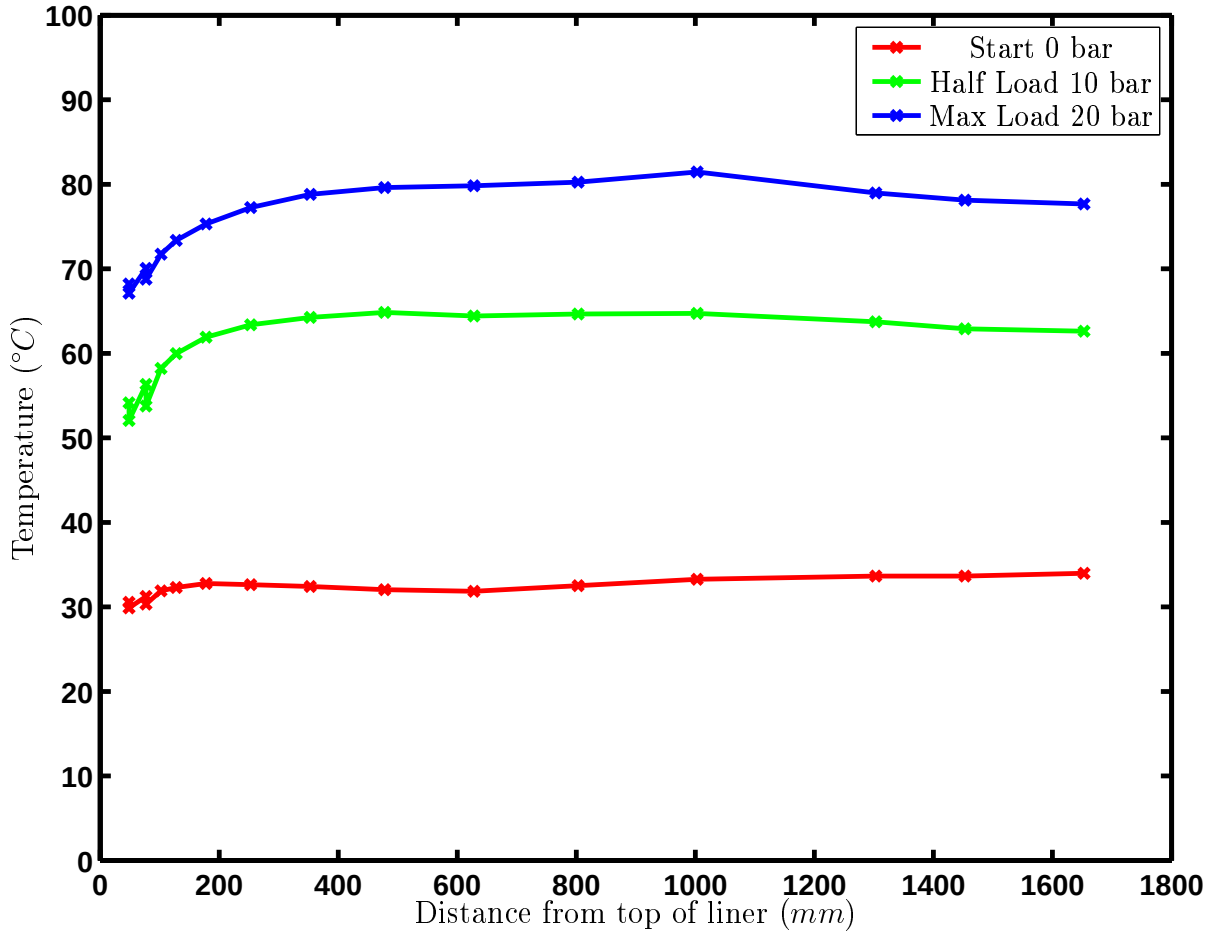

Figure 14.11: Measured temperatures at 16 locations at the liner surface for 3 running conditions at 70 rpm with different loading of the piston rings. The marks are measurement positions according to figure 14.1.

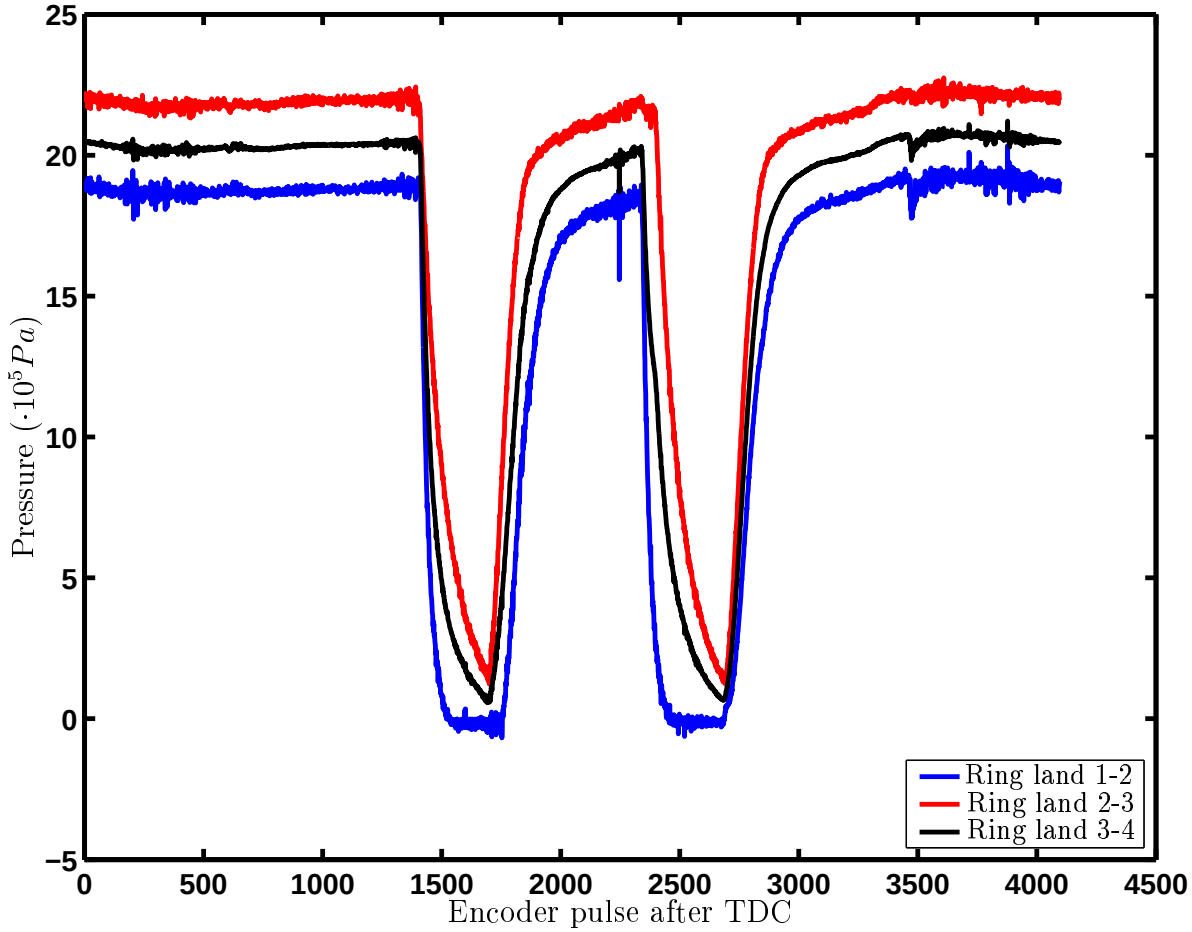

Figure 14.12: Measured inter ring pressures for 70 rpm ($P_{avg} = 20bar$)

14.8 Measurement Results (Output Parameters)

14.8.1 Oil Film Thickness Measurements

These measurements are also shown for the same configuration. There were 14 measurement points which were coinciding in location as the temperature measurement points. Measurement point 1 is shown in figures 14.13 and 14.14.

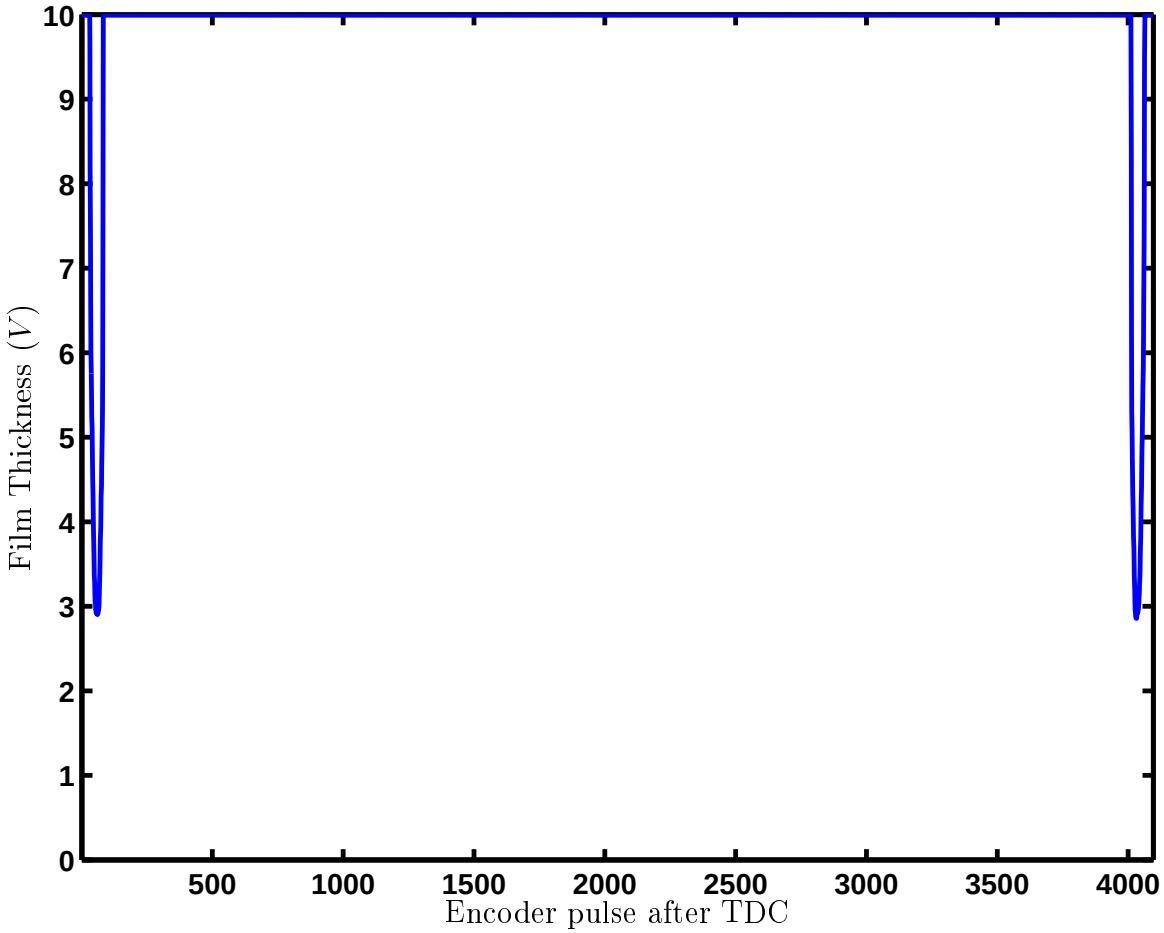

Figure 14.13: Measured oil film thickness for 70 rpm (Sensor 1)

The values presented above are averaged values, where the averaging is performed over 10 revolutions. Unfortunately the experimental values were unusable since a calibration of the sensors was impossible after installation in the cylinder liner.

14.8.2 Liner Friction

Since a lot of tests with this configuration was carried out only a small fraction is presented here. The conversion of the measured values was performed in the same manner as for the guide shoe measurements - see chapter 9. After a local averaging a least squares data fit was

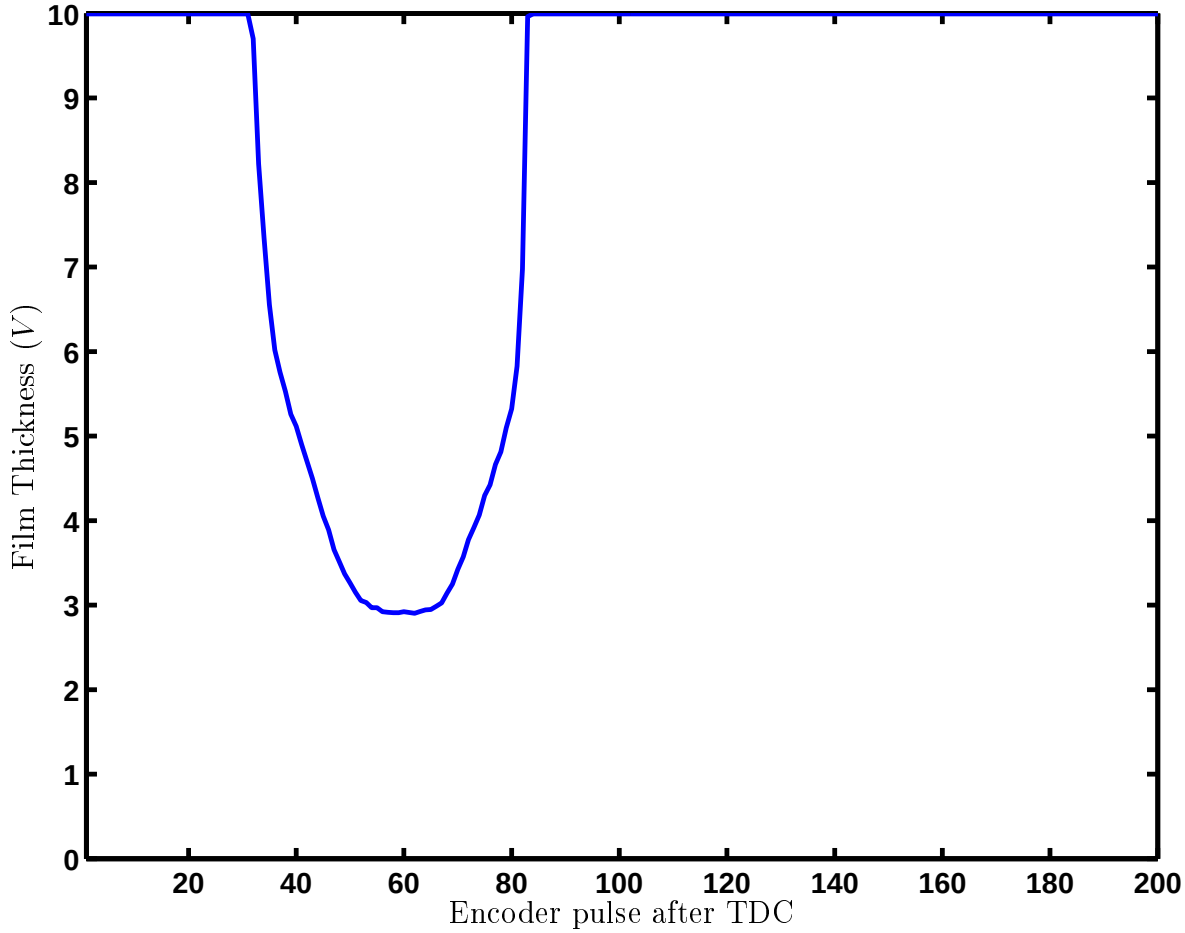

Figure 14.14: Closer view of measured oil film thickness for 70 rpm (Sensor 1)

applied in order to filter away some of the noise. The average friction force is plotted versus the average pressure acting behind the piston rings for various variations.
Plotting the friction loss as a function of the pressure acting behind the rings for 2 different oil feed situations revealed the graphs shown in figure 14.15 and 14.16.

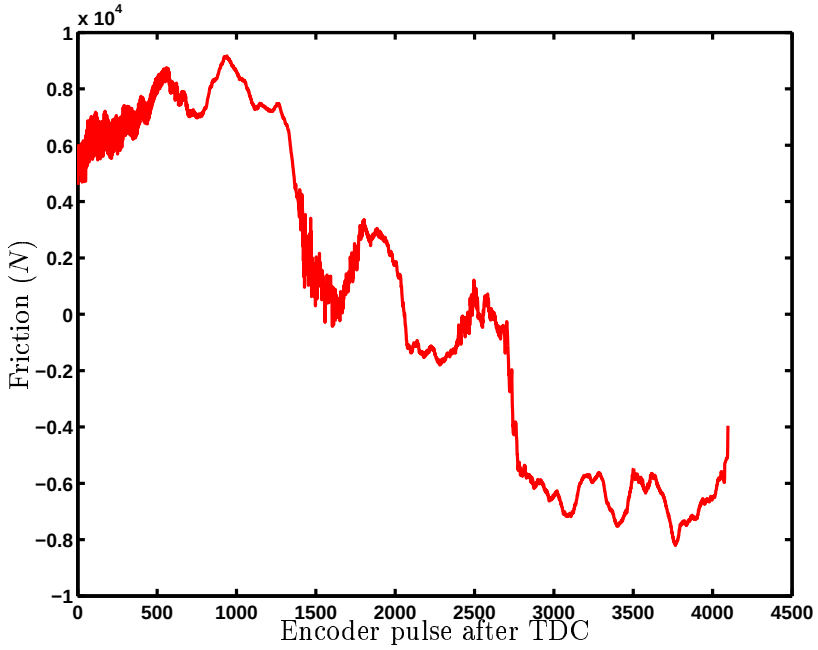

Figure 14.15: Measured friction force for 70 rpm - OIL OFF

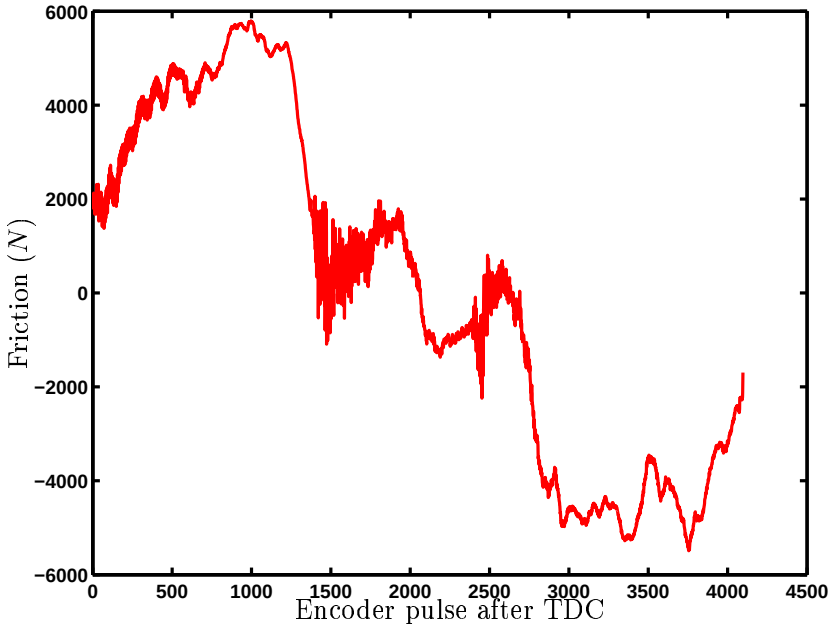

Figure 14.16: Measured friction force for 70 rpm - OIL ON

The difference between the two measurements is that oil was supplied at the nominal rate in figure 14.16 afterwards the supply was stopped and the recorded friction signal is shown in figure 14.15.
The number of tests were categorized. The average power loss was plotted for each measurement versus the load behind the piston rings for the different configurations. In figure 14.17 the power loss is shown for three different test series. The power loss is shown as a function of the load behind the rings and as a function of the speed of the engine.

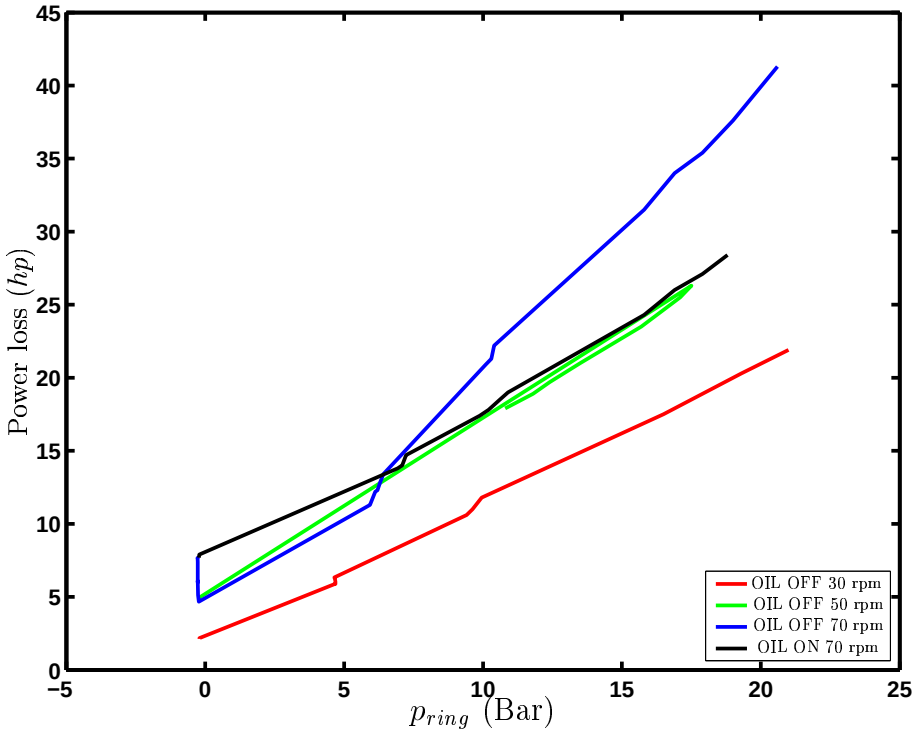

Figure 14.17: Power loss for 3 speeds for different average pressures in piston ring pack with 4 rings

The graphs reveal the size of the power loss to be about $3 - 42hp$ depending on the number of rings, the pressure acting behind the rings and the lubrication condition.

14.9 Summary

A experimental setup to measure oil film thickness, pressure, temperature and friction was constructed. An experimental programme was carried out which revealed that the frictional loss was strongly influenced by the speed and the average pressure acting behind the rings and the amount of lube oil. A large setback was the lack of usable oil film thickness measurements. These would have been able to be used for tuning of the numerical model, but this was not possible.

Chapter 15

Calculation = Measurement for Piston Rings ?

The chapter compares the experimental values with the ones generated by simulations using the theory presented in chapter 12.
The calculated terms shown in the current chapter are generated using the numerical model. All inputs for the numerical description were identical to the running conditions for the experimental apparatus derived in the previous chapter if the data were available. Since the main objective of this study is related to the frictional loss these quantities are natural for comparisons - shown in figures 15.3-15.5.
The input parameters for the simulation are presented in chapter 14. The temperatures are the ones from figure 14.2 and 14.11. Their mutual mean value were inserted into equation 8.1 in order to get the viscosity.
The loading were generated by the use of the measured pressure drop in the ring package - see figure 14.12. The roughness terms were measured after the experiment and also the surface profiles of the piston rings.

15.1 Simulated Condition

A simulation where the engine was running at $70\,rpm$ is shown below for 3 different loadings behind the rings ($p_{avg} = 0, 10, 19\,bar$).

Oil Film Thickness

The oil film thickness measurements were unusable for verification of the numerical model due to calibration problems. The simulated values are shown in figure 15.1 - for $p_{avg} = 19bar$. This reveals oil film thickness' from 1 to 15 μm and the fact that the oil film thickness is smallest on the up stroke and largest on the down stroke.

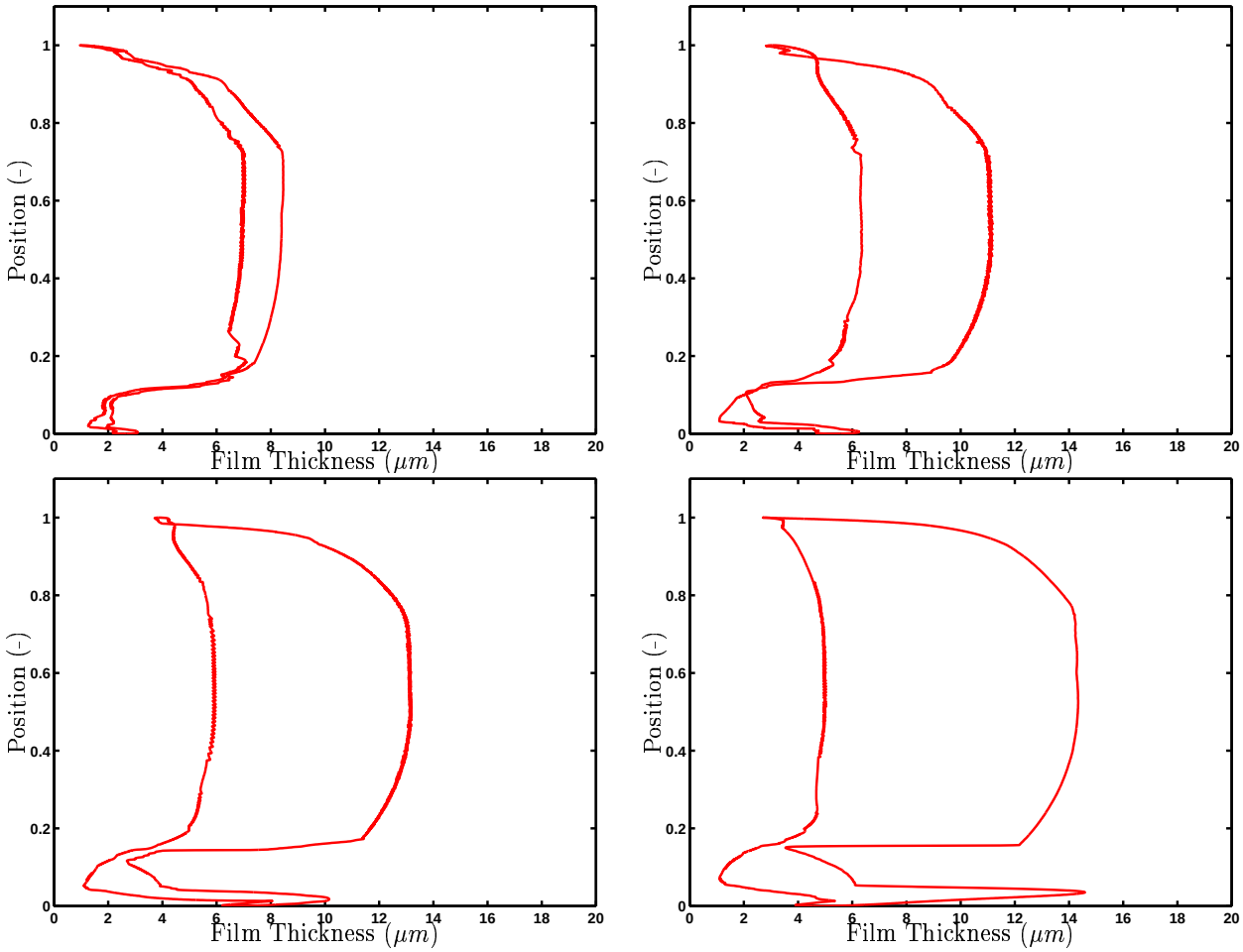

Figure 15.1: Minimum Oil Film Thickness Upper Left: Ring 1. Upper Right: Ring 2. Lower Left: Ring 3. Lower Right: Ring 4.

Pressure History

The simulated oil film pressure distributions are shown in figure 15.2 - for $p_{avg} = 19bar$.

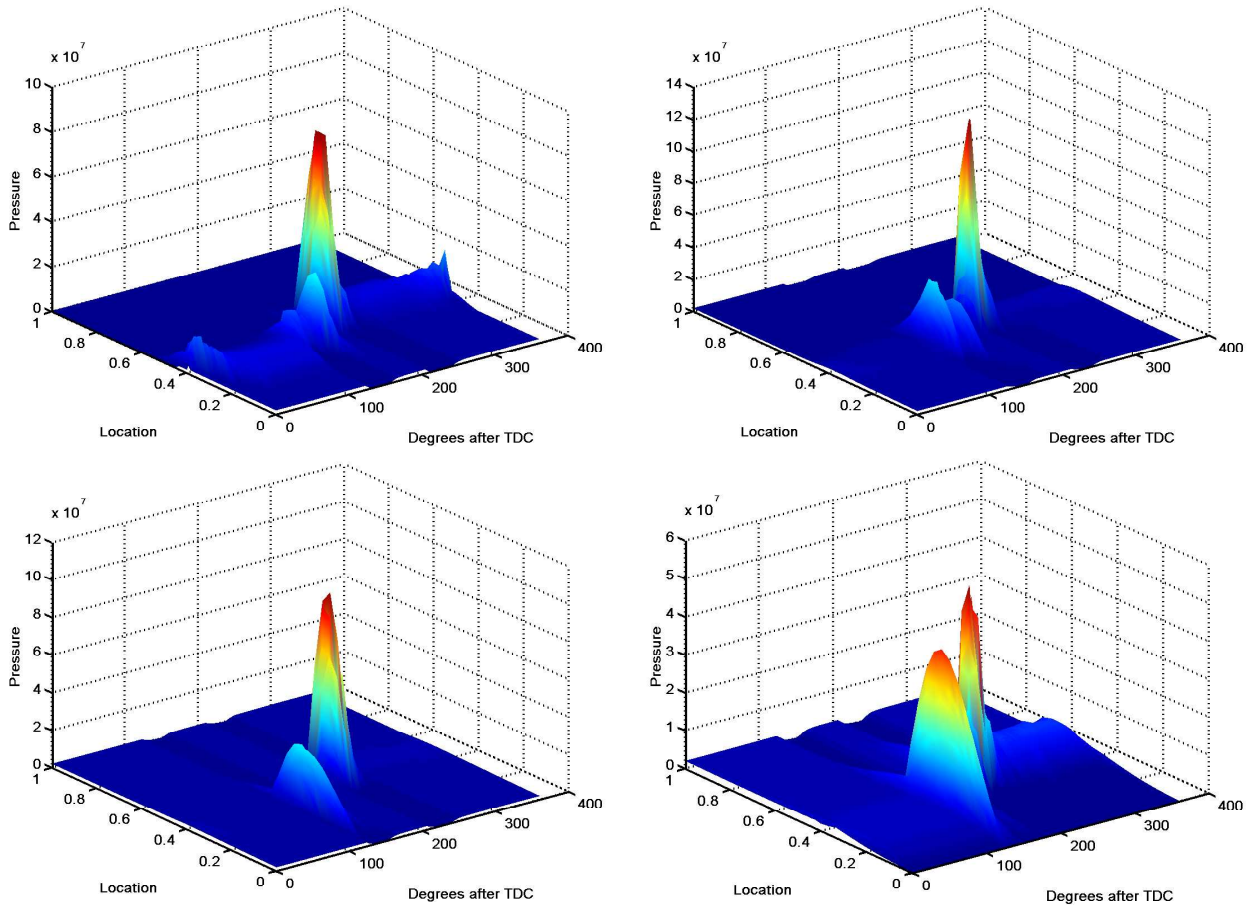

Figure 15.2: Pressure History. Upper Left: Ring 1. Upper Right: Ring 2. Lower Left: Ring 3. Lower Right: Ring 4.

The large peaks in the lower part of the stroke originate from the rings passing the scavenging ports. This is due to the fact that the bearing area is drastically reduced once the ring is sliding on the scavenging port ribs. In the rest of the stroke only small pressures are observed.

15.2 Friction

The objective of the experiment and the simulation was to determine the frictional loss. The simulated values and calculated values are shown in the following.
Collecting all the contributions gives the total friction from the piston and this is presented

in figures 15.3 - 15.5, for different pressures acting behind the rings. It is observed that the maximum friction force lies within the range from $-5000N$ to $6000N$ for the three tests shown.

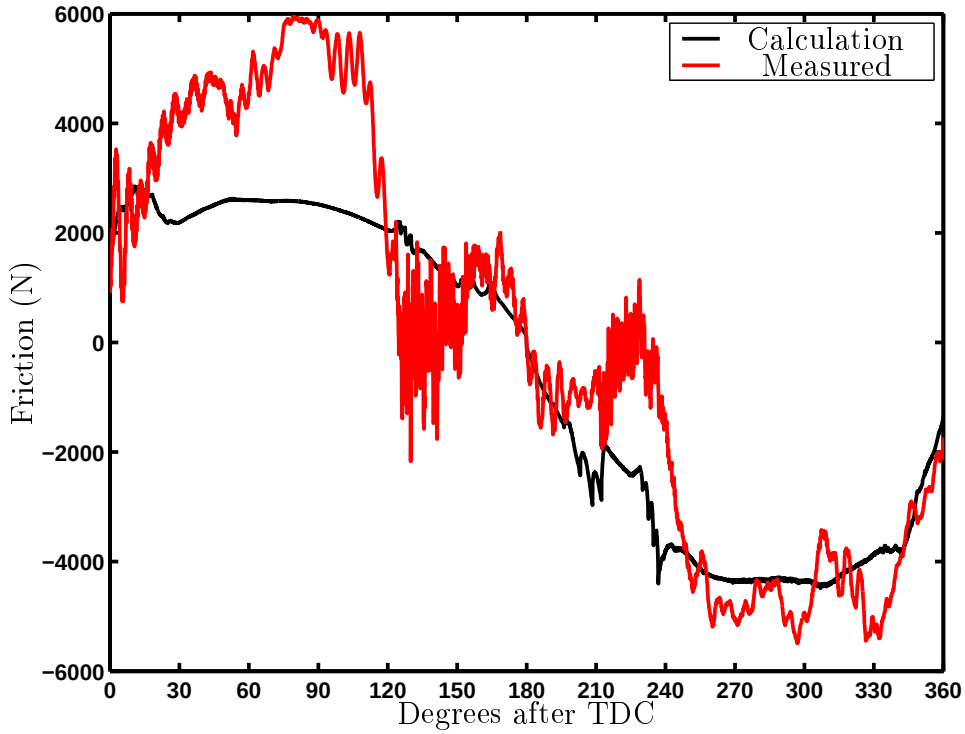

Figure 15.3: Friction total - 70 rpm $p_{avg} = 19bar$

15.3 Correlation Between Measurement and Calculation

Since the oil film thickness measurements were not useful for comparisons only the measured frictional values could be compared with the ones generated by the simulation.
The frictional values were compared for the case of the lubricated condition. The figures 15.3-15.4 reveal that the measured values are more or less similar to the measured values for the up stroke (180 to 360 degrees after TDC). But the simulated values for the down stroke reveal significantly smaller values than the measured values. The explanation may be found in the boundary conditions. The fully flooded boundary condition on ring 4 may be too optimistic compared to the running conditions in the experiment. The problem in this context is the lack of oil film thickness measurement results in order to investigate this further. Shifting to the last figure 15.5 the situation is reversed, now it is the opposite which is present. Good correlation on the down stroke and poor correlation on the up stroke. Focusing on the area where the rings are passing the scavenging ports is seems as blow by occurs. The ring is not

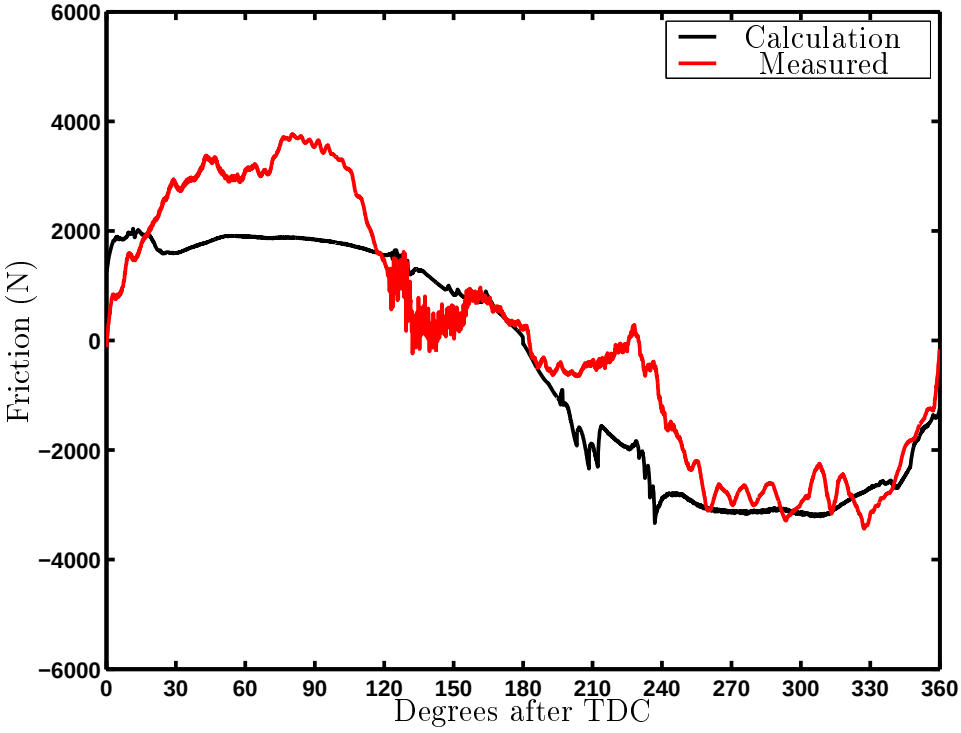

Figure 15.4: Friction total - 70 rpm $p_{avg} = 10bar$

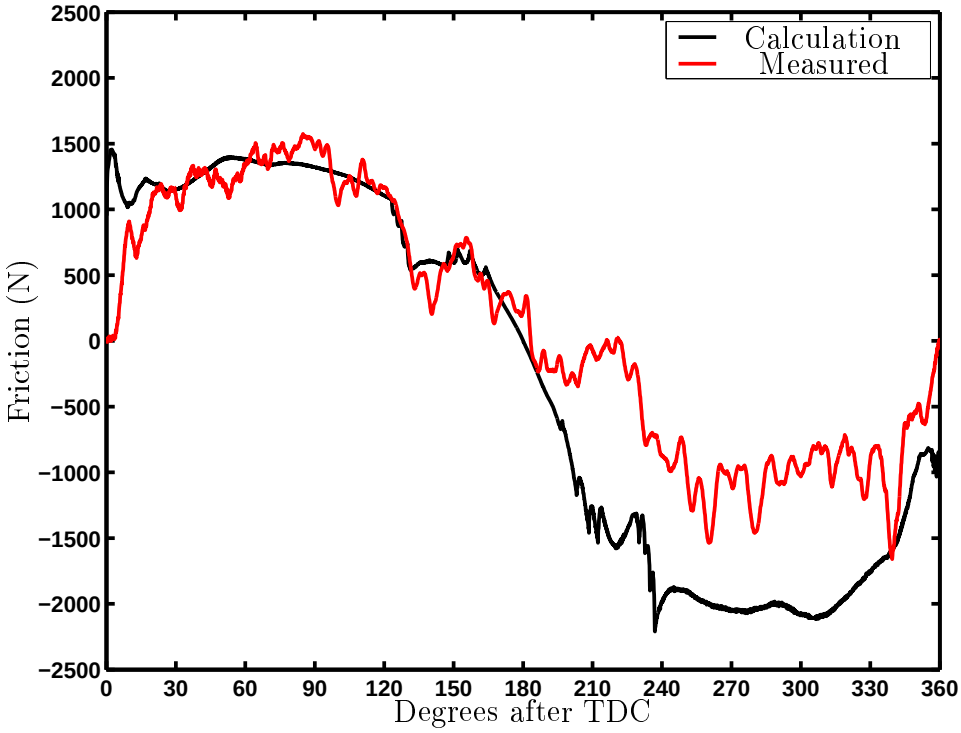

Figure 15.5: Friction total - 70 rpm $_{avg} = 0bar$

in contact with the scavenging port ribs. The friction force is dropping to almost zero which is not revealed by the simulations. The numerical model assumes that blow by cannot occur. This is also the explanation for the sudden drop in oil film thickness for the simulated values shown in figure 15.1.

15.4 Summary

All together the correlation between the measurements and calculations seem to correspond to a satisfactory degree in the last part of the stroke for heavily loaded rings while the correlation in the first part of the stroke is poor. The situation is the opposite for the unloaded case.
This experiment was carried out at very low temperatures $(50 - 80°C)$ compared to the running conditions, where the temperature is about $(200°C)$. This reduces the effect of the choice of starvation model on the down stroke because the viscosity is so much lower. The need for a refinement in the numerical model of the starvation problem is preferable. Once the full load experiments are conducted the need for alternative models of this property will be revealed.
The conclusion to be drawn at this stage is that more theoretical work is needed before predictions concerning future designs become more reliable. By doing that a better correlation may be observed than the experiments conducted so far has revealed.

Chapter 16

Reducing Piston Ring Frictional Loss

In the present chapter a discussion of friction reduction in the piston rings is presented. The basis is reduction of friction force. Since wear is present in the piston assembly it is not enough to reduce the overall power loss if an increased wear is observed - usually near the dead centers.

Numerous researchers have been working in this field. Many of these have come to different conclusions concerning the reduction of frictional loss. Only a fraction of the work conducted in this area is mentioned in the following.

A lot of experiments concerning different lube oils containing different additives have been investigated which have revealed that this might be beneficial in smaller engines. Wakuri et al. [1995] showed that the frictional loss could be lowered at mid stroke where hydrodynamic lubrication is present for a lower viscosity oil. This however increases the friction peak at the dead centers, and therefore a friction modifier should be added the lube oil. Furthermore, it was experimentally verified that the frictional loss could be lowered if the width of the rings is lowered. This again increases the friction peak at the top dead center. It is stated that a ceramic coating of the top ring could reduce the friction peak at the top dead centers.

Mehmet and Patterson [1984] showed that a friction modifier should be added the lube oil to reduce the friction near the dead centers by an experimental approach. The reduction was up to 30-40 %.

Halsband [1995] showed that a surface coating of the liner could reduce the overall fuel consumption up to 1% on a small four stroke engine.

A problem in this context is the large amount of lubrication oil used - approximately $0.45 - 1.0 \frac{g}{BHPh}$ for the large two stroke marine diesel engines. This calls for mineral oils only and the additives which can be quite expensive is not preferable in this context.

The size and shape of the piston rings have not been investigated. The reason for this is the wear subjected to these rings. The rings will attain their geometry according to the wear profile.

The number of piston rings might affect the over all frictional loss. The viscosity may also influence the result. Lastly the height of the rings may be significant in this frictional study.

To summarize the degrees of freedom are:

- Number of rings
- Width of rings
- Viscosity
- Shape of ring
- Amount of oil input in the liner

Looking at friction reduction properties the power loss is interesting but also the maximum friction force during one cycle since this quantity is related to the wear properties of the ring pack. Furthermore, the fraction of friction generated by hydrodynamic lubrication is interesting.

16.0.1 Number of Rings

The experimental part revealed the number of rings might influence the power loss (Not shown in the thesis). This has been varied and the result is seen in table 16.1

Case	Offset C_r	N_{ring}	$\frac{F_{fric,hyd}}{F_{fric,tot}}$ (%)	F_{max} (N)	P_{lost} (hp)
1	0.4	1	39	2850 (ring 1)	3.4
2	0.4	2	46	2850 (ring 1)	7.5
3	0.4	3	54	2800 (ring 1)	13.4
4	0.4	4	60	2600 (ring 1)	19.5

Table 16.1: Result ring number variation

The analysis clearly reveals the effect of reducing the total number of rings. The problem in doing this is the relative lower fraction of averaged hydrodynamic friction force compared to the total friction force. As shown in the table the amount of boundary friction increases which may be directly correlated to the wear of the cylinder liner. At the same time the largest friction force increases. The same is revealed by the study carried out by Halsband [1995]. But a potential for optimization is clearly present for this parameter. A drawback of the starvation model is observed here. The fully flooded condition for the lowest ring has a relative larger influence on lubrication condition once the number of rings are lowered. Another issue not addressed here is the larger normal load on the ring land and the effect this might have on the wear of this contact face.

16.0.2 Viscosity Variation

Altering the viscosity is another tool for optimization the result is shown in table 16.2. The effect of increasing the viscosity reduces the amount of boundary friction but has only small effect on the overall loss. Lowering the viscosity reduced the frictional loss but created a larger fraction of boundary lubrication. This effect has been reported by many researchers - see for instance Hamatake et al. [2001].

SAE	Offset C_r	r_p (m)	$\frac{F_{frac,hyd}}{F_{fric,tot}}$ (%)	F_{max} (N)	P_{lost} (hp)
30	0.4	3	51	2750 (ring 1)	18.3
40	0.4	3	55	2650 (ring 1)	18.8
50	0.4	3	60	2600 (ring 1)	19.5
60	0.4	3	64	2500 (ring 1)	20.3

Table 16.2: Result viscosity variation

16.0.3 Radius of Curvature of Ring

The radius of curvature is a parameter which most likely can not be altered due to the wear process. The result of this theoretical variation is shown in table 16.3. Decreasing the radius of curvature increases the fraction of boundary friction and also increases the overall loss.

Case	Offset C_r	r_p (m)	$\frac{F_{fric,hyd}}{F_{fric,tot}}$ (%)	F_{max} (N)	P_{lost} (hp)
1	0.4	2	58	2400 (ring 1)	18.5
2	0.4	3	60	2600 (ring 1)	19.5
3	0.4	4	62	2800 (ring 1)	19.8
4	0.4	5	63	2900 (ring 1)	20.3
5	0.4	6	63	3000 (ring 1)	20.6

Table 16.3: Result radius variation

16.0.4 Offset of Radius of Curvature of Ring

The offset is another parameter which most likely cannot be altered due to the wear of the ring profile. The result of this theoretical variation is shown in table 16.4.

Case	Offset C_r C	r_p (m)	$\frac{F_{fric,hyd}}{F_{fric,tot}}$ (%)	F_{max} (N)	P_{lost} (hp)
1	0.3	3	64	2350 (ring 1)	21.1
2	0.4	3	60	2600 (ring 1)	19.5
3	0.5	3	57	2700 (ring 1)	18.6
4	0.6	3	53	2950 (ring 1)	17.9
5	0.7	3	50	3000 (ring 1)	17.3
6	0.8	3	48	3050 (ring 1)	16.9

Table 16.4: Result offset variation

Some variation is seen, but again with the same effect. The frictional loss can be lowered but not without an increase in the boundary friction peak.

16.0.5 Width of Rings

The width is scaled relative to the standard design (1.0) table 16.5.

Case	$\frac{W}{W_{ring}}$	r_p (m)	$\frac{F_{fric,hyd}}{F_{fric,tot}}$ (%)	F_{max} (N)	P_{lost} (hp)
1	1.2	3	58	2900 (ring 1)	21.2
2	1.0	3	60	2600 (ring 1)	19.5
3	0.8	3	62	2500 (ring 1)	18.2
4	0.6	3	65	2200 (ring 1)	17.1
5	0.4	3	77	1200 (ring 1)	15.7
6	0.2	3	98	550 (ring 2)	13.7

Table 16.5: Result width variation

In the table the frictional loss shifts from a mixed regime to a almost hydrodynamic regime. This is caused by the fact that the radius of curvature of the ring is kept constant although the ring height is altered. This is probably not realistic since the surface profile of the ring is generated by a wear mechanism. The temperature of the ring may increase due to the reduced size such that the transportation of the generated heat in the contact is more difficult which again increases the temperature and thereby decreases the viscosity. This may have a demolishing effect of the lubrication condition.

16.0.6 Lube Oil Amount

If the amount of lube oil can be increased such that ring 4 is flooded on the down stroke and ring 1 is fully flooded on the up stroke the frictional loss is reduced from 19.6 hp to 10.0 hp - see table 16.6.

Case	DOWN FF	UP FF	$\frac{F_{fric,hyd}}{F_{fric,tot}}$ (%)	F_{max} (N)	P_{lost} (hp)
1	1	4	66	2200 (ring 1)	10.0
2	-	4	60	2600 (ring 1)	19.5

Table 16.6: Result lube oil

This really affects the frictional loss, but if this were the case in an actual running engine a large lube oil consumption had to pay for this an effect which is not good from an economical view.

16.1 Design Proposal

Collecting the studies carried out in the previous section may be utilized in order to create a new ring pack. It was shown that the number of rings and their width had great influence on the total power loss which is the aim of the analysis.

The design proposal is :

$$
\begin{aligned}
N_{ring} &= 2 \\
W_{ring} &= 0.010m \\
r_p &= 3.0m \\
C_r &= 0.40 \\
Oil &= SAE60
\end{aligned}
\tag{16.1}
$$

The calculation results of this proposal is shown in figures 16.1-16.6.

16.1.1 OFT History

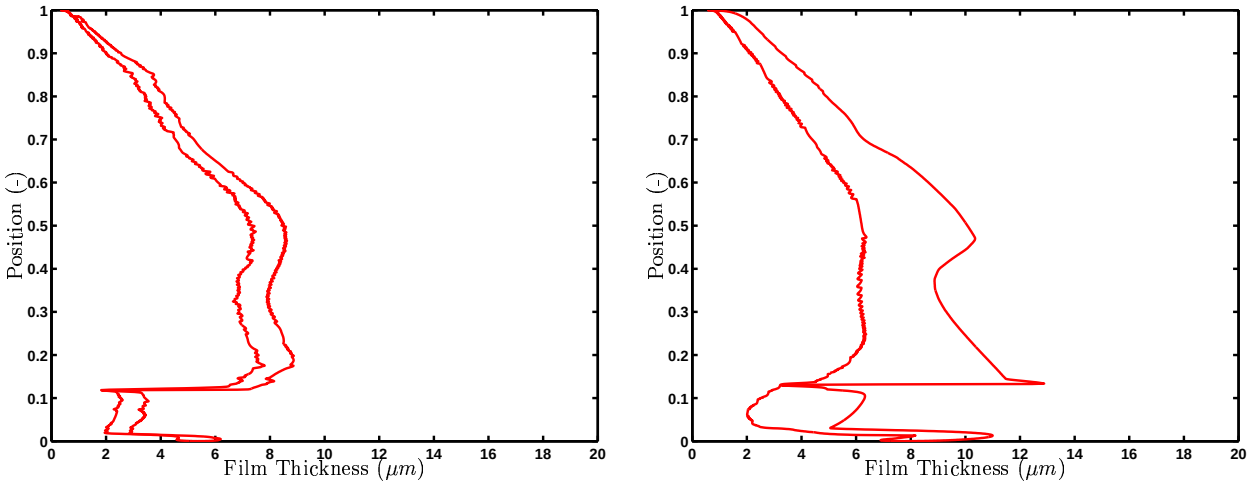

Figure 16.1: Minimum Oil film thickness. Left: Ring 1. Right: Ring 2

16.1.2 Pressure History

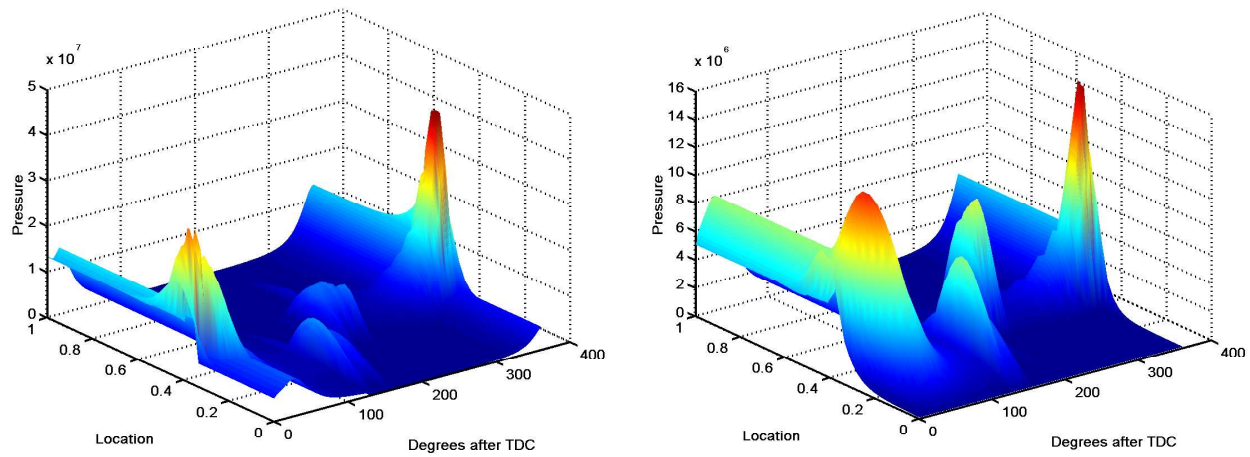

Figure 16.2: Pressure history. Left: Ring 1. Right: Ring 2.

16.1.3 Cavitation / Starvation of Piston Rings

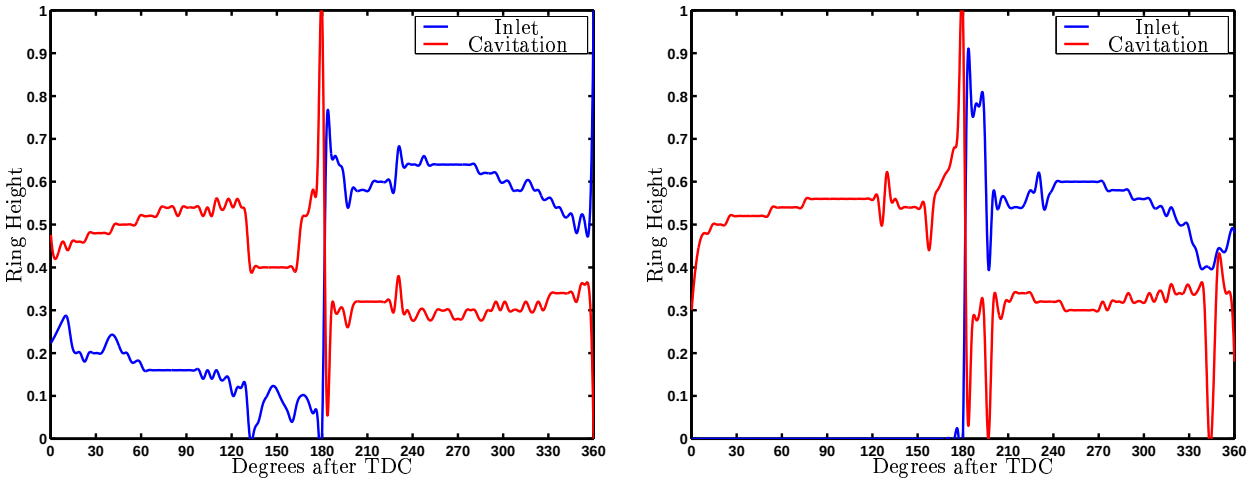

Figure 16.3: Location of cavitation/inlet position. Left: Ring 1 Right: Ring 2.

16.1.4 Friction History

The friction history is presented in figure 16.4 and the total amount in figure 16.5. This can be converted to lost power - presented in figure 16.6.

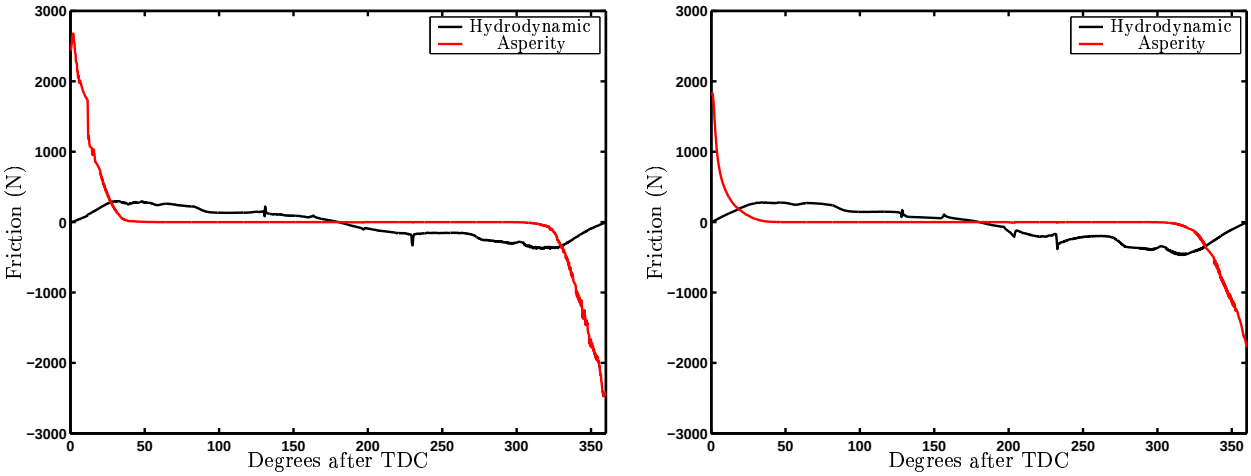

Figure 16.4: Friction force. Left: Ring 1. Right: Ring 2

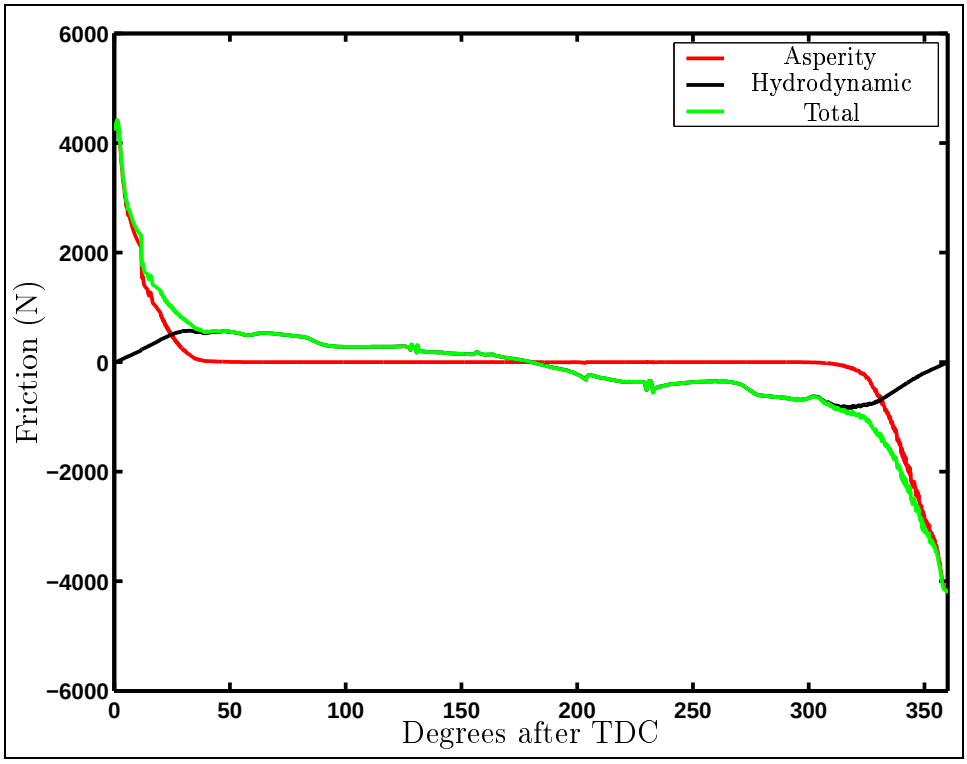

Figure 16.5: Friction total

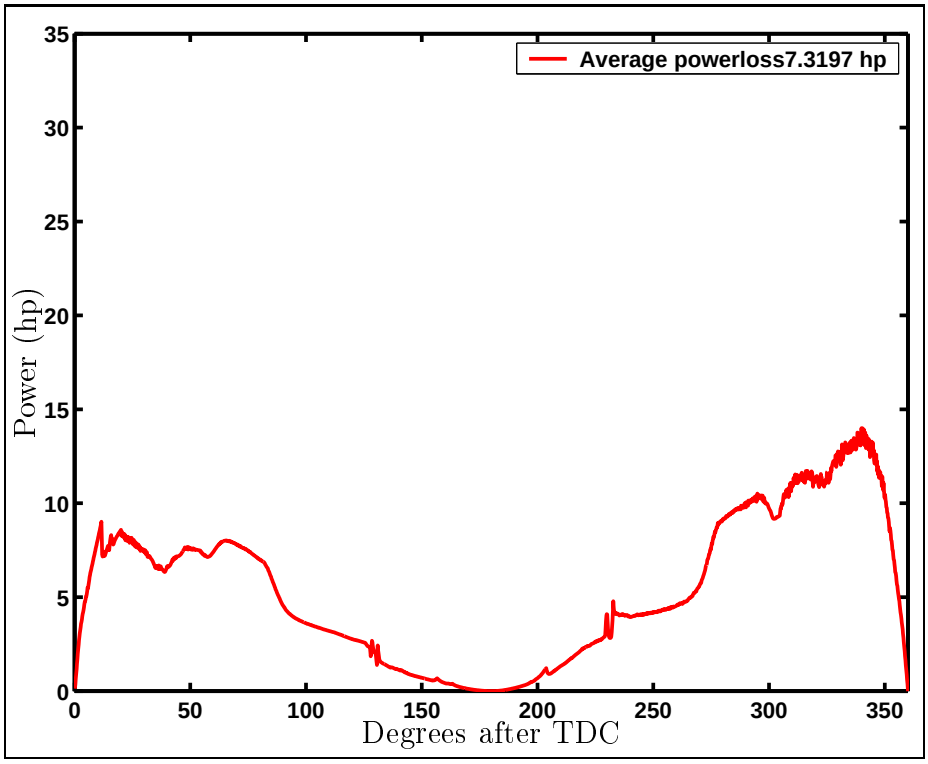

Figure 16.6: Power loss

16.2 Summary

Comparing the figures with the simulations for the standard design performed in Chapter 12 reveal a large difference between the total power loss (from 7.3 to 19.6 hp). The size of the maximum asperity force is slightly higher in the two ring case than the reference calculation. The amount of boundary friction is almost 30% higher. At the same time the number of rings are reduced which might maintain the wear rate of the liner surface at the same level. With the chosen numerical model it appears to be a simple task to reduce the overall loss. However, a more refined model of the starvation condition in the ring package is necessary in order to be able to predict the conditions more accurately. Until then experiments may reveal the effect of reducing the number of rings and width of rings within the ring package.

Chapter 17

Conclusion

The conducted work is summarized in the present chapter. A general description of the lubrication model applicable for determination of the characteristics for each bearing is presented. A time stepping device is presented along with cavitation criteria. Two tools for the determination of frictional loss are presented - one for the guide shoe bearing and one for the piston rings. The achievements are presented in the two following sections for each bearing.

17.1 Friction in Guide Shoe Bearing

A numerical study revealing the important parameters controlling the guide shoe characteristics have been established. Elasticity was found to be significant in the determination of guide shoe characteristics. Another significant term was the pre-deformed guide plane arising from the assembly process of the engine. Including the attitude angle in the model was also found to have significant influence on the characteristics. The power loss for the guide shoe bearing was found to be 1.1% of the generated power.

The theoretical model was verified experimentally. An experimental programme was carried out in order to verify the numerical model. Satisfactory correlation between theory and experiment was observed.

The verified model was used for studying the friction properties of the guide shoe bearing. The study revealed an almost 60 % friction reduction potential. The new design contains no oil grooves and is generated by a bearing layout whose length to width ratio is altered. A design where the Length-Width ratio was close to one was found to be optimal. A study of a new design fitting inside the existing frame box revealed that a 40 % reduction could be attained. This could be attained by removing the oil grooves and shortening the length with about 20 % and at the same time increasing the clearance ratio with 50 %. The lubricant should be added in a new way - described in one of the two patent applications currently being evaluated concerning future guide shoe designs.

17.2 Friction in Piston Ring Bearings

A numerical model for calculating frictional loss in the piston ring package has been established. Asperity interaction was found to be very significant in the determination of frictional behaviour. The most significant term however was the lubrication condition of the piston ring package. The total power loss was calculated to be 0.9% of the total generated power.
Measurements of the frictional loss in the piston ring package were performed. Due to instrumentation problems only a limited amount of usable parameters were measured. The measured frictional terms compared to the numerical model revealed that large deviations between the two were found. The likely explanation was the starvation algorithm. More work must be conducted in this area.
A frictional reduction study was carried out where a number of parameters were varied. A large potential exits in the reduction of the number of rings and the widths of the rings more than 50%. This has to be verified experimentally. The need for a refinement in the numerical model of the starvation problem is obvious. Until then experiments may reveal the effect of reducing the number of rings within the ring package.

17.3 General

The investigated bearings have revealed that the overall loss for the bearings examined here is 2%. Lowering the frictional loss is possible for both bearing types without altering the performance of the individual bearing significantly. Still there are shortcomings in the presented work which will be mentioned in the following chapter.

Chapter 18

Future Aspects

In the current chapter some of the future aspects of the conducted work are presented.

18.1 Guide Shoe Friction

The numerical and experimental work conducted in this area revealed that an acceptable model was established for the determination of guide shoe characteristics. One of the aspects to be dealt with in the near future is a redesign of the lubrication system such that the oil grooves may be removed from the bearing. This is proposed in a patent application Vølund [Filed: 18 may 2002a]. A new experiment reusing the measurement apparatus with a new lubricating system along with the elimination of the oil grooves is under consideration. Furthermore modeling another degree of freedom for the guide shoe is interesting. Rotation of the guide shoe around the x-axis (see figure 7.1). This may be achieved by including the cross head pin bearing in the numerical model. Thereby the guide shoe will be floating in 3 fluid film bearings. Another aspect of the model is to do calculations of the characteristics of the other existing designs of guide shoes and frame boxes in order to gain further knowledge about the optimization potential of this bearing.

18.2 Piston Ring Friction

The measurements performed on this bearing had diverging conclusions. One of the forthcoming tasks is to do the measurements under firing conditions. The design of the components were prepared for this - but a lack of time prevented the experiment from being conducted. Furthermore, the oil film thickness measurement probes have to be either replaced or a re-machining of the liner must be performed in order to make the sensors flush the surface and afterwards a calibration must be issued. Maybe an installation of some of these sensors in the piston rings should be considered. The numerical model is established and is waiting for more useful measurements in order to reveal the handles to adjust in the numerical description. Implementing a starvation model which opens for the possibility to eliminate the fully

flooded condition for ring 4 on the down stroke would be a step toward more realistic running conditions. The properties determined may be utilized to predict wear and thereby to examine the change in lubrication condition over time.

Appendix A

Appendix

A.1 Drawings

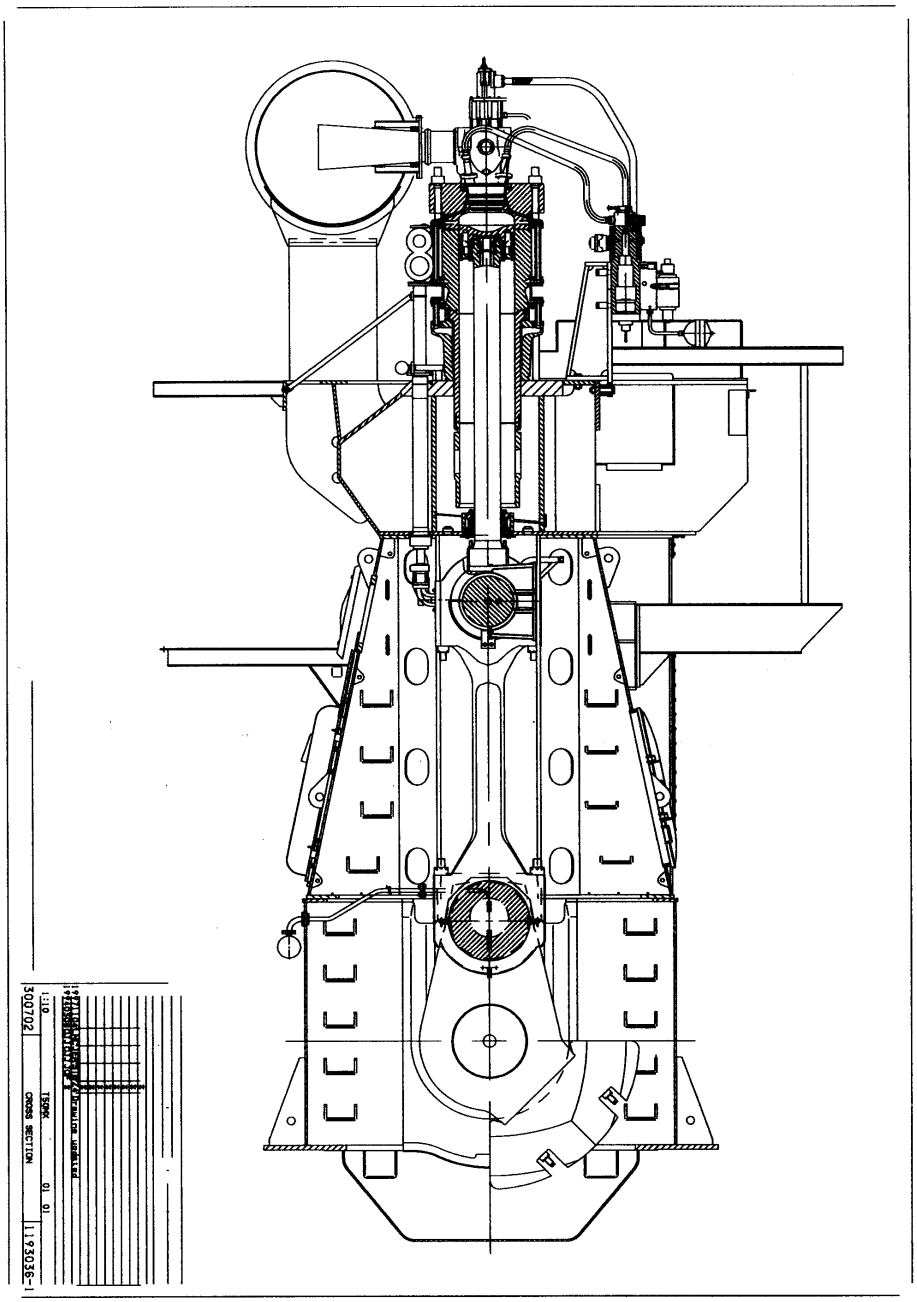

Figure A.1: Cross Section View

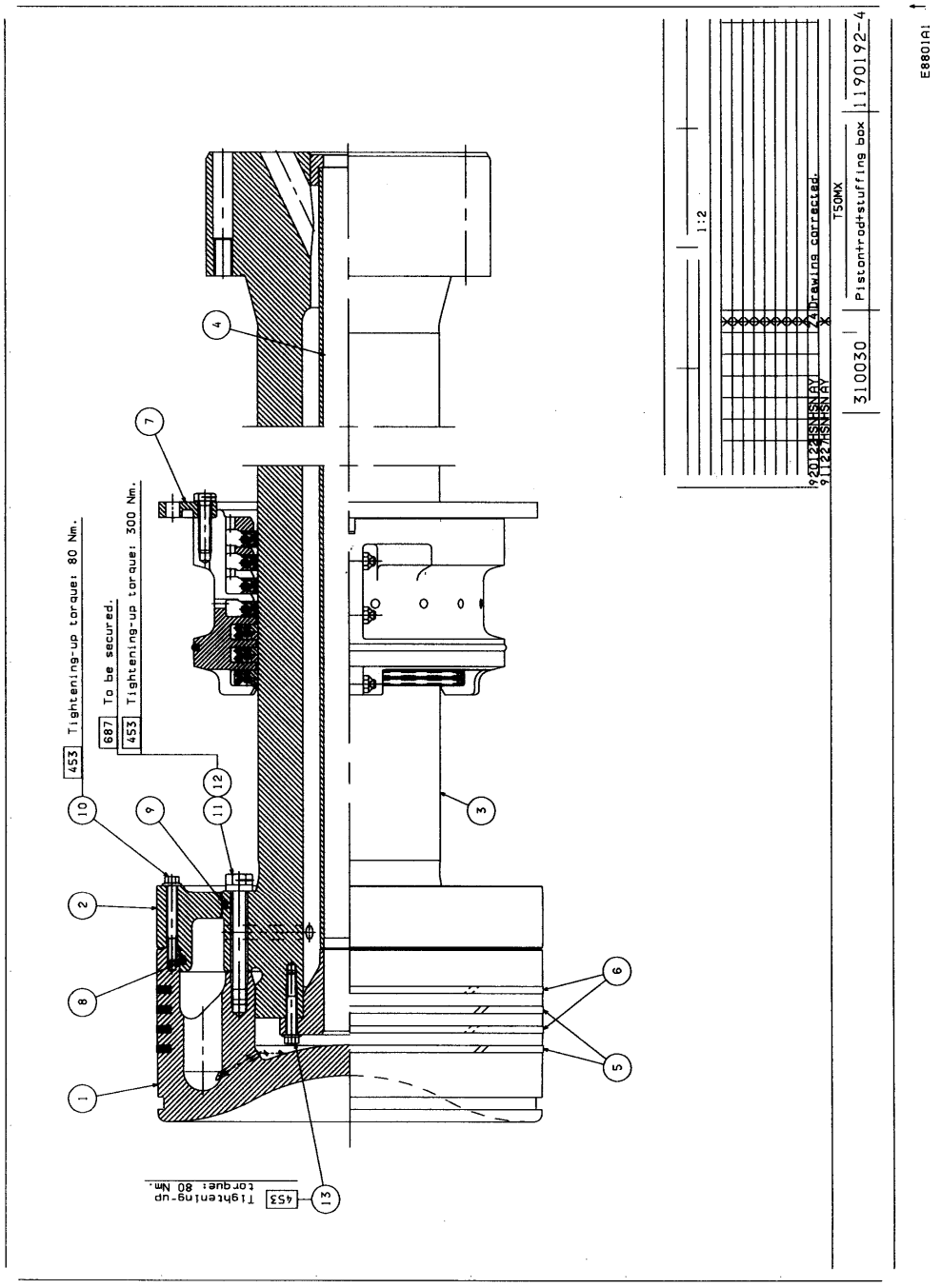

Figure A.2: Piston Assembly

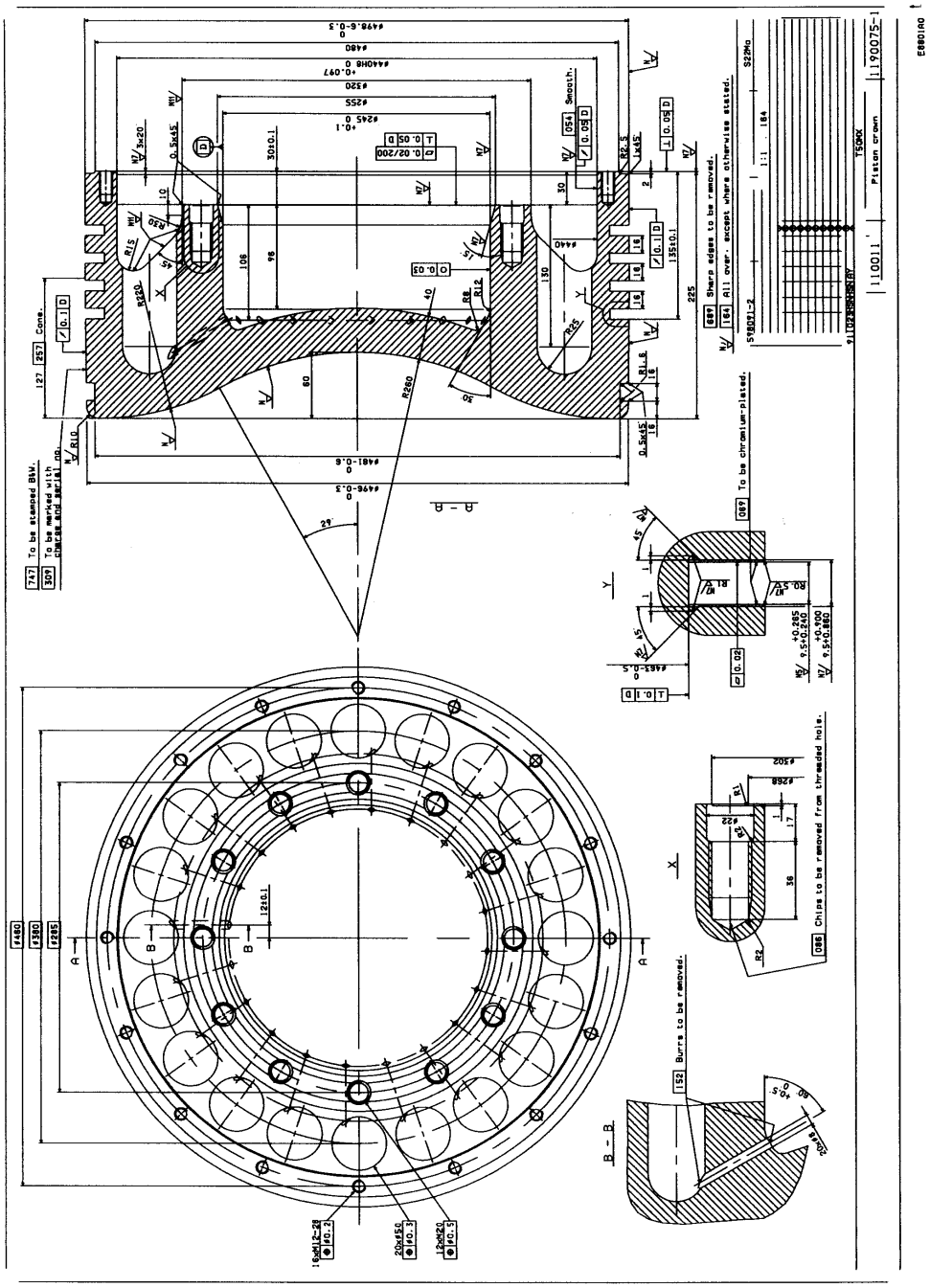

Figure A.3: Piston Crown

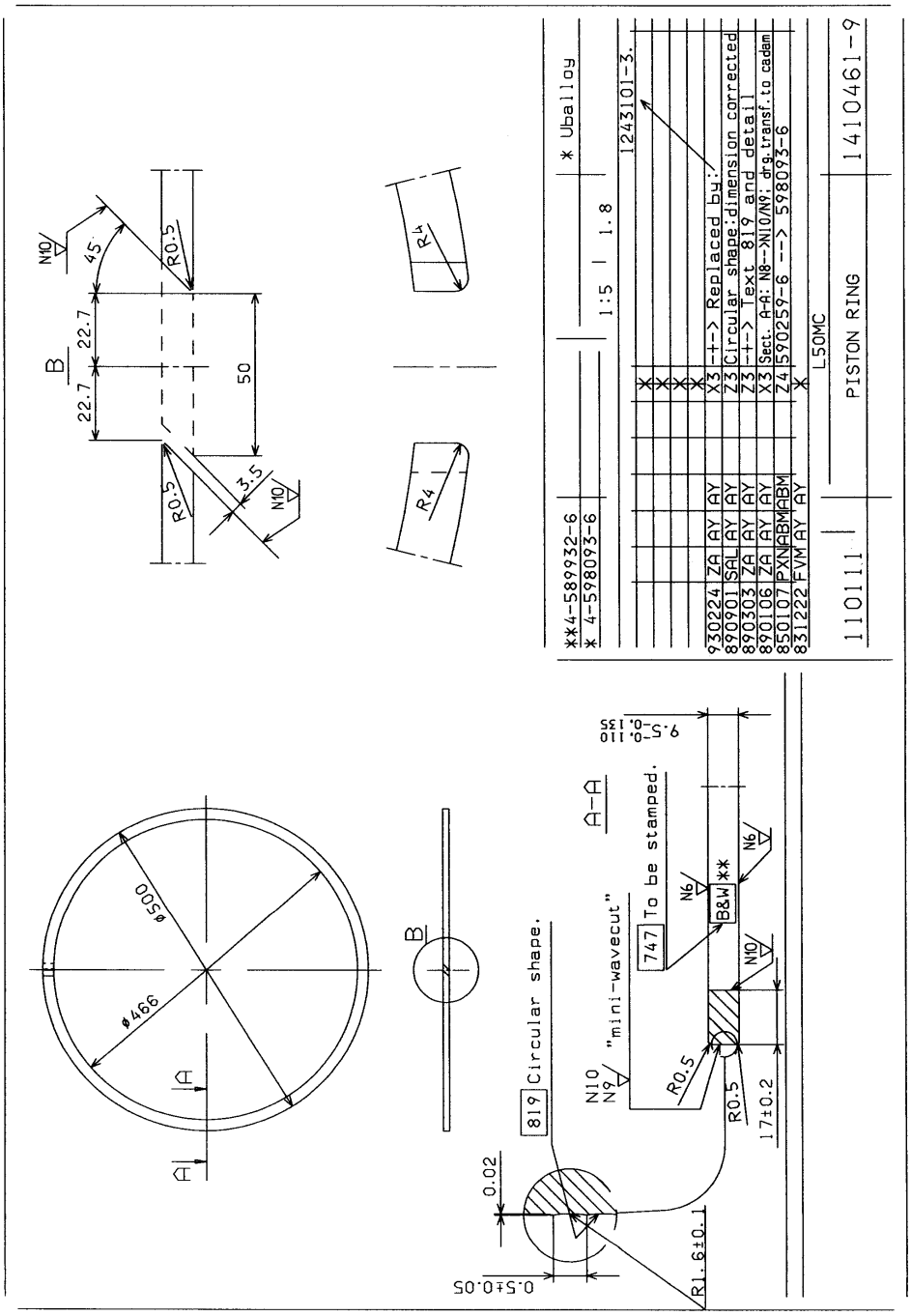

Figure A.4: Piston Ring

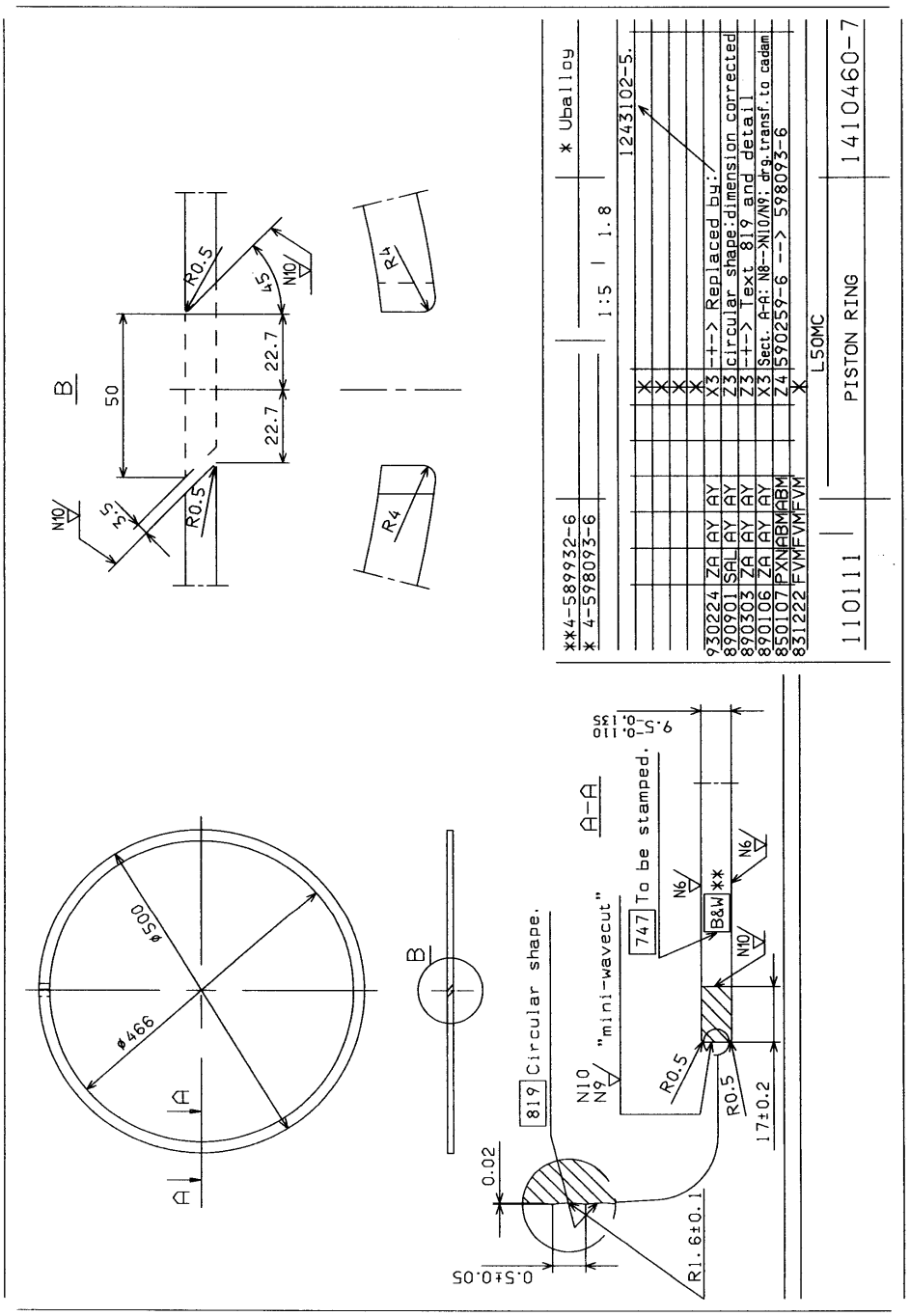

Figure A.5: Piston Ring

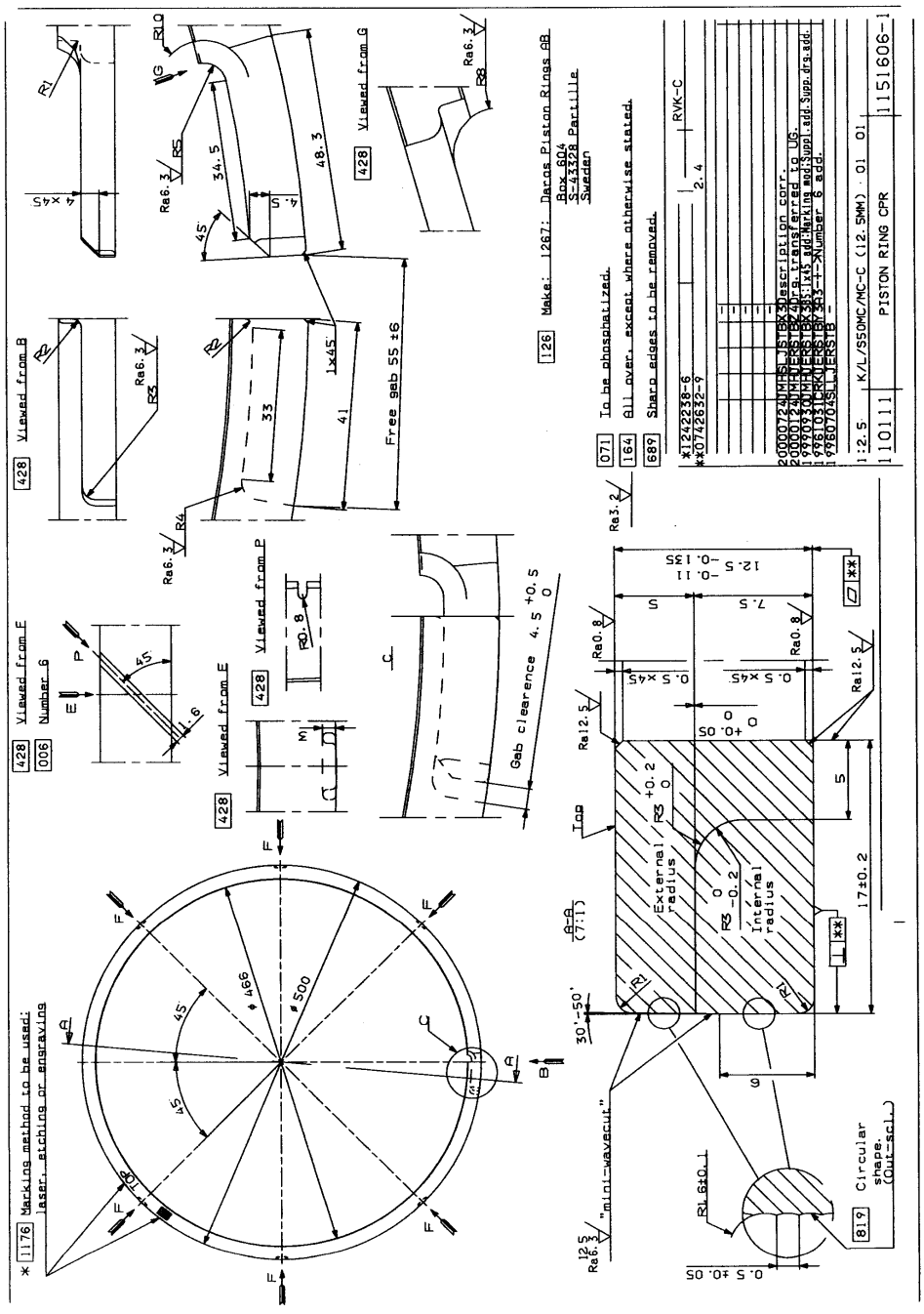

Figure A.6: Piston Ring CPR

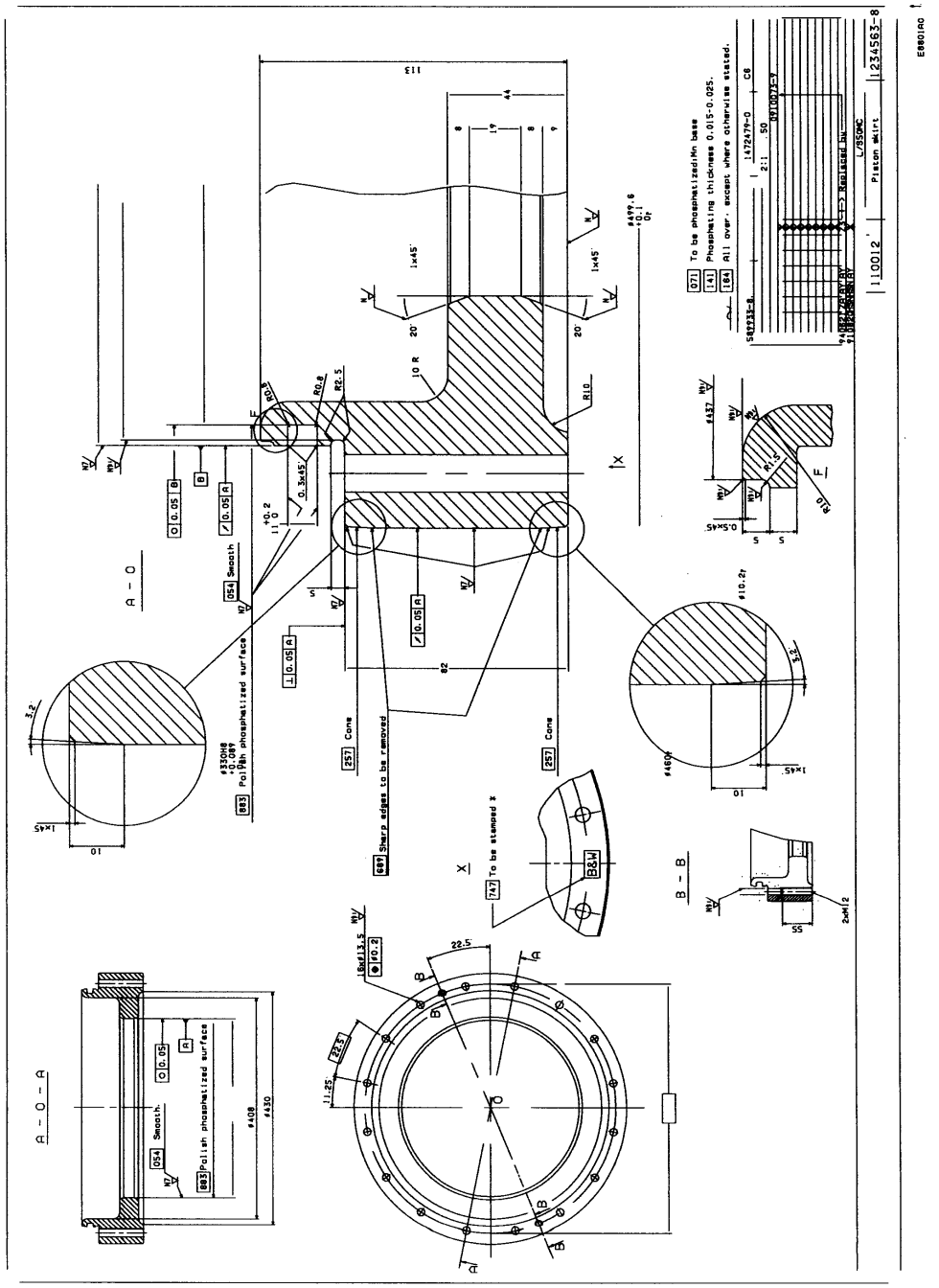

Figure A.7: Piston Skirt

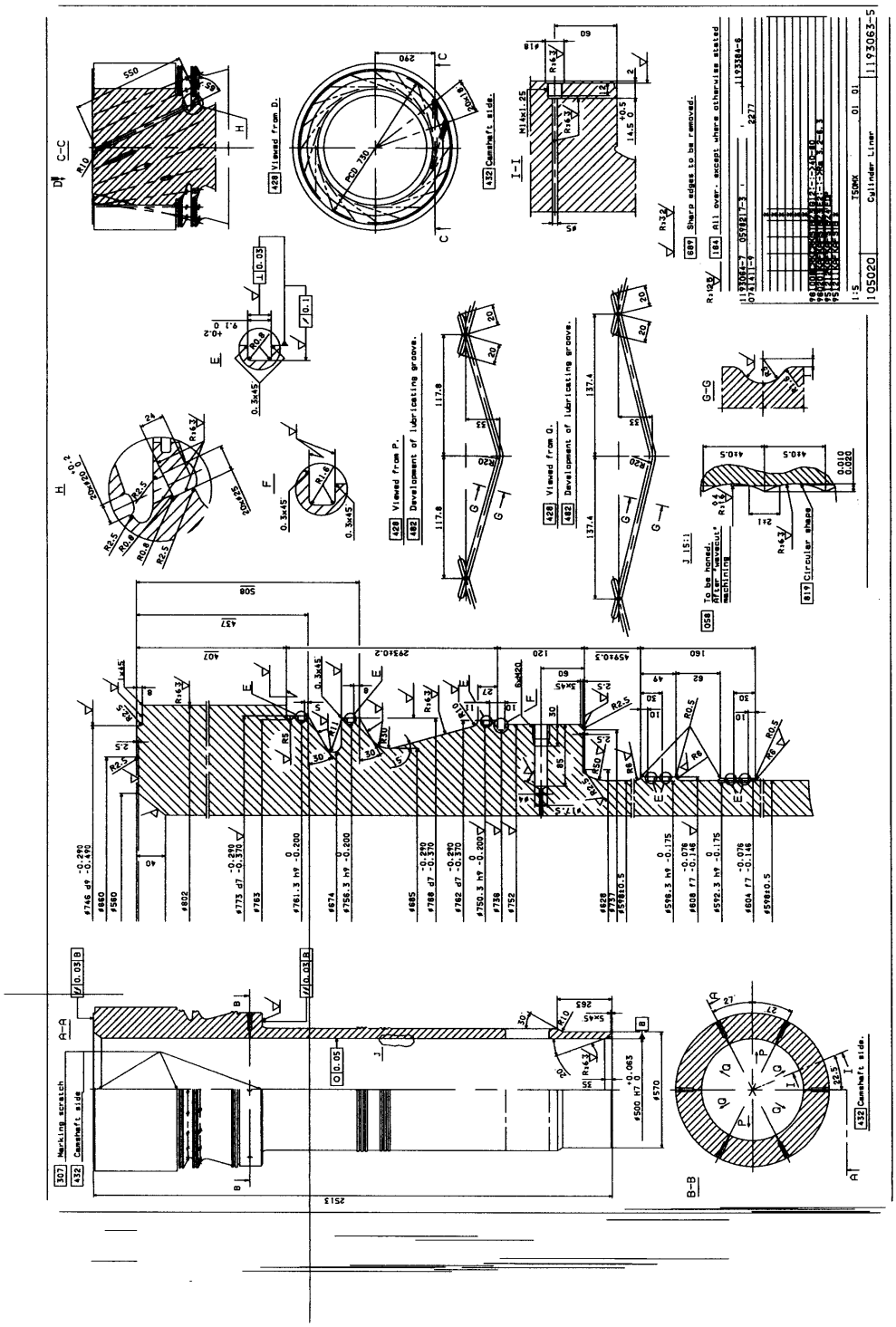

Figure A.8: Liner

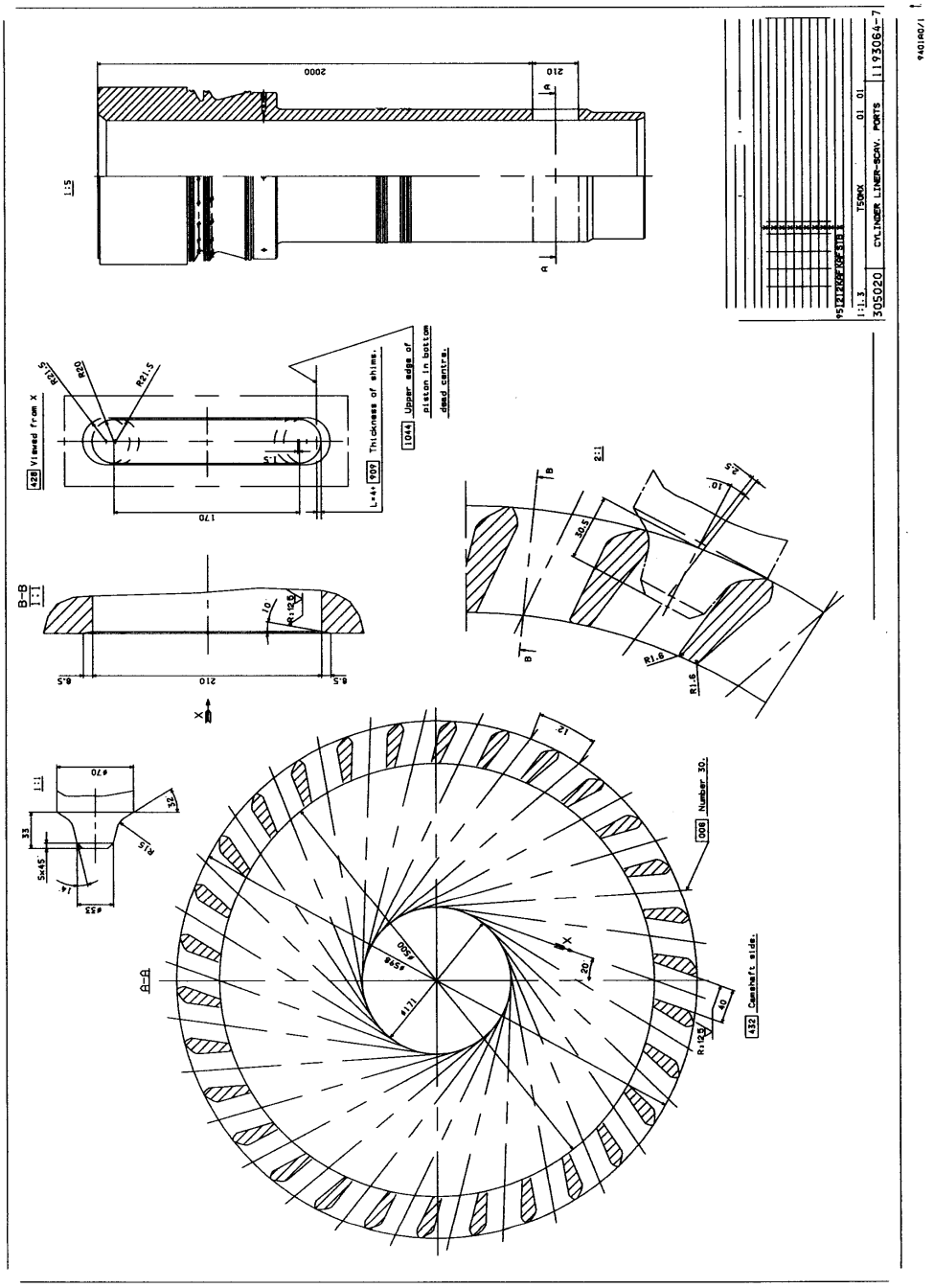

Figure A.9: Scavenging Ports

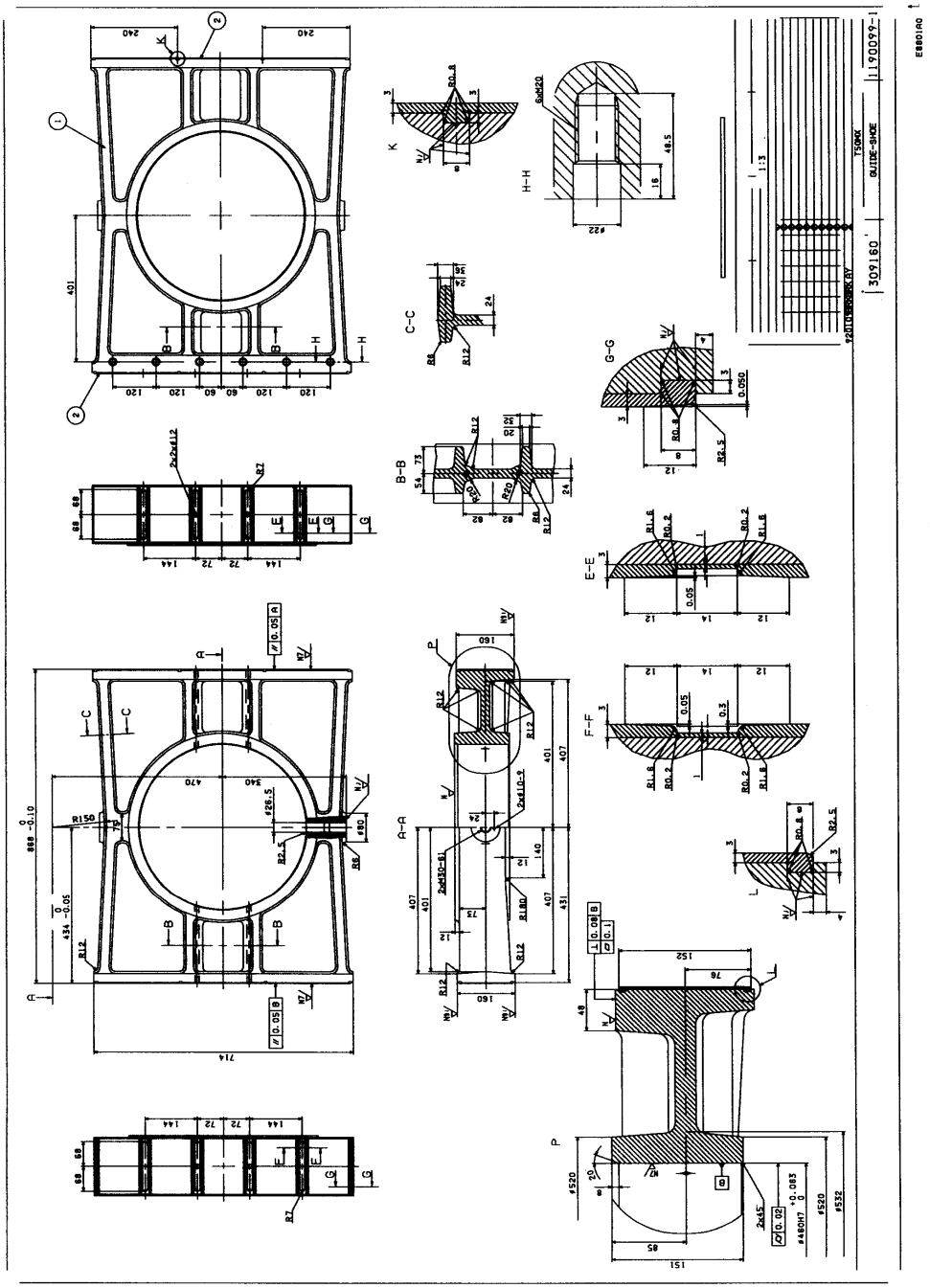

Figure A.10: Guide Shoe

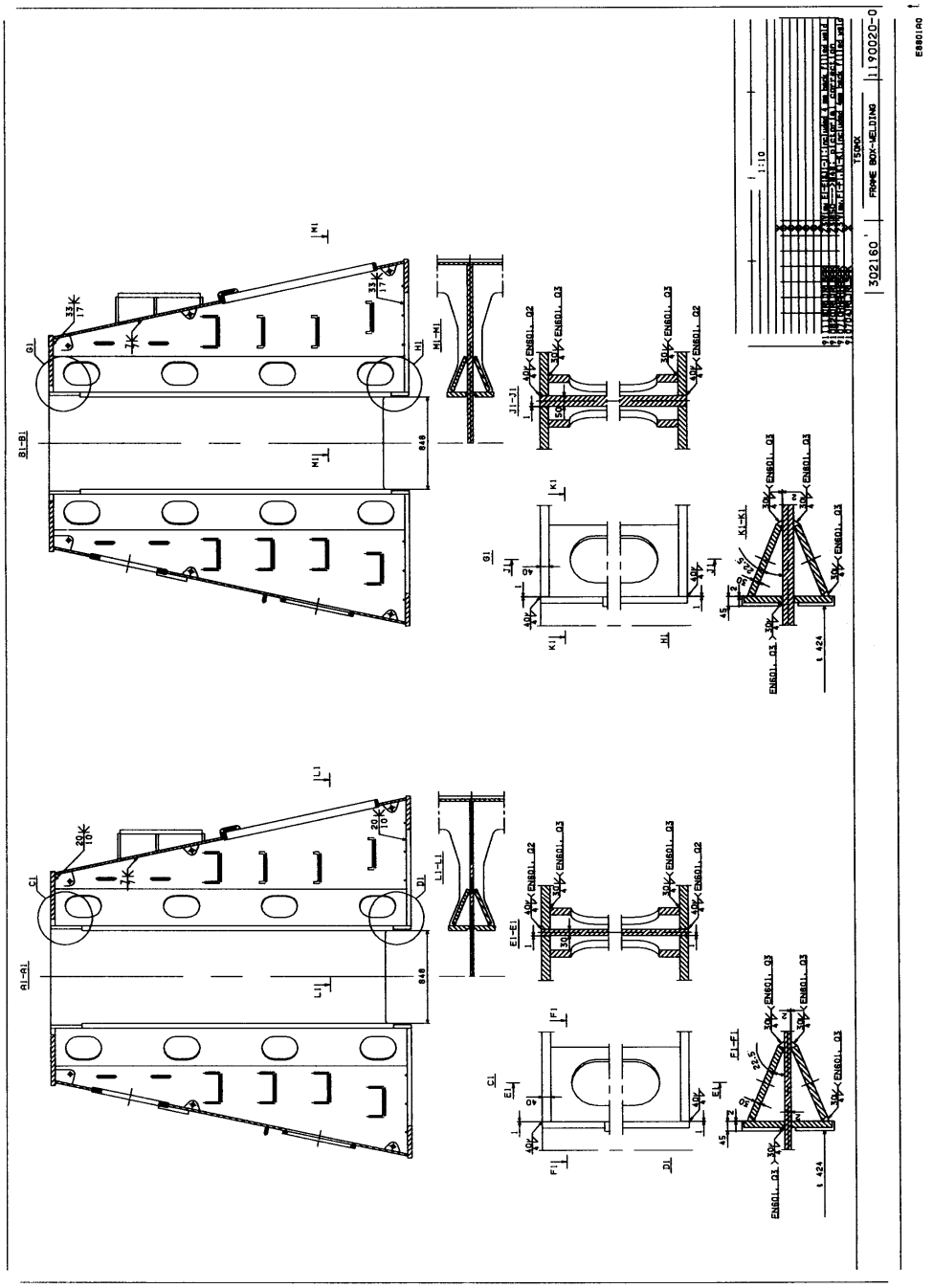

Figure A.11: Frame Box

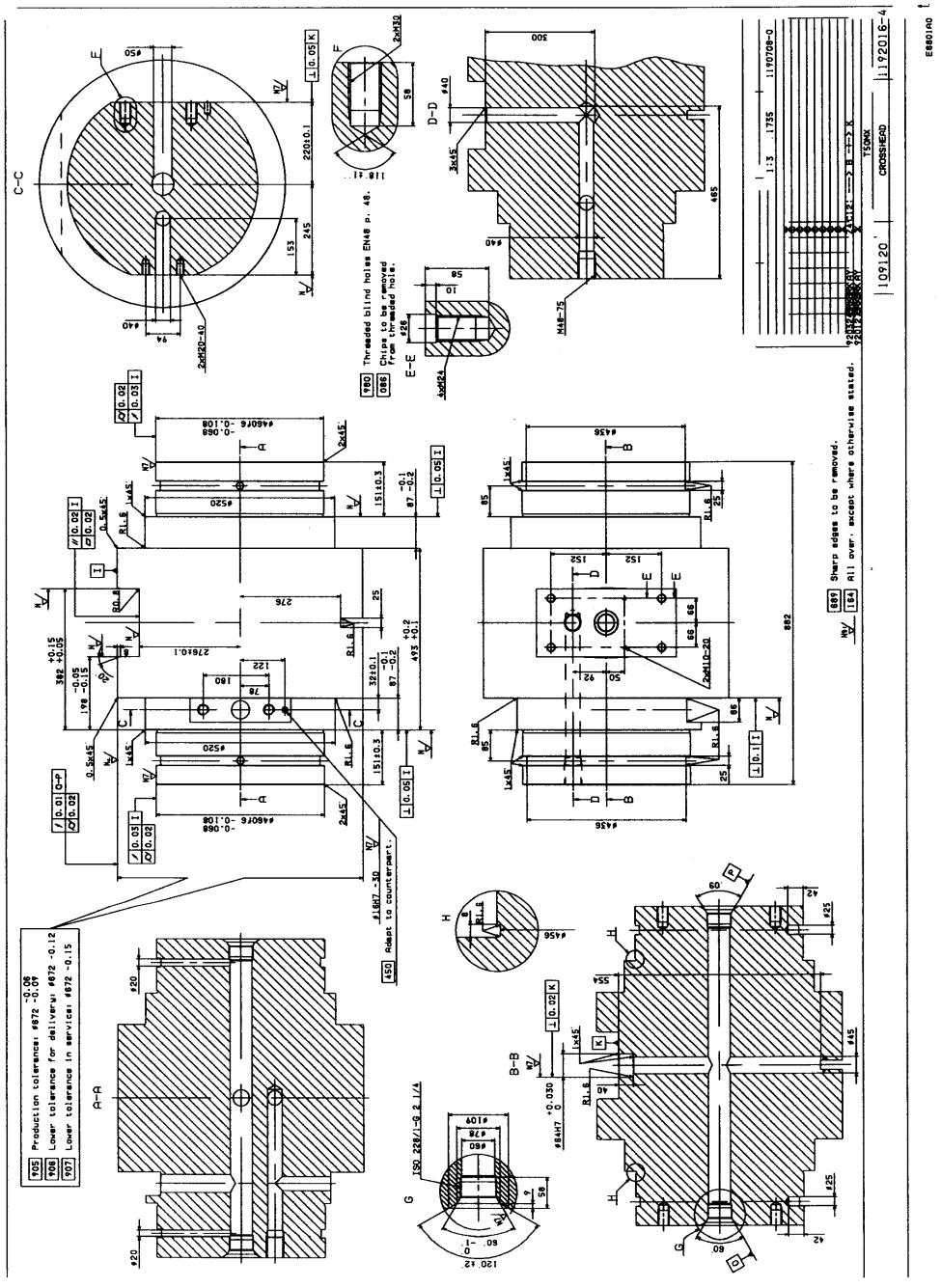

Figure A.12: Crosshead

A.2 Pressure Drop in Piston Ring Package

Since a very important parameter on the piston ring performance depends on the pressure drop a model for predicting pressure drop in a piston ring package has been made. This has been done by adopting the model originally proposed by Ting and Mayer [1974a], Ting and Mayer [1974b] superimposing some extra effects. The included extra effects is the thermal expansion of the components such that the time dependency of the ring gab sizes can be included.
This model assumes that the pressure in between the piston rings can be seen as an unsteady adiabatic flow fulfilling the perfect gas law. It is assumed that the flow is one-dimensional and that the discharge coefficient is constant. Furthermore, is assumed that the pressure in the combustion chamber and below the position is independent of the flow through the ring gabs. The flow system looks like the one presented in figure A.13.

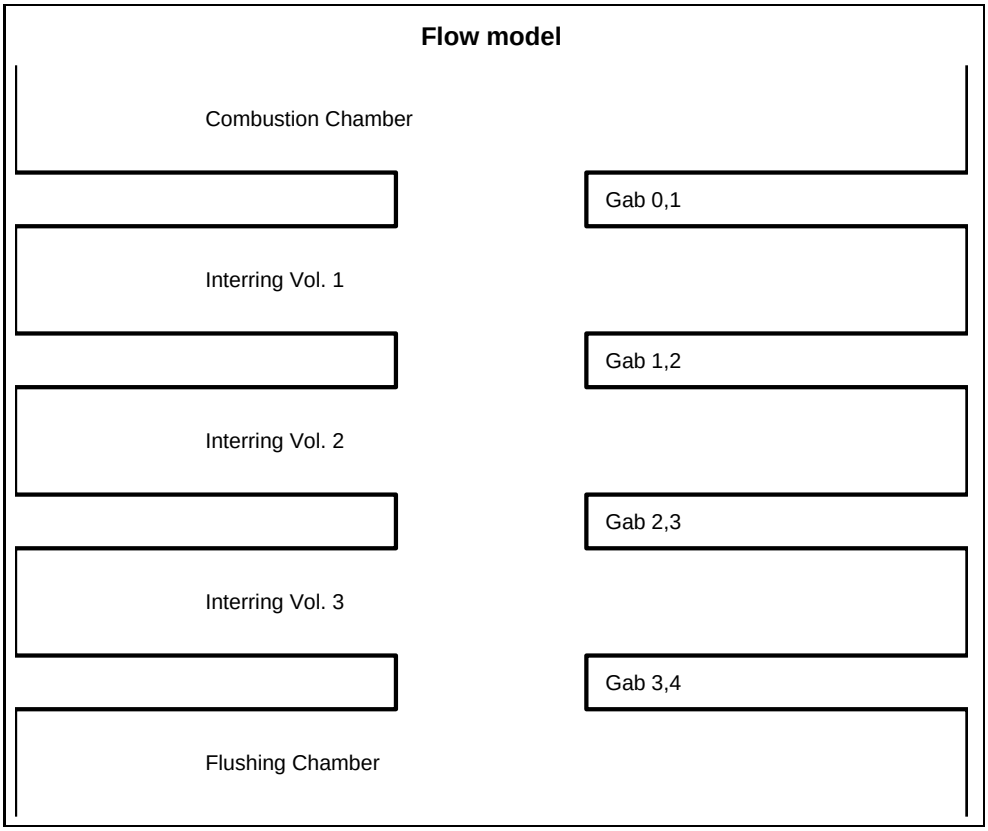

Figure A.13: Flow model for pressure drop calculation

There are some notes concerning the model. **Characteristics for gab i-1,i:**

- Ring gab area ($A_{i-1,i}$)
- Discharge Coefficient ($K_{i-1,i}$)

Case	
1	$p_{i-1} > p_i > p_{+1}$
2	$p_{i-1} > p_i < p_{i+1}$
3	$p_{i-1} < p_i < p_{i+1}$
4	$p_{i-1} < p_i > p_{i+1}$

Figure A.14: Flow possibilities in inter ring volume i

Characteristics for inter ring volume i:

- Mass of gas (M_i)
- Temperature of gas (T_i)
- Pressure of gas (P_i)

It is assumed that all the flow is passing through the piston ring gabs.

A.2.1 Equations

Focusing on one chamber - inter ring volume i.
The mass of gas in the chamber at time t_i is given by A.1

$$M_i = \frac{p_i V_i}{R_g T_i} \tag{A.1}$$

However, steady state is not present because gas flows in and out of the chamber. There are four possible flow conditions and they are listed in figure A.14.
This gives four different equations depending on which one of the the cases it is.
Assume case 2 is present. The flow through Gab $i-1, i$ is presented in (A.2) and the flow through Gab $i, i+1$ is presented in (A.3).

$$\frac{dM_{i-1}}{dt} = K_c A_{i-1,i} \sqrt{\frac{2gk}{R_g(k-1)T_{i-1}}} p_{i-1} (\frac{p_i}{p_{i-1}})^{\frac{1}{k}} \sqrt{1 - (\frac{p_i}{p_{i-1}})^{\frac{k-1}{k}}} \tag{A.2}$$

$$\frac{dM_{i+1}}{dt} = -K_c A_{i,i+1} \sqrt{\frac{2gk}{R_g(k-1)T_{i+1}}} p_{i+1} (\frac{p_i}{p_{i+1}})^{\frac{1}{k}} \sqrt{1 - (\frac{p_i}{p_{i+1}})^{\frac{k-1}{k}}} \tag{A.3}$$

Observing the perfect gas law in differential form the pressure gradient due to the flow becomes:

$$\frac{dp_i}{dt} = T_i \frac{V_i}{V_o} \left[\frac{dM_{i-1}}{dt} + \frac{dM_{i+1}}{dt} \right] \tag{A.4}$$

This is done for each ring gab and that gives a system of first order differential equations. Since there are 3 inter ring volumes and 4 ring gabs this gives a system of equations consisting

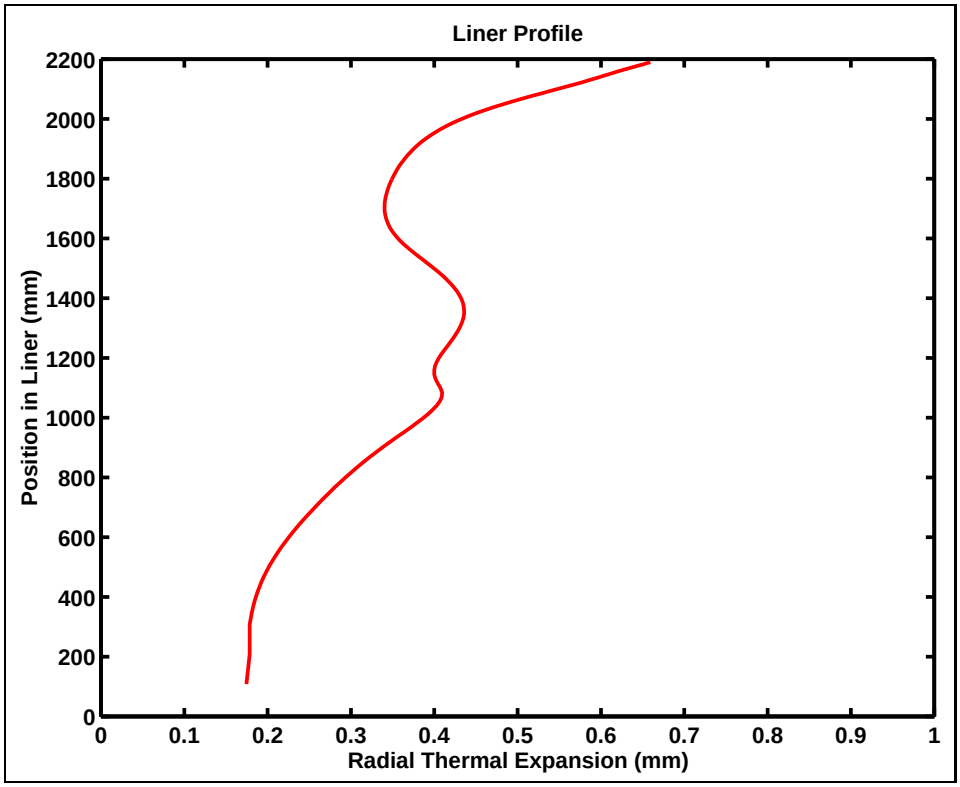

Figure A.15: Thermal expansion of liner

of 7 first order differential equations. This boundary value problem can be solved using an appropriate time stepping technique. Since a resolution of 2048 calculation steps to cover 360 degrees a simple time stepping technique has been used.

Limitations of the flow.

If the pressure difference between 2 adjacent inter ring volumes becomes critical action must be taken for that. The critical pressure ratio is given by

$$\frac{p_{crit}}{p_i} = \left(\frac{2}{k+1}\right)^{\frac{k}{k-1}} \tag{A.5}$$

Once the critical pressure ratio is reached the flow rate stays constant

A.2.2 Thermal Expansion

The size of the ring gab depends on the position of the piston since the liner is thermally expanded. The thermal distortion is presented in figure A.15. It is seen that the size of the radial expansion varies from 0.15 to 0.7 mm. This can be converted to the ring gab and that shows that the variation is from $1mm$ to $4.2mm$ depending on the piston position and that is a large variation considering that the ring gab is $4.5mm$ on a new ring.

The piston thermally expands. Calculated values (FEM-calculation) are used for the thermal expansion model.

Ring	Temperature(ΔT)	Elongation (mm)
1	200	3.48
2	170	2.96
3	150	2.62
4	100	1.74

Figure A.16: Temperature of rings

Lastly the piston rings are thermally expanded. It is assumed that the thermal expansion of a piston ring can be calculated using an average temperature of the current piston ring. Temperatures of the piston rings have shown that the rings are heated to the values given in figure A.16

A.2.3 Ring Lift

Ring lift has been included in the model. Including this gives a system of equations. This is solved by monitoring the forces in axial direction such that the contact pressure on the lower ring land is monitored.

$$M_{ring}\ddot{X} = F_{press} - F_{contact} - F_{friction} \tag{A.6}$$

Neglecting gravity and friction and solving for $F_{contact}$ reduces the system of equation to:

$$F_{contact} = F_{press} - M_{ring}\ddot{X} \tag{A.7}$$

Ring data: $M_{ring} = 2.9kg$, $550N < M_{ring}\ddot{X} < 750N$
The force due to the pressure is in the range $0N < F_{pres} < 900kN$
If $F_{contact} < 0$ then ring lift is present. This changes the inter ring volumes Since the term $M_{ring}\ddot{X}$ is not significant this term will be neglected. Further examination shows that ring 1 will lift about 35 degrees after TDC. From the measurements of the inter ring pressures it does not seem that the other rings will lift in the high pressure region of the stroke. The calculated lifts in the piston pack can be seen in figure A.17.

A.2.4 Result of Pressure Drop Calculation

Using the model described above and the input data for the current engine the calculations concerning pressure drop has been conducted. The calculated pressures in the piston pack can be seen in figure A.18.
Some measurements were made of the inter ring pressures with sensors mounted in the piston. The measured values can be seen in figure A.19.
These data will be used for input values for the OFT history calculation.

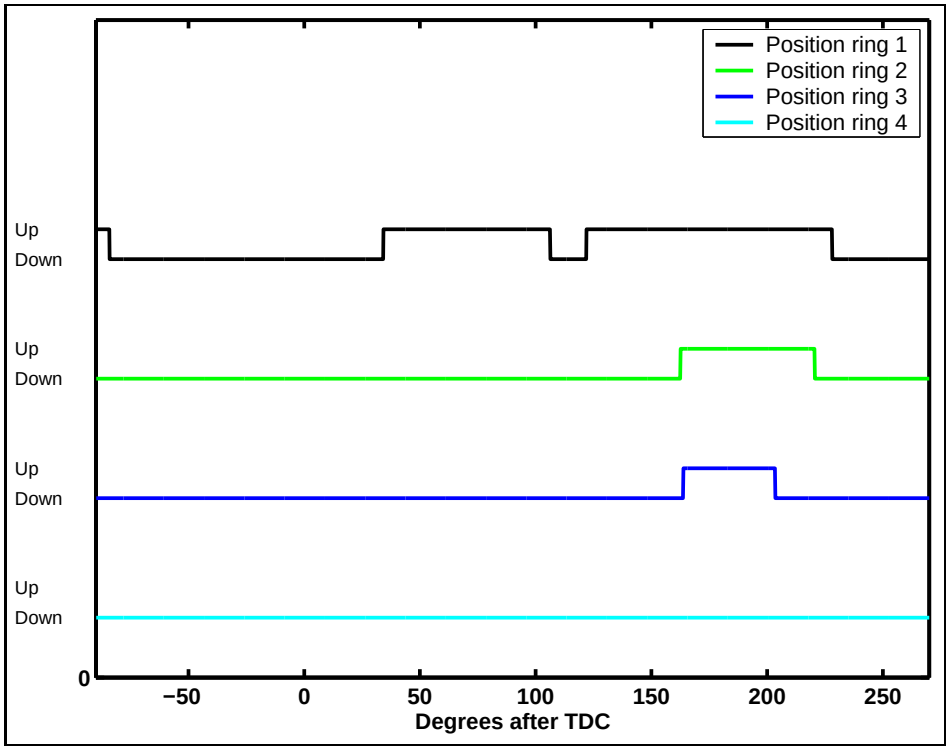

Figure A.17: Ring lift in piston pack

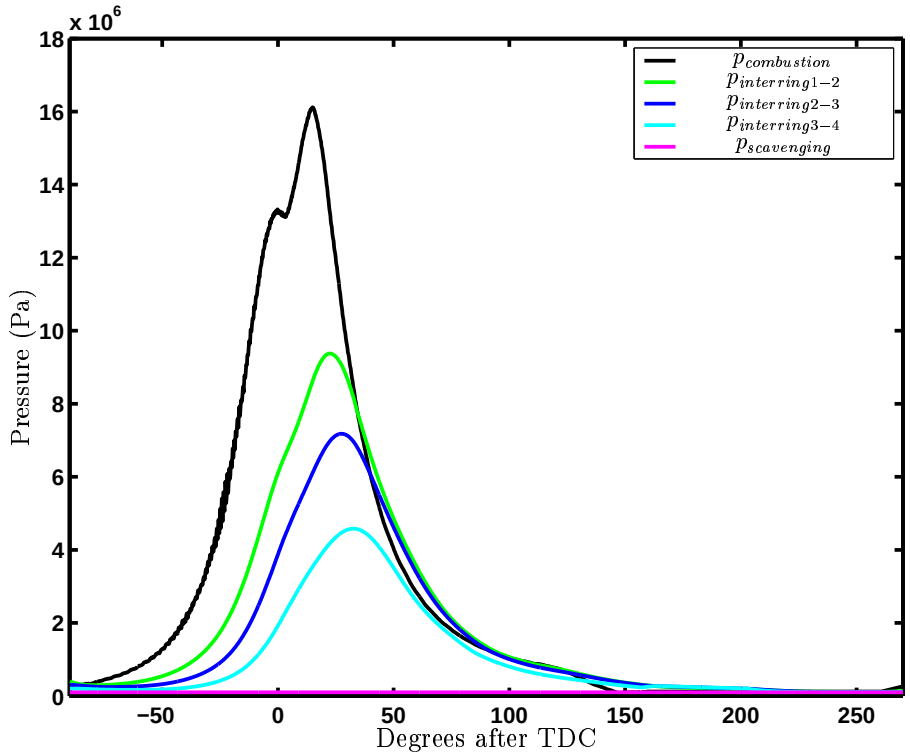

Figure A.18: Pressure in piston ring package

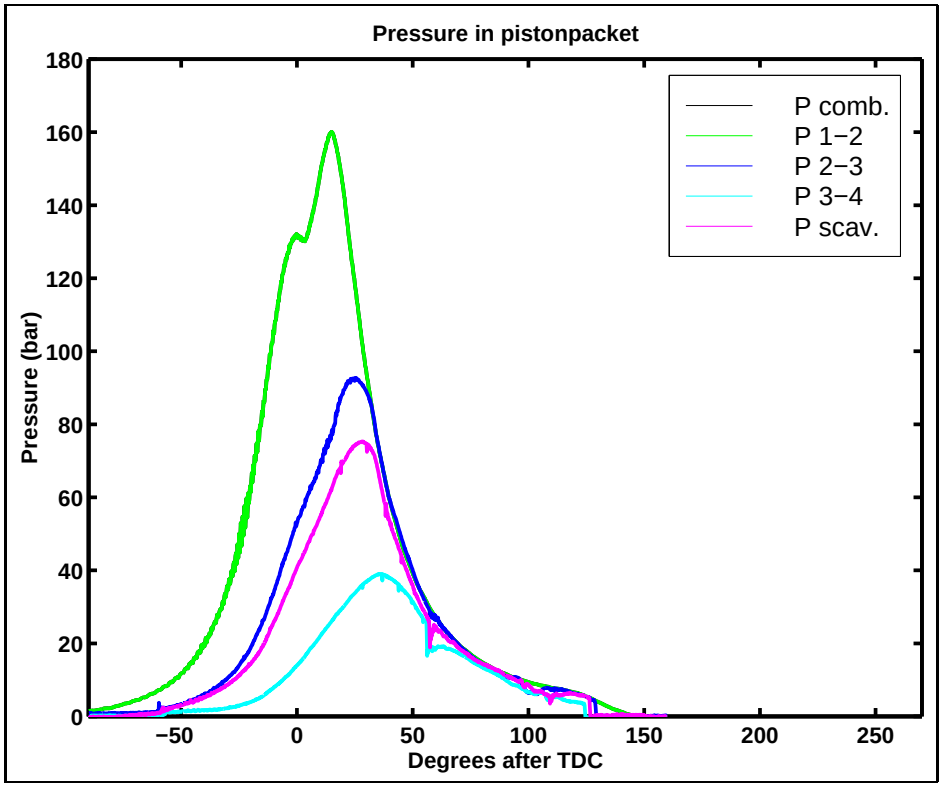

Figure A.19: Measured pressure distribution in piston pack

Bibliography

S. Abanteriba. *Vergleich der Reibungsverluste eines Zweitakt-Kreuzkopf- und eines Viertakt-Tauchkolbenmotors gleicher Zylinderleistung.* VDI Forschritt-Berichte, Reihe 12, Nr. 151, 1995. ISBN 3-18-145112-6.

5.6 Ansys. *Ansys User Manual.* Ansys, Inc., 1999.

D. Dowson, P.N. Economou, B.L. Ruddy, P.J. Strachan, and A.J.S. Baker. Piston ring lubrication - part ii theoretical analysis of a single ring and a complete ring pack. *Energy Conservation Through Fluif Film Lubrication Technology: Frontiers in Research and Design*, ASME:23–52, 1979.

M. Fillon, J. Frene, and C. Chan Hew Wai. Dynamic analysis of tilting-pad journal bearing - influence of pad deformations. *Journal of Tribology*, pages 621–628, 1994.

S. Furuhama and M. Takiguchi. Measurement of piston friction force in actual operating diesel engines. *SAE*, 790855:1447–1451, 1979.

J. A. Greenwood and J. H. Tripp. The contact of two nominally flat rough surfaces. *Institution of Mechanical Engineers*, IME. Proceedings,185:625–633, 1971.

M. Halsband. Measurement of piston assembly friction in small high speed gasoline engines. *Proceedings of the International Tribology Conference*, Yokohama:1447–1451, 1995.

T. Hamatake, Y. Wakuri, and A. T. Kitahara. Some studies on the tribology of diesel engineas. *Proceedings CIMAC*, 4, 2001.

B.J. Hamrock. *Fundamentals of Fluid Film Lubrication.* McGraw-Hill, 1994. ISBN 0-07-113356-9.

B.J. Hamrock, Esfahanian M., and Elsharkawy A.A. On the hydrodynamic lubrication of piston rings. *Lubrication Science*, 10-4, August 1998.

Dong-Chul Han and Jae-Seon Lee. Analysis of the piston ring lubrication with a new boundary condition. *Tribology International*, 31,number 12:753–760, 1998.

P. Klit and A. Vølund. Shaft center orbit for dynamically loaded journal bearings. *Proceedings of Nordtrib 2002*, CD-ROM, 2002.

K. Liu, Y.B. Xie, and C.L. Gui. A two-dimensional lubrication study of piston ring pack. *Proc. Institution for Mechanical Engineers*, 212:215–220, 1998.

J. W. Lund. Dynamic coefficients for fluid film journal bearings. *Journal of Lubricating Technology, ASME*, 89, Series F:605–616, 1968.

J. W. Lund and K. K. Thomsen. A calculation method and data for the dynamic coefficients of oil-lubricated journal bearings. *Topics in Fluid Film Bearing and Rotor Bearing System Design and Optimization, The Design Engineering Conference, Chicago, Illinois*, pages 1–28, 1978.

H.U. Mehmet and D.J. Patterson. Measurement of piston and ring assembly friction instantaneous imep method. *SAE*, 830416:1–14, 1983.

H.U. Mehmet and D.J. Patterson. Effect of some lubricant and engine variables on instantaneous piston and ring assembly friction. *SAE, International Congress & Exposition Detroit, Michigan*, 840178:1–13, 1984.

H. Nakai, N. Ino, and H. Hashimoto. Piston-ring lubrication problems for refrigeration compressors considering combined effects of oil supply quantity and surface roughness. *Journal of Tribology*, Transactions of the ASME, 118:286–291, 1996.

N. Patir and H.S. Cheng. An average flow model for determining effects of three-dimensional roughness on partial hydrodynamic lubrication. *Transactions of ASME*, 108:12–17, 1978.

N. Patir and H.S. Cheng. Application of average flow model to lubrication between rough sliding surfaces. *Journal of Lubrication*, Technology Transactions of the ASME,101:220–230, 1979.

C.S. Ping and A. Susumu. Piston ring pack friction of an automotive engine using a mixed lubrication model. *SAE*, 931937:1–15, 1993.

W.H. Press, S. A. Teukolsky, V. T. Vetterling, and B. P. Flannery. *Numerical Recipes in C : The Art of Scientific Computing*. Cambridge University Press, 1996. ISBN 0-512-43108-5.

M. Priest, D. Dowson, and C.M. Taylor. Automobile engine - approaching thesurface. *The Institution of Engineers Australia*, Austrib '98:353–363, 1998.

M. Priest, D. Dowson, and C.M. Taylor. Theoretical modelling of cavitation in piston ring lubrication. *Journal of Mechanical Engineering Science*, Proceedings Part C,214:435–447, 2000.

C. M. Rodkiewicz and Dayson C. The thermally boosted oil lubricated sliding thrust bearing. *Transactions of ASME*, july:322–328, 1974.

S. M. Rohde and Ping Oh Kong. A thermoelastohydrodynamic analysis of a finite slider bearing. *Transactions of ASME*, july:450–460, 1975.

B.L. Ruddy, D. Dowson, and P.N. Economus. A theoretical analysis of the twin land type of oil-control piston ring. *Journal of Mechanical Engineering Science*, 23 no. 2:51–62, 1981.

B.L. Ruddy and M.L. Hildyard. A review of tribological aspects of piston assembly design. *Leeds-Lyon 1993*, pages 93–103, 1993.

S. Saburi, Dowson D., and Taylor C.M. An analytical stydy of oil film thickness between piston rings and a cylinder liner of a long stroke and slow speed marine diesel engine. *Proceedings of the International Tribology Conference*, Yokohoma:1435–1440, 1995.

S. Sanda, M. Murukama, and et al. Analysis of lubrication of a piston ring package. *JSME International Journal*, Series B vol 40:478–486, 1997.

I. Sherrington, D.G. Clarke, and E.H. Smith. The floating liner method applied to measure instantaneous piston assembly friction force in a motored engines. *CIMAC*, pages 1447–1451, 1991.

I. Sherrington, M. T. Ma, and E.H. Smith. A three-dimensional analysis of piston ring lubrication part1:modelling. *Proc. Institution for Mechanical Engineers*, 209:1–14, 1995a.

I. Sherrington, M. T. Ma, and E.H. Smith. A three-dimensional analysis of piston ring lubrication part2:sensitivity analysis. *Proc. Institution for Mechanical Engineers*, 209:15–27, 1995b.

A. Stodola. Kritische wellenstörung infolge der nachgebigkeitdes oelpolsters in lager. *Schweizerische Bauzeitung*, 85:265–266, 1925.

K. K. Thomsen. Teoretisk og eksperimental undersøgelse af hydrodynamiske radiallejers stabilitetsforhold. *Technical University of Denmark*, phd thesis, 1975.

L.L. Ting and J.E. Mayer. Piston ring lubrication and cyliner bore wear analysis, part i theory. *Journal of Lubrication Technology*, Transactions of the ASME, 96:305–314, 1974a.

L.L. Ting and J.E. Mayer. Piston ring lubrication and cyliner bore wear analysis, part ii theory verification. *Journal of Lubrication*, Technology Transactions of the ASME, 95: 258–266, 1974b.

A. Vølund. On the interaction between structure and oil film of a guide shoe bearing. *Proceedings of the 2nd World Tribology Conrerence*, CD-ROM, 2001.

A. Vølund. Measurement of oil film thickness and friction of the guide shoe bearing in a large marine diesel engine. *Proceedings of the 10th Nordtrib*, CD-ROM, 2002.

A. Vølund. German patent application. *No 10222312.0*, Filed: 18 may 2002a.

A. Vølund. German patent application. *No 10222312.2*, Filed: 18 may 2002b.

A. Vølund and P. Klit. Guide bearing characteristics. *Proceedings of the 9th Nordtrib*, 2: 521–531, 2000.

Y. Wakuri, T. Hamatake, and A. T. Kitahara. Friction characteristics of piston rings in diesel engines. *Proceedings of the International Tribology Conference*, Yokohama:1453–1458, 1995.

Q. Yang and Jr. T.G. Keith. Two-dimensional piston ring lubrication part1: Rigid ring and liner solution. *Tribology Transactions*, 39:757–768, 1996a.

Q. Yang and Jr. T.G. Keith. Two-dimensional piston ring lubrication partii: Elastic ring considerations. *Tribology Transactions*, 39:870–880, 1996b.